Tunable Thermal Bioswitches as a Control Modality for Next Generation Therapeutics

Thesis by

Dan Piraner

In Partial Fulfillment of the Requirements for

the degree of

Biochemistry and Molecular Biophysics

CALIFORNIA INSTITUTE OF TECHNOLOGY

Pasadena, California

2019

(Defended February 26, 2019)

Dan Piraner
ORCID: 0000-0003-3857-9487

ACKNOWLEDGEMENTS

This thesis was completed due to the help, support, and encouragement of numerous friends and mentors. I would like to first express my gratitude to Professor Mikhail Shapiro for taking a chance on me when he arrived at Caltech and guiding me throughout this journey. I know that my mind could bounce around like a particle in a box, and I am grateful for your patience and guidance, and for setting reasonable boundary conditions while letting me explore and sometimes tunnel beyond them. Your enthusiasm is infectious and inspiring, and I am thrilled to have had the experience of learning how to do science under your mentorship. I am also indebted to my committee members, Profs. Frances Arnold, Dave Tirrell, and Ellen Rothenberg, for discussions, suggestions, and helpful critiques. Thank you to Frances and Dave again for the experience of working in your labs – I learned lessons that served me well for the remainder of my graduate career. Ellen, thank you for our delightful discussions – I never got to work with you directly, but you somehow were always on top of my project and progress, and I really appreciate your advice as I discovered how fascinating immunology is and started to explore applications therein.

When I began my PhD, I had little in the way of wet lab experience and a lot in the way of doubts and confusion. I cannot express enough how much I appreciate, especially in retrospect, the patience and guidance of Prof. Fei Sun, who mentored me during my first rotation in the Arnold Lab. I hope that my follies during the first few months were as amusing to you then as they are to me now. Thanks as well to Alborz Mahdavi, who supervised me during my rotation in the Tirrell Lab and provided me with invaluable academic and career advice.

It seems unfair to single out anyone in the Shapiro Lab by name, as everyone has made such a delightful impact on my grad school experience. Nevertheless, a few people must be explicitly mentioned. Pradeep, being part of the first batch of Shapiro students with you was amazing. I'm glad we got to share so many adventures. Chapter 3 of this thesis could not have been completed without Mohamad Abedi. I've never had a chance to work with such a uniquely driven researcher before – I hope that someday I will again have a collaboration

that's so genuinely fulfilling, fun, and productive. Thank you also to Anupama Lakshmanan for always having a smile and kind words of encouragement. I sincerely value the privilege of having mentored Di Wu and Echo Wu during their early graduate careers, as well as Sasha Zemsky and Yiwei Jiang in their undergraduate research. I learned a lot about teaching from each of you – sorry that you had to be my guinea pigs. Thanks as well to friends outside of Spalding, particularly to David Angeles, Heather Curtis, and Sushant Sundaresh for all of the wonderful memories. And thank you to Brittany Moser, who made the first observation of TlpA-gated gene expression in our lab when it was hiding in plain sight. Sometimes it's not obvious that the system you've painstakingly built actually works, and you have to try a little harder to see it – thanks for teaching me that.

One of the most important acknowledgements I can make is to my family. To my parents, Ilya and Irina Piraner, for raising me and instilling in me the spirit of hard effort and appreciation for my opportunities. To my grandparents, Lev and Liza Piraner and Mark and Anna Zelikman for being proud of me and letting me know it. To my brother Alex and sister in-law Stephanie, for trailblazing the way to Southern California and always being there when I needed support. To my extended family, for extensive encouragement. And again to Brittany Moser, who is not only a fantastic scientist but also a wonderful partner in life, and who has always lifted me up without reservation. I'm thrilled that the rest of our life journeys, both in and out of science, will be shared.

ABSTRACT

Synthetic biology is rapidly contributing to the field of therapeutic development to create increasingly potent agents for the treatment of a variety of diseases. These living "designer therapeutics" are capable of integrating multiple sensory inputs into decision making processes to unleash an array of powerful signaling and effector responses. Included in the great therapeutic potential of these agents, however, is a cognate risk of severe toxicity resulting from runaway on-target or erroneously induced off-target activity. The ability to remotely control engineered therapeutic cells after deployment into patient tissue would drastically reduce the potential dangers of such interventions. However, among existing biological control methods, systemic chemical administration typically lacks the spatial precision needed to modulate activity at specific anatomical locations, while optical approaches suffer from poor light penetration into biological tissue. On the other hand, temperature can be controlled both globally and locally — at depth — using technologies such as focused ultrasound, infrared light and magnetic particle hyperthermia. In addition, body temperature can serve as an indicator of the patient's condition. Overall, temperature is a versatile signal which can provide a handle to actuate a biological response for the control of therapeutic agents.

In this thesis, a tunable and modular system is developed to respond to thermal perturbations in cellular environments and affect a biological response. At the core of this system is a pair of single-component thermosensing proteins whose dimerization is strongly and sharply coupled to their thermal environment. These domains are first utilized in their native context as negative regulators of transcription in prokaryotes, wherein they are integrated into genetic circuits to control expression of reporter genes. These gene circuits show strong and sharp thermal activation and can be utilized in multiplex to affect higher order logical operations. Cells imbued with these circuits demonstrate transcriptional activation upon global thermal elevation within the host animal within which they reside (fever) or upon a spatiotemporally localized temperature shift imparted by focused ultrasound hyperthermia. In subsequent work, one of these bioswitches is introduced into mammalian cells where it functions as a modular Protein-Protein Interaction (PPI) domain, conferring temperature-dependent protein localization.

The work conducted in this thesis demonstrates the feasibility of utilizing temperature as a stimulus for biological activity. This technology can be harnessed to regulate therapeutically relevant processes in bacterial and mammalian cells such as transcriptional regulation and protein localization, and potentially broader protein function. The thermal bioswitches described herein could be utilized to engineer an array of research tools and biological therapies with actuation driven by spatiotemporally precise noninvasively applied stimuli or by real-time sensing of host conditions.

PUBLISHED CONTENT AND CONTRIBUTIONS

Piraner, D. et al. (2017). “Tunable thermal bioswitches for in vivo control of microbial therapeutics”. In: *Nature Chemical Biology* 13, pp. 75–80. doi: 10.1038/nchembio.2233

D.P. participated in the conception of the project, constructed and tested genetic circuits in vitro and in vivo, prepared the data, and participated in the writing of the manuscript.

Piraner, D. et al. (2017). “Going Deeper: Biomolecular Tools for Acoustic and Magnetic Imaging and Control of Cellular Function”. In: *Biochemistry* 56.39, pp. 5202-5209. doi: 10.1021/acs.biochem.7b00443

D.P. participated in the writing of the manuscript.

TABLE OF CONTENTS

LIST OF ILLUSTRATIONS AND/OR TABLES

C h a p t e r 1

LIVING CELLS AS A NEXT-GENERATION THERAPEUTIC MODALITY

1.1: The Necessity of Novel Therapeutic Platforms

The difficulty of treating diseases at the molecular scale has driven a great deal of innovation, and a corresponding increase in complexity, in the structure of therapeutic agents[1]. Initially, drugs consisted of small molecules which were isolated from natural sources[2]. Industrialization brought about a revolution in the capabilities of organic synthesis, leading to the creation of natural products from non-natural precursors, the derivatization of these molecules into novel chemical species, and the discovery of new medicinal chemicals[3]. The advent of high throughput screening brought about yet another method of developing small molecules into therapeutic entities, enabling diverse sets of synthetic chemicals to be rapidly examined for their ability to display potentially beneficial activities[4]. As the field of molecular biology developed, rational drug design became a viable proposition. Overall, the pharmaceutical industry has been largely dominated by small molecule drugs to date[5].

Despite the enormous success of small molecules at treating disease, a stubborn set of diseases remains refractory to treatment. Illnesses such as multi-drug resistant infections[6], many viral infections[7–9], neurodegenerative disorders such as dementias and motor impairments[10–13], and chemotherapeutic-unresponsive cancers[14] remain incurable and only partially treatable with conventional small molecule methods. These failings often stem from the fundamental structural properties of small organic molecules: their lack of size inherently

results in a relatively small contact area with their therapeutic targets, and their simplicity precludes them from executing logical computations such as sensing their environments and converting signals from their surroundings into structural rearrangements and altered modes of action[15,16]. The size of small molecule drugs limits their targets to those containing "druggable pockets," or molecular crevices which are able to maximize topological interactions with the contact surface of the drug molecule, and not all disease-driving molecules contain such sites. Furthermore, the lack of environmental sensing results in biological activity both "on target" (at the site of disease) and "off target" (in healthy tissue), resulting in side effects which are often dose-limiting[17,18].

To address the limitations in the specificity of small molecule drugs, new targeting systems are under constant development. Most notably, lipid-based drug carriers such as micelles and liposomes can overcome some of the targeting challenges associated with bare small molecules. In the context of cancer, the larger size of liposomes renders them susceptible to the Enhanced Permeability and Retention (EPR) effect, resulting in preferential deposition in the tumor via escape from the local abnormal and leaky vasculature[19]. This effect can be augmented by decorating the lipid coat with molecular targeting moieties, thereby enhancing drug deposition within specific environments[20]. Using environmentally-labile chemical linkages such as pH-cleavable bonds, these targeting agents can even induce transcytosis into physiological compartments that are traditionally difficult for therapeutic agents to access[21]. While nanoparticle-based drug delivery shows great promise, the method is not a panacea. Ultimately the small molecule payload cannot, upon delivery, discriminate between diseased vs. healthy tissue, and the ultimate therapeutic potency depends on the biological activity of the drug rather than of the carrier, thereby limiting molecular targets to those within the

druggable repertoire. Additionally, EPR-directed accumulation in tumors, while significant, leads to on-target delivery slightly in excess of off-target deposition in vital organs[22]. Furthermore, single-target guidance of the nanoparticles is often insufficient for disease discrimination, although more complex targeting strategies are in development[23,24]. Finally, the chemical simplicity of lipid membranes limits the variety of behaviors that these nanoparticles and drug carriers can display relative to more complicated, dynamic, and energy-driven systems, and these behaviors are often responsive to broad biological effects such as pH rather than the subtle molecular differences that can differentiate diseased tissue from an off-target, healthy environment.

In the 1980s, antibody-based therapeutics were introduced to the clinic[25]. Unlike traditional drugs, antibodies are large, complicated, and multifunctional molecules which can overcome some of the key disadvantages of small compounds. Antibodies contain a relatively large and genetically designable binding surface suitable for targeting non-cleft-like molecular surfaces, thereby greatly expanding the array of druggable protein targets[26]. Furthermore, in addition to simple binding and inhibition of molecular machinery, antibodies can interact with the host immune system by way of phenomena such as antibody-dependent cytotoxicity (ADCC), thereby increasing therapeutic potency beyond that conferred intrinsically by binding of the molecule to its target[27]. Due in large part to these expanded capabilities, antibodies have become a prominent portion of the modern therapeutic arsenal[28]. However, antibody-based therapies have their own limitations. Despite their favorable pharmacokinetics relative to small molecule drugs, antibody half-life is still measured on the order of days[29], which typically necessitates multiple expensive and uncomfortable infusion procedures[30]. Additionally, the large size of antibodies prohibits passive diffusion across the

cell membrane and endocytosis into the target cell typically depends on prior binding to an extracellular receptor[31], which precludes targeting of cytoplasmic antigens. The large size of antibodies also inhibits their transport from the blood to the diseased tissue[29]. Furthermore, the specificity of antibodies for a single molecular target can preclude them from being able to sufficiently distinguish healthy cells from diseased tissue, which often requires multiple markers[32–34]. Finally, the difficulty in controlling the therapeutic potency of antibodies *in situ* often leads to adverse effects related to runaway effects, particularly in biologics targeting the immune system[35].

The high complexity of extant therapeutic challenges has led to a concomitant increase in the complexity of the therapeutic agents engineered to treat them. Viruses represent a new class of such drugs, with a complexity exceeding even that of antibodies and nanoparticles[36]. Viruses consist of genetic material encapsulated by a protein, and sometimes lipid, shell. These biological particles are decorated with surface receptors that enable the complicated and coordinated molecular behavior required for efficient entry into the target cell. In the intracellular environment, the virus can act on targets in the cytoplasm or in the nucleus, and can alter cell function via transcriptional programs. Some types of viruses are even capable of integrating into the cell's genome, thereby enabling permanent modification of the cell's functionality. While viral therapy remains a novel research area, some clinical successes have already been achieved, culminating in the 2012 EMA approval of Glybera[37] and the 2017 FDA endorsement of Luxturna[38]. The relatively high complexity of viruses enables them to display some of the most desirable characteristics in therapeutic agents, such as precision targeting based on the molecular environment[39] and a broad and controllable range of biological activities[40]. However, as a natural environmental agent, viruses must combat the

intrinsic immunological defenses of the human body[41]. Not only does immunity severely limit the efficacy of viral therapy, it can also lead to significant and sometimes fatal toxicity by generating massive immune reactions at therapeutically-relevant doses[42]. While viruses remain an exciting therapeutic platform for treating some types of diseases, the fact that viral administration intrinsically renders the therapy at odds with the host immune system fundamentally limits the efficacy and persistence of this approach[43].

The past two decades have seen enormous progress in the development of technologies to engineer and control living cells. Many cell types, both microbial and animal, can be genetically altered and reprogrammed to execute arbitrary biological functions. Such engineered cells have found a variety of applications, ranging from the efficient production of biofuels to the manufacture of precursors for clothing[44] and other materials[45]. Such cells can also be used to produce both small molecule[46] and large molecule[47] therapeutic agents. Bioengineering and biotechnology have emerged as major industries within the United States and other developed nations, with one report estimating conservatively that in 2012 these sectors represented over 2% of the US GDP[48]. A particularly exciting area of application for engineered cells, whose leading edge is just now entering the clinic, is the engineering of live cells for direct therapeutic applications[49].

Cells offer a host of advantages over other therapeutic modalities. Their enormous complexity provides a plethora of biological “knobs” to tune – cells can be engineered to preferentially replicate under specific and multiparametric environmental stimuli, enabling the sensing of complex heuristics to differentiate between diseased and healthy tissue[50]. Cells can also persist for much longer than non-biological entities[51,52], and autologous cell grafts

do not compete with the host immune system for survival as is the case for viral therapeutics. Additionally, cells can proliferate at the site of disease[53–55], which can amplify therapeutics effects while also decreasing the required dosage for administration, thus reducing cost and potential off-target spread. Finally, cells can employ a suite of biological programs to interface with the local environment, interacting with the local immune system and augmenting[56] or ameliorating[57] inflammation as required by the given therapeutic context. The tremendous range of possibilities afforded by engineering cells for therapeutic applications has led to a great deal of pre-clinical and translational investigation, and the first wave of cell-based therapies has entered the clinic[58].

1.2: Microbial Therapeutic Agents

Bacteria were the first living cells to be utilized in a clinical setting. The idea of cell-based therapy is often attributed to Dr. William Coley, an American surgeon who, in the late nineteenth century, recognized that cancer patients suffering from infection occasionally displayed spontaneous tumor regression[59]. Coley began injecting his patients with Erisypelas (now formally known as *Streptococcus pyogenes*) and observed some degree of therapeutic efficacy[60], although insufficient recordkeeping has rendered his results difficult to reproduce or justify as a modern therapeutic intervention. Additionally, Coley's use of non-engineered pathogenic bacteria was associated with the expected adverse effects of microbial infections such as sepsis and upon the development of X-ray radiation therapy and improvement of surgical techniques in the early twentieth century, Coley's method of treatment fell out of favor in the medical community[61,62].

An increased understanding of bacteriology and bioengineering has led to a resurgence in microbial therapeutics. Discovery of bacterial strains with restricted pathogenicity has enabled safe administration in the clinical setting, with some forms of microbes often purchased and consumed over the counter[63]. These naturally occurring bacteria have applications in the treatment of some disorders, particularly those of the gastrointestinal tract[64–66]. Some probiotic strains of bacteria, particularly *E. coli* Nissle 1917[67] and *L. lactis* NK34[68], have demonstrated anti-cancer activity in addition their conventional role in the GI tract.

Microbes are a versatile biological platform for modification and engineering. Decades of experience in bioengineering has resulted in the robust ability to engineer many strains of bacteria by the introduction of foreign nucleic acids, either by way of extrachromosomal DNA molecules (e.g. plasmids) or via chromosomal editing (such as via Lambda Red recombination)[69–71]. The expanded ability to manipulate and program microbial cells with novel functions has resulted in the design of strains that can sense disease states and either report their presence[72,73] or treat them *in situ*[63,74]. Such facile control over bacterial genetics has generated a great deal of interest in the scope of potential applications for microbial therapies[75,76].

One of the main limitations of conventional therapeutic molecules is the challenge of targeted delivery. After injection or ingestion, the drug molecule forms a concentration gradient away from the site of administration, often resulting in relatively low dosage to the disease site while maintaining an elevated level in circulation and at potential off-target tissues. Microbes can be utilized as *in situ* "micropharmacies" to directly synthesize therapeutic agents within

a diseased tissue[67,77–79]. By injecting microbes that directly home to the site of disease, the drug of interest can be locally produced, thereby maintaining the highest concentration at the target site and diluting at distal, healthy organs[80]. This method of drug delivery can mitigate the toxicity observed in the systemic administration of highly bioactive molecules, as has been limiting for IL-2 therapy for cancer[81].

Microbes can also be utilized to directly destroy diseased tissue, a behavior which has been of particular interest in cancer therapy. The majority of research into this targeting behavior has focused on the ability of microbes such as *Salmonella*[82,83] and *Clostridium*[84] to traffic to tumors and colonize them. Obligate anaerobic bacteria such as *Clostridium*[85] and *Bifidobacterium*[86] suffer toxicity from oxygen exposure and are thus restricted to surviving in the hypoxic cores of poorly vascularized tumors. In contrast, facultative anaerobes such as *E. coli*[87], *Salmonella*[88], and *Listeria*[89] are able to tolerate the presence of oxygen. These microbes can display preferential tumor accumulation by active chemotaxis to necrotic and nutrient-rich regions[90,91], engineered auxotrophy for necrosis-associated molecules[92] and by growth restriction to immune-privileged regions such as the tumor microenvironment[93]. While some destruction of diseased tissue is inherently caused by the colonization and replication of these microbes, this activity can be enhanced by augmenting bacteria with non-natural payloads[94]. Microbes have been engineered to deliver bacterial toxins[95], pro-apoptotic factors[96–98], cytokines[99,100], chemokines[101], anti-antiogenesis agents[102], tumor-specific siRNA[103,104], plasmid DNA bearing tumor-suppressive genes[105], pro-drug converting enzymes[106,107], and antibodies[108]. Additionally, the foreign surface markers of microbes can render them potent immune adjuvants[109,110], and delivering novel immunogenic proteins can further enhance the inflammatory response stimulated by these

agents[111]. Arming microbes with disease-related peptides, proteins, or nucleic acids can prime the host immune system to recognize antigens which it would otherwise tolerate, an application of interest for inducing recognition of tumor-associated self-antigens that are frequently protected by immunological tolerance[112–116].

Attenuation of bacterial strains can also result in growth restriction to diseased tissue which can be harnessed in a clinical setting[117]. In the early 1900s, researchers at the Pasteur Institute searched for avirulent strains of Bacillus for use as vaccination strains against *Mycobacterium tuberculosis*, the causative agent of tuberculosis infection. By passaging a slightly attenuated strain on glycerine potato medium, the scientists generated a sufficiently avirulent line of *Bacillus* for use as a vaccine, and this became the strain utilized in the well-accepted BCG vaccination for tuberculosis[118]. In the 1970s this strain was found to promote tumor regression in non-muscle-invasive bladder cancer (NMIBC) patients, and intravesical administration of live BCG is now a standard treatment for this disease[119]. The mechanism of BCG homing and therapeutic activity against bladder tumors is not fully determined, although recent research has suggested a model in which the microbe binds to the carcinoma surface[120] and becomes internalized via micropinocytosis[121] stimulating a host immune response[122], a process which may be accelerated in cells mutated in the PTEN tumor suppressor[123]. Biosimilar strains have subsequently been developed, and expanded therapeutic applications such as treatment of colorectal cancer are under investigation. The strategy of virulence attenuation has since resulted in the development of the therapeutic bacterial strains *Salmonella* VNP20009[124], AR-1[92], and ΔppGpp[125], *Clostridium Novyi* NT[126], and others promising variants including a derivative of *S. pyogenes*, the bacterium that launched the field of microbial therapeutics[127].

Progress in bacterial therapy has been hindered by several factors. First, the fact that microbes are immunologically foreign objects in a patient's body renders them subject to immune reaction and as such, the dosages are restricted to minimize the severity of potential immune reactions[128]. Even BCG therapy, despite its clinical approval, must be prematurely terminated in a small number of patients due to toxicity[129]. Additionally, while some specific disorders such as NMIBC possess cognate bacteria which display strong replicative preference for the diseased tissue, many bacterial therapies are reliant on more general environmental cues for targeting. Such signals include hypoxia and the metabolic profile within the tumor core. Some other compartments within the body such as the bone marrow can share some of these molecular heuristics[130] and induce off-target colonization and therapeutic activity. Even in experiments demonstrating successful targeting of a disease site, a substantial concentration of bacteria can accumulate in healthy organs such as the spleen and liver[131]. Finally, there have been notable failures of pre-clinically successful therapeutic strategies failing to translate from animal models into human trials[132], and most positive effects observed in humans have been non-curative[133–137]. In the most notable failed trial, a patient injected with an engineered *Listeria* strain to vaccinate against HPV-positive oropharyngeal cancer suffered systemic listeriosis, resulting in the halt of the trial[138]. The modest success of translating efficacious microbial interventions from animal models to the clinic suggests that a significant amount of research and development must be undertaken to augment the potency of microbial therapeutics while restricting their action to sites of disease.

1.3: Mammalian Therapeutic Agents

The first implementation of mammalian cells as therapeutic agents in human patients was arguably in 1818, when the British physician James Blundell performed a blood transfusion to treat hemorrhage[139]. In the early 1900s, preliminary molecular research enabled physicians to segregate patients according to blood type, thereby establishing the paradigm of antigen matching in cell transplantation[140,141]. The 1950s saw another type of transplantation enter medical acceptance: that of stem cells[142]. Using this newly discovered, non-terminally differentiated cell type, physicians could rebuild the hematopoietic system in cancer patients who received high doses of chemotherapy. Both RBC transfusions and HSC transplantations have revolutionized aspects of healthcare and are enduring components of the modern medical industry.

In the mid-1990s, Steven Rosenberg's group at the NIH demonstrated that immune cells could also be used in a therapeutic context[143]. Reasoning that T-cells activated within the tumor environment could be expected to attack the surrounding malignancy, Rosenberg and colleagues isolated T-cells from the tumors of melanoma patients, expanded them *ex vivo*, and then reinfused them in large numbers back into the patient of origin. These artificially selected T-cells resulted in regression of the melanoma, thereby establishing cell-mediated adoptive immunotherapy as a viable therapeutic strategy. Autologous immunotherapy was subsequently utilized for dendritic cells as well. In 2010, the US FDA approved Sipuleucel-T, a blood product generated by treating peripheral blood mononuclear cells with a fusion protein consisting of GM-CSF to enrich dendritic cells and Prostatic Acid Phosphatase, a common prostate cancer antigen, to generate cognate antigens[144]. Other artificially stimulated dendritic cells generated via exposure to tumor-derived peptides, nucleic acids, or raw lysates are currently in late stage clinical trials[145].

The advent of reliable genetic modification of mammalian cells revolutionized the field by expanding the scope of accessible biological functions and providing novel strategies to control their activation[146]. Gene delivery into mammalian cells via chemical (cationic and polycationic complexes)[147,148], physical (electroporation or mechanoporation)[149,150], and biological (viral)[36] mechanisms, as well as precision gene editing via customized proteins and biomolecular complexes such as Zinc Finger Nucleases, TALENs, and CRISPR-Cas9[151], enables unprecedented control over cell function and fate. Aided by the 1970s revolution in recombinant DNA technology, which enabled facile manipulation of DNA sequences, gene delivery technologies offered a host of potential therapeutic modalities. A landmark experiment in 1980 demonstrated safe *ex vivo* transfer of recombinant plasmid DNA into human bone marrow cells followed by reinfusion into the patients of origin[152]. Although this study failed to demonstrate clinical efficacy and was roundly criticized as premature within the scientific and medical communities, it also opened the door for later studies of gene therapies.

One of the first technological beneficiaries of recombinant DNA technology was viral gene therapy, which can repair defective patient cells or introduce therapeutic functionality into host cells *de novo*[40]. Viruses had been explored (largely unsuccessfully) as therapeutic agents in their wild type context, but the ability to edit their genomes and utilize them to deliver arbitrary genes of interest garnered a great deal of scientific and public attention[152]. This ambition led to the use of recombinant viruses in clinical trials, with the first attempt aiming to correct X-SCID, a deficiency in immune cell maturation, in a batch of pediatric patients at the turn of the millennium[153,154]. While the field of gene therapy encountered significant turbulence during its inception[36], more recent research has yielded promising results and

several clinical approvals. The first viral gene therapy was approved in China to treat head- and neck squamous cell cancer in 2003[155] and another therapeutic adenovirus was brought to this market in 2005[156]. 2012 saw the landmark EMA approval of Glybera[157], an adeno-associated virus carrying lipoprotein lipase to correct a hereditary deficiency in this enzyme[158]. The first viral gene therapy approved in the U.S. was Luxturna, an AAV carrying a transgene to restore retinoid cycle function in a subset of retinal dystrophy patients, in 2017[38]. A large array of clinical trials for *in vivo* and *ex vivo* gene therapies for a variety of diseases is currently ongoing (reviewed by Dunbar et al[40]). Genetically engineered viruses have also garnered significant attention for oncolytic therapy via the wide array of alterations that bias viral replication to preferentially occur in tumor cells[159], with Amgen's Imlygic being the first to receive FDA approval in 2015[158].

In the past two decades, the use of genetic engineering to modify human cells for therapeutic efficacy has become a focus of significant research interest. Cells can also be extracted from a patient, genetically modified *ex vivo,* and subsequently reintroduced into the host[160]. The main advantage of this therapeutic approach is that the cells can be manipulated under controlled conditions, evaluated for quality, and then reinfused as a pre-modified product. Two cell types, hematopoeietic stem cells (HSCs) and leukocytes (particularly T-cells), have been of particular interest in this context[40]. HSCs are progenitor cells found in the bone marrow and are able to differentiate into adult blood cells of virtually any type. HSCs had previously found application in the context of allogenic transplantation of unmodified patient cells for treatment of chemotherapy-associated lymphodepletion[161]. T-cells are the main immune cell subtype involved in the adaptive cytotoxic response. By virtue of their unique T-Cell Receptor (TCR), which is randomized and selected during T-cell development, they

are able to recognize unique antigens presented on the Major Histocompatibility Complex (MHC) of potential target cells and selectively kill or otherwise direct an immune response against these specific targets[162]. The serial killing behavior of this cell type renders it ideal for applications such as cancer therapy in which cell ablation, rather than reprogramming, is required to treat the disease.

New advances in gene editing have enabled *ex vivo* modification of HSCs from patients with genetic defects in blood cell function such as β-Thalassemia, Sickle cell anemia, Adenosine deaminase deficiency (ADA), and several others[40]. After genetic reprogramming, these cells are reinfused into the patient and migrate back to the bone marrow, where they subsequently serve as progenitors to functionally repaired blood cell progeny[163]. Addition or replacement of mutant alleles in the HSCs has resulted in several successful clinical trials as well as the 2016 EU approval of Strimvelis for ADA.

Immunotherapies have also benefitted tremendously from advances in gene delivery. Following the pioneering work of the Rosenberg group in the 1990s on expanding tumor-specific lymphocytes, the past decade has seen a great deal of interest in the *ex vivo* genetic modification of T-cells and other lymphocytes for improved efficacy against cancer[164–166]. One of the first instances of *ex vivo* genetic engineering was the modification of T-cells with a genetic tracer for evaluation of their biodistribution following infusion into a patient[167]. A great deal of subsequent work has aimed to augment T-cell function for the treatment of cancers. A seminal paper by Eshhar and colleagues described genetic retargeting of T-cells toward native (non-MHC-presented) surface antigens by a hybrid protein consisting of an extracellular single-chain antibody domain for recognition of novel antigens and an

intracellular domain from the CD3ζ chain of the TCR for activation of the T-cell effector functions[168]. The extracellular domain in this design is modular and this fundamental architecture, now known as the Chimeric Antigen Receptor (CAR) has since been optimized and retargeted against the B-cell antigen CD19 for treatment of B-lineage blood cancers, culminating in the 2018 FDA approvals of Yescarta and Kymriah, the first CAR-T therapies[58].

Despite the immense progress which has been made in the genetic conversion of patient cells into therapeutic agents, significant challenges in the field remain. For direct viral gene delivery into patients, immunotoxicity and genotoxicity are the two key concerns. Viruses can elicit a strong immune response which can inhibit therapeutic efficacy by vector inactivation[41,169]. This immune reaction can also destroy virally modified cells by directing T-cell responses against viral capsid proteins or therapeutic transgenes presented by the MHC molecules of the genetically modified cells, thereby blunting the therapeutic effect[170]. Finally, the immune response may amplify from a local to a systemic phenomenon, driving signal transduction cascades that result in life-threatening systemic inflammation. Such a runaway immune response was famously responsible for the death of Jesse Gelsinger, a patient enrolled in an adenoviral gene therapy trial for Ornithine Transcarbamylase Deficiency[171]. This tragedy not only killed the patient, but also brought significant public and regulatory scrutiny toward the field, highlighting the safety concerns of these approaches. Another highly publicized mishap in the history of gene therapy occurred in one of the earliest clinical trials against SCID-X1. While the initial results of the intervention were highly promising, with immune functionality partially restored in the majority of subjects[172], several of the enrolled patients subsequently developed leukemia[173,174]. This result

underscores the potential for viral integration-induced genotoxicity, in which the process of viral insertion can disrupt the innate cellular machinery responsible for regulation of cell division, leading to malignant transformation. Similarly, a potential pitfall of stem cell-based therapy is the uncontrolled proliferation of undifferentiated cells, or teratocarcinoma[175]. While this phenomenon has not been observed in humans, several rodent studies have demonstrated it to be a concerning possibility in such therapeutic approaches[163,176].

Cell-based T-cell therapy has also demonstrated significant dangers. Antigen-redirected T-cells can mount a significant immunological response which, similar to the effect induced by high doses of viral genetic vectors, can prompt runaway and potentially fatal inflammatory reactions, which are termed Cytokine Release Syndrome (CRS)[177]. While modest CRS is an expected corollary to CAR-T therapy and in fact can serve as a biomarker of therapeutic efficacy, severe CRS has proven fatal in multiple cases[178]. Engineered T-cells can also demonstrate toxicity by erroneously attacking off-target tissues. This has occurred by way of "off-target, off tumor" toxicity in which the cells mistakenly recognize a healthy tissue antigen with structural similarity to the tumor antigen[179], or via "on-target, off tumor" behavior in which the target antigen is found, contrary to prior expectation, to be expressed on healthy tissue as well as in the cancer cells[180,181]. Both modes of mis-targeting have resulted in fatal reactions during clinical trials. In a trial of an affinity-enhanced TCR against the MAGE-A3 melanoma antigen, a patient suffered fatal cardiac toxicity when the engineered T-cells recognized and attacked Titin, a protein expressed in striated muscle[182]. "On target, off tumor" attack has been more common, with several trials reporting deaths from this mode of toxicity[180,183]. Improving the safety of viral and mammalian cell-based

therapeutics without compromising therapeutic efficacy remains the primary challenge of the field.

1.4: Common Challenges in Gene and Cell-Based Therapy

While viral and nonviral gene therapy, engineered bacterial therapeutics, and cell-based therapies are disparate strategies with their own idiosyncratic challenges, several overarching themes unify the obstacles that must be overcome before these next-generation interventions become standard clinical practices. The tissue and organ specificity of next-generation therapeutics must be well controlled to ensure that only sites of disease are treated or modified. The complex, and in some cases self-renewing, nature of these therapies is correlated with a high degree of potency, the regulation of which is critical for ensuring patient health. In cases where the intervention proves deleterious, such as malignant expansion of engineered cells[184] or life-threatening activity-related toxicity[185], physicians must be able to robustly abort the therapy. Finally, the structural and manufacturing complexity of next generation therapies leads to high cost, and as such, the therapeutic designs should be controllable by *ex vivo* factors to avoid necessitating premature cessation of the treatment.

The targeting specificity of genetic modification therapies is largely dictated by the method of transduction. While *ex vivo* editing of mammalian cells pre-selects against off-target genetic modification by physically separating the desired cells from the patient prior to modification[186], control of *in vivo* gene delivery specificity largely relies on the vector for editing. In some cases, differential viral tropism for specific tissues can bias entry and delivery, although natural viral tropism is rarely exclusive to single tissue types[187,188].

Tropism can be modified via engineering of viral surface proteins, yielding vectors with altered infectivity profiles[189]. Utilization of tissue-specific promoters to drive expression of the genetic payload can further increase specificity of gene delivery[190]. As a whole, the cell-type specificity of systemically administered genetic interventions is virtually never as precise as that of *ex vivo* engineered approaches due to the inability to pre-sort the target cell population prior to editing. Introducing methods to control the timing and location of gene delivery within the patient has the potential to vastly improve the safety and efficacy of such methods.

The spatial specificity of cell-based therapies is also of great interest, due largely in part to the aforementioned observations of off-tumor toxicity. With the exception of HSC engineering, where activity is usually restricted to its intended niche via the stem cells' useful property of intrinsic homing and engraftment into the patient's bone marrow after reinfusion[161], cell-based therapies are largely limited by off-target adverse effects. Bacterial homing and growth specificity are largely governed by the permissivity of the surrounding environment. Despite the wealth of available mechanisms to support bacterial proliferation in tumors, off-target colonization can occur in organs such as the spleen and liver, and in "tumor-like" niches such as the bone marrow. Additionally, some diseases for which cell-based therapies would be beneficial do not have obvious environmental markers that would promote bacterial growth. In contrast to bacterial therapies, the spatial localization of cell-based immunotherapies is mostly guided by the location of the target antigen[191]. Ligation of the antigen with the TCR or CAR results in strong pro-inflammatory signaling leading to local immune cell proliferation and recruitment. Unfortunately, this mechanism of spatial localization leaves therapies such as CAR-T vulnerable to off-target expression of antigens

or target antigen misrecognition, both of which can result in efficacy and toxicity in healthy tissues. As such, a great deal of work is being invested into improving molecular recognition using inhibitory receptors[192], logic-gated receptor systems[193], and even novel receptor platforms such as modular synthetic variants of the Notch receptor (SynNotch)[194] which can be utilized to orthogonally modulate specific biological functions including expression of the primary antigen receptor.

In some cases the administration of a therapy can go awry, leading to unpleasant or potentially fatal side effects that justify abortion of the therapy. The field of gene therapy has observed several such instances, such as the death of an adenoviral therapy patient due to severe and systemic inflammation[171] and the onset of leukemia in pediatric SCID patients[195]. CAR-T based therapies have also resulted in patient deaths during clinical trials due to off-target antigen recognition[196]. As such, the potency of next generation living therapeutics justifies engineered control strategies to enable abortion of the therapy at the whim of the administrating physician. Artificial control over the viability of the treatment can largely address this necessity. In bacterial therapy, auxotrophic strains which require continuous delivery of a nutrient for survival have been developed[197]. Additionally, kill switches which rely on detection of exogenous factors have been developed to inducibly halt bacterial growth or damage viability[198]. These methods can be utilized in combinatorial fashion for highly effective biocontainment[199,200]. For gene therapy and mammalian cell therapy, in which the modified cells are typically patient-derived, complex metabolic engineering is often not an option. Therefore, control of viability is typically enacted in kill switch fashion using inducible pro-drug-conversion enzymes such as HSV-tk[201] or intrinsically lethal proteins such as iCasp9[202]. A key obstacle to auxotrophy and kill switch-mediated control systems is

mutation[203]. Introduction of a genetic system that damages viability exerts a strong selection pressure on cells, and leaky selection strategies enable populations of escape variants to grow out, thereby continuing the undesired biological activity. This phenomenon is more prevalent in the bacterial setting, in which polymerase fidelity is not as robust as in mammalian cells and where proliferation can thus occur rapidly.

The relative expense of biological therapies in comparison to conventional drugs results in abortion of treatment being a last resort. Instead, exogenous modulation of therapeutic efficacy can be engineered to allow physicians to tune the potency of the intervention without necessitating complete elimination. A common strategy is the design of systems dependent on inducible gain of function. These include therapeutic genes which are natively transcribed at low levels but can be induced upon detection of an exogenous stimulus, such as engineered T-cells harboring a chimeric antigen receptor driven by a doxycyline-inducible promoter[204] and CAR-Ts in which receptor signaling is dependent on chemically-induced dimerization enabled by an infused drug[205]. While such systems are useful to prevent severe toxicity, the requirement for constant or repeated infusion of the inducer can render them unsuitable for long-term therapies, such as repair of genetic deficiencies. To address this issue, genetic state switches which can toggle in response to external stimuli are under investigation[206].

Gene therapies, bacterial cell-based therapies, and mammalian cell therapies are exciting and potentially revolutionary treatment modalities which may enable treatment of previously undruggable targets and diseases. The molecular complexity of these systems renders them highly engineerable and customizable, and also enables a high degree of therapeutic efficacy and specificity. Nevertheless, off-target activities and undesirable behaviors largely remain

to be addressed. The next generation of biological therapies will likely carry engineered therapeutic modules, possibly in multiplex, to enable precise control over biological behavior. The ability to exert novel biological programs, coupled with exogenous strategies to modulate of abort the intervention if needed, will render these “programmable” therapies a powerful tool in the armament of future physicians.

1.5: References

1. Drews, J. Drug Discovery: A Historical Perspective. *Science (80-.).* **287**, 1960–1964 (2000).
2. Pina, A. S., Hussain, A. & Roque, A. C. A. An Historical Overview of Drug Discovery. in *Methods in Molecular Biology* **572**, 3–12 (2010).
3. Jones, A. W. Early drug discovery and the rise of pharmaceutical chemistry. *Drug Test. Anal.* **3**, 337–344 (2011).
4. Coussens, N. P. *et al.* Small-Molecule Screens : A Gateway to Cancer Therapeutic Agents with Case Studies of Food and Drug Administration – Approved Drugs. *Pharmacol. Rev.* **69**, 479–496 (2017).
5. Munos, B. Lessons from 60 years of pharmaceutical innovation. *Nat. Rev. Drug Discov.* **8**, 959–968 (2009).
6. Maria, R. Antibiotic resistance : What is so special about multidrug-resistant Gram-negative bacteria ? Antibiotikaresistenz : Was ist so besonders an den Gram-negativen. *GMS Hyg. Infect. Control* **12**, 1–24 (2017).
7. Davis, B. M., Rall, G. F. & Schnell, M. J. Everything You Always Wanted to Know About Rabies Virus (But Were Afraid to Ask). *Annu. Rev. Virol.* **2**, 451–471 (2015).
8. Robilotti, E., Deresinski, S. & Pinsky, B. A. Norovirus. *Clin. Microbiol. Rev.* **28**, 134–164 (2015).
9. Sharma, V., Kaushik, S. & Kaushik, S. Emerging trends of Nipah virus : A review. *Rev Med Virol* **e2010**, 1–6 (2018).
10. Casey, D. A., Antimisiaris, D. & Brien, J. O. Drugs for Alzheimer ' s Disease : Are They Effective ? **35**, 208–211 (2010).
11. Folch, J. *et al.* Memantine for the Treatment of Dementia : A Review on its Current and Future Applications. *J. Alzheimer's Dis.* **62**, 1223–1240 (2018).
12. Overshott, R., Burns, A. & Inhibitors, C. TREATMENT OF DEMENTIA. *J Neurol Neurosurg Psychiatry* **76**, 53–59 (2005).
13. Matthews, P. M. New drugs and personalized medicine for multiple sclerosis. *Nat. Publ. Gr.* **11**, 614–616 (2015).
14. Longacre, M., Snyder, N. & Sarkar, S. Drug Resistance in Cancer: An Overview. *Cancers (Basel).* **6**, 1769–1792 (2014).
15. Crews, C. M. Targeting the Undruggable Proteome : The Small Molecules of My Dreams Crosstalk. *Chem. Biol.* **17**, 551–555 (2010).
16. Dang, C. V, Reddy, E. P., Shokat, K. M. & Soucek, L. Drugging the 'undruggable' cancer targets. *Nat. Rev. Cancer* **17**, 502–508 (2017).
17. Karaman, R. *Commonly Used Drugs - Uses, Side Effects, Bioavailability & Approaches to Improve it*. (2015). doi:10.13140/RG.2.1.1444.4640
18. Berger, S. I. & Iyengar, R. Role of systems pharmacology in understanding drug adverse events. *WIREs Syst. Biol. Med.* **3**, (2011).
19. Maeda, H., Nakamura, H. & Fang, J. The EPR effect for macromolecular drug delivery to solid tumors : Improvement of tumor uptake , lowering of systemic toxicity , and distinct tumor imaging in vivo. *Adv. Drug Deliv. Rev.* **65**, 71–79 (2013).
20. Kang, T. *et al.* iNGR-modified PEG-PLGA nanoparticles that recognize tumor vasculature and penetrate gliomas. *Biomaterials* **35**, 4319–32 (2014).
21. Wyatt, E. A. & Davis, M. E. Method of establishing breast cancer brain metastases affects brain uptake and efficacy of targeted , therapeutic nanoparticles. *Bioeng. Transl. Med.* 30–37 (2019). doi:10.1002/btm2.10108
22. Nakamura, Y., Mochida, A., Choyke, P. L. & Kobayashi, H. Nanodrug Delivery : Is the

Enhanced Permeability and Retention E ff ect Su ffi cient for Curing Cancer ? *Bioconjug. Chem.* (2016). doi:10.1021/acs.bioconjchem.6b00437
23. Dimers, D. N. *et al.* Multiplexed mRNA Sensing and Combinatorial-Targeted Drug Delivery Using DNA-Gold Nanoparticle Dimers. *ACS Nano* **12**, 3333–3340 (2018).
24. Giordano, R. J., Edwards, J. K., Tuder, R. M., Arap, W. & Pasqualini, R. Combinatorial Ligand-directed Lung Targeting. *Proc Am Thorac Soc* **6**, 411–415 (2009).
25. Liu, J. K. H. The history of monoclonal antibody development - Progress , remaining challenges and future innovations. *Ann. Med. Surg.* **3**, 113–116 (2014).
26. Chiu, M. L. & Gilliland, G. L. Engineering antibody therapeutics. *Curr. Opin. Struct. Biol.* **38**, 163–173 (2016).
27. Zahavi, D., AlDeghaither, D., O'Connell, A. & Weiner, L. Enhancing Antibody-Dependent Cell-Mediated Cytotoxicity (ADCC): A Strategy for Improving Antibody-based Immunotherapy. *Antib. Ther.* (2018). doi:10.1093/abt/tby002/5057809
28. Chames, P., Regenmortel, M. Van, Weiss, E. & Baty, D. Therapeutic antibodies : successes , limitations and hopes for the future. *Br. J. Pharmacol.* **157**, 220–233 (2009).
29. Ryman, J. T. & Meibohm, B. Pharmacokinetics of Monoclonal Antibodies. *CPT Pharmacometrics Syst. Pharmacol* **6**, 576–588 (2017).
30. Hendrikx, J. *et al.* Fixed Dosing of Monoclonal Antibodies in Oncology. *Oncologist* **22**, 1212–1221 (2017).
31. Riedl, T., Boxtel, E. Van, Bosch, M., Parren, P. W. H. I. & Gerritsen, A. F. High-Throughput Screening for Internalizing Antibodies by Homogeneous Fluorescence Imaging of a pH-Activated Probe. *J. Biomol. Screen.* **21**, 12–23 (2016).
32. Kim, W. & Ryu, C. J. Cancer stem cell surface markers on normal stem cells. *BMB Rep.* **50**, 285–298 (2017).
33. Lazar, I. M., Hoeschele, I., Morais, J. & Tenga, M. J. Cell Cycle Model System for Advancing Cancer Biomarker Research. *Sci. Rep.* **7**, 1–12 (2017).
34. Krupka, C., Lichtenegger, F. S., Liu, X., Kerbs, P. & Spiekermann, S. S. K. H. M. K. Coexpression profile of leukemic stem cell markers for combinatorial targeted therapy in AML. *Leukemia* **33**, 64–74 (2019).
35. Descotes, J. Immunotoxicity of monoclonal antibodies. *MAbs* **1**, 104–111 (2009).
36. Lundstrom, K. Viral Vectors in Gene Therapy. *Diseases* **6**, 42 (2018).
37. Authorization, M. *et al.* Lessons Learned from the Clinical Development and Market Authorization of Glybera. *Hum. GENE Ther. Clin. Dev.* **24**, 55–64 (2013).
38. Smalley, E. First AAV gene therapy poised for landmark approval. *Nat. Biotechnol.* **35**, 998–999 (2017).
39. Baker, A. T. Designer Oncolytic Adenovirus : Coming of Age. *Cancers (Basel).* **10**, 1–39 (2018).
40. Dunbar, C. E. *et al.* Gene therapy comes of age. *Science (80-.).* **359**, eaan4672 (2018).
41. Wang, Y. Oncolytic Viral Therapy and the Immune System : A Double-Edged Sword Against Cancer. *Front. Immunol.* **9**, 1–8 (2018).
42. Cotrim, A. P. & Baum, B. J. Gene Therapy: Some History, Applications, Problems, and Prospects. *Toxicol. Pathol.* **36**, 97–103 (2008).
43. Filley, A. C. & Dey, M. Immune System, Friend or Foe of Oncolytic Virotherapy? *Front. Immunol.* **7**, 1–8 (2017).
44. Natalio, F. *et al.* Biological fabrication of cellulose fibers with tailored properties. *Science (80-.).* **357**, 1118–1122 (2017).
45. Keasling, J. D. Synthetic Biology for Synthetic Chemistry. *ACS Chem. Biol.* **3**, 64–76 (2007).
46. Ro, D. *et al.* Production of the antimalarial drug precursor artemisinic acid in engineered yeast. *Nature* **440**, 3–6 (2006).
47. Manuel, J. *et al.* A synthetic biology approach for consistent production of plant-made

recombinant polyclonal antibodies against snake venom toxins. *Plant Biotechnol. J.* **16**, 727–736 (2018).
48. Carlson, R. Estimating the biotech sector ' s contribution to the US economy. *Nat. Publ. Gr.* **34**, 247–255 (2016).
49. Fesnak, A. D., June, C. H. & Levine, B. L. Engineered T cells: the promise and challenges of cancer immunotherapy. *Nat. Rev. Cancer* **16**, 566–81 (2016).
50. Sedlmayer, F., Aubel, D. & Fussenegger, M. Synthetic gene circuits for the detection, elimination and prevention of disease. *Nat. Biomed. Eng.* **2**, 399–415 (2018).
51. Savoldo, B. *et al.* CD28 costimulation improves expansion and persistence of chimeric antigen receptor – modified T cells in lymphoma patients Find the latest version : Brief report CD28 costimulation improves expansion and persistence of chimeric antigen receptor – modified. *J. Clin. Invest.* **121**, 1822–1826 (2011).
52. Levrat, E. *et al.* Very Long Term Stability of Mixed Chimerism after Allogeneic Hematopoietic Stem Cell Transplantation in Patients with Hematologic Malignancies. *Bone Marrow Res.* **2015**, (2015).
53. Cheng, Z. *et al.* In Vivo Expansion and Antitumor Activity of Coinfused CD28- and 4-1BB-engineered CAR-T Cells in Patients with B-Cell Leukemia. *Mol. Ther.* **26**, 976–985 (2018).
54. Vedvyas, Y. *et al.* Longitudinal PET imaging demonstrates biphasic CAR T cell responses in survivors. *JCI Insight* **1**, 1–17 (2016).
55. Bajgain, P. *et al.* CAR T cell therapy for breast cancer : harnessing the tumor milieu to drive T cell activation. *J. Immunother. Cancer* **6**, 1–13 (2018).
56. Yeku, O. O., Purdon, T. J., Koneru, M., Spriggs, D. & Brentjens, R. J. Armored CAR T cells enhance antitumor efficacy and overcome the tumor microenvironment. *Sci. Rep.* **7**, 10541 (2017).
57. Choi, J., Yoo, S. & Park, S. Mesenchymal stem cells overexpressing interleukin- 10 attenuate collagen-induced arthritis in mice. *Clin. Exp. Immunol.* **153**, 269–276 (2008).
58. Yip, A., Webster, R. M. & Car, C. The market for chimeric antigen receptor T cell therapies. *Nat. Publ. Gr.* **17**, 161–162 (2018).
59. Hoption Cann, S. A., van Netten, J. P. & van Netten, C. Dr William Coley and tumour regression: a place in history or in the future. *Postgrad. Med. J.* **79**, 672–680 (2003).
60. COLEY, W. B. I. The Treatment of Malignant Tumors by Repeated Inoculations of Erysipelas. *Ann. Surg.* **18**, (1893).
61. Kramer, M. G., Masner, M., Ferreira, F. A. & Hoffman, R. M. Bacterial therapy of cancer: Promises, limitations, and insights for future directions. *Front. Microbiol.* **9**, 1–9 (2018).
62. McCarthy, E. F. The Toxins of William B. Coley and the Treatment of Bone and Soft-Tissue Sarcomas. *Iowa Orthop. J.* **26**, 154–158 (2006).
63. Álvarez, B. & Fernández, L. Á. Sustainable therapies by engineered bacteria. *Microb. Biotechnol.* **10**, 1057–1061 (2017).
64. Chua, K. J., Kwok, W. C., Aggarwal, N., Sun, T. & Chang, M. W. Designer probiotics for the prevention and treatment of human diseases. *Curr. Opin. Chem. Biol.* **40**, 8–16 (2017).
65. Hwang, I. Y. *et al.* Engineered probiotic Escherichia coli can eliminate and prevent Pseudomonas aeruginosa gut infection in animal models. *Nat. Commun.* **8**, 1–11 (2017).
66. Riglar, D. T. *et al.* Engineered bacteria can function in the mammalian gut long-term as live diagnostics of inflammation. *Nat. Publ. Gr.* **35**, 653–658 (2017).
67. Stritzker, J. *et al.* Tumor-specific colonization , tissue distribution , and gene induction by probiotic Escherichia coli Nissle 1917 in live mice. *Int. J. Med. Microbiol.* **297**, 151–162 (2007).
68. Han, K. J., Lee, N.-K., Park, H. & Paik, H.-D. Anticancer and Anti-Inflammatory Activity of Probiotic Lactococcus lactis NK34. *J. Microbiol. Biotechnol* **25**, 1697–1701 (2015).
69. Chan, W., Verma, C. S., David, P. & Gan, S. K. A comparison and optimization of methods

and factors affecting the transformation of Escherichia coli. *Biosci. Rep.* **33**, 931–944 (2013).
70. Wilharm, G. *et al.* A simple and rapid method of bacterial transformation. *J. Microbiol. Methods* **80**, 215–216 (2010).
71. Yu, D. *et al.* An efficient recombination system for chromosome engineering in Escherichia coli. *Proc. Natl. Acad. Sci.* **97**, 5978–5983 (2000).
72. Courbet, A., Endy, D., Renard, E., Molina, F. & Bonnet, J. Detection of pathological biomarkers in human clinical samples via amplifying genetic switches and logic gates. *Sci. Transl. Med.* **7**, 289ra83-289ra83 (2015).
73. Kotula, J. W. *et al.* Programmable bacteria detect and record an environmental signal in the mammalian gut. *Proc. Natl. Acad. Sci. U. S. A.* **111**, 4838–43 (2014).
74. Isabella, V. M. *et al.* Development of a synthetic live bacterial therapeutic for the human metabolic disease phenylketonuria. *Nat. Biotechnol.* **36**, (2018).
75. Chien, T., Doshi, A. & Danino, T. Advances in bacterial cancer therapies using synthetic biology. *Curr. Opin. Syst. Biol.* **5**, 1–8 (2017).
76. Zhou, S., Gravekamp, C., Bermudes, D. & Liu, K. Tumour-targeting bacteria engineered to fight cancer. *Nat. Rev. Cancer* 1 (2018). doi:10.1038/s41568-018-0070-z
77. Arrach, N., Zhao, M., Porwollik, S., Hoffman, R. M. & McClelland, M. Salmonella promoters preferentially activated inside tumors. *Cancer Res.* **68**, 4827–4832 (2008).
78. Mengesha, A. *et al.* Development of a flexible and potent hypoxia-inducible promoter for tumor-targeted gene expression in attenuated Salmonella. *Cancer Biol. Ther.* **5**, 1120–8 (2006).
79. Deyneko, I. V, Kasnitz, N., Leschner, S. & Weiss, S. Composing a Tumor Specific Bacterial Promoter. *PLoS One* **11**, e0155338 (2016).
80. Forbes, N. S. Engineering the perfect (bacterial) cancer therapy Neil. *Nat. Rev. Cancer* **10**, 785–794 (2013).
81. Mellaert, L. Van *et al.* Secretory production of biologically active rat interleukin-2 by Clostridium acetobutylicum DSM792 as a tool for anti-tumor treatment. *FEMS Microbiol. Lett.* **246**, 67–73 (2005).
82. Toneri, M., Miwa, S., Zhang, Y., Hu, C. & Yano, S. Tumor-targeting Salmonella typhimurium A1-R inhibits human prostate cancer experimental bone metastasis in mouse models. *Oncotarget* **6**, 31335–31343 (2015).
83. Luo, X. *et al.* Antitumor Effect of VNP20009 , an Attenuated Salmonella , in Murine Tumor Models. *Oncol. Res.* **12**, 501–508 (2002).
84. Heap, J. T. *et al.* Spores of Clostridium engineered for clinical efficacy and safety cause regression and cure of tumors in vivo ABSTRACT : *Oncotarget* **5**, 1761–1769 (2014).
85. Edwards, A. N., Suárez, J. M. & Mcbride, S. M. Culturing and Maintaining Clostridium difficile in an Anaerobic Environment. *J. Vis. Exp.* **79**, e50787 (2013).
86. Ruas-madiedo, L. R. P. How do bifidobacteria counteract environmental challenges ? Mechanisms involved and physiological consequences. *Genes Nutr* **6**, 307–318 (2011).
87. Conway, T., Krogfelt, K. A. & Cohen, P. S. The Life of Commensal Escherichia coli in the Mammalian Intestine. *EcoSal Plus* **1**, 1–16 (2013).
88. Yamamoto, N. & Droffner, M. L. Mechanisms determining aerobic or anaerobic growth in the facultative anaerobe Salmonella typhimurium. *Proc. Natl. Acad. Sci.* **82**, 2077–2081 (1985).
89. Lungu, B., Ricke, S. C. & Johnson, M. G. Growth , survival , proliferation and pathogenesis of Listeria monocytogenes under low oxygen or anaerobic conditions : A review. *Anaerobe* **15**, 7–17 (2009).
90. Kasinskas, R. W., Forbes, N. S., Kasinskas, R. W. & Forbes, N. S. Salmonella typhimurium Lacking Ribose Chemoreceptors Localize in Tumor Quiescence and Induce Apoptosis Salmonella typhimurium Lacking Ribose Chemoreceptors Localize in Tumor Quiescence and

Induce Apoptosis. *Cancer Res.* **67**, 3201–3209 (2007).
91. Panteli, J. T. & Forbes, N. S. Engineered bacteria detect spatial profiles in glucose concentration within solid tumor cell masses. *Biotechnol. Bioeng.* **113**, 2474–2484 (2016).
92. Zhao, M. *et al.* Targeted Therapy with a Salmonella Typhimurium Leucine-Arginine Auxotroph Cures Orthotopic Human Breast Tumors in Nude Mice. *Cancer Res.* **66**, 7647–7653 (2006).
93. Clairmont, C. *et al.* Biodistribution and Genetic Stability of the Novel Antitumor Agent VNP20009 , a Genetically Modified Strain of Salmonella typhimurium. *J. Infect. Dis.* **181**, 1996–2002 (2000).
94. Uchugonova, A., Zhang, Y., Salz, R. & Liu, F. Imaging the Different Mechanisms of Prostate Cancer Cell- killing by Tumor-targeting Salmonella typhimurium A1-R. *Anticancer Res.* 5225–5229 (2015).
95. Jean, A. T. S., Swofford, C. A., Panteli, J. T., Brentzel, Z. J. & Forbes, N. S. Bacterial Delivery of Staphylococcus aureus α -Hemolysin Causes Regression and Necrosis in Murine Tumors. *Mol. Ther.* **22**, 1266–1274 (2014).
96. Zhang, Y. *et al.* Escherichia coli Nissle 1917 targets and restrains mouse b16 melanoma and 4T1 breast tumors through expression of azurin protein. *Appl. Environ. Microbiol.* **78**, 7603–7610 (2012).
97. Ganai, S., Arenas, R. B. & Forbes, N. S. Tumour-targeted delivery of TRAIL using Salmonella typhimurium enhances breast cancer survival in mice. *Br. J. Cancer* **101**, 1683–1691 (2009).
98. Loeffler, M., Negrate, G. Le, Krajewska, M. & Reed, J. C. Inhibition of Tumor Growth Using Salmonella Expressing Fas Ligand. *J Natl Cancer Inst* **100**, 1113–1116 (2008).
99. Loeffler, M., Negrate, G. Le, Krajewska, M. & Reed, J. C. IL-18-producing Salmonella inhibit tumor growth. *Cancer Gene Ther.* **15**, 787–794 (2008).
100. Chang, Z., Zhang, W., Wang, Q., Ding, S. & Zhao, W. Clostridium sporogenes delivers interleukin-12 to hypoxic tumours , producing antitumour activity without significant toxicity. *Lett. Appl. Microbiol.* **59**, 580–586 (2014).
101. Loe, M., Gaelle, Z., Negrate, L., Krajewska, M. & Reed, J. C. Salmonella typhimurium engineered to produce CCL21 inhibit tumor growth. *Cancer Immunol. Immunother.* **58**, 769–775 (2009).
102. Lee, C., Wu, C. & Shiau, A. Endostatin gene therapy delivered by Salmonella choleraesuis in murine tumor models. *J. Gene Med.* **6**, 1382–1393 (2004).
103. Zhang, L. *et al.* Intratumoral Delivery and Suppression of Prostate Tumor Growth by Attenuated Salmonella enterica serovar typhimurium Carrying Plasmid-Based Small Interfering RNAs. *Cancer Res.* **67**, 5859–64 (2007).
104. Yang, N., Li, S., Lü, Y., Chen, L. & Ren, D. Attenuated Salmonella typhimurium carrying shRNA- expressing vectors elicit RNA interference in murine bladder tumors. *Nat. Publ. Gr.* **32**, 368–374 (2011).
105. Fu, W., Chu, L., Han, X., Liu, X. & Ren, D. Synergistic antitumoral effects of human telomerase reverse transcriptase-mediated dual-apoptosis-related gene vector delivered by orally attenuated Salmonella enterica Serovar Typhimurium in murine tumor models. *J. Gene Med.* **10**, 690–701 (2008).
106. Theys, J. *et al.* Specific targeting of cytosine deaminase to solid tumors by engineered Clostridium acetobutylicum. *Cancer Gene Ther.* **8**, 294–297 (2001).
107. Lemmon, M. J. *et al.* Anaerobic bacteria as a gene delivery system that is controlled by the tumor microenvironment. *Gene Ther.* **4**, 791–796 (1997).
108. Groot, A. J. *et al.* Functional antibodies produced by oncolytic clostridia. *Biochem. Biophys. Res. Commun.* **364**, 985–989 (2007).
109. Kienle, G. S. Fever in Cancer Treatment: Coley's Therapy and Epidemiologic Observations.

Glob. Adv Heal. Med **1**, 92–100 (2012).
110. Gunn, G. R., Zubair, A. & Peters, C. Two Listeria monocytogenes Vaccine Vectors That Express Different Molecular Forms of Human Papilloma Virus-16 (HPV-16) E7 Induce Qualitatively Different T Cell Immunity That Correlates with Their Ability to Induce Regression of Established Tumors Immortal. *J. Immunol.* **167**, 6471–6479 (2001).
111. Zheng, J. H. *et al.* Two-step enhanced cancer immunotherapy with engineered Salmonella typhimurium secreting heterologous flagellin. *Sci Transl Med* **9**, 1–11 (2017).
112. Niethammer, A. G. *et al.* A DNA vaccine against VEGF receptor 2 prevents effective angiogenesis and inhibits tumor growth. *Nat. Med.* **8**, 1369–1375 (2002).
113. Fensterle, J. *et al.* Cancer immunotherapy based on recombinant Salmonella enterica serovar Typhimurium aroA strains secreting prostate-specific antigen and cholera toxin subunit B. *Cancer Gene Ther.* **15**, 85–93 (2008).
114. Shahabi, V., Seavey, M. M., Maciag, P. C., Rivera, S. & Wallecha, A. Development of a live and highly attenuated Listeria monocytogenes- based vaccine for the treatment of Her2 / neu-overexpressing cancers in human. *Cancer Gene Ther.* **18**, 53–62 (2010).
115. Kim, S. H. *et al.* Mage-b vaccine delivered by recombinant Listeria monocytogenes is highly effective against breast cancer metastases. *Br. J. Cancer* **99**, 741–749 (2008).
116. Maciag, P. C., Seavey, M. M., Pan, Z., Ferrone, S. & Paterson, Y. Cancer Immunotherapy Targeting the High Molecular Weight Melanoma-Associated Antigen Protein Results in a Broad Antitumor Response and Reduction of Pericytes in the Tumor Vasculature. *Cancer Res.* **68**, 8066–8076 (2008).
117. Lin, I. Y. C., Van, T. T. H. & Smooker, P. M. Live-Attenuated Bacterial Vectors: Tools for Vaccine and Therapeutic Agent Delivery. *Vaccines* **3**, 940–972 (2015).
118. Herr, H. W. & Morales, A. History of Bacillus Calmette-Guerin and Bladder Cancer : An Immunotherapy Success Story. *J. Urol.* **179**, 53–56 (2008).
119. Burger, M. *et al.* EAU Guidelines on Non – Muscle-invasive Urothelial Carcinoma of the Bladder : Update 2016. *Eur. Urol.* **71**, 447–461 (2017).
120. Hao, W. Z. *et al.* Role of a Bacillus Calmette-Guerin Fibronectin Attachment Protein in BCG-Induced Antitumor Activity. *Int. J. Cancer* **86**, 83–88 (2000).
121. Redelman-sidi, G., Iyer, G., Solit, D. B. & Glickman, M. S. Oncogenic Activation of Pak1-Dependent Pathway of Macropinocytosis Determines BCG Entry into Bladder Cancer Cells. *Cancer Res.* **73**, 1156–1167 (2013).
122. Prescott, S., Jackson, A. M., Hawkyard, S. J., Alexandroff, A. B. & James, K. Mechanisms of Action of Intravesical Bacille Calmette-Guerin : Local Immune Mechanisms. *Clin. Infect. Dis.* **31**, S91-3 (2000).
123. Huang, G., Redelman-Sidi, G., Rosen, N., Glickman, M. S. & Jiang, X. Inhibition of mycobacterial infection by the tumor suppressor PTEN. *J. Biol. Chem.* **287**, 23196–23202 (2012).
124. Low, K. B. *et al.* Lipid A mutant Salmonella with suppressed virulence and TNFalpha induction retain tumor-targeting in vivo. *Nat. Biotechnol.* **17**, 37–41 (1999).
125. Sam, H. *et al.* Immune response induced by Salmonella typhimurium defective in ppGpp synthesis. *Vaccine* **24**, 2027–2034 (2006).
126. Dang, L. H., Bettegowda, C., Huso, D. L., Kinzler, K. W. & Vogelstein, B. Combination bacteriolytic therapy for the treatment of experimental tumors. *Proc. Natl. Acad. Sci. U. S. A.* **98**, 15155–60 (2001).
127. Maletzki, C., Linnebacher, M., Kreikemeyer, B. & Emmrich, J. Pancreatic cancer regression by intratumoural injection of live Streptococcus pyogenes in a syngeneic mouse model. *Gut* **57**, 483–491 (2008).
128. Wang, C.-Z. *et al.* Strains, Mechanism, and Perspective: *Salmonella* -Based Cancer Therapy. *Int. J. Microbiol.* **2016**, 1–10 (2016).

129. Brausi, M. *et al.* Side Effects of Bacillus Calmette-Gue´rin (BCG) in the Treatment of Intermediate- and High-risk Ta, T1 Papillary Carcinoma of the Bladder: Results of the EORTC Genito-Urinary Cancers Group Randomised Phase 3 Study Comparing One-third Dose with Full Dose a. *Eur. Urol.* **65**, 69–76 (2014).
130. Zhang, C. C. & Sadek, H. A. Hypoxia and Metabolic Properties of Hematopoietic Stem Cells. *Antioxid. Redox Signal.* **20**, 1891–1901 (2014).
131. Felgner, S. *et al.* Engineered Salmonella enterica serovar Typhimurium overcomes limitations of anti-bacterial immunity in bacteria-mediated tumor therapy. *Oncoimmunology* **7**, 1–12 (2017).
132. J.F., T. *et al.* Phase I study of the intravenous administration of attenuated Salmonella typhimurium to patients with metastatic melanoma. *J. Clin. Oncol.* **20**, 142–152 (2002).
133. Nemunaitis, J. *et al.* Pilot trial of genetically modified, attenuated Salmonella expressing the E. coli cytosine deaminase gene in refractory cancer patients. *Cancer Gene Ther.* **10**, 737–744 (2003).
134. Maciag, P. C., Radulovic, S. & Rothman, J. The first clinical use of a live-attenuated Listeria monocytogenes vaccine: A Phase I safety study of Lm-LLO-E7 in patients with advanced carcinoma of the cervix. *Vaccine* **27**, 3975–3983 (2009).
135. Roberts, N. J. *et al.* Intratumoral injection of Clostridium novyi-NT spores induces antitumor responses. *Sci Transl Med* **6**, 249ra111 (2014).
136. Heppner, F. & Mose, J. R. The Liquefaction (Oncolysis) of Malignant Gliomas by a Non Pathogenic Clostridium. *Acta Neurochir. (Wien).* **125**, 123–125 (1978).
137. Carey, R. W., Holland, J. F., Whang, H. Y., Neter, E. & Bryant, B. Clostridial Oncolysis in Man. *Eur. J. Cancer* **3**, 37–46 (1967).
138. Sacco, J. J. *et al.* Systemic listeriosis following vaccination with the attenuated Listeria monocytogenes therapeutic vaccine , ADXS11-001. *Hum. Vaccin. Immunother.* **12**, 1085–1086 (2016).
139. Ellis, H. James Blundell, pioneer of blood transfusion. *Surg. Anniv.* **68**, 447 (2007).
140. Farhud, D. D. Karl Landsteiner (1868-1943). *Iran J Public Heal.* **47**, 777–778 (2018).
141. Hart, S. & Mccluskey, S. A. Red cell transfusion and the immune system. *Anaesthesia* **70**, 38–45 (2015).
142. Henig, I. & Zuckerman, T. Hematopoietic Stem Cell Transplantation — 50 Years of Evolution and Future Perspectives. *Rambam Maimonides Med. J.* **5**, 1–15 (2014).
143. Rosenberg, S. A. *et al.* Use of Tumor-Infiltrating Lymphocytes and Interleukin-2 in the Immunotherapy of Patients with Metastatic Melanoma. *N. Engl. J. Med.* **319**, 1676–1680 (1988).
144. Higano, C. S. *et al.* Sipuleucel-T. *Nat. Rev. Drug Discov.* **9**, 513–514 (2010).
145. Palucka, K. & Banchereau, J. Cancer immunotherapy via dendritic cells. *Interact. Immune Cancer Cells* **12**, 75–89 (2014).
146. Kim, T. K. & Eberwine, J. H. Mammalian cell transfection : the present and the future. *Anal Bioanal Chem* **397**, 3173–3178 (2010).
147. Ling, G. *et al.* Optimizing conditions for calcium phosphate mediated transient transfection. *Saudi J. Biol. Sci.* **24**, 622–629 (2017).
148. Modra, K., Dai, S., Zhang, H., Shi, B. & Bi, J. Polycation-mediated gene delivery : Challenges and considerations for the process of plasmid DNA transfection. *Eng. Life Sci.* **15**, 489–498 (2015).
149. Seki, A. & Rutz, S. Optimized RNP transfection for highly efficient CRISPR/Cas9-mediated gene knockout in primary T cells. *J. Exp. Med.* jem.20171626 (2018). doi:10.1084/jem.20171626
150. Meacham, J. M., Durvasula, K., Degertekin, F. L. & Fedorov, A. G. Enhanced intracellular delivery via coordinated acoustically driven shear mechanoporation and electrophoretic

insertion. *Sci. Rep.* 1–10 (2018). doi:10.1038/s41598-018-22042-0
151. Ain, Q. U., Chung, J. Y. & Kim, Y. H. Current and future delivery systems for engineered nucleases: ZFN, TALEN and RGEN. *J. Control. Release* **205**, 120–127 (2015).
152. Friedmann, T. A brief history of gene therapy. *Nat. Genet.* **2**, 93–98 (1992).
153. Cavazzana-calvo, A. M. *et al.* Gene Therapy of Human Severe Combined Immunodeficiency (SCID) -X1 Disease. *Science (80-.).* **288**, 669–672 (2000).
154. Mccormack, M. P. & Rabbitts, T. H. Activation of the T-Cell Oncogene LMO2 after Gene Therapy for X-Linked Severe Combined Immunodeficiency. *N. Engl. J. Med.* **350**, 913–922 (2004).
155. Raty, J., Pikkarainen, J., Wirth, T. & Yla-Herttuala, S. Gene Therapy: The First Approved Gene-Based Medicines, Molecular Mechanisms and Clinical Indications. *Curr. Mol. Pharmacol.* **1**, 13–23 (2008).
156. Wirth, T., Parker, N. & Ylä-Herttuala, S. History of gene therapy. *Gene* **525**, 162–169 (2013).
157. Gaudet, D. *et al.* Efficacy and long-term safety of alipogene tiparvovec (AAV1-LPL S447X) gene therapy for lipoprotein lipase deficiency: An open-label trial. *Gene Ther.* **20**, 361–369 (2013).
158. Ginn, S. L., Amaya, A. K., Alexander, I. E., Edelstein, M. & Abedi, M. R. Gene therapy clinical trials worldwide to 2017: An update. *J. Gene Med.* **20**, 1–16 (2018).
159. Warner, S. G., O'Leary, M. P. & Fong, Y. Therapeutic oncolytic viruses: Clinical advances and future directions. *Curr. Opin. Oncol.* **29**, 359–365 (2017).
160. Wang, X. & Rivière, I. Clinical manufacturing of CAR T cells : foundation of a promising therapy. *Mol. Ther. — Oncolytics* **3**, 16015 (2016).
161. Hatzimichael, E. & Tuthill, M. Hematopoietic stem cell transplantation. *Stem Cells Cloning Adv. Appl.* **3**, 105–117 (2010).
162. Pennock, N. D. *et al.* T cell responses : naïve to memory and everything in between. *Adv Physiol Educ* **37**, 273–283 (2013).
163. Zwaka, T. Use of Genetically Modified Stem Cells in Experimental Gene Therapies. in *Gene and Cell Therapy* 731–735 (CRC Press, 2008). doi:10.1201/9780849387999.ch34
164. Holzinger, A., Barden, M. & Abken, H. The growing world of CAR T cell trials: a systematic review. *Cancer Immunol. Immunother.* 1–18 (2016). doi:10.1007/s00262-016-1895-5
165. Bollino, D. & Webb, T. J. Chimeric antigen receptor–engineered natural killer and natural killer T cells for cancer immunotherapy. *Transl. Res.* (2017). doi:10.1016/j.trsl.2017.06.003
166. Voss, J. E. *et al.* Reprogramming the antigen specificity of B cells using genome-editing technologies. *Elife* **8**, e42995 (2019).
167. Rosenberg, S. A. *et al.* Gene Transfer into Humans — Immunotherapy of Patients with Advanced Melanoma, Using Tumor-Infiltrating Lymphocytes Modified by Retroviral Gene Transduction. *N. Engl. J. Med.* **323**, 570–578 (1990).
168. Eshhar, Z., Waks, T., Gross, G. & Schindler, D. G. Specific activation and targeting of cytotoxic lymphocytes through chimeric single chains consisting of antibody-binding domains and the gamma or zeta subunits of the immunoglobulin and T-cell receptors. *Proc. Natl. Acad. Sci. U. S. A.* **90**, 720–724 (1993).
169. Thaci, B., Ulasov, I. V, Wainwright, D. A. & Lesniak, M. S. The Challenge for Gene Therapy : Innate Immune Response to Adenoviruses. *Oncotarget* **2**, 113–121 (2011).
170. Carpentier, M. *et al.* Intrinsic Transgene Immunogenicity Gears CD8 + T-cell Priming After rAAV-Mediated Muscle Gene Transfer. *Mol. Ther.* **23**, 697–706 (2015).
171. Raper, S. E. *et al.* Fatal systemic inflammatory response syndrome in a ornithine transcarbamylase deficient patient following adenoviral gene transfer. *Mol. Genet. Metab.* **80**, 148–158 (2003).
172. Hacein-Bey-Abina, S. *et al.* Sustained Correction of X-Linked Severe Combined Immunodeficiency by ex Vivo Gene Therapy. *N. Engl. J. Med.* **346**, 1185–1193 (2002).

173. Hacein-Bey-Abina, S. *et al.* A Serious Adverse Event after Successful Gene Therapy for X-Linked Severe Combined Immunodeficiency. *N. Engl. J. Med.* **348**, 255–256 (2003).
174. Hacein-Bey-Abina, S. *et al.* LMO2-Associated Clonal T Cell Proliferation in Two Patients after Gene Therapy for SCID-X1. *Science (80-.).* **302**, 415–419 (2003).
175. Herberts, C. A., Kwa, M. S. G. & Hermsen, H. P. H. Risk factors in the development of stem cell therapy. *J. Transl. Med.* **9**, 29 (2011).
176. Bulic-Jakus, F. *et al.* Of mice and men: Teratomas and teratocarcinomas. *Coll. Antropol.* **30**, 921–924 (2006).
177. Jin, Z. *et al.* The severe cytokine release syndrome in phase I trials of CD19-CAR-T cell therapy : a systematic review. (2018).
178. Neelapu, S. S. *et al.* Chimeric antigen receptor T-cell therapy-assessment and management of toxicities. *Nat. Rev. Clin. Oncol.* **15**, 47–62 (2018).
179. Linette, G. P. *et al.* Cardiovascular toxicity and titin cross-reactivity of affinity-enhanced T cells in myeloma and melanoma. *Blood* **122**, 863–871 (2013).
180. Morgan, R. a *et al.* Case report of a serious adverse event following the administration of T cells transduced with a chimeric antigen receptor recognizing ERBB2. *Mol. Ther.* **18**, 843–851 (2010).
181. Lamers, C. H. J. *et al.* Treatment of Metastatic Renal Cell Carcinoma With Autologous T-Lymphocytes Genetically Retargeted Against Carbonic Anhydrase IX : First Clinical Experience. *J. Clin. Oncol.* **24**, e20–e22 (2006).
182. Linette, G. P. *et al.* Cardiovascular toxicity and titin cross-reactivity of affinity-enhanced T cells in myeloma and melanoma. *Blood* **122**, 863–871 (2013).
183. Morgan, R. A. *et al.* Cancer Regression and Neurological Toxicity Following Anti-MAGE-A3 TCR Gene Therapy. *J. Immunother.* **36**, 133–151 (2013).
184. Ruella, M. *et al.* Induction of resistance to chimeric antigen receptor T cell therapy by transduction of a single leukemic B cell. *Nat. Med.* **24**, 1499–1503 (2018).
185. Gust, J., Taraseviciute, A. & Turtle, C. J. Neurotoxicity Associated with CD19 - Targeted CAR - T Cell Therapies. *CNS Drugs* (2018). doi:10.1007/s40263-018-0582-9
186. Levine, B. L., Miskin, J., Wonnacott, K. & Keir, C. Global Manufacturing of CAR T Cell Therapy. *Mol. Ther. Methods Clin. Dev.* **4**, 92–101 (2017).
187. Lykken, E. A., Shyng, C., Edwards, R. J., Rozenberg, A. & Gray, S. J. Recent progress and considerations for AAV gene therapies targeting the central nervous system. *J. Neurodev. Disord.* **10**, 1–10 (2018).
188. Hellström, M. *et al.* Cellular tropism and transduction properties of seven adeno-associated viral vector serotypes in adult retina after intravitreal injection. *Gene Ther.* **16**, 521–532 (2009).
189. Perabo, L. *et al.* In vitro selection of viral vectors with modified tropism: The adeno-associated virus display. *Mol. Ther.* **8**, 151–157 (2003).
190. Zheng, C. & Baum, B. J. Evaluation of Promoters for Use in Tissue-Specific Gene Delivery. in *Gene Therapy Protocols* **100**, 205–219 (Humana Press, 2008).
191. Sackstein, R., Schatton, T. & Barthel, S. R. T-lymphocyte homing: an underappreciated yet critical hurdle for successful cancer immunotherapy. *Lab. Investig.* 1–29 (2017). doi:10.1038/labinvest.2017.25
192. Fedorov, V. D., Themeli, M. & Sadelain, M. PD-1- and CTLA-4-based inhibitory chimeric antigen receptors (iCARs) divert off-target immunotherapy responses. *Sci. Transl. Med.* **5**, 1–12 (2013).
193. Sukumaran, S. *et al. Enhancing the Potency and Specificity of Engineered T Cells for Cancer Treatment*. *Cancer Discovery* (2018). doi:10.1158/2159-8290.CD-17-1298
194. Roybal, K. T. *et al.* Precision Tumor Recognition by T Cells With Combinatorial Antigen-Sensing Circuits. *Cell* **164**, 770–779 (2016).

195. Hacein-Bey-Abina, S. *et al.* Insertional oncogenesis in 4 patients after retrovirus-mediated gene therapy of SCID-X1. *J. Clin. Invest.* **118**, 3132–3142 (2008).
196. Schmidt, C. The struggle to do no harm. *Nature* **552**, S74–S75 (2017).
197. Thompson, R. J., Bouwer, H. G. A. & Portnoy, D. A. Pathogenicity and Immunogenicity of a Listeria monocytogenes Strain That Requires D -Alanine for Growth. *Infect. Immun.* **66**, 3552–3561 (1998).
198. Chan, C. T. Y., Lee, J. W., Cameron, D. E., Bashor, C. J. & Collins, J. J. 'Deadman' and 'Passcode' microbial kill switches for bacterial containment. *Nat. Chem. Biol.* 1–7 (2015). doi:10.1038/nchembio.1979
199. Gallagher, R. R., Patel, J. R., Interiano, A. L., Rovner, A. J. & Isaacs, F. J. Multilayered genetic safeguards limit growth of microorganisms to defined environments. *Nucleic Acids Res.* **43**, 1945–54 (2015).
200. Lee, J. W., Chan, C. T. Y., Slomovic, S. & Collins, J. J. Next-generation biocontainment systems for engineered organisms. *Nat. Chem. Biol.* **14**, 1 (2018).
201. Ciceri, F. *et al.* Infusion of suicide-gene-engineered donor lymphocytes after family haploidentical haemopoietic stem-cell transplantation for leukaemia (the TK007 trial): a non-randomised phase I-II study. *Lancet. Oncol.* **10**, 489–500 (2009).
202. Gargett, T. & Brown, M. P. The inducible caspase-9 suicide gene system as a 'safety switch' to limit on-target, off-tumor toxicities of chimeric antigen receptor T cells. *Front. Pharmacol.* **5**, 1–7 (2014).
203. Stirling, F. *et al.* Rational Design of Evolutionarily Stable Microbial Article Rational Design of Evolutionarily Stable Microbial Kill Switches. *Mol. Cell* **68**, 686-697.e3 (2017).
204. Sakemura, R. *et al.* A Tet-On Inducible System for Controlling CD19-Chimeric Antigen Receptor Expression upon Drug Administration. *Cancer Immunol. Res.* **4**, 658–668 (2016).
205. Wu, C.-Y., Roybal, K. T., Puchner, E. M., Onuffer, J. & Lim, W. A. Remote control of therapeutic T cells through a small molecule-gated chimeric receptor. *Science (80-.).* **350**, (2015).
206. Chakravarti, D., Caraballo, L. D., Weinberg, B. H. & Wong, W. W. Inducible gene switches with memory in human T cells for cellular immunotherapy. *bioRxiv* 1–24 (2018). doi:10.1101/346783

C h a p t e r 2

NONINVASIVE BIOLOGICAL CONTROL VIA TEMPERATURE MODULATION

2.1: Engineered Control over Biological Systems

Engineered bacterial and mammalian genetic and cell-based therapies offer unprecedented opportunities for fine-grained control of function, but they also display the potential for severe and sometimes fatal side effects. The management and suppression of these toxicities is at the forefront of current biomedical research. Challenges and opportunities for improvement exist at all stages of therapeutic implementation: during gene editing or delivery, during *in vivo* administration, and after infusion of the drug product. Advances in control over these processes have progressed in recent years, but current implementations generally lack spatial specificity or noninvasive access. As such, there remains a significant need for the implementation of a biomodulation modality with these characteristics.

Control of gene editing has been investigated in the context of the linear space of DNA sequence, and also in terms of the three-dimensional spatial coordinates within the target organism. The recognition of viral genotoxicity has prompted investigation into site-specific delivery and integration methods. Avenues of interest include non-integrating retroviruses which enable high efficiency episomal gene delivery[1] and also integration targeting via fusion of the viral integrase with sequence-specific DNA-binding proteins[2–4]. Recently, RNA-programmable recombinases generated via fusion to CRISPR components have also

been explored[5]. Non-viral methods of gene delivery are also candidates for novel control strategies. Site-directed nucleases such as Cas9, Zinc Finger Nucleases (ZFNs), and TALENs significantly reduce the risk of genotoxicity by utilizing sequence-specific interactions with DNA to guide cleavage, although the latter two methods require protein engineering development for each new target, resulting in significant investment in labor and a delivery vector with a relatively large cargo capacity[6].

Controlling dosage or potency of delivery is highly desirable for biological therapies with potentially severe side effects. Some genetic payloads are amenable to inducible expression via promoters with intrinsic sensitivity to chemical stimuli such as exogenous drug administration (such as doxycycline derivatives[7]) or by communicating with neighboring cells to threshold gene expression based on population density[8]. Strategies have also been developed to titrate cell behavior at the post-translational level. The high risk of severe cytokine release syndrome in CAR-T therapy has prompted the development of several modified chimeric antigen receptor designs which can be inducibly activated to affect intracellular signaling and subsequent T-cell activation but which otherwise remain quiescent[9,10].

Temporal and spatial control of gene delivery and activation has also been widely investigated. As with dosage modulation, temporal control is often achieved via use of chemically inducible promoters to drive the transgene of interest, with doxycycline-inducible systems in particular finding widespread use in the literature[11,12]. Temporal control can also be implemented on the protein level using ligand-inducible activation or dimerization systems, as has been implemented for chemically-triggered Cas9 gene editing[13]. Spatial

control of biological therapy is also of interest to restrict activity to specific physical regions within a patient. Spatial localization can be conferred via environmental sensing if the target site of the therapy can be sufficiently differentiated from healthy tissue via molecular markers. This strategy has been explored extensively in CAR-T therapy, wherein homing strategies have been developed using split primary and secondary (co-stimulatory) T-cell surface receptor signaling to affect AND logic[14], and dominant inhibitory receptors to enact NOT logic[15]. Novel combinatorial sensing systems can integrate multiple signals in parallel. In a recently reported tri-partite configuration, a CAR is utilized to sense the primary tumor antigen while a chimeric co-receptor against the normally immunosuppressive cytokine TGF-β provides co-stimulation and a third chimeric receptor against IL-4 provides a tertiary signal for expansion and cytokine production[16]. Platform technologies such as synthetic notch receptors, which couple arbitrary extracellular ligand binding to any desired internal transcriptional program, are also under investigation for improved CAR-T homing to target tissues[17].

A new direction in controlling the spatial targeting of next generation therapies relies on engineering biological systems to sense external stimuli which can be precisely administered by a scientist or clinician. Image-guided interventions such as radiation therapy, laser and RF ablation, and focused ultrasound are established clinical techniques that utilize geometric information about the spatial coordinates of the disease site to direct the application of the treatment[18], but which have largely been ignored as cues for the controlled induction of biological activity.

One of the most successful spatially-directed modes of biological modulation is optogenetics, the control of biological materials with light. This technology has enabled spatiotemporal control via applications such as conjugation of photocleavable inhibitory compounds to viral capsids[19], engineering photoactivatable nuclear entry of the viral payload[20], and delivery of light-activatable biological cargo[21]. Optical control of non-viral genetic editing systems such as Cas9[22] and ZFNs[23] has also been developed. A key drawback of optical approaches is the poor accessibility of deep tissues; because light scattering through tissue occurs on the length scale of millimeters, at-depth access relies on invasive surgical intervention[24]. This places a severe constraint on the applications wherein this form of spatial targeting is relevant because a multitude of factors such as patient age and frailty, as well as the proximity of disease to highly sensitive tissues such as brain regions and blood vessels, can render surgery unsuitable or impossible[25–27]. To overcome this limitation, technologies with noninvasive penetrance through human tissue are being investigated.

A variety of noninvasive techniques are already in use for disease ablation, such as X-ray irradiation, magnetic hyperthermia, and focused ultrasound. These systems are under investigation for biomodulation, albeit not as extensively as their optogenetic counterparts. One such system utilized oxidative stress and DNA damage-responsive transcription factor binding sites to construct an artificial X-ray responsive promoter, which demonstrates up to 20-fold upregulation of gene expression upon exposure to X-ray photons[28]. However, DNA damage induced by ionizing radiation can result in deleterious or potentially oncogenic mutations, suggesting that other approaches may be safer moving forward. Magnetic fields are highly tissue-penetrant, enabling noninvasive imaging (MRI)[29], and are the subject of much recent work for modulation of biological function. Organ-specific genome editing has

been achieved via delivery of CRISPR components in a baculovirus coated with magnetic nanoparticles which enhance cellular uptake under a regionally-applied alternating magnetic field, enabling payload delivery that outpaces immune inactivation of the vector[30]. Magnetic nanoparticles have also been utilized to drive gene expression from a heat-inducible promoter via RF-induced hyperthermia[31], to control neural function directly via activation of MNP-affixed ion channels[32], and for drug delivery via mechanically-induced disruption of endothelial junctions by magnetic actuation[33]. Two drawbacks limit the utility of MNP-based control strategies. First, the difficulty in focusing magnetic fields limits the achievable spatial resolution and no sub-organ targeting has yet been demonstrated using this approach[34,35]. Additionally, as abiological components, synthetic magnetic nanoparticles cannot replicate as engineered cells or biomolecules multiply, thereby limiting the duration for which they can be stimulated. Biologically encoded magnetic nanoparticles and nanostructures, which could be expressed constitutively by engineered cells, are under development. The iron chelating protein Ferritin was genetically fused to the TRPV1 calcium channel and was able to stimulate an RF-mediated channel opening[36]; however, the weak paramagnetism of Ferritin has raised some controversy regarding the mechanism of this magnetic actuation[37]. Stronger biomagnetic structures exist, such as magnetosomes from naturally magnetotactic bacteria[38] but these have yet to be expressed in a heterologous, therapeutically useful host organism. Efforts are under way to engineer biomolecules capable of generating more highly magnetized biological structures and recent advances have enabled magnetic trapping of *E. coli* expressing these structures at defined spatial coordinates[39]; however, actuation of biological functions or behaviors using engineered highly magnetic biomolecules has yet to be achieved.

Focused ultrasound (FUS) represents an alternative tissue-penetrant signaling modality with high potential for intrinsic and engineered biomodulation. Focused ultrasound is a pressure wave emitted by a single concave piezoelectric element or by a set of transducer elements in a concave array[40]. The ultrasonic waves are produced at an intensity such that they propagate through tissue with minimal biological effect but constructively interfere at the transducer's focal zone, locally increasing the amplitude of the mechanical perturbation and the resulting energy deposition. As a result, the tissue at the focal point undergoes significant mechanical stress and, if ultrasound is supplied at a sufficient intensity and duration, heating[41]. The volume of the focal zone is wavelength-dependent and can be quite small, with an achievable cross-sectional full width half max (FWHM) of less than 10 microns in aqueous media[42] or less than 100 microns in low-impedance tissues such as the eye[43] using ultra-high frequency (~>40 MHz) transducers. Attenuation, and therefore depth penetration, is also frequency-dependent; while ultra-high frequency ultrasound is useful for ocular control or imaging[44], most FUS transducers operate in the 0.5 – 3 MHz range, producing a theoretical diffraction limited resolution of approximately 0.25 – 1.5 mm according to the Abbe diffraction limit. In practice, resolution can be diminished by scattering or nonlinear propagation of the sound wave, as well as transducer geometry. Typical FWHM values for *in vivo* focused ultrasound range from 1 - 5 mm laterally and 1 – 4 cm axially, and this frequency range can accommodate focal depths on the order of 10 cm[45–47] in tissue.

Focused ultrasound has previously been investigated for biological manipulation via stimulation of endogenous cellular components. One method of ultrasound biomodulation is via non-thermal perturbation. The precise mechanism of this mode of stimulation is under active investigation, but is generally thought to be mediated by mechanosensitive cellular

components such as ion channels[48]. One of the most widely studied applications of this technique is neuromodulation of the brain, which has been demonstrated in cell cultures and tissue slices[49] as well as in living animals[50,51]. Stimulation of other CNS components such as the retina has also been achieved with high precision[43], as has modulation of the peripheral nervous system[52]. Image-guided ultrasound pulse planning using penetrative imaging modalities such as MRI enables quantitative prediction of through-skull sound propagation and consequently the application of focused ultrasound to the brain in a transcranial, fully noninvasive manner[53,54]. This in turn has enabled noninvasive neuromodulation of the brain in human subjects[55].

Biomodulation via engineered responses to mechanostimulation is gaining traction as a viable method of interfacing with cells and tissues. Local chemical stimulation can be achieved in the brain by taking advantage of the specialized tissue at the interface between the vasculature and the brain, known as the Blood-Brain Barrier (BBB), which is resistant to the diffusive trafficking of biomolecules and most small-molecule drugs[56]. Mechanically-induced aberrations in the BBB can be imparted with spatial precision using FUS, resulting in transient gaps through which drugs can transport and induce their biological activity in a localized manner[57,58]. This approach has been extended to gate the brain access of therapeutic antibodies[59] and even of recombinant viruses which were evolved to resist trafficking through the BBB without physical disruption[60], thus enabling spatial control over transgene delivery in the brain. While localized BBB disruption enables selective brain access, other tissues are more permeable to foreign molecules and require other approaches to affect ultrasound-mediated control. Mechanical control can be exerted via ectopic expression of stretch-sensitive ion channels such as TRP-4, as has been demonstrated in *C. elegans*[61]. A

similar strategy relying on the native expression of the mechanosensitive cation channel Piezo1 in T-cells has been utilized to gate transcription from the calcium/NFAT signal transduction pathway in CAR-T lymphocytes[62]. However, both of these strategies rely on perturbing ionic flux, which is typically regulated by multiple channel and pump proteins[63], and these techniques are dependent on local pressure amplification by inorganic microbubbles which will dilute out as the cells divide. As such, while mechanical control is an intriguing mechanism for noninvasive biological stimulation, there remains a vacancy in the repertoire of biological components for a fully genetic method to control cell function in response to focused ultrasound.

2.2: Ultrasound Hyperthermia as a Noninvasive Biological Stimulus

One of the primary clinical applications for focused ultrasound is hyperthermic tissue ablation. High intensity pulses sustained for sufficient duration are able to destroy tissue at the focal point by locally raising the temperature past the thermal limit of tissue viability, enabling selective and noninvasive destruction of diseased regions[64]. Such ablative treatments are currently utilized for elimination of uterine fibroids and a variety of solid tumors[47,65]. Transcranial ultrasound ablation has also been utilized to relieve symptoms of essential tremor[66] and Parkinson's disease[67]. Over 80,000 patients had undergone image-guided HIFU therapy as of 2014, demonstrating the widespread clinical adoption of this treatment modality and hardware capability[68]. Although the primary clinical application of focused ultrasound is destructive in nature, not all stimulation regimes result in tissue ablation. Using real-time monitoring via technology such as MRI thermometry alongside rapid feedback control, mild hyperthermia can be maintained at sub-ablative temperatures[69].

Such moderate thermal elevation can therefore be utilized as a signal to control biological responses.

Focused ultrasound is not unique in its ability to noninvasively elevate tissue temperature[70]. Radiofrequency electromagnetic radiation can capacitatively heat tissue; however, the absorbance of RF radiation by tissue restricts >200 MHz radiowaves to an operating depth of less than 4 cm[71]. For deeper applications, energy can be deposited by inductive heating via oscillating magnetic fields which induce eddy currents in tissue (Magnetic Induction), or which rapidly reorient paramagnetic or ferromagnetic particles (Magnetic Particle Hyperthermia). Capacitative RF heating between two electrodes also has good depth penetration, but the heating is concentrated at the electrodes themselves, rendering spatial control difficult at intermediate locations. The spatial specificity of Magnetic Particle Hyperthermia is typically mediated by the location of the particles rather than the location of the field gradients due to the poor spatial resolution of field focusing[34]. Finally, phased RF array heating uses constructive interference between electromagnetic waves to affect localized temperature elevation; however, the focal volumes tend to be large relative to the size of the patient[72] and interference along bone-tissue interfaces can result in deviations from the expected heating pattern[73]. Altogether, focused ultrasound is currently unique in its ability to noninvasively direct controlled temperature elevation at millimeter length scales.

Biomodulation via hyperthermia has previously been achieved mainly via stimulation of endogenous temperature-sensitive promoters. While most bacterial heat shock promoters demonstrate relatively low fold-change in expression upon induction[74,75], mammalian heat

shock promoters (particularly those of the HSP70 family) show robust switch-like behavior. Genetically engineered biological reporter genes such as luciferase and fluorescent proteins have been gated by HSP70 promoters and triggered via laser-induced hyperthermia *in vitro*[76] and *in vivo*[77]. Magnetic hyperthermia has also been utilized to activate stress-inducible promoters for expression of imaging[78] or therapeutic transgenes, typically to induce tumoricidal payloads[79,80]. Despite the multitude of research and clinical studies invested in magnetic nanoparticle-mediated hyperthermia, the technique suffers from fundamental limitations in spatial resolution (with spatial specificity generally conferred by localized physical administration of the nanoparticles), constraints on input power due to generation of eddy currents in off-target tissues, and the inability of synthetic magnetic nanoparticles to replicate along with the cells which they are to control.

Critically, HSP70 has also been activated *in vivo* using FUS stimulation in genetically modified murine models[81,82] in wild-type animals wherein the HSP70 and reporter were delivered as viral transgenes[83], and in *ex vivo*-engineered cells after implantation into a model organism[84]. Hinting at the potential for thermal control of semi-autonomous cell therapies, a recent study generated chimeric animals wherein hematopoietic stem cells from an HSP-reporter mouse were administered intravenously into a reporter-null recipient mouse, homed to tumor sites (and bone marrow), and underwent selective activation via MRI-guided HIFU hyperthermia[85].

While the heat shock promoter system provides a convenient endogenous control strategy for transcriptional programming, it suffers from several important limitations. First, because

the primary stimulus for this signal transduction pathway is an upregulation of unfolded proteins, the heat shock pathway has crosstalk with other inputs, such as chemical and metabolic stresses[86–89], low pH[90], oxidative stress[91], signaling molecules such as some prostaglandins[92,93], drugs such as anti-inflammatory agents[94] and proteasome inhibitors[89], energy deprivation[95], and potentially mechanical stress[96]. An important corollary of this activation mechanism is that the thermal threshold for the activation of the heat shock response is highly dependent on the thermostability of the cell proteome rather than on an intrinsic molecule of the heat shock machinery. This prediction has been confirmed by the observation that the human HSF1 transcription factor, which coordinates the overall heat shock promoter activation, demonstrates an altered setpoint when expressed in *Drosophila* cells which more closely matches the induction threshold of the host organism's HSF1[97]. This result implies that tuning the activation threshold of heat shock promoters may be challenging. An additional factor which may interfere with HSP-dependent control of cell function in the clinical setting is the activation of heat shock promoters by hypoxia[98–102]. This phenomenon suggests that care should be taken in the use of these promoters in motile cell types which could potentially reach naturally hypoxic niches in the body such as the bone marrow[103] or cartilage[104], and in patients suffering from cancer-associated anemia[105] and consequent hypoxia[106]. A further layer of complexity is added by the differential performance of heat shock promoters across various cell types[107,108] and by the impaired HSP promoter response in some cell lineages, particularly in the brain[109–112]. In bacteria, the inducibility of heat shock promoters is typically low (on the order of ten-fold)[74] and they can suffer from significant basal leakage. Additionally, due to the mechanistic complexity of the heat shock pathway[113] (discussed in more detail below), the prospect of engineering this

system to tune its induction threshold and switching sharpness is a daunting task. Finally, because the modular switch in the heat shock pathway is a transcriptional promoter, it would be difficult to utilize this system to exert rapid control over cell function on the timescale of seconds to minutes, as would be possible by fusing a thermal switch directly to a protein of interest. More rapid thermoswitching mechanisms have been explored in the context of temperature-sensitive untranslated regions in RNA, such as naturally occurring ROSE[114] and FourU[115] elements as well as synthetic sequences[116], which form thermo-labile stem-loop structures to prevent translation or polymerase procession[117]. While more rapid than transcriptional control, this strategy is still slower than direct protein regulation, often demonstrates switching only over a broad temperature range, and typically demonstrates low fold-changes in resulting gene expression[118–120]. Additionally, this gating paradigm is largely restricted to prokaryotes. As such, a tunable biological system with intrinsic thermosensitivity and a simplicity that lends itself to control of cell function on the transcriptional and post-translational levels would be highly desirable for noninvasive modulation of biological activity.

2.3: Temperature in Biological Systems

In order to utilize temperature for biomodulation, the effects of this variable on the cell must be understood and accounted for. Temperature is a globally pervasive parameter in biological systems. The thermodynamics of all reactions are dictated by the relative scaling of their energies to kT, where k is the Boltzmann constant; thus, temperature affects equilibrium reaction quotients[121]. Additionally, the rate of a reaction is dictated by its activation energy[122],

which is also scaled by kT; therefore reaction rates are also temperature-dependent. Structural transitions in macromolecules also occur with thermal dependence. These transitions can be confined to the submicroscopic scale, as is the case for free cytosolic proteins, or they can influence the macroscopic structure of the cell, as is the case for the thermal denaturation of the cytoskeletal protein spectrin above 43 °C[123]. As such, thermal perturbations can induce widespread effects on the structure and function of the cell.

2.4: The Cellular Response to Temperature

As may be expected, cells have evolved numerous strategies to cope with stress associated with fluctuations in temperature. Upon sufficient hyperthermia (or other forms of damage such as hypoxia, osmotic stress, mechanical stress, ionizing radiation, organic denaturants, and heavy metals[124,125]), cells upregulate the transcription and synthesis of a set of 50-200 (depending on the organism) proteins termed "heat shock proteins" (HSPs)[125]. These proteins, which are typically named according to their molecular weight, attempt to protect the cell by preventing or reversing damage to the cell's components. These proteins can be grouped into seven functional classes. The most abundant class represents molecular chaperones, which act to disaggregate denatured proteins and protect monomers from re-aggregation. A second class consists of proteolytic enzymes which degrade irreversibly aggregated or misfolded proteins. The third class consists of nucleic acid damage repair proteins which detect non-native covalent modifications of DNA or RNA and attempt to repair them. A fourth, understudied class of proteins alters metabolic flux, presumably to compensate for changes in reaction rates due to altered enzyme stability or thermal

equilibrium. This class of proteins is overrepresented in the stress response of unicellular organisms, while multicellular organisms appear to rely more heavily on chaperones. The fifth class of HPSs consists of transcriptional regulators which effect further changes in gene expression to upregulate downstream stress response pathways or inhibit stress-sensitive pathways. The sixth group of HSPs assists in maintaining the structural integrity of the cytoskeleton, while the final class performs miscellaneous membrane-associated functions such as regulating membrane fluidity and transporting toxins out of the cell.

The most well studied, class of heat shock response proteins are chaperones. This diverse family of proteins acts to prevent aggregation of misfolded proteins, stabilize unfolded intermediates until they spontaneously sample their native conformation, assist in the targeting of proteolytic degradation, and aid in other functions such as protein translocation between organelles[126]. Notably, chaperones are more highly inducible in multicellular organisms, whereas unicellular organisms distribute the workload of damage repair more evenly among the many classes of stress-inducible genes. In accordance with their stoichiometric mode of activity, chaperones are the most highly upregulated set of proteins in the stress response of most organisms, and are also strongly constitutively expressed[125]. Chaperones recognize conserved features of denatured proteins such as hydrophobic patches and motifs, and also specific sequences. Chaperones can be further divided into subclasses. “Holdases” such as sHSPs are typically expressed at high levels only upon detection of denaturation or stress and are ATP-independent agents that simply bind to unfolded proteins and sequester them from aggregation. In contrast, “foldases” such as Hsp70 and its constitutive paralog Hsc70 bind unfolded or misfolded protein segments and then utilize

ATP hydrolysis to undergo a conformational change to modify their internal environment, presenting the client protein with an alternate energy landscape which may induce it to refold into its native state. This group of chaperones is typically expressed from both inducible and constitutive promoters as separate, homologous genes. Another group of heat shock proteins that assist in chaperone-mediate refolding is the HSP100 family, which pulls single polypeptide chains through a central pore in an ATP-dependent manner, thereby removing it from a misfolded state or pulling it out of an aggregate and subsequently enabling spontaneous or chaperone-assisted refolding. This family of heat shock proteins is generally restricted to bacteria and lower eukaryotes, implying that higher eukaryotes have an alternate mechanism for disaggregating proteins.

The trigger for HSP induction is complex, although the foundational events appear similar between bacteria and higher organisms. The master regulator transcription factor of the heat shock response, termed σ32 in bacteria and HSF1 in mammalian cells, is sequestered by constitutively expressed members of the chaperone family itself and prevented from affecting transcription[125]. Accumulation of unfolded proteins shifts the equilibrium of chaperone binding away from the heat shock regulator and toward their unfolded clients, thereby releasing the transcription factor and initiating the expression of stress response genes. In bacteria, induction of HSPs induces a feedback inhibition loop to control σ32 function via modulation of its translation, activity, and degradation[127]. Translation of σ32 is further regulated by an intrinsic RNA thermometer in the 5' UTR of its transcript[128]. In higher organisms, HSF1 regulation is an even more complex phenomenon wherein intrinsic structural thermosensitivity of the HSF1 regulatory domain, together with post-translational

modifications such as phosphorylation, acetylation, and SUMOylation, modulate HSF1 activity[113]. Additionally, the accessory protein eEF1A1, which loads charged tRNAs into the ribosomal A site, is released during stress-associated translational inhibition and redistributes to the nucleus, where it both stabilizes the interaction of HSF1 to its cognate binding sequence in heat shock promoters and also facilitates mRNA export from the nucleus via the 3'UTR of HSP promoter transcripts[129].

2.5: Temperature in Cellular Viability

Despite the wide array of cytoprotective responses to thermal perturbation, temperature still influences the growth and survival of cells. Investigation of the molecular mechanisms of temperature-associated changes in viability has been undertaken, but no single "weak link" has been established as the critical mediator of survival. While both biochemical reaction imbalances and structural transitions of cellular components could potentially influence viability, the activation energies of most metabolic reactions are on the order of 10 kcal/mol whereas structural transitions are typically on the order of 100 kcal/mol[123]. Because the thermal energy required to impair cell viability is also on the order of 100 kcal/mol, it is assumed that these structural transitions, rather than metabolic unbalancing, are the principal cause of hyperthermia-mediated cell death[123]. These transitions are typically attributed to protein unfolding, although the identity, number, and quantity of damaged proteins that result in cell death have not been elucidated. Protein denaturation results in inactivation of function due to loss of structure and typically also in aggregation due to exposure of previously buried hydrophobic residues. Other large-scale transitions, such as changes in membrane fluidity,

have been determined unlikely to contribute significantly to the impairment of viability upon hyperthermia[130]. While large-scale transitions in DNA occur only at temperatures around 90 °C, it is possible that structural reorganization in microdomains influences viability, although this has not been investigated in detail. Covalent breaks in DNA are not thought to occur in response to mild hyperthermia (up to 47 °C), although DNA damage can occur secondary to thermal stress due to inactivation of the protein machinery responsible for DNA damage repair[131]. Likewise, the unfolding of RNA species such as tRNAs and UTR regions could also influence cell health. Cytoskeletal reorganization also occurs upon even mild hyperthermia (for durations on the order of 30 minutes), but different cytoskeletal components (e.g. microfilaments, microtubules, or intermediate filaments) are disrupted in different cell types and it is unclear if a link exists between structural reorganization and viability[132]. This reorganization can be reversible and the thermal dosage threshold for reversibility differs between cell types, and likely is dependent on the stage of the cell cycle at which the cells are exposed to hyperthermia[132]. Disruption of the cortical cytoskeletal system, such as the interface between actin and integrins, is likely to affect signal transduction but the effect of this disruption on viability is unclear.

Differential scanning calorimetry analysis of mammalian cells show that erythrocytes, which lack a nucleus, show a single structural transition at a T_m of 70 °C while V79 cells, which contain a nucleus, demonstrate a more complicated transition profile with an onset near 40 °C[130]. Thus it is tempting to conclude that the lethal structural transitions occur in the nuclear compartment, a hypothesis bolstered by evidence that heat-treated cells have altered nuclear density and demonstrate intra-nuclear protein aggregation. However, both the nuclear and

cytosolic compartments demonstrate endothermic peaks at temperatures in excess of 50 °C, but also onset of excess C_p near 40 °C, indicating that both compartments contain a small fraction of thermo-labile components which may be the determining factors for temperature tolerance[130]. It should be noted that the critical transition or transitions responsible for cell death may be within or between supramolecular structures rather than within single macromolecules.

Structural transitions such as protein unfolding occur even during physiological temperatures, and the ability of cells to survive depends on their capacity to compensate for or repair these insults[123]. Indeed, it has been suggested that a small fraction (on the order of 0.2%) of cells in culture at 37 °C is lost by virtue of "thermal noise" that cells cannot recover from[133]. In accordance with this postulate, cells constitutively express a baseline level of chaperone machinery that is responsible for repairing stress-mediated denaturation and damage[125]. The ability of cells to compensate for such damage has also been characterized *in vitro*; CHL V79 cells are able to tolerate 5% denaturation with minimal effect on viability whereas 10% protein denaturation results in nearly full lethality[123]. The ability of cells to compensate for some amount of thermal denaturation appears in multiple kingdoms of life, as differential scanning calorimetry analysis of several bacterial strains demonstrates that the optimal growth temperature is generally several degrees higher than the onset of thermal structural transitions.

The timing of heating with respect to cell cycle also influences thermotolerance. Structural aberrations have been observed in the macroscopic structure of chromatids during

hyperthermia. Correspondingly, cells are most heat-sensitive during mitosis, less so during the S-phase of the cell cycle, and minimally thermo-sensitive during G1[123]. Induction of hyperthermia during S-phase typically leads to a DNA replication blockade, resulting in entry into mitosis prior to full replication of the chromosomes and subsequent death via mitotic catastrophe[131]. Interestingly, cellular synthesis of DNA while the DNA repair machinery is inactivated appears to also strongly contribute to cell death – when DNA synthesis is chemically inhibited during and after heat shock, cells are rescued from what would be lethal DNA lesions[131]. Correspondingly, thermal damage to cell cycle checkpoint proteins can induce cell death by permitting the cell to proceed to mitosis without first completing DNA replication[131].

Most models of cellular thermal viability are phenomenological in nature. It has generally been observed that cells *in vitro* display a biphasic survival profile in response to hyperthermia (**Fig. 2-1**)[130]. The curve is typically characterized by a pre-exponential phase for the first few minutes of hyperthermia, after which point survival decays in an exponential manner. It should be noted that the decrease in survival can be partially ameliorated by pre-exposing cells to mild heat stress, as is depicted in curve C. While this increase in robustness is typically attributed to pre-expression of heat shock proteins, which aid the cell in repairing the effects of

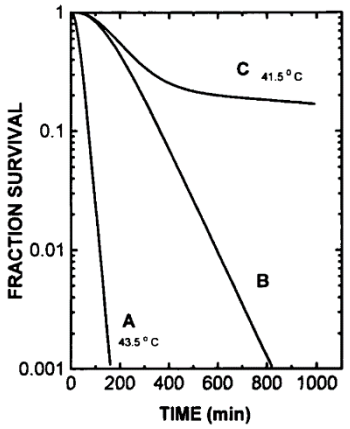

Figure 2-1: *In vitro* cell viability as a function of time at varying temperatures. Note the initial slow rate of death followed by an acceleration and, at permissive temperature, a stabilization of viability due to chaperone production. Reproduced from (Lepock 2003[123]) courtesy of Taylor & Francis Publishing.

thermal denaturation, it is unclear why some cells are able to remain viable while others succumb to heat stress.

The threshold at which cells accumulate significantly more damage than they can repair (i.e. the temperature at which viability decays sharply) is dependent on many factors. While the aforementioned V79 CHO cells demonstrated decreased viability upon even brief exposure to temperatures of 43.5 °C, other cell types such as PC3 prostate cancer cells demonstrate little change in metabolism or survival at the same temperatures and tolerate short, high temperature hyperthermia (48 °C for 10 minutes) or milder, long duration hyperthermia (44 °C for 60 minutes) with little measurable change in viability[124]. Additionally, the use of 3D cultures, which more accurately mimic the tissue environment, appears to increase post-heat shock viability relative to 2D culture controls via unidentified mechanisms, calling into question the applicability of a wealth of early data collected on monolayer cultures[124]. It should be noted that Arrhenius analysis indicates that human cells are slightly more thermotolerant than rodent cells, as indicated by their higher "thermal break point" in the slope of the Arrhenius plot and the general shallower slope shape indicating slower killing[134,135] (**Fig. 2-2**). In clinical practice, temperature has been found empirically to influence tumor viability in an integrated dose-dependent fashion[70]. A variety of mathematical

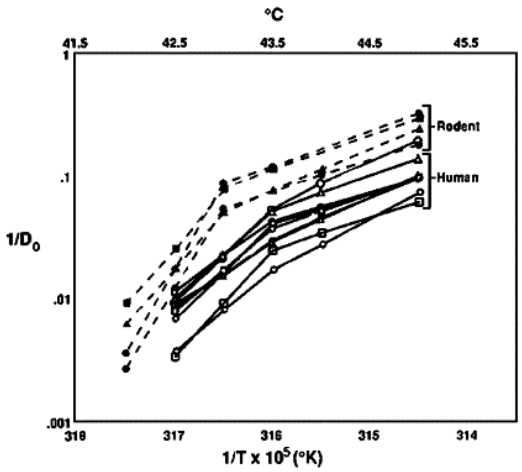

Figure 2-2: An example of the exponential dependence of *in vitro* cell viability on hyperthermic dose. The killing rate for human cells is generally lower than that of rodent cultures. Reproduced with permission from Roizin-Towle and Pirro (1991)[135].

models have been established to predict cell viability as a function of thermal dose. To date, all of these models are empirical in nature, with all constants fit to data rather than derived from fundamental thermodynamic or biological considerations[131]. The dependence of cell survival on temperature above the physiological baseline follows an exponential relationship, as demonstrated in **Fig. 2-2**. To standardize equivalent thermal exposures, the convention in the field is to use the "Cumulative Equivalent Minutes at 43 °C" (CEM 43 °C), which is defined by **Equation 1-1**

$$\boldsymbol{Equation\ 1-1}: CEM\ 43\ ^{\circ}C = tR^{(43-T)}$$

where t is the duration of treatment, T is the average temperature for the given treatment interval, and R is an empirically determined constant set to 0.5 or 0.25, depending on if T is greater than or less than the thermal "break point" of human cells (43 °C on average)[136]. A large body of literature has been assembled over the past four decades regarding tissue viability after varying CEM43 doses[134]. These data encompass many different temperatures and durations and indicate that, within the same tissue type and species, the CEM43 conversion is robust regardless of the input temperature. This metric is therefore the "gold standard" for prediction of biological effects upon hyperthermic exposure.

2.6: Thermal Regimes for Safe Biomodulation

The establishment of the CEM43 metric of thermal dosage enables the categorization of temperature/duration landscapes according to their predicted biological effects. While the

non-specific effects of hyperthermia such as protein denaturation and metabolic reaction rate imbalances are unavoidable in thermal therapy, the most important parameter with respect to temperature-switchable therapeutic agents is the thermal dosage limit below which tissue damage is negligible. In the context of cancer therapeutics, damage to malignant tissue surrounding the thermoswitchable agents can be dismissed or even be deemed beneficial. However, in a general setting the bystander tissue must be spared of the toxic effects of hyperthermia as much as possible. **Fig. 2-3** depicts a representative thermal dosage landscape which could be used to inform stimulation intensities and durations. The area below a threshold curve denotes a region of parameters which would be predicted to be safe for stimulation. Above this curve, non-specific cell death is expected to occur and the corresponding parameters would therefore be unsuitable for stimulation of therapeutic agents. The mode of cell death upon exposure to hyperthermia varies between cell types, thermal doses, and possibly the timing of exposure relative to the cell cycle[131]. Within the so-called hyperthermic range of 40 – 47 °C, most cell death occurs via mitotic catastrophe or apoptosis (or a combination thereof). In the ablation range of 48 – 60 °C, protein denaturation and aggregation is much more widespread and the cell typically coagulates. The objective of FUS hyperthermia-activated therapy would be to operate within the bounds of the safe thermal envelope to ensure that the effect on tissue health is specifically modulated by the function of the therapeutic agent.

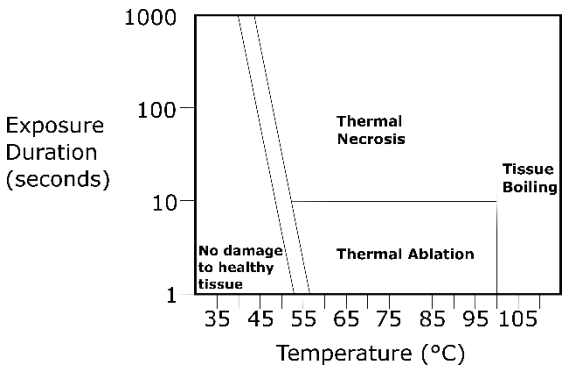

Figure 2-3: Schematic of the thermal landscape and the regimes in which different hyperthermic temperature / duration exposures can fall. Image adapted from The Focused Ultrasound Foundation.

Determining a safe thermal regime requires evaluating viability and damage in native living tissue, as cells in culture can display altered temperature sensitivity[124] while *ex-vivo* tissue can suffer from confounding effects such as poor perfusion and oxygen delivery[137]. Additionally, anatomical context is crucial for understanding and predicting thermal damage. Much as *in vitro* cell viability under hyperthermic conditions depends on the identity of the cell line, thermal damage thresholds also differ between tissues within the same species and between different species[137]. Due to the experimental and ethical difficulty of conducting experiments on thermal viability in human patients and organs, animal models have been utilized as proxies for most studies. A comprehensive review of previous literature across a variety of animal models by the MRI + EUREKA research consortium's Thermal Workshop on RF Hotspots led to the recommendation of a CEM43 limit of 9 minutes for RF-induced heating during MRI imaging[138]. It should be noted that the panel also recommended a ceiling of 39 °C exposure regardless of duration. While this thermal dosage limit was set conservatively for imaging applications and therapeutic interventions may warrant more relaxed criteria, the data analyzed by the consortium suggests that a CEM43 on the order of 10 minutes is a reasonable preliminary approximation of the thermal envelope within which focused ultrasound may be utilized for safe biomodulation. As the field evolves and more applications of FUS-stimulated therapeutics are demonstrated in pre-clincal models (particularly in the context of non-tumor tissue, such as in the intestine for management of gastrointestinal disorders), more rigorous thresholds will be established, likely in a tissue-specific manner.

2.7: Temperature in Cancer Medicine and Immunology

One of the primary potential applications of next-generation biological therapeutic agents is the treatment of cancer. Hyperthermia-mediated modulation of engineered therapeutic agents has the potential to synergize with a variety of beneficial effects of temperature elevation for tumor destruction[139]. While ablation of tumor mass by temperatures in excess of 60 °C directly reduces tumor burden, mild (sub-ablative) hyperthermia and fever-range (39 °C – 41 °C)[140] temperatures may also benefit cancer treatment by modifying the tumor microenvironment and potentiating the immune response.

One of the primary intrinsic benefits of hyperthermia is its ability to mobilize and activate the immune system. Temperature elevation induces immunostimulatory changes in the tumor and associated tissue and also directly in various immune cell compartments. Hyperthermia can alter the surface protein expression profile of tumor vasculature to facilitate extravasation of cytotoxic T-lymphocytes from the bloodstream into the tumor[141]. As a result of either this altered expression profile or of increased blood perfusion, 42 °C microwave hyperthermia enables enhanced tumor access by T-cells, Natural Killer (NK) cells, and dendritic cells while decreasing the population and activity of immunosuppressive T-reg and myeloid-derived suppressor cells[142]. Thermal shifts can also alter the surface proteome on tumor cells to dysregulate the camouflaging balance of surface receptors upon which cancer cells rely for immune evasion. In some tumors, 43 °C hyperthermia enhances MHC-I expression on the tumor surface, increasing the probabiliry of recognition by patrolling CTLs[143]. In contrast, hyperthermia can inhibit MHC presentation in other tumor

types, thereby promoting their recognition and destruction by Natural Killer (NK) cells[144]. Hyperthermia sensitizes some cancer lines to NK cell-mediated lysis via HSF1-mediated overexpression of MICA, a target of the NKG2D activating receptor in NK cells[145,146]. Hyperthermia can also induce some tumors to produce chemokines such as CCL2, CCL5, and CXCL10, which actively recruit pro-inflammatory immune cells to the site of disease[142].

The adaptive immune system also demonstrates temperature-responsive stimulation. In CTLs, hyperthermia increases the rate of contact with antigen presenting cells, possibly via increasing the membrane fluidity of the T-cells[147]. Fever-range hyperthermia induces PKC relocalization[148] and potentiates activation of cytotoxic function in a TCR pathway-dependent manner, as indicated by increased phosphoroylation of the LAT and PKCθ signaling mediators[149]. Mild hyperthermia also increases expression of the death ligand FasL on T-cells, potentially via augmentation of NF-κB and NFAT nuclear translocation or via direct HSF1-mediated transcription[150]. Exposure to 42 °C further augmented pro-inflammatory cytokine production by tumor-infiltrating T-cells[142].

In addition to cells of the lymphoid lineage, myeloid immune cells are also biased toward activation at elevated temperatures. Mild hyperthermia recruits monocytes to the tumor, which can then differentiate into macrophages and present tumor-associated antigens to the adaptive immune system[151]. The induction of monocyte trafficking may be driven largely by the overproduction of CXCL2 and other chemokines by heat-treated tumors[152]. In macrophages, fever-range hyperthermia in combination with recognition of soluble damage motifs promotes increased phagocytosis and synthesis of cytotoxic effector molecules[153–155].

These damage signals can also augment IL-12 secretion by monocyte-derived dendritic cells and bone marrow dendritic cells, resulting in increased T-cell proliferation[156,157]. Hyperthermia also promotes dendritic cell maturation[158] and secretion of the inflammatory cytokine TNF-α[142].The general immunostimulatory effect of mild hyperthermia has been corroborated by the observation of abscopal, $CD8^+$ T-cell dependent tumor retardation in a mouse model where a contralateral tumor was treated with magnetic hyperthermia[152]. When devising therapeutic stimulation protocols for engineered thermo-responsive cancer therapies, it will be worthwhile to optimize the heating parameters for both the triggering of the temperature switch and also the effector functions of the relevant immune cells, which can diminish upon prolonged exposure to super-febrile thermal regimes[154,155].

Heat shock proteins, whose conventionally studied role is as molecular chaperones to promote homeostasis, also function as signaling molecules to promote immune activity. This behavior is prominent in tumors undergoing therapeutic hyperthermia or fever. Hsp70, Hsp90, Hsc70, and gp96 are released by damaged tumor cells and bind to TLR4 on the cancer cell surface in a paracrine manner, thereby inducing chemokine production and promoting dendritic cell infiltration[142]. Hsp70, Hsp90, and Calreticulin are overexpressed and trafficked to the membrane of chemotherapeutically stressed cancer cells where they promote phagocytosis and maturation of dendritic cells[159]. These proteins also ligate the immune surface receptor CD91[160] on dendritic cells, wherein they induce cross-presentation of chaperoned antigens and upregulation of co-stimulatory surface receptors[161]. In dendritic cells, internal Hsp90 activity appears necessary for maturation, thereby intrinsically linking

this process to fever and hyperthermia[158]. Ligation of TLR4 by damage-associated Hsp70 from tumor cells also promotes maturation[160].

There is clear consensus in the literature that temperature elevation promotes the immune response against tumors. However, the mechanisms of immune action can differ depending on context, such as the identity of the tumor cells and their specific response to hyperthermia (e.g. MICA upregulation, MHC up or down-regulation, chemokine release, etc.) and also of the immune cells which are able to infiltrate into the tumor structure during the application of thermal stimulus. Additionally, most reported works suggest that temperature-stimulated immune activation is optimal at or below 41 °C, above which deleterious effects and damage begin to outpace stimulatory pathways[140]. It is important to note, however, that inducing a focal thermal elevation above fever conditions at the tumor core to stimulate engineering thermo-responsive therapeutics will result in temperature dissipation along a gradient to the periphery. Tumor-infiltrating immune cells further from the focal stimulation zone are expected to experience more optimal temperatures in the fever range and may therefore act as a secondary mechanism to promote tumor rejection.

In addition to potentiating the immune response against tumors, local hyperthermia has complementary effects with other therapeutic modalities[139]. The most significant benefits are likely to occur due to temperature-associated increase in blood perfusion[70]. This enhanced blood transport reoxygenates hypoxic tumors, which are otherwise resistant to radiotherapy[162]. It also increases the local availability of passively transported therapeutic agents such nanoparticles. Cells in S-phase of the replication cycle, while relatively resistant

to radiation therapy, are sensitized to hyperthermia[123]. Actively mitotic cells are also sensitive to hyperthermia, with experiments in CHO cells demonstrating complete destruction of the centriole upon a thermal dose of 45 °C for 15 minutes[132]. A variety of clinical trials have demonstrated that combination therapy incorporating local hyperthermia improves treatment outcomes across multiple cancer types[71] and this modality is regarded as a leading adjuvant for chemotherapy and radiation therapy[163].

2.8: Ultrasound Hyperthermia: Potential for Biological Control

Noninvasive technologies have the potential to address many of the shortcomings of next-generation therapeutic agents, such as engineered cells and viruses. Focused Ultrasound Hyperthermia is a signaling modality capable of nearly full-body access and confined spatial resolution on the order of millimeters, rendering it an ideal choice for communicating with endogenous biological agents with spatiotemporal precision. FUS hyperthermia can be measured in real time to ensure that a sub-ablative thermal regime is maintained, and mild hyperthermic exposures have now been sufficiently characterized to ensure minimal deleterious effects to the stimulated tissue. The hardware for HIFU stimulation is clinically available and appears to be gaining market penetrance. As such, the infrastructure for specific ultrasound biomodulation is available and awaiting novel engineered biological agents to take advantage of its potential.

2.9: References

1. Jin, C. *et al.* Safe engineering of CAR T cells for adoptive cell therapy of cancer using long-term episomal gene transfer. *EMBO Mol. Med.* **8**, 702–711 (2016).
2. Holmes-Son, M. L. & Chow, S. A. Correct integration mediated by integrase-LexA fusion proteins incorporated into HIV-1. *Mol. Ther.* **5**, 360–370 (2002).
3. Tan, W. *et al.* Fusion proteins consisting of human immunodeficiency virus type 1 integrase and the designed polydactyl zinc finger protein E2C direct integration of viral DNA into specific sites. *J. Virol.* **78**, 1301–13 (2004).
4. Gordley, R. M., Gersbach, C. A. & Barbas, C. F. Synthesis of programmable integrases. *Proc. Natl. Acad. Sci.* **106**, 5053–5058 (2009).
5. Chaikind, B., Bessen, J. L., Thompson, D. B., Hu, J. H. & Liu, D. R. A programmable Cas9-serine recombinase fusion protein that operates on DNA sequences in mammalian cells. *Nucleic Acids Res.* **147**, 9758–9770 (2016).
6. Ain, Q. U., Chung, J. Y. & Kim, Y.-H. Current and future delivery systems for engineered nucleases: ZFN, TALEN and RGEN. *J. Control. Release* **205**, 120–127 (2014).
7. Sakemura, R. *et al.* A Tet-On Inducible System for Controlling CD19-Chimeric Antigen Receptor Expression upon Drug Administration. *Cancer Immunol. Res.* **4**, 658–668 (2016).
8. Hwang, I. Y. *et al.* Reprogramming microbes to be pathogen-Seeking killers. *ACS Synth. Biol.* **3**, 228–237 (2014).
9. Wu, C.-Y., Roybal, K. T., Puchner, E. M., Onuffer, J. & Lim, W. A. Remote control of therapeutic T cells through a small molecule-gated chimeric receptor. *Science (80-.).* **350**, (2015).
10. Juillerat, A. *et al.* Design of chimeric antigen receptors with integrated controllable transient functions. *Sci. Rep.* **6**, 18950 (2016).
11. Agha-Mohammadi, S. *et al.* Second-generation tetracycline-regulatable promoter: repositioned tet operator elements optimize transactivator synergy while shorter minimal promoter offers tight basal leakiness. *J. Gene Med.* **6**, 817–28 (2004).
12. Papadakis, E. D., Nicklin, S. a, Baker, a H. & White, S. J. Promoters and control elements: designing expression cassettes for gene therapy. *Curr. Gene Ther.* **4**, 89–113 (2004).
13. Liu, K. I. *et al.* A chemical-inducible CRISPR–Cas9 system for rapid control of genome editing. *Nat. Chem. Biol.* **12**, (2016).
14. Kloss, C. C., Condomines, M., Cartellieri, M., Bachmann, M. & Sadelain, M. Combinatorial antigen recognition with balanced signaling promotes selective tumor eradication by engineered T cells. *Nat. Biotechnol.* **31**, 71–75 (2012).
15. Fedorov, V. D., Themeli, M. & Sadelain, M. PD-1- and CTLA-4-based inhibitory chimeric antigen receptors (iCARs) divert off-target immunotherapy responses. *Sci. Transl. Med.* **5**, 1–12 (2013).
16. Sukumaran, S. *et al. Enhancing the Potency and Specificity of Engineered T Cells for Cancer Treatment*. *Cancer Discovery* (2018). doi:10.1158/2159-8290.CD-17-1298
17. Roybal, K. T. *et al.* Precision Tumor Recognition by T Cells With Combinatorial Antigen-Sensing Circuits. *Cell* **164**, 770–779 (2016).
18. Haigron, P., Dillenseger, J.-L., Limin Luo & Coatrieux, J.-L. Image-Guided Therapy: Evolution and Breakthrough. *IEEE Eng. Med. Biol. Mag.* **29**, 100–104 (2010).
19. Pandori, M. W. *et al.* Spatial Control of Gene Transduction Using Photo-Activatable Viral Vectors. *Mol. Ther.* **5**, S150 (2002).
20. Gomez, E. J., Gerhardt, K., Judd, J., Tabor, J. J. & Suh, J. Light-Activated nuclear translocation of adeno-Associated virus nanoparticles using phytochrome B for enhanced, tunable, and spatially programmable gene delivery. *ACS Nano* **10**, 225–237 (2016).

21. Iyer, S. M. *et al.* Virally mediated optogenetic excitation and inhibition of pain in freely moving nontransgenic mice. *Nat. Biotechnol.* (2014). doi:10.1038/nbt.2834
22. Nihongaki, Y., Kawano, F., Nakajima, T. & Sato, M. Photoactivatable CRISPR-Cas9 for optogenetic genome editing. *Nat. Biotechnol.* **33**, (2015).
23. Chou, C. & Deiters, A. Light-activated gene editing with a photocaged zinc-finger nuclease. *Angew. Chemie - Int. Ed.* **50**, 6839–6842 (2011).
24. Piraner, D. I. *et al.* Going Deeper: Biomolecular Tools for Acoustic and Magnetic Imaging and Control of Cellular Function. *Biochemistry* **56**, (2017).
25. Kawaguchi, T. *et al.* Practical surgical indicators to identify candidates for radical resection of insulo-opercular gliomas. *J. Neurosurg.* **51**, 1124–1132 (2014).
26. Ramesh, H. S., Boase, T. & Audisio, R. A. Risk assessment for cancer surgery in elderly patients. *Clin. Interv. Aging* **1**, 221–227 (2006).
27. Chand, M., Armstrong, T., Britton, G. & Nash, G. F. How and why do we measure surgical risk? *J. R. Soc. Med.* **100**, 508–512 (2007).
28. Ogawa, R. *et al.* Construction of X-ray-inducible promoters through cis-acting element elongation and error-prone polymerase chain reaction. *J. Gene Med.* **10**, 316–324 (2008).
29. Mukherjee, A., Davis, H. C., Ramesh, P., Lu, G. J. & Shapiro, M. G. *Biomolecular MRI Reporters: evolution of new mechanisms*. *Progress in Nuclear Magnetic Resonance Spectroscopy* (2017). doi:10.1016/j.pnmrs.2017.05.002
30. Zhu, H. *et al.* Spatial control of in vivo CRISPR–Cas9 genome editing via nanomagnets. *Nat. Biomed. Eng.* 1 (2018). doi:10.1038/s41551-018-0318-7
31. Yamaguchi, M., Ito, A., Ono, A., Kawabe, Y. & Kamihira, M. Heat-Inducible Gene Expression System by Applying Alternating Magnetic Field to Magnetic Nanoparticles. *ACS Synth. Biol.* **3**, 273–279 (2014).
32. Wheeler, M. A. *et al.* Genetically targeted magnetic control of the nervous system. *Nat. Neurosci.* **19**, 756–761 (2016).
33. Qiu, Y. *et al.* Magnetic forces enable controlled drug delivery by disrupting endothelial cell-cell junctions. *Nat. Commun.* **8**, 15594 (2017).
34. Choi, B. H., Kim, J. H., Cheon, J. P. & Rim, C. T. Synthesized Magnetic Field Focusing Using a Current-Controlled Coil Array. *IEEE Magn. Lett.* **7**, 2–5 (2016).
35. Shapiro, B. Towards dynamic control of magnetic fields to focus magnetic carriers to targets deep inside the body. *J. Magn. Magn. Mater.* **321**, 1594–1599 (2009).
36. Stanley, S. A., Sauer, J., Kane, R. S., Dordick, J. S. & Friedman, J. M. Remote regulation of glucose homeostasis in mice using genetically encoded nanoparticles. *Nat. Med.* **21**, 92–98 (2015).
37. Meister, M. Physical limits to magnetogenetics. *Elife* **5**, 1–14 (2016).
38. Faivre, D. & Schüler, D. Magnetotactic Bacteria and Magnetosomes. *Chem. Rev.* **108**, 4875–4898 (2008).
39. Ramesh, P. *et al.* Ultraparamagnetic Cells Formed through Intracellular Oxidation and Chelation of Paramagnetic Iron. *Angew. Chemie Int. Ed.* **57**, 12385–12389 (2018).
40. Choi, E. & Roh, Y. Optimal design of a concave annular high intensity focused ultrasound transducer for medical treatment. *Sensors Actuators A Phys.* **263**, 91–101 (2017).
41. O'Brien, W. D. Ultrasound-biophysics mechanisms. *Prog. Biophys. Mol. Biol.* **93**, 212–55 (2007).
42. Yoon, S. *et al.* Direct and sustained intracellular delivery of exogenous molecules using acoustic-transfection with high frequency ultrasound. *Sci. Rep.* **6**, 1–11 (2016).
43. Menz, M. D., Oralkan, O., Khuri-Yakub, P. T. & Baccus, S. a. Precise neural stimulation in the retina using focused ultrasound. *J. Neurosci.* **33**, 4550–60 (2013).
44. Silverman, R. H. *et al.* 75 MHz Ultrasound Biomicroscopy of Anterior Segment of Eye. *Ultrason. Imaging* **28**, 179–188 (2006).

45. ter Haar, G. & Coussios, C. High intensity focused ultrasound: Physical principles and devices. *Int. J. Hyperth.* **23**, 89–104 (2007).
46. Canney, M. S., Bailey, M. R., Crum, L. A., Khokhlova, V. A. & Sapozhnikov, O. A. Acoustic characterization of high intensity focused ultrasound fields: A combined measurement and modeling approach. *J. Acoust. Soc. Am.* **124**, 2406–2420 (2008).
47. Zhou, Y.-F. High intensity focused ultrasound in clinical tumor ablation. *World J. Clin. Oncol.* **2**, 8 (2011).
48. Kubanek, J. Neuromodulation with transcranial focused ultrasound. *Neurosurg. Focus* **20**, E14 (2018).
49. Tyler, W. J. *et al.* Remote excitation of neuronal circuits using low-intensity, low-frequency ultrasound. *PLoS One* **3**, e3511 (2008).
50. Tufail, Y. *et al.* Transcranial pulsed ultrasound stimulates intact brain circuits. *Neuron* **66**, 681–94 (2010).
51. Ye, P. P., Brown, J. R. & Pauly, K. B. Frequency Dependence of Ultrasound Neurostimulation in the Mouse Brain. *Ultrasound Med. Biol.* **42**, 1512–1530 (2016).
52. Downs, M. E. *et al.* Non-invasive peripheral nerve stimulation via focused ultrasound in vivo. *Phys. Med. Biol.* **63**, 035011 (2018).
53. Aubry, J.-F., Tanter, M., Pernot, M., Thomas, J.-L. & Fink, M. Experimental demonstration of noninvasive transskull adaptive focusing based on prior computed tomography scans. *J. Acoust. Soc. Am.* **113**, 84 (2003).
54. White, J., Clement, G. & Hynynen, K. Transcranial ultrasound focus reconstruction with phase and amplitude correction. *... Freq. Control. ...* **52**, 1518–1522 (2005).
55. Legon, W. *et al.* Transcranial focused ultrasound modulates the activity of primary somatosensory cortex in humans. *Nat. Neurosci.* **17**, 322–9 (2014).
56. Pardridge, W. M. Drug transport across the blood-brain barrier. *J. Cereb. Blood Flow Metab.* **32**, 1959–1972 (2012).
57. Alonso, A. Ultrasound-induced blood-brain barrier opening for drug delivery. *Front. Neurol. Neurosci.* **36**, 106–115 (2015).
58. Jordão, J. F. *et al.* Amyloid-β plaque reduction, endogenous antibody delivery and glial activation by brain-targeted, transcranial focused ultrasound. *Exp. Neurol.* **248**, 16–29 (2013).
59. Alecou, T., Giannakou, M. & Damianou, C. Amyloid β plaque reduction with antibodies crossing the blood-brain barrier, which was opened in 3 sessions of focused ultrasound in a rabbit model. *J. Ultrasound Med.* **36**, 2257–2270 (2017).
60. Szablowski, J. O., Lee-Gosselin, A., Lue, B., Malounda, D. & Shapiro, M. G. Acoustically targeted chemogenetics for the non-invasive control of neural circuits. *Nat. Biomed. Eng.* **2**, 475–484 (2018).
61. Ibsen, S., Tong, A., Schutt, C., Esener, S. & Chalasani, S. H. Sonogenetics is a non-invasive approach to activating neurons in Caenorhabditis elegans. *Nat. Commun.* **6**, 1–12 (2015).
62. Pan, Y. *et al.* Mechanogenetics for the remote and noninvasive control of cancer immunotherapy. *Proc. Natl. Acad. Sci.* **115**, 992–997 (2018).
63. Bronner, F. Extracellular and Intracellular Regulation of Calcium Homeostasis. *Sci. World J.* **1**, 919–925 (2001).
64. Jolesz, F. A., Hynynen, K., McDannold, N. & Tempany, C. MR imaging-controlled focused ultrasound ablation: A noninvasive image-guided surgery. *Magn. Reson. Imaging Clin. N. Am.* **13**, 545–560 (2005).
65. Kennedy, J. E. High-intensity focused ultrasound in the treatment of solid tumours. *Nat. Rev. Cancer* **105**, 321–327 (2005).
66. Elias, W. J. *et al.* A Pilot Study of Focused Ultrasound Thalamotomy for Essential Tremor. *N. Engl. J. Med.* **369**, 640–648 (2013).
67. Martínez-Fernández, R. *et al.* Focused ultrasound subthalamotomy in patients with

asymmetric Parkinson's disease: a pilot study. *Lancet Neurol.* **17**, 54–63 (2018).
68. Tyshlek, D. *et al.* Focused ultrasound development and clinical adoption: 2013 update on the growth of the field. *J. Ther. Ultrasound* **2**, 1–7 (2014).
69. Partanen, A. *et al.* Mild hyperthermia with magnetic resonance-guided high-intensity focused ultrasound for applications in drug delivery. *Int. J. Hyperth.* **28**, 320–336 (2012).
70. Viglianti, B. L., Stauffer, P., Repasky, E., Vujaskovic, Z. & Dewhirst, M. Hyperthermia. in *Holland-Frei Cancer Medicine* (ed. Hong, W. K.) 528–540 (People's Medical Publishing House, 2010).
71. Van Rhoon, G. C. External Electromagnetic Methods and Devices. in *Physics of Thermal Therapy Fundamentals and Clinical Applications* (ed. Moros, E. G.) (CRC Press, 2012).
72. Turner, P. F. Regional Hyperthermia with an Annular Phased Array. *EEE Trans. Biomed. Eng.* **BME-31**, 106–114 (1984).
73. Nadobny, J., Wlodarczyk, W., Westhoff, L., Gellermann, J. & Felix, R. A Clinical Water-Coated Antenna Applicator for MR-Controlled Deep-Body Hyperthermia : A Comparison of Calculated and Measured 3-D Temperature Data Sets. *IEEE Trans. Biomed. Eng.* **52**, 505–519 (2005).
74. Zhao, K., Liu, M. & Burgess, R. R. The global transcriptional response of Escherichia coli to induced Sigma32 protein involves Sigma32 regulon activation followed by inactivation and degradation of Sigma32 in vivo. *J. Biol. Chem.* **280**, 17758–17768 (2005).
75. Tilly, K., Erickson, J., Sharma, S. & Georgopoulos, C. Heat shock regulatory gene rpoH mRNA level increases after heat shock in Escherichia coli. *J. Bacteriol.* **168**, 1155–1158 (1986).
76. O'Connell-Rodwell, C. E. *et al.* A genetic reporter of thermal stress defines physiologic zones over a defined temperature range. *FASEB J.* **18**, 264–271 (2004).
77. O'Connell-Rodwell, C. E. *et al.* In vivo analysis of heat-shock-protein-70 induction following pulsed laser irradiation in a transgenic reporter mouse. *J. Biomed. Opt.* **13**, 030501 (2014).
78. Sandre, O. *et al.* In vivo imaging of local gene expression induced by magnetic hyperthermia. *Genes (Basel).* **8**, (2017).
79. Ito, A., Shinkai, M., Honda, H. & Kobayashi, T. Heat-inducible TNF-α gene therapy combined with hyperthermia using magnetic nanoparticles as a novel tumor-targeted therapy. *Cancer Gene Ther.* **8**, 649–654 (2001).
80. Luo, J. *et al.* Radiofrequency hyperthermia promotes the therapeutic effects on chemotherapeutic-resistant breast cancer when combined with heat shock protein promoter-controlled HSV-TK gene therapy: Toward imaging-guided interventional gene therapy. *Oncotarget* **7**, (2016).
81. Kruse, D. E., Mackanos, M. a, O'Connell-Rodwell, C. E., Contag, C. H. & Ferrara, K. W. Short-duration-focused ultrasound stimulation of Hsp70 expression in vivo. *Phys. Med. Biol.* **53**, 3641–3660 (2008).
82. Deckers, R. *et al.* Image-guided, noninvasive, spatiotemporal control of gene expression. *Proc. Natl. Acad. Sci.* **106**, 1175–1180 (2009).
83. Silcox, C. E. *et al.* MRI-guided ultrasonic heating allows spatial control of exogenous luciferase in canine prostate. *Ultrasound Med. Biol.* **31**, 965–970 (2005).
84. Eker, O. F. *et al.* Combination of cell delivery and thermoinducible transcription for in vivo spatiotemporal control of gene expression: a feasibility study. *Radiology* **258**, 496–504 (2011).
85. Fortin, P.-Y. *et al.* Spatiotemporal control of gene expression in bone-marrow derived cells of the tumor microenvironment induced by MRI guided focused ultrasound. *Oncotarget* **6**, 23417–23426 (2015).
86. Cha, H. J., Srivastava, R., Vakharia, V. N., Rao, G. & Bentley, W. E. Green Fluorescent Protein as a Noninvasive Stress Probe in Resting Escherichia coli Cells Green Fluorescent

Protein as a Noninvasive Stress Probe in Resting Escherichia coli Cells. *Appl. Environ. Microbiol.* **65**, 409–414 (1999).
87. Li, C., Yi Ping Tao & Simon, L. D. Expression of different-size transcripts from the clpP-clpX operon of Escherichia coli during carbon deprivation. *J. Bacteriol.* **182**, 6630–6637 (2000).
88. Hever, N. & Belkin, S. A dual-color bacterial reporter strain for the detection of toxic and genotoxic effects. *Eng. Life Sci.* **6**, 319–323 (2006).
89. Mathew, A. N. U. *et al.* Stress-Specific Activation and Repression of Heat Shock Factors 1 and 2. *Mol. Cell. Biol.* **21**, 7163–7171 (2001).
90. Morimoto, R. Cells in stress: transcriptional activation of heat shock genes. *Science (80-.).* **259**, 1409–1410 (1993).
91. Freeman, M. L. *et al.* Characterization of a signal generated by oxidation of protein thiols that activates the heat shock transcription factor. *J. Cell. Physiol.* **164**, 356–366 (1995).
92. Amici, C., Sistonen, L., Santoro, M. G. & Morimoto, R. I. Antiproliferative prostaglandins activate heat shock transcription factor. *Proc. Natl. Acad. Sci. U. S. A.* **89**, 6227–31 (1992).
93. Santoro, M. G., Garaci, E. & Amici, C. Prostaglandins with antiproliferative activity induce the synthesis of a heat shock protein in human cells. *Proc Natl Acad Sci U S A* **86**, 8407–8411 (1989).
94. Jurivich, D., Sistonen, L., Kroes, R. & Morimoto, R. Effect of sodium salicylate on the human heat shock response. *Science (80-.).* **255**, 1243–1245 (1992).
95. Sciandra, J. J. & Subjeck, J. R. The Effects of Glucose on Protein Synthesis and Thermosensitivity in Chinese Hamster Ovary Cells. *J. Biol. Chem.* **258**, 12091–12093 (1983).
96. Xu, Q., Schett, G., Li, C., Hu, Y. & Wick, G. Mechanical Stress–Induced Heat Shock Protein 70 Expression in Vascular Smooth Muscle Cells Is Regulated by Rac and Ras Small G Proteins but Not Mitogen-Activated Protein Kinases. *Circ. Res.* **86**, 1122–1128 (2000).
97. Clos, J., Rabindran, S., Wisniewski, J. & Wu, C. Induction temperature of human heat shock factor is reprogrammed in a Drosophila cell environment. *Nature* **364**, 252–255 (1993).
98. Patel, B. *et al.* Hypoxia induces HSP 70 gene expression in human hepatoma (HEP G2) cells. *Biochem Mol Biol Int* **36**, 907–912 (1995).
99. Mestril, R., Chi, S. H., Sayen, M. R. & Dillmann, W. H. Isolation of a novel inducible rat heat-shock protein (HSP70) gene and its expression during ischaemia/hypoxia and heat shock. *Biochem. J.* **298**, 561–569 (1994).
100. Iwaki, K., Chi, S. H., Dillmann, W. H. & Mestril, R. Induction of HSP70 in cultured rat neonatal cardiomyocytes by hypoxia and metabolic stress. *Circulation* **87**, 2023–2032 (1993).
101. Benjamin, I. J., Kroger, B. & Williams, R. S. Activation of the heat shock transcription factor by hypoxia in mammalian cells. *Proc. Natl. Acad. Sci.* **87**, 6263–6267 (1990).
102. Dillmann, W. H. *et al.* Ischemia of the dog heart induces the appearance of a cardiac mRNA coding for a protein with migration characteristics similar to heat-shock/stress protein 71. *Circ. Res.* **59**, 110–114 (1986).
103. Zhang, C. C. & Sadek, H. A. Hypoxia and Metabolic Properties of Hematopoietic Stem Cells. *Antioxid. Redox Signal.* **20**, 1891–1901 (2014).
104. Fernández-Torres, J., ZaFernández-Torres, J., Zamudio-Cuevas, Y., Martínez-Nava, G. A., & López-Reyes, A. G. (2017). Hypoxia-Inducible Factors (HIFs) in the articular cartilage: a systematic review. European Review for Medical and Pharmacological Sciences, 21(12), 2800–2810.mu, Y., Martínez-Nava, G. A. & López-Reyes, A. G. Hypoxia-Inducible Factors (HIFs) in the articular cartilage: a systematic review. *Eur. Rev. Med. Pharmacol. Sci.* **21**, 2800–2810 (2017).
105. Gilreath, J. A., Stenehjem, D. D. & Rodgers, G. M. Diagnosis and treatment of cancer-related anemia. *Am. J. Hematol.* **89**, 203–212 (2014).
106. Zander, R. The oxygen status of arterial human blood. *Scand. J. Clin. Lab. Invest.* **50**, 187–

196 (1990).
107. Leppa, S. Differential Induction of Hsp70-encoding Genes in Human Hematopoietic Cells. *J. Biol. Chem.* **276**, 31713–31719 (2001).
108. Gothard, L. Q. Lowered Temperature Set Point for Activation of the Cellular Stress Response in T-lymphocytes. *J. Biol. Chem.* **278**, 9322–9326 (2003).
109. Nishimura, R. N. & Dwyer, B. E. Evidence for different mechanisms of induction of HSP70i: a comparison of cultured rat cortical neurons with astrocytes. *Brain Res. Mol. Brain Res.* **36**, 227–239 (1996).
110. Marcuccilli, C. J., Mathur, S. K., Morimoto, R. I. & Miller, R. J. Regulatory differences in the stress response of hippocampal neurons and glial cells after heat shock. *J. Neurosci.* **16**, 478–485 (1996).
111. Oza, J., Yang, J., Chen, K. Y. & Liu, A. Y.-C. Changes in the regulation of heat shock gene expression in neuronal cell differentiation. *Cell Stress Chaperones* **13**, 73–84 (2008).
112. Batulan, Z. *et al.* High threshold for induction of the stress response in motor neurons is associated with failure to activate HSF1. *J. Neurosci.* **23**, 5789–5798 (2003).
113. Anckar, J. & Sistonen, L. Regulation of HSF1 function in the heat stress response: implications in aging and disease. *Annu. Rev. Biochem.* **80**, 1089–1115 (2011).
114. Grosso-Becera, M. V., Servín-González, L. & Soberón-Chávez, G. RNA structures are involved in the thermoregulation of bacterial virulence-associated traits. *Trends Microbiol.* **23**, 1–10 (2015).
115. Waldminghaus, T., Heidrich, N., Brantl, S. & Narberhaus, F. FourU: A novel type of RNA thermometer in Salmonella. *Mol. Microbiol.* **65**, 413–424 (2007).
116. Neupert, J., Karcher, D. & Bock, R. Design of simple synthetic RNA thermometers for temperature-controlled gene expression in Escherichia coli. *Nucleic Acids Res.* **36**, 1–9 (2008).
117. Krajewski, S. S. & Narberhaus, F. Temperature-driven differential gene expression by RNA thermosensors. *Biochim. Biophys. Acta - Gene Regul. Mech.* **1839**, 978–988 (2014).
118. Kortmann, J., Sczodrok, S., Rinnenthal, J., Schwalbe, H. & Narberhaus, F. Translation on demand by a simple RNA-based thermosensor. *Nucleic Acids Res.* **39**, 2855–2868 (2011).
119. Roßmanith, J., Weskamp, M. & Narberhaus, F. Design of a temperature-responsive transcription terminator. *ACS Synth. Biol.* acssynbio.7b00356 (2017). doi:10.1021/acssynbio.7b00356
120. Waldminghaus, T., Kortmann, J., Gesing, S. & Narberhaus, F. Generation of synthetic RNA-based thermosensors. *Biol. Chem.* **389**, 1319–1326 (2008).
121. Phillips, R., Kondev, J., Theriot, J. & Garcia, H. G. Entropy Rules! in *Physical Biology of the Cell* (ed. Scholl, S.) 237–279 (Taylor & Francis, 2012).
122. Smith, I. W. M. The temperature-dependence of elementary reaction rates: beyond Arrhenius. *Chem. Soc. Rev.* **37**, 812–826 (2008).
123. Lepock, J. R. Cellular effects of hyperthermia : relevance to the minimum dose for thermal damage. *Int. J. Hyperth.* **3**, 252–266 (2003).
124. Song, A. S. Thermally Induced Apoptosis , Necrosis , and Heat Shock Protein Expression in 3D Culture. **136**, 1–10 (2014).
125. Richter, K., Haslbeck, M. & Buchner, J. The Heat Shock Response : Life on the Verge of Death. *Mol. Cell* **40**, 253–266 (2010).
126. Saibil, H. Chaperone machines for protein folding , unfolding and disaggregation. *Nat. Publ. Gr.* **14**, 630–642 (2013).
127. Yura, T. Regulation and conservation of the heat-shock transcription factor σ 32. *Genes to Cells* **1**, 277–284 (1996).
128. Morita, M. T. *et al.* Translational induction of heat shock transcription factor ς 32 : evidence for a built-in RNA thermosensor. *Genes Dev. Dev.* **13**, 655–665 (1999).

129. Vera, M. *et al.* The translation elongation factor eEF1A1 couples transcription to translation during heat shock response. *Elife* **3**, 1–19 (2014).
130. Lepock, J. R. Protein Denaturation During Heat Shock. in *Advances in Molecular and Cell Biology* 223–259 (1997). doi:10.1016/S1569-2558(08)60079-X
131. Roti Roti, J. L. Cellular responses to hyperthermia (40 – 46 C): Cell killing and molecular events. *Int. J. Hyperth.* **24**, 3–15 (2008).
132. Cosst, R. A. & Linnemans, W. A. M. The effects of hyperthermia on the cytoskeleton. *Int. J. Hyperth.* **12**, 173–196 (1996).
133. Johnson, H. A. & Pavelec, M. Thermal Noise in Cells. *Am. J. Pathol.* **69**, 119–130 (1972).
134. Dewhirst, M. W., Viglianti, B. L., Lora-Michiels, M., Hanson, M. & Hoopes, P. J. Basic principles of thermal dosimetry and thermal thresholds for tissue damage from hyperthermia. *Int. J. Hyperth.* **19**, 267–294 (2003).
135. Roizin-Towle, L. & Pirro, J. P. The Response of Human and Rodent Cells to Hyperthermia. *Int. J. Radiat. Oncol. Biol. Phys.* **20**, 751–756 (1991).
136. Sapareto, S. & Dewey, W. Thermal dose determination in cancer therapy. *… J. Radiat. Oncol. Biol. Phys.* **10**, 787–800 (1984).
137. Yarmolenko, P. S. *et al.* Thresholds for thermal damage to normal tissues : An update. *Int. J. Hyperth.* **6736**, (2011).
138. van Rhoon, G. C. *et al.* CEM43°C thermal dose thresholds: a potential guide for magnetic resonance radiofrequency exposure levels? *Eur. Radiol.* **23**, 2215–2227 (2013).
139. Repasky, E. A., Evans, S. S. & Dewhirst, M. W. Temperature Matters! And Why It Should Matter to Tumor Immunologists. *Cancer Immunol. Res.* **1**, 210–216 (2013).
140. Toraya-Brown, S. & Fiering, S. Local tumour hyperthermia as immunotherapy for metastatic cancer. *Int. J. Hyperth.* **30**, 531–539 (2014).
141. Fisher, D. T. *et al.* IL-6 trans-signaling licenses mouse and human tumor microvascular gateways for trafficking of cytotoxic T cells. *J. Clin. Invest.* **121**, 3846–3859 (2011).
142. Chen, T., Guo, J., Han, C., Yang, M. & Cao, X. Heat Shock Protein 70, Released from Heat-Stressed Tumor Cells, Initiates Antitumor Immunity by Inducing Tumor Cell Chemokine Production and Activating Dendritic Cells via TLR4 Pathway. *J. Immunol.* **1**, (2009).
143. Ito, A. *et al.* Tumor regression by combined immunotherapy and hyperthermia using magnetic nanoparticles in an experimental subcutaneous murine melanoma. *Cancer Sci.* **94**, 1–6 (2003).
144. Dayanc, B. E., Beachy, S. H., Ostberg, J. R. & Repasky, E. A. Dissecting the role of hyperthermia in natural killer cell mediated anti-tumor responses. *Int. J. Hyperth.* **24**, 41–56 (2008).
145. Ostberg, J. R., Dayanc, B. E., Yuan, M., Oflazoglu, E. & Repasky, E. A. Enhancement of natural killer (NK) cell cytotoxicity by fever- range thermal stress is dependent on NKG2D function and is associated with plasma membrane NKG2D clustering and increased expression of MICA on target cells Abstract : Circulating NK cells n. *J. Leukoc. Biol.* **82**, 1322–1331 (2007).
146. Dayanc, B. E., Bansal, S., Gure, A. O., Gollnick, S. O. & Repasky, E. A. Enhanced sensitivity of colon tumour cells to natural killer cell cytotoxicity after mild thermal stress is regulated through HSF1-mediated expression of MICA. *Int. J. Hyperth.* **29**, 480–490 (2013).
147. Mace, T. a. *et al.* Differentiation of CD8+ T cells into effector cells is enhanced by physiological range hyperthermia. *J. Leukoc. Biol.* **90**, 951–962 (2011).
148. Wang, X., Ostberg, J. R. & Elizabeth, A. Effect of Fever-Like Whole-Body Hyperthermia on Lymphocyte Spectrin Distribution, Protein Kinase C Activity, and Uropod Formation. *J. Immunol.* **162**, 3378–3387 (1999).
149. Mace, T. A., Zhong, L., Kokolus, K. M. & Repasky, E. A. Effector CD8 $^{+}$ T cell IFN- γ production and cytotoxicity are enhanced by mild hyperthermia. *Int. J. Hyperth.* **28**, 9–18 (2012).

150. Cippitelli, M. *et al.* Hyperthermia Enhances CD95-Ligand Gene Expression in T Lymphocytes. *J. Immunol.* **174**, 223–232 (2005).
151. Kubeš, J., Svoboda, J., Rosina, J., Starec, M. & Fišerová, A. Immunological Response in the Mouse Melanoma Model after Local Hyperthermia. *Physiol. Res.* **57**, 459–465 (2008).
152. Toraya-Brown, S. *et al.* Local hyperthermia treatment of tumors induces CD8+ T cell-mediated resistance against distal and secondary tumors. *Nanomedicine Nanotechnology, Biol. Med.* **10**, 1273–1285 (2014).
153. Pritchard, M. T., Li, Z. & Repasky, E. A. Nitric oxide production is regulated by fever-range thermal stimulation of murine macrophages Abstract : As macrophages are often called to. *J. Leukoc. Biol.* **78**, 630–638 (2005).
154. Bruggen, I. V. A. N. & Robertson, T. A. The Effect of Mild Hyperthermia on the Morphology and Function of Murine Resident Peritoneal Macrophages. *Exp. Mol. Pathol.* **55**, 119–134 (1991).
155. Yoshioka, H., Koga, S., Maeta, M. & Shimizu, N. The Influence of Hyperthermia in vitro on the Functions of Peritoneal Macrophages in Mice. *Jpn. J. Surg.* **20**, 119–122 (1990).
156. Peng, J. C. *et al.* Monocyte-derived DC Primed With TLR Agonists Secrete IL-12p70 in a CD40-dependent Manner Under Hyperthermic Conditions. *J. Immunother.* **29**, 606–615 (2006).
157. Tournier, J. *et al.* Fever-like thermal conditions regulate the activation of maturing dendritic cells. *J. Leukoc. Biol.* **73**, 493–501 (2003).
158. Basu, S. & Srivastava, P. K. Fever-like temperature induces maturation of dendritic cells through induction of hsp90. *Int. Immunol.* **15**, 1053–1061 (2003).
159. Fucikova, J. *et al.* Human Tumor Cells Killed by Anthracyclines Induce a Tumor-Specific Immune Response. *Cancer Res.* **71**, 4821–4833 (2011).
160. Milani, V. *et al.* Heat shock protein 70: role in antigen presentation and immune stimulation. *Int. J. Hyperth.* **18**, 563–575 (2002).
161. Zhou, Y. J. & Binder, R. J. A molecular description of tumor immunosurveillance The Heat Shock Protein-CD91 pathway. *Oncoimmunology* **3**, e28222 (2014).
162. Song, C. W., Park, H. & Griffin, R. J. Improvement of Tumor Oxygenation by Mild Hyperthermia. *Radiat. Res.* **155**, 515–528 (2001).
163. van Rhoon, G. C. Is CEM43 still a relevant thermal dose parameter for hyperthermia treatment monitoring? *Int. J. Hyperth.* **32**, 50–62 (2016).

C h a p t e r 3

TUNABLE THERMAL BIOSWITCHES FOR IN VIVO CONTROL OF MICROBIAL THERAPEUTICS

Piraner, D. I., Abedi, M. H., Moser, B. A., Lee-Gosselin, A., & Shapiro, M. G. (2017). Tunable thermal bioswitches for in vivo control of microbial therapeutics. *Nature Chemical Biology*, *13*(1), 75–80. https://doi.org/10.1038/nchembio.2233

3.1: Introduction

Rapid advances in synthetic biology[1, 2] are driving the development of genetically engineered microbes as therapeutic[3-6] and diagnostic[7-10] agents for a multitude of human diseases. A critical capability for many envisioned applications is the ability to control the function of engineered microbes *in situ* to enable spatially and temporally specific activation at anatomical and disease sites such as the gastrointestinal tract or tumors[2]. However, among existing control methods, systemic chemical administration typically lacks the spatial precision needed to modulate activity at specific anatomical locations, while optical approaches suffer from poor light penetration into tissues[11]. On the other hand, temperature can be controlled both globally and locally – at depth – using technologies such as focused ultrasound[12], infrared light[13] and magnetic particle hyperthermia[14]. In addition, body temperature can serve as an indicator of microbial entry and exit from the host organism and of the host's condition (*e.g.*, fever).

Given this potential, remarkably few high-performance thermal bioswitches are available to control gene expression in engineered microbes. The ideal bioswitch should have a sharp thermal transition resulting in a large change in activity (> 100-fold over a few degrees), and its switching temperature should be tunable to enable a broad range of applications. In addition, the bioswitch should be orthogonal to endogenous cellular machinery and compatible with other thermo-responsive components to allow multiplexed thermal logic. Existing temperature-dependent regulators of gene expression – including microbial heat shock factors, membrane-associated proteins, RNA thermometers, and transcriptional repressors – fail to fulfill these criteria. Microbial heat shock promoters undergo a relatively low level of thermal induction (~10-fold)[15], have crosstalk with other stimuli such as chemical stress[16], and may be difficult to tune without deleterious effects on the cell. Likewise, the switching temperature of membrane-associated proteins depends on bilayer composition and occupies second messenger pathways[17]. Meanwhile, RNA thermometers, while orthogonal to the host and amenable to tuning, generally have small dynamic ranges (< 10-fold) and broad transitions (> 10 °C)[18-25]. Of the available molecular machinery, several natural and mutant transcriptional repressors have the most robust thermal switching and potential for orthogonality[26-32]. However, their relative performance has not been characterized, they have not been systematically engineered to operate at specific transition temperatures, and their potential utility for *in vivo* microbial therapy applications has not been demonstrated.

To address the need for robust, tunable, orthogonal thermal control of engineered microbial systems, we systematically screened candidate transcriptional regulators, developed two

orthogonal families of high-performance thermal bioswitches with tunable thresholds within the biomedically relevant range of 32ºC to 46ºC, and demonstrated the potential utility of these devices in three distinct *in vivo* scenarios relevant to mammalian microbial therapy. These scenarios include spatially selective activation within a mammalian host using focused ultrasound, sensing and response to a fever, and self-destruction at ambient temperatures to prevent environmental contamination after leaving the intended host.

3.2: Results

3.2a: High-Performance Thermal Bioswitches

In order to engineer new families of robust, tunable, orthogonal thermal bioswitches, we began by characterizing the performance of six temperature-dependent transcriptional repressors and six endogenous heat shock promoters. Our panel included TlpA, a transcriptional autorepressor from the virulence plasmid of *Salmonella typhimurium*. This protein contains an approximately 300 residue C-terminal coiled-coil domain that undergoes sharp, temperature-dependent uncoiling between 37ºC and 45ºC , and an N-terminal DNA binding domain that, in its low-temperature dimeric state, blocks transcription from the 52 bp TlpA operator/promoter[26, 32]. In addition, we tested a well-known temperature-sensitive variant of the bacteriophage λ repressor cI (mutant cI^{857}, here referred to as TcI) acting on a tandem pR/pL operator/promoter[27]. In most previous applications, TcI repression has been modulated via large changes in temperature (e.g., steps from 30°C to 42°C)[27]. However, its original description as a virulence factor suggested that much sharper switching may be

possible[28]. Alongside TlpA and TcI, we tested four reported temperature-sensitive mutants of the *E. coli* repressors TetR (A89D and I193N)[29] and LacI (A241T and G265D)[30, 31], together with a panel of endogenous heat shock promoters, including GrpE, HtpG, Lon, RpoH, Clp and DnaK (**Fig. 3-1a**).

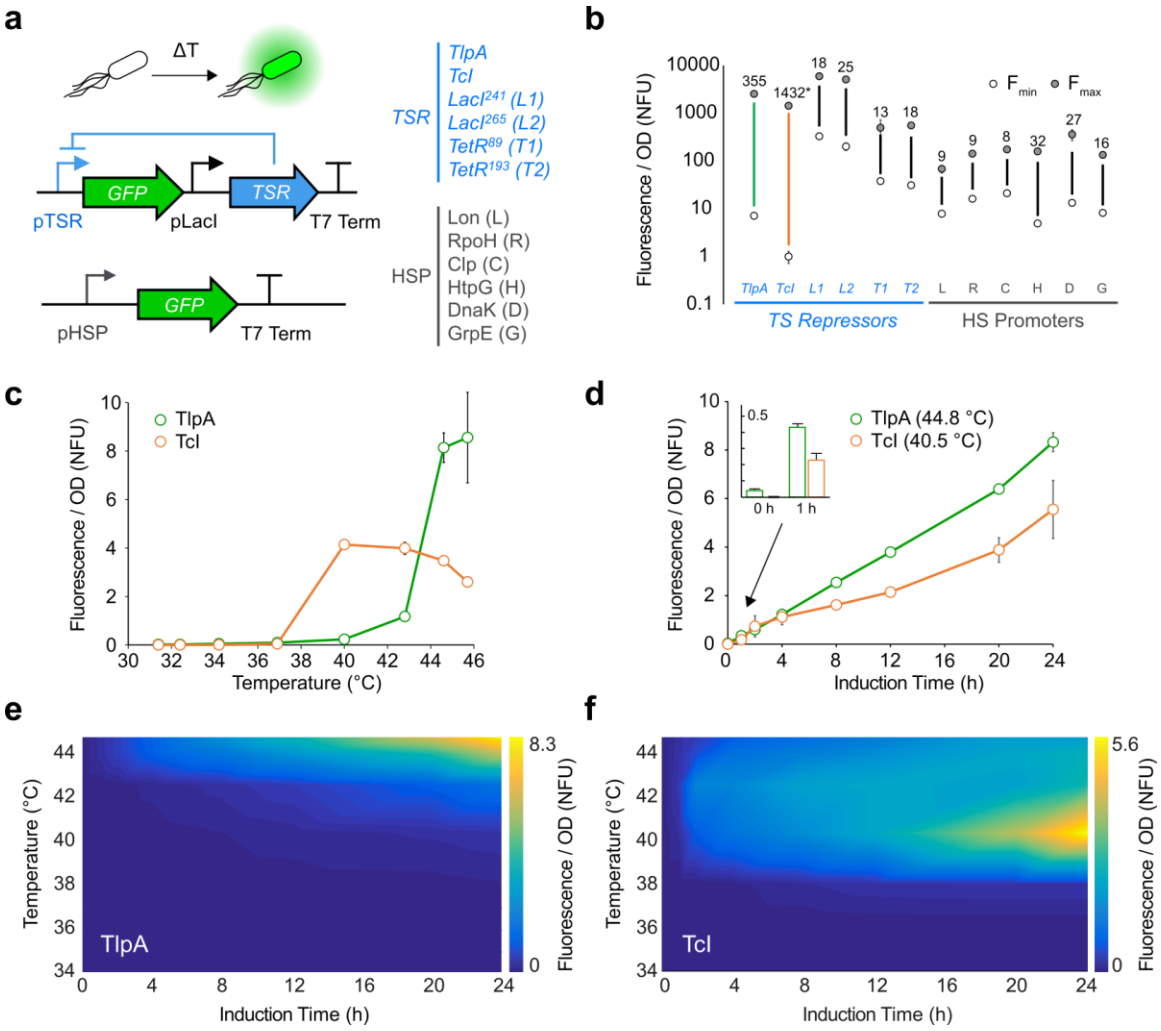

Figure 3-1: High-performance thermal bioswitches. (**a**) Constructs used to assay the performance of temperature-sensitive repressors (TSr, top) and heat shock promoters (HSP, bottom). The specific repressors and promoters assayed are listed in blue and gray, respectively. (**b**) optical density (oD)-normalized fluorescence after 12 h of thermal induction for the constructs shown in a. nFu, normalized fluorescence units. Fmin represents expression at 31.4 °C; Fmax is the maximum fluorescence intensity measured for each construct, measured up to 45.7 °C. The fold changes between Fmin and Fmax are listed above each sample. Where not seen, error bars are smaller than the symbol. N = 4 for TSrs and N = 3 for HSPs. The Fmin for TcI (indicated by *) is reported from

measurement at 34.2 °C because expression at lower temperatures was below the detection limit of the assay. (**c**) oD-normalized fluorescence from the Tlpa- and TcI-regulated constructs as a function of induction temperature for a fixed duration of 12 h. N = 4. (**d**) oD-normalized fluorescence as a function of thermal induction duration at the maximal induction temperature for the Tlpa and TcI constructs. N = 4. (**e**,**f**) oD-normalized fluorescence landscapes for Tlpa- and TcI-gated constructs, respectively, as a function of both incubation temperature and duration. Data shown interpolated from an 8 × 8 sampling matrix. all samples in d–f were maintained at 30 °C after the indicated period of thermal induction for a total experimental duration of 24 h before measurement. Error bars represent ± s.e.m.

The performance of these constructs is summarized in **Figure 3-1b**. TlpA and TcI had by far the largest dynamic ranges (355 ± 45 and >1,432, respectively), reflecting a combination of tighter repression at sub-threshold temperatures and stronger promoter activity above threshold. Both of these repressors show sharp thermal transitions, with greater than 30-fold induction over ranges of 5ºC and 3ºC centered at 43.5°C and 39.5ºC for TlpA and TcI, respectively (**Fig. 3-1c**). Furthermore, both systems are capable of rapid induction, with greater than 10-fold changes in expression observed after a 1 hour thermal stimulus (**Fig. 3-1d**). Complete time-temperature induction profiles for TlpA and TcI are shown in **Figure 3-1, e–f**. In addition to their high performance, TlpA and TcI are expected to be more orthogonal to cellular machinery than both the native heat shock promoters and the engineered TetR and LacI repressors, the latter of which are utilized in multiple endogenous and engineered gene circuits[33-35]. A homology search[36] showed that TlpA and TcI repressors are present in far fewer bacterial species than either TetR or LacI (**Supplementary Fig. 3-S1**). Based on these factors, we chose TlpA and TcI as our starting points for further bioswitch engineering.

Since the TlpA operator/promoter has not been studied in *E. coli*, we characterized its molecular mechanisms to inform its utilization in genetic circuits. As shown in

Supplementary Figure 3-S2, the TlpA operator is a strong promoter (88-fold stronger than $LacI^{Q}$) driven by the transcription factor σ^{70}. Interestingly, this promoter has bidirectional activity with identical thermal regulation in both orientations, but approximately 200-fold lower maximal expression in the reverse direction (**Supplementary Fig. 3-S2, c–d**). This property will enable convenient adjustment of TlpA-regulated expression according to circuit requirements.

3.2b: Tuning Bioswitch Activation Temperatures

Applications in microbial therapy require thermal bioswitches that activate at different transition temperatures. For example, a host colonization sensor should be activated at 37ºC, while a fever detector may work best with a thermal threshold of 39ºC, and a focused ultrasound-activated switch may require a transition point of 41ºC to avoid nonspecific actuation. Synthetic biology applications outside biomedicine may likewise have a variety of thermal requirements. It is thus highly desirable to be able to tune thermal bioswitches to activate at new temperatures while retaining sharp, robust switching performance. To enable such tuning of TlpA and TcI, we devised a simple and effective high-throughput assay based on colony fluorescence. We grew *E. coli* expressing GFP under the control of mutant repressors (generated by error-prone PCR) on solid media and replica-plated the colonies onto separate plates for simultaneous incubation at desired "off" and "on" temperatures (**Supplementary Fig. 3-S3a**). We then imaged the plates with wide-field fluorescence, as shown in **Figure 3-2a**. As expected, many colonies show constitutive expression (ostensibly due to loss of repressor function) while others fail to de-repress (most likely retaining their

original high transition point). However, several colonies show thermal induction in the desired regime. Within each screen, we selected several such colonies to undergo liquid phase characterization of induction temperature, switching sharpness, and expression levels (**Fig. 3-2b**). From these variants, we selected mutants that retained the desirable performance characteristics of the wild type repressor, but with shifted transition temperatures.

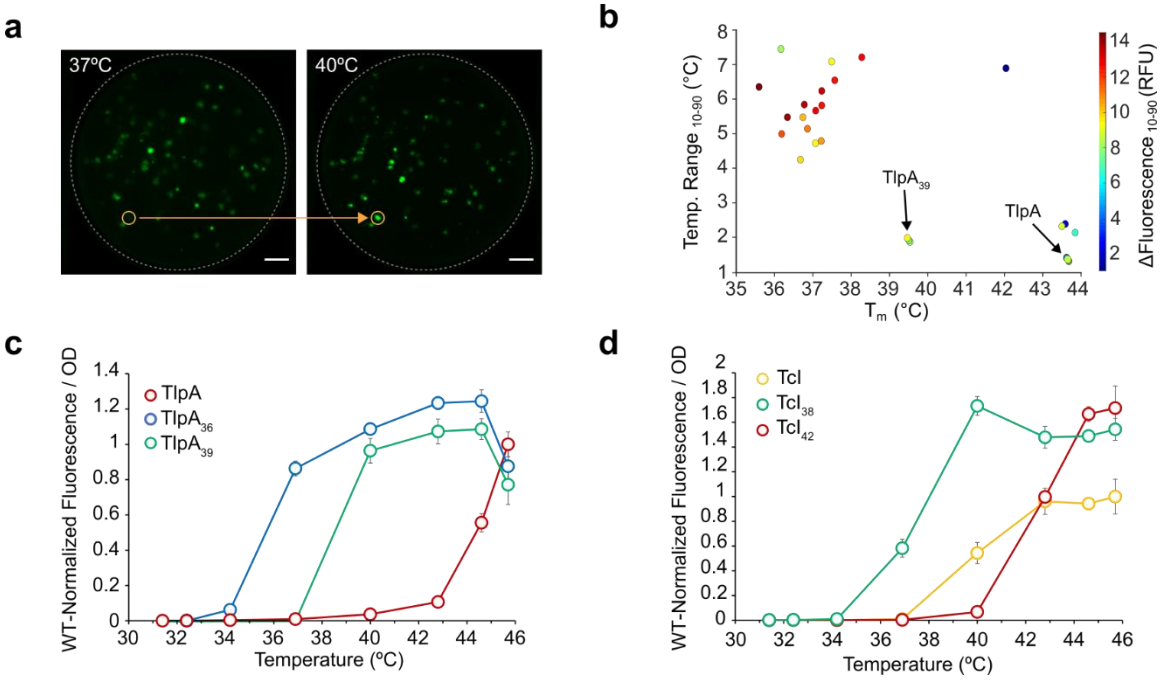

Figure 3-2: Tuning the transition temperature of thermal bioswitches. (**a**) Fluorescence image of replica plates used to screen for TlpA variants turning on between 37 °C and 40 °C. One colony selected for further assay is indicated by the orange circle. Scale bars, 1 cm. (**b**) TlpA variants plotted by their measured midpoint transition temperatures (T50) and 10–90% transition range (T10–90), estimated by linear interpolation. The color of each data point maps to the change in fluorescence over the T10–90 span. (**c**) OD-normalized fluorescence of the novel Tlpa variants normalized to wild type (WT). (**d**) OD-normalized fluorescence of the novel TcI variants normalized to wild type. N = 4 for c and d. RFR, relative fluorescence units. Error bars represent ± s.e.m.

Screening of TlpA mutants at off-on temperatures of 30–37ºC and 37–40ºC produced high-performance bioswitches centered at 36 °C and 39 °C, respectively, which we named $TlpA_{36}$ and $TlpA_{39}$ (**Fig. 3-2c**). For TcI, we selected both downshifted (TcI_{38}, T_m = 38 °C) and upshifted (TcI_{42}, T_m = 42 °C) variants relative to the original protein (**Fig. 3-2d**). Together,

the engineered TlpA and TcI repressor families cover the biomedically relevant range of 32ºC to 46ºC (**Supplementary Fig. 3-S3b**) while demonstrating a dynamic range similar to that of the wild type protein (**Supplementary Table 3-T1**). The amino acid substitutions identified in these bioswitch variants are shown in **Supplementary Figure 3-S4**. The observed decrease in fluorescence at the highest temperatures tested may be due to thermal instability of the cell's transcriptional and translational machinery. Remarkably, a single round of mutagenesis was sufficient in all cases to obtain at least one variant with the desired switching behavior, suggesting that both TlpA and TcI are highly tunable for a broad range of applications.

3.2c: Thermal Logic Circuits Using Orthogonal Bioswitches

To enable microbial therapy applications, it is useful to develop thermal logic circuits capable of controlling multiple functions at different temperatures or confining activity to within a narrow thermal range. This would enable cells to, for example, initiate one therapeutic function upon host colonization and switch to a different function during a host fever response or local activation with focused ultrasound. We hypothesized that since TlpA and TcI act on orthogonal target sequences, we could combine them in circuits designed for multiplexed thermal control or band-pass activation of microbial function. To assess the first possibility (**Fig. 3-3a**), we made a construct encoding a GFP modulated by $TlpA_{36}$ and an RFP regulated by TcI (**Fig. 3-3b**). As predicted, upon exposure to a range of temperatures, the two reporter genes were activated independently at their expected thresholds, with no apparent crosstalk in their induction (**Fig. 3-3c**). Independent thermal control of the co-

expressed circuits is illustrated by spatially patterned bacterial variants incubated at 37ºC and 42ºC (**Fig. 3-3d**). Next, to develop a thermal band-pass filter (**Fig. 3-3e**), we engineered a circuit placing the expression of RFP under the control of the lambda operator, gated by both TcI (turning on above 36ºC) and the temperature-independent wild type cI repressor, which was itself placed under the control of TlpA (activating above 43ºC) as shown in **Figure 3-3f**. The cI open reading frame was preceded by a T7 terminator and a weak ribosome binding site to reduce buildup of this repressor at 40–43 °C due to leakage of the upstream TlpA operon. This resulted in RFP expression confined between 36 and 44ºC, while simultaneously turning on GFP above RFP's turn-off temperature (**Fig. 3-3, g–h**).

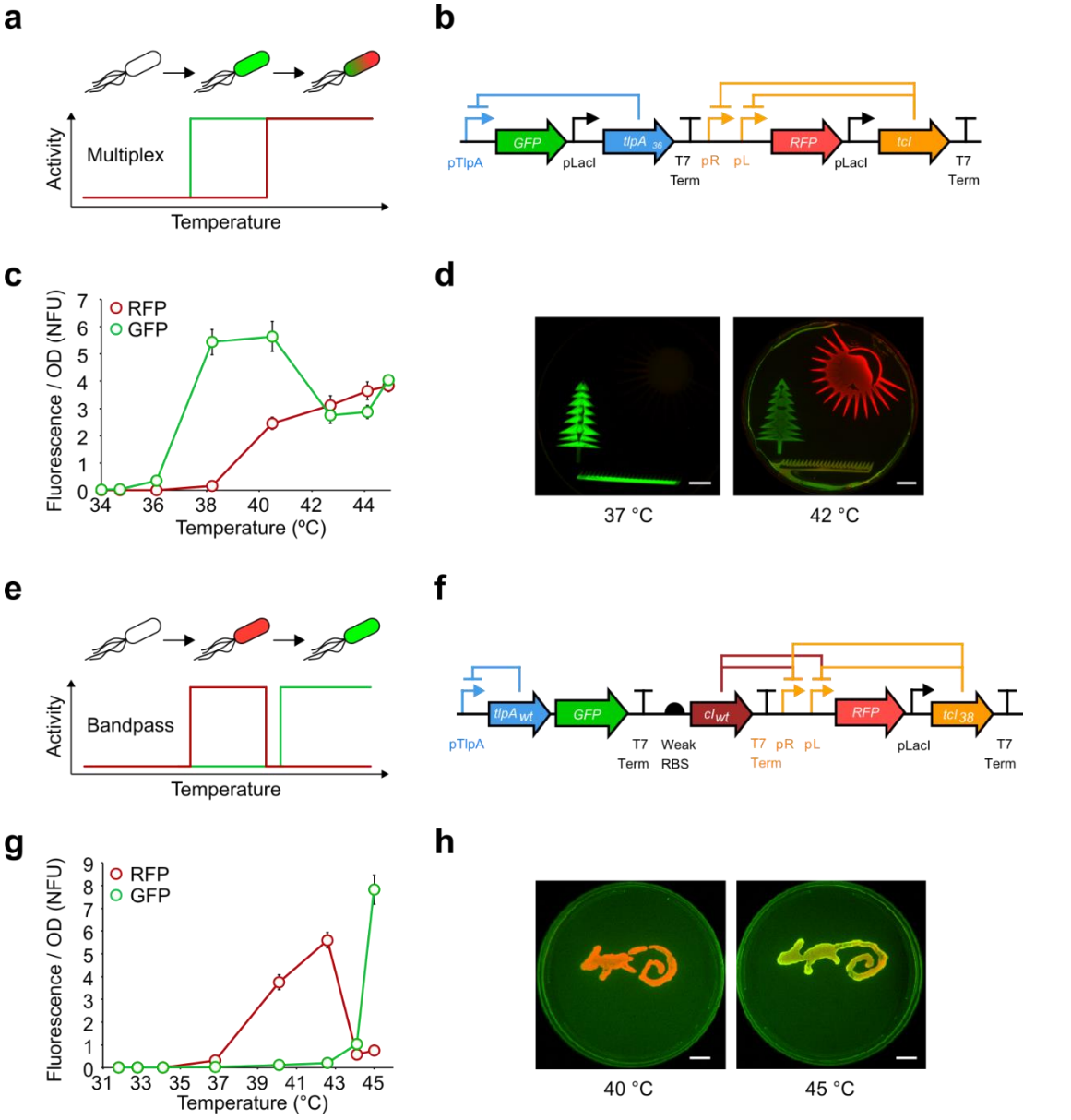

Figure 3-3: Thermal logic circuits. (**a**) Diagram illustrating multiplexed thermal activation. (**b**) Circuit diagram of the pCali2 plasmid, which contains GFP gated by $TlpA_{36}$ and RFP gated by TcI. (**c**) Expression of GFP and RFP from pCali2-containing *E. coli* over the indicated range of temperatures (12-h incubation). (**d**) Plate images of overlaid GFP and RFP fluorescence from the pCali2 plasmid (grass) and plasmids expressing only the green (tree) and red (sun) components. Note that at 42 °C the grass shows both green and red fluorescence. (**e**) Diagram illustrating a thermal bandpass filter. (**f**) Circuit diagram of the pThermeleon plasmid, in which RFP is gated by TcI_{38} and also by the wild-type cI repressor. GFP is gated by $TlpA_{wt}$ on the same plasmid, which also weakly drives the expression of cI_{wt} through a T7 terminator and weak ribosome-binding site. (**g**) Thermal expression profile of RFP and GFP from pThermeleon-containing *E. coli* (12 h incubation). (**h**) Overlaid GFP and RFP fluorescence images of plated bacteria containing pThermeleon cultured at 40 °C and 45 °C. Scale bars, 1 cm. N = 4 for **c** and **g**. Error bars represent ± s.e.m.

3.2d: Spatially Targeted Control Using Focused Ultrasound

After developing TlpA and TcI-based thermal bioswitches, we demonstrated their utility in three prototypical microbial therapy scenarios. First, we tested the ability of thermal bioswitches to mediate spatially-selective control of microbial therapies using focused ultrasound, a modality that is well established in its ability to elevate temperatures in deep tissues with millimeter spatial precision [12] and utilized clinically to treat diseases such as cancer[37] and essential tremor[38]. Focused ultrasound has been used to activate gene expression in mammalian cells[39], but has not, to our knowledge, been employed to control the activity of microbes *in vivo*. Such control could be highly advantageous in applications where the activity of a systemically administered microbial therapy needs to be localized to a specific anatomical site, such as a deep-seated tumor or section of the gastrointestinal tract, which would be difficult to reach with optogenetic triggers. To test this concept, we first activated gene expression using focused ultrasound in tissue-mimicking phantoms under the guidance of magnetic resonance imaging (MRI)[40] (**Fig. 3-4a**). This guidance enabled precise spatial targeting of the ultrasound focus and real-time monitoring and adjustment of local temperature. We first applied this technique to a flat lawn of *E. coli* containing the multiplexed expression circuit shown in **Figure 3-3b**. This specimen was assembled with a tissue-mimicking tofu phantom, and steady-state focal heating over 45 minutes resulted in a radial thermal gradient with an average focal temperature of 42ºC, as observed by real-time MRI thermometry (**Fig. 3-4b**). A corresponding pattern of spatially localized fluorescence is seen in **Figure 3-4c**.

To establish the feasibility of this approach *in vivo*, we injected *E. coli* expressing GFP under the control of $TlpA_{36}$ subcutaneously into both hindlimbs of a nude mouse and applied MRI-guided focused ultrasound to one location (**Fig. 3-4d**) to produce a local steady-state temperature of 41ºC for 45 min to 1 hour. This thermal dose is below the damage thresholds for mammalian tissues such as muscle and brain[41, 42]. *In vivo* fluorescence imaging four hours after ultrasound treatment showed robust expression of GFP specifically at the ultrasound-targeted anatomical site (**Fig. 3-4e**). Two additional animals undergoing the same procedure are shown in **Supplementary Figure 3-S5**. $TlpA_{36}$ was selected as the thermal bioswitch for these experiments because its activation threshold is approximately 4ºC above the typical murine cutaneous temperature[43], a sufficient difference for site-specific ultrasound activation.

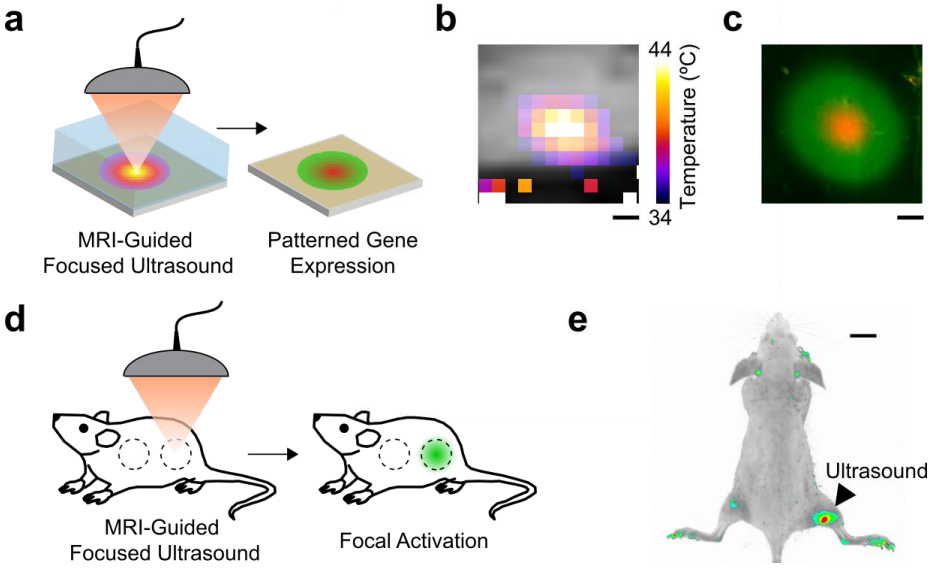

Figure 3-4: Remote control of bacterial agents using focused ultrasound. (**a**) Illustration of the *in vitro* focused ultrasound experiment: focused ultrasound is used to heat a target area of a bacterial culture lawn through a tofu phantom (depicted as translucent) under MRI guidance, followed by fluorescence imaging. (**b**) MRI-based temperature map of the bacterial specimen during steady-state ultrasound application, overlaid on a raw grayscale MRI image of the phantom. (**c**) Fluorescence image of the region targeted by ultrasound, showing activation consistent with a bacterial construct expressing GFP under the control of $TlpA_{36}$ and RFP regulated by TcI. (**d**) Illustration of the *in vivo* experiment, in which focused ultrasound is used to activate subcutaneously injected bacterial agents

at a specific anatomical site. (**e**) Representative thresholded fluorescence map of a mouse injected subcutaneously in both left and right hindlimbs with *E. coli* expressing GFP under the control of $TlpA_{36}$, following ultrasound activation directed at only the right hindlimb. Scale bars, 2 mm (**b**,**c**) and 1 cm (**e**).

3.2e: Programmed Responses to Mammalian Host Temperature

Next, we sought to develop autonomous thermosensitive microbes responsive to endogenous changes in host temperature. First, we investigated whether bacteria can be engineered to sense and respond to a host fever (**Fig. 5a**). We subcutaneously injected one flank of a nude mouse with *E. coli* expressing GFP under the control of $TlpA_{36}$, and the other flank with *E. coli* expressing GFP controlled by wild type TlpA as a high-threshold control for non-specific activation. The mouse was then housed at 41ºC for two hours in an established fever model paradigm[44]. *In vivo* fluorescent imaging four hours after fever induction shows robust expression of GFP in the flank injected with $TlpA_{36}$–regulated bacteria (**Fig. 5b**). No significant activation is seen in the opposite flank or in a mouse housed at room temperature (**Fig. 5c**). Two additional replicates of this experiment are shown in **Supplementary Figure 6**.

Second, we tested whether a thermal bioswitch operating at 37ºC could be used to confine the activity of genetically engineered microbes to the *in vivo* environment of a mammalian host and thereby limit the potential for environmental contamination. Towards this end, we designed a genetic circuit in which $TlpA_{36}$ controls the expression of CcdA, a bacterial antitoxin, while constitutively expressing the toxin CcdB, thereby restricting growth to temperatures above 37ºC (**Fig. 5d**). A degradation tag was fused to CcdA to accelerate cell

death at non-permissive temperatures. Bacteria carrying this plasmid grew normally above this permissive temperature, while bacteria incubated at 25ºC had significantly reduced survival as demonstrated by their CFU counts in **Figure 5e**. We administered these bacteria to mice by oral gavage and collected fecal pellets after five hours to allow transit through the gastrointestinal tract. The pellets were kept for 24 hours at either 25ºC, corresponding to excretion into the ambient environment, or at 37ºC, equivalent to persistent residence in the gut, and subsequently assayed for colony formation. The survival of cells excreted into ambient temperature was reduced by ten thousand fold compared to cells maintained under host conditions (**Fig. 5f**).

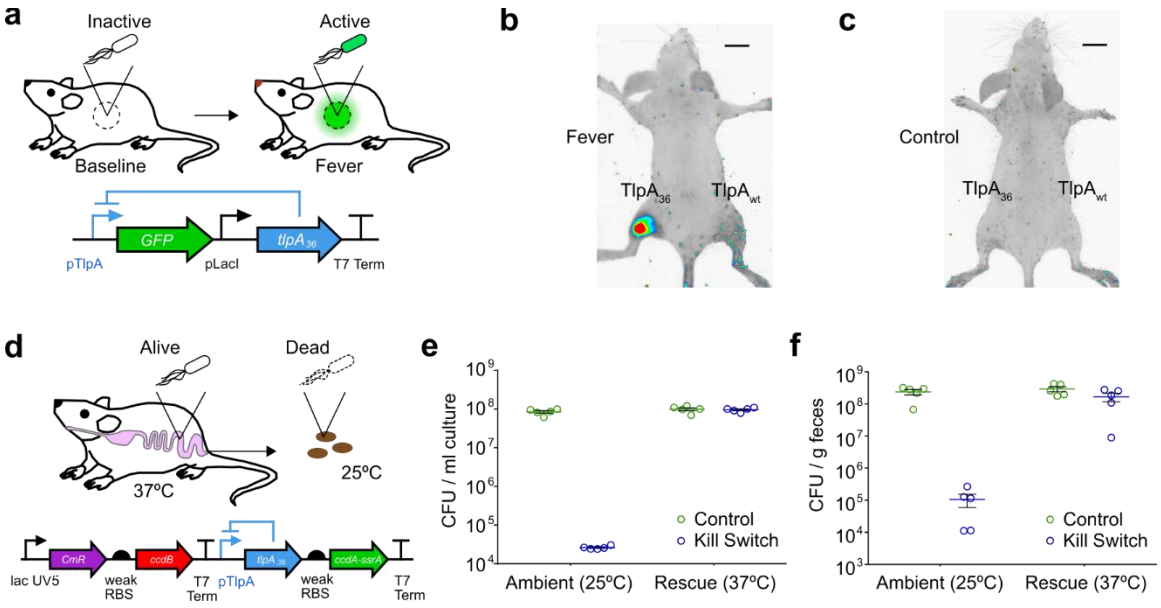

Figure 3-5: Programmed responses to mammalian host temperature. (**a**) Illustration of the fever-induced activation experiment and circuit diagram of the corresponding *E. coli* construct. (**b**) Representative thresholded fluorescence map of a mouse that underwent fever induction after being injected subcutaneously with plasmids expressing TlpaA$_{36}$- and TlpA-regulated GFP into the left and right hindlimbs, respectively. (**c**) Representative thresholded fluorescence map of a mouse that was prepared identically to the animal in **b** but maintained at room temperature. (**d**) Illustration of the temperature- based host confinement strategy, and circuit diagram of the thermal kill switch permitting bacterial survival only at temperatures above 36 °C, at which antitoxin expression is derepressed by TlpA$_{36}$. (**e**) Colony counts from liquid cultures of kill-switch-containing cells and controls (containing no toxin system) after 24 h of incubation at the indicated temperature. P = 0.0002

for kill switch versus control cells at 25 °C and P < 0.0001 for kill switch at 25 °C versus 37 °C. N = 5. (**f**) Colony counts in fecal samples freshly collected from N = 5 mice 5 h after oral gavage of kill-switch-containing *E. coli* or controls. The feces were incubated at a temperature representative of post-defecation conditions (25 °C) or were rescued at 37 °C. P = 0.0067 for kill switch versus control cells at 25 °C and P = 0.0275 for kill switch at 25 °C versus 37 °C. N = 5. Error bars represent ± s.e.m. Scale bars, 1 cm.

3.3: Discussion

Our results establish two new families of high-performance, orthogonal thermal bioswitches with tunable activation thresholds to enable a variety of biotechnology applications. Both TlpA- and TcI-based switches respond to temperature with hundreds-fold changes in gene expression. If needed, this response could be further boosted using well-established strategies such as tandem operators and positive feedback amplification[45, 46]. In addition, the temporal response of thermal bioswitch circuits could be made either more transient, by manipulating the lifetime of the resulting transcripts and proteins, or longer-lasting using genetic toggle switches or recombinase-based architectures[30, 47]. This may enable persistent functions to be controlled with thermal stimuli shorter than those used in this study.

Our strategy for tuning the thermal response of TlpA and TcI is rapid and simple to implement. The fact that we could identify high-performance variants with new transition temperatures by screening several hundred mutants suggests that many different sequences could satisfy a given thermal requirement. Here, we focused on bioswitches operating between 32 and 46ºC, in keeping with potential therapeutic applications and the thermal tolerance of our bacterial chassis. We expect that a similar selection strategy using thermophilic or cryophilic bacteria could be used to tune TlpA and TcI over a yet broader temperature range for industrial applications such as biofuel production. The thermal stability

of the regulated gene product will need to be taken into account in these scenarios. Within the temperature range tested in this study, GFP, RFP and CcdA were functional.

The presented bioswitches have sequences orthogonal to bacterial host machinery and to each other, enabling multiplexed thermal actuation. If desired, additional multiplexing could be accomplished by replacing the DNA-binding domains of TlpA or TcI with those of other dimeric repressors. Additional engineering may be needed to adapt this technology to other host organisms. Certain species of therapeutic microbes, such as *Lactobacillus spp.*, are able to use some promoters transferred directly from *E. coli*[48]. Others may require incorporation of the relevant operator sequences into promoters native to the host[49]. Alternatively, fusions of TlpA and TcI with DNA binding domains from other microbes or eukaryotes could adapt TlpA and TcI for use in these species.

The three *in vivo* scenarios demonstrated in this work will inform the use of thermal bioswitches in future microbial therapy applications. For example, the ability to detect a host's fever provides a potential safety mechanism with which to curtail effector activity in response to runaway inflammation, a major and sometimes lethal side-effect of antitumor cell therapy[50]. In addition, temperature-dependent kill switches can be used to restrict the survival of enterically-administered microbes to host body temperature and thereby mitigate the risk of patients shedding genetically modified, pharmaceutically active organisms into the surrounding environment. Such kill switches can be incorporated into recently developed multilayered and multi-input containment circuits for greater efficiency in preventing mutational escape[51, 52]. Furthermore, the ability to activate microbial function at specific anatomical sites using focused ultrasound opens new therapeutic avenues by potentially

allowing a physician to locally target therapeutic effects that would be intolerable via systemic administration. Additionally, the ability to trigger gene expression *in vivo* can be combined with genetically encoded genomic or proteomic tools[53-55] to enable the study of cellular signaling within the context of mammalian hosts.

3.4: Methods

Plasmid Construction and Molecular Biology

All constructs were made via restriction cloning, KLD mutagenesis, or Gibson Assembly using enzymes from New England Biolabs. All plasmids and their sources of genetic material are described in **Supplementary Table 3-T2**. All constructs were cloned in Mach1 *E. coli* (Thermo Fisher) and the sequence-validated plasmids were assayed in NEB10β *E. coli* (NEB). Fluorescent reporters referred to in the text as GFP and RFP are mWasabi and mCherry, respectively[56, 57].

Thermal Regulation Assay

2 mL cultures of 2xYT media with 100 µg/mL ampicillin were inoculated with a single colony per culture and grown at 30 °C, 250 rpm for 20 hours. After dilution to OD_{600} = 0.1 in LB (Sigma) with 100 µg/mL ampicillin, the cells were propagated at 30 °C, 250 rpm for 1.5 hours, after which OD_{600} was measured using a Nanodrop 2000c (Thermo Scientific) in cuvette mode every 10 minutes. At OD_{600} = 0.25, the cultures were dispensed in 25 µL aliquots into 8 well PCR strips with optically transparent caps (Bio-Rad) using a multichannel pipette and placed into a spatial temperature gradient formed by a Bio-Rad C1000 Touch thermocycler with the lid set to 50 °C. The temperature in each thermocycler

well was verified using a TEF-30-T thermocouple (J-KEM Scientific) immersed in 25 µL of pure water within a PCR tube. After the prescribed thermal stimulus, PCR strips were removed, vortexed, spun down on a tabletop centrifuge and the fluorescence was measured using a Stratagene MX3005p qPCR (Agilent). Immediately after measurement, the cultures were diluted with 75 µL LB/Amp and mixed, after which 90 µL of culture was transferred into 96 well plates (Costar black / clear bottom) for measurement of OD_{600} using a SpectraMax M5 plate reader (Molecular Devices). For studies of gene expression as a function of thermal induction time (Fig. 1, d–f), samples were returned to incubation at 30 °C after their indicated thermal induction periods such that the total experimental duration was 24 hours. Fluorescence measurements were made at the end of this period. Gene expression (*E*) was determined according to Equation 1:

$$E = \frac{F_{sample} - F_{blank}}{OD_{sample} - OD_{blank}} - \frac{F_{background} - F_{blank}}{OD_{background} - OD_{blank}} \qquad (1)$$

Here, *F* is the raw fluorescence of the given sample and *OD* is the OD of the given sample at 600 nm. Raw OD measurements for all experiments are provided in **Supplementary Figure 3-S7**. As expected, bacterial growth is highest in the physiological range of 35 ºC to 39 ºC. The value of blank fluorescence was determined as the average of all 96 wells in a qPCR plate filled with 25 µL LB. Blank OD was taken as the y-intercept of a standard curve of 90 µL non-fluorescent E. coli cultures whose OD_{600} values were determined by cuvette measurements in a Nanodrop 2000c spectrophotometer (96 samples total). Background fluorescence was measured from a non-fluorescent construct derived by mutating the chromophore of mWasabi [58] in the pTlpA-Wasabi plasmid (pTlpA-Wasabi-NF). Fluorescence measurements for the thermal expression landscapes of TlpA and TcI were performed using the plate reader due to signal saturation of the qPCR at the 24 hour time

point (Sample N = 3; Background N = 2 for each time point and temperature). Errors from background measurements were propagated by addition in quadrature. Errors from blank measurements were negligible relative to sample-to-sample variation (relative standard deviation < 2%) and were omitted from the calculation.

Colony Screening for TlpA Tuning

Error-prone PCR was performed on pTlpA-Wasabi (Stratagene GeneMorph II kit) and on pTcI-Wasabi (NEB Taq Polymerase/0.2 mM $MnCl_2$) and the PCR products were inserted into the parent constructs using Gibson Assembly. The resulting libraries were transformed into NEB10β *E. coli* and plated on LB Agar. Following overnight incubation at 30 °C and the appearance of colonies, a Replica-Plating Tool (VWR 25395-380) was used to replicate each seed plate into two receiver plates. One receiver plate was grown overnight at the desired repressed temperature, and the other at the intended activation temperature. Upon the appearance of visible colonies, plates were imaged in a Bio-Rad ChemiDoc MP imager using blue epifluorescent illumination and the 530/28 nm emission filter. Images were examined manually for colonies that appeared dark or invisible on the "off plate" but showed bright fluorescence on the "on plate". Approximately 10^3 colonies were screened per library. These colonies were picked and subjected to the liquid culture thermal activation assay described above, whereupon their thermal induction profile was compared to that of their parent plasmid. Variants that demonstrated sharp switching and large dynamic range between the desired new transition temperatures were sequenced, re-transformed, and assayed using a higher number of replicates.

In Vitro *Toxin-Antitoxin Assays*

NEB10β cells were transformed with the thermally regulated toxin-antitoxin plasmid and allowed to grow at 37 °C overnight. Because reversion of plasmids carrying toxic genes such as CcdB is known to be a common phenomenon, we used a replica plate screen to isolate colonies that maintained a functional thermal kill switch after transformation. To this end, we replica plated the original transformation into two new plates, one incubated at 25°C and the other maintained at 37 °C. Colonies that grew at the permissive temperature of 37 °C and not at 25°C were used in downstream *in vitro* or *in vivo* experiments. For *in vitro* experiments, the selected colonies were grown in 2xYT media with 100 µg/mL ampicillin at 37°C with shaking until OD_{600} of 0.6 whereupon they were diluted and plated onto LB agar plates. The plates were incubated overnight at either 25°C or 37°C, after which colony forming units (CFU) were counted.

Focused Ultrasound

MRI-guided focused ultrasound treatment was performed using a 16-channel ultrasound generator, motorized MRI-compatible transducer positioning system and an annular array transducer operating at 1.5 MHz (Image Guided Therapy, Pessac, France). Targeting and real-time imaging was performed using a Bruker Biospec/Avance 7T MRI system with RF excitation delivered by a 7.2 cm diameter volume coil and detection via a 3 cm diameter surface coil. Temperature monitoring was performed using a continuously applied Fast Low Angle Shot sequence with a T_R of 75 ms and T_E of 2.5 ms, matrix size of 32 x 32, and varying FOVs as listed below. Phase images were processed in real time using ThermoGuide software (Image Guided Therapy) and temperature was calculated from the per-pixel phase accumulation due to a decrease in proton precession frequency of 0.01 ppm/°C.

For *in vitro* heating, 100 μL of a saturated NEB10β culture expressing the temperature-inducible reporter circuit was plated overnight at 30 °C and incubated for approximately 12 hours to form a lawn on a plate containing 0.24 %w/v LB (Sigma) and 0.32 %w/v Bacto Agar (BD). An approximately 3 cm x 3 cm square of agar was excised from the plate and placed, with the bacterial side facing up, onto a comparably sized pad of 1 cm thick extra firm tofu (O Organics) coated with SCAN ultrasound gel (Parker Laboratories) to exclude air at the interface. A 1 cm high plastic washer made by drilling through the lid of a VWR 35 mm plastic tissue culture dish was placed onto the bacteria and the assembly was inverted and placed onto the surface coil such that the bacterial lawn, facing down, was supported by the washer. The ultrasound transducer was positioned above the assembly, in contact with the tofu through another thin layer of ultrasound gel. To provide a reference to compensate for global phase drift during the experiment, a second piece of tofu was placed within the field of view but spatially separated by a 1 cm air gap from the object under insonation. A fiber optic thermometer (Neoptix T1) was inserted into the reference tofu, and the difference between the MRI-derived reference temperature and thermometer-reported temperature was accounted for at the site of insonation when calculating the true focal heating.

Ultrasound was applied with the focus aimed at the tofu immediately adjacent to the agar layer with manual control of power level and duty cycle so as to maintain a temperature of 41.5–43 °C for 45 minutes. Imaging was performed as described above with a matrix size of 5.39 x 5.05 cm and a slice thickness of 2 mm. The plate was subsequently returned to 30 °C for 5 hours and imaged using a Bio-Rad ChemiDoc MP imager with blue epi illumination and a 530/28 nm emission filter (mWasabi) and also green epi illumination and a 605/50 nm filter (mCherry).

Animal Procedures

All animal procedures were performed under a protocol approved by the California Institute of Technology Institutional Animal Care and Use Committee (IACUC). 9-week old BALB/c female mice and 4-week old NU/J 2019 female mice were purchased from Jackson Laboratory (JAX); 4-week old SCID/SHC female mice were purchased from Charles River. For *in vivo* ultrasound actuation, *E. coli* expressing the pTlpA36-Wasabi plasmid were grown to OD 0.6, pelleted, and resuspended to OD 24. A 100 μL bolus was injected subcutaneously into both hindlimbs of a nude mouse (SCID or NU/J2019). Mice were anaesthetized using a 2% isoflurane-air mixture and placed on a dedicated animal bed with the surface coil positioned below the target limb of the mouse. Anesthesia was maintained over the course of the ultrasound procedure using 1–1.5% isoflurane. Respiration rate was maintained at 20–30 breaths per minute and temperature and respiration rate were continuously monitored using a pressure pad (Biopac Systems) and a fiber optic rectal thermometer (Neoptix). The target limb was thermally activated by elevating the temperature to 41°C and maintaining the elevated temperature for 45 min to 1 hour. Temperature monitoring and adjustment was performed as described above for *in vitro* experiments. Following ultrasound treatment, the mouse was returned to its cage for four hours, anaesthetized, and imaged using a Bio-Rad ChemiDoc MP imager with blue epi illumination and the 530/28 nm emission filter (mWasabi).

For host fever sensing experiments, SCID mice injected with bacteria as described above were housed in an incubator preset to 41°C for two hours and control mice were housed at room temperature. Following treatment, all mice were housed at room temperature for four

hours, anaesthetized, and imaged using a Bio-Rad ChemiDoc MP imager with blue epi illumination and the 530/28 nm emission filter (mWasabi).

Mouse images are representative of three independent *in vivo* experiments. Fever-induced and control mice were littermates randomly selected for each experimental condition. Investigators were not blinded to group allocation because no subjective evaluations were performed.

For host confinement experiments, BALB/c mice were given drinking water containing 0.5 mg/mL of ampicillin for 24h, and then starved for food overnight. *E.coli* were grown in 2xYT media containing ampicillin at 37°C with shaking until OD_{600} of 0.6. Cultures were pelleted and resuspended at 10^8 cells/mL in PBS containing 1.5% $NaHCO_3$. 200 µL of the suspension was administered orally using a gavage needle. Food was returned to the mice and the drinking water contained ampicillin throughout the entire experiment. Fresh fecal samples were collected from each mouse 5 hrs after gavage and incubated at 37°C or 25°C for 24h, then weighed, homogenized in PBS at 0.1 g/mL, diluted and plated onto LB agar plates containing ampicillin. Plates were then incubated overnight at 25°C and 37°C. Bacterial colonies were counted as described above for *in vitro* toxin-antitoxin experiments. The sample size was N = 5 mice, which was chosen based on preliminary experiments indicating that it would be sufficient to detect significant differences in mean values.

Electrophoretic Mobility Shift Assay

Interaction between TlpA, σ^{70}-RNAp holoenzyme and DNA was demonstrated using a gel shift assay. For this, 50 pmoles of fluorescein-labeled double stranded DNA representing the TlpA operator with flanking padding sequences (70 base pairs in total) was incubated with either 50 pmoles of TlpA protein or 5 Units (8.5 pmoles) σ^{70}-RNAp holoenzyme (NEB

M0551S) individually in 50 uL reaction buffer comprising 40 mM Tris-HCl, 150 mM KCl, 10mM MgCl2, .01% Triton-X-100 and 1 mM DTT at a pH of 7.5. As a negative control, the wildtype TlpA operator was replaced with a scrambled version. Following incubation at 37ºC for 30 minutes, 10 uL of the reaction mixture was supplemented with glycerol to a final concentration of 5 % and loaded in a nondenaturing 4 % polyacrylamide resolving gel. The gel was run at 65 V for 90 minutes in buffer comprising 45 mM Tris-borate and 1 mM EDTA at a pH of 8.3. DNA was visualized using Bio-Rad ChemiDoc MP imager using blue epifluorescent illumination and the 530/28 nm emission filter.

Statistics and Replicates

Data is plotted and reported in the text as the mean ± SEM. Sample size is N = 4 biological replicates in all *in vitro* experiments unless otherwise stated. This sample size was chosen based on preliminary experiments indicating that it would be sufficient to detect significant differences in mean values. P-values were calculated using a two-tailed unpaired heteroscedastic t-test.

3.5: References

1. Ford, T.J. & Silver, P.A. Synthetic biology expands chemical control of microorganisms. *Current opinion in chemical biology* **28**, 20-28 (2015).
2. Fischbach, M.A., Bluestone, J.A. & Lim, W.A. Cell-based therapeutics: the next pillar of medicine. *Science translational medicine* **5**, 179ps177-179ps177 (2013).
3. Steidler, L. et al. Treatment of murine colitis by Lactococcus lactis secreting interleukin-10. *Science* **289**, 1352-1355 (2000).
4. Daniel, C., Roussel, Y., Kleerebezem, M. & Pot, B. Recombinant lactic acid bacteria as mucosal biotherapeutic agents. *Trends in biotechnology* **29**, 499-508 (2011).
5. Claesen, J. & Fischbach, M.A. Synthetic microbes as drug delivery systems. *ACS synthetic biology* **4**, 358-364 (2014).
6. Wells, J.M. & Mercenier, A. Mucosal delivery of therapeutic and prophylactic molecules using lactic acid bacteria. *Nature Reviews Microbiology* **6**, 349-362 (2008).
7. Courbet, A., Endy, D., Renard, E., Molina, F. & Bonnet, J. Detection of pathological biomarkers in human clinical samples via amplifying genetic switches and logic gates. *Science translational medicine* **7**, 289ra283-289ra283 (2015).
8. Danino, T. et al. Programmable probiotics for detection of cancer in urine. *Science translational medicine* **7**, 289ra284-289ra284 (2015).
9. Kotula, J.W. et al. Programmable bacteria detect and record an environmental signal in the mammalian gut. *Proceedings of the National Academy of Sciences* **111**, 4838-4843 (2014).
10. Archer, E.J., Robinson, A.B. & Süel, G.r.M. Engineered E. coli that detect and respond to gut inflammation through nitric oxide sensing. *ACS synthetic biology* **1**, 451-457 (2012).
11. Ntziachristos, V. Going deeper than microscopy: the optical imaging frontier in biology. *Nature methods* **7**, 603-614 (2010).
12. Haar, G.T. & Coussios, C. High intensity focused ultrasound: physical principles and devices. *International journal of hyperthermia : the official journal of European Society for Hyperthermic Oncology, North American Hyperthermia Group* **23**, 89-104 (2007).
13. Huang, X., El-Sayed, I.H., Qian, W. & El-Sayed, M.A. Cancer cell imaging and photothermal therapy in the near-infrared region by using gold nanorods. *Journal of the American Chemical Society* **128**, 2115-2120 (2006).
14. Thiesen, B. & Jordan, A. Clinical applications of magnetic nanoparticles for hyperthermia. *International journal of hyperthermia* **24**, 467-474 (2008).
15. Zhao, K., Liu, M. & Burgess, R.R. The global transcriptional response of Escherichia coli to induced sigma 32 protein involves sigma 32 regulon activation followed by inactivation and degradation of sigma 32 in vivo. *The Journal of biological chemistry* **280**, 17758-17768 (2005).
16. de Marco, A., Vigh, L., Diamant, S. & Goloubinoff, P. Native folding of aggregation-prone recombinant proteins in Escherichia coli by osmolytes, plasmid- or benzyl alcohol-overexpressed molecular chaperones. *Cell stress & chaperones* **10**, 329-339 (2005).
17. Inda, M.E. et al. A lipid-mediated conformational switch modulates the thermosensing activity of DesK. *Proceedings of the National Academy of Sciences* **111**, 3579-3584 (2014).
18. Kortmann, J., Sczodrok, S., Rinnenthal, J., Schwalbe, H. & Narberhaus, F. Translation on demand by a simple RNA-based thermosensor. *Nucleic Acids Res* **39**, 2855-2868 (2011).
19. Neupert, J., Karcher, D. & Bock, R. Design of simple synthetic RNA thermometers for temperature-controlled gene expression in Escherichia coli. *Nucleic Acids Res* **36**, e124 (2008).
20. Waldminghaus, T., Kortmann, J., Gesing, S. & Narberhaus, F. Generation of synthetic RNA-based thermosensors. *Biological chemistry* **389**, 1319-1326 (2008).

21. Hoynes-O'Connor, A., Hinman, K., Kirchner, L. & Moon, T.S. De novo design of heat-repressible RNA thermosensors in E. coli. *Nucleic acids research* **43**, 6166-6179 (2015).
22. Satija, R., Sen, S., Siegal-Gaskins, D. & Murray, R.M. Design of a Toolbox of RNA Thermometers. *bioRxiv*, 017269 (2015).
23. Waldminghaus, T., Kortmann, J., Gesing, S. & Narberhaus, F. Generation of synthetic RNA-based thermosensors. *Biological chemistry* **389**, 1319-1326 (2008).
24. Neupert, J., Karcher, D. & Bock, R. Design of simple synthetic RNA thermometers for temperature-controlled gene expression in Escherichia coli. *Nucleic acids research* **36**, e124-e124 (2008).
25. Wieland, M. & Hartig, J.S. RNA quadruplex-based modulation of gene expression. *Chemistry & biology* **14**, 757-763 (2007).
26. Hurme, R., Berndt, K.D., Namork, E. & Rhen, M. DNA binding exerted by a bacterial gene regulator with an extensive coiled-coil domain. *The Journal of biological chemistry* **271**, 12626-12631 (1996).
27. Valdez-Cruz, N.A., Caspeta, L., Perez, N.O., Ramirez, O.T. & Trujillo-Roldan, M.A. Production of recombinant proteins in E. coli by the heat inducible expression system based on the phage lambda pL and/or pR promoters. *Microbial cell factories* **9**, 18 (2010).
28. Sussman, R. & Jacob, F. Sur un systeme de repression thermosensible chez le bacteriophage lambda d'Escherichia coli. *Comptes rendus hebdomadaires des séances de l'Académie des sciences*, 1517-1519 (1962).
29. Wissmann, A. et al. Selection for Tn10 tet repressor binding to tet operator in Escherichia coli: isolation of temperature-sensitive mutants and combinatorial mutagenesis in the DNA binding motif. *Genetics* **128**, 225-232 (1991).
30. Chao, Y.P., Chern, J.T., Wen, C.S. & Fu, H. Construction and characterization of thermo-inducible vectors derived from heat-sensitive lacI genes in combination with the T7 A1 promoter. *Biotechnology and bioengineering* **79**, 1-8 (2002).
31. McCabe, K.M., Lacherndo, E.J., Albino-Flores, I., Sheehan, E. & Hernandez, M. LacI(Ts)-regulated expression as an in situ intracellular biomolecular thermometer. *Applied and environmental microbiology* **77**, 2863-2868 (2011).
32. Hurme, R., Berndt, K.D., Normark, S.J. & Rhen, M. A proteinaceous gene regulatory thermometer in Salmonella. *Cell* **90**, 55-64 (1997).
33. Wilson, C.J., Zhan, H., Swint-Kruse, L. & Matthews, K.S. The lactose repressor system: paradigms for regulation, allosteric behavior and protein folding. *Cellular and molecular life sciences : CMLS* **64**, 3-16 (2007).
34. Bertram, R. & Hillen, W. The application of Tet repressor in prokaryotic gene regulation and expression. *Microbial biotechnology* **1**, 2-16 (2008).
35. Jensen, P.R., Westerhoff, H.V. & Michelsen, O. The use of lac-type promoters in control analysis. *European journal of biochemistry / FEBS* **211**, 181-191 (1993).
36. Altschul, S.F. et al. Gapped BLAST and PSI-BLAST: a new generation of protein database search programs. *Nucleic acids research* **25**, 3389-3402 (1997).
37. Al-Bataineh, O., Jenne, J. & Huber, P. Clinical and future applications of high intensity focused ultrasound in cancer. *Cancer treatment reviews* **38**, 346-353 (2012).
38. Elias, W.J. et al. A pilot study of focused ultrasound thalamotomy for essential tremor. *New England Journal of Medicine* **369**, 640-648 (2013).
39. Deckers, R. et al. Image-guided, noninvasive, spatiotemporal control of gene expression. *Proceedings of the National Academy of Sciences* **106**, 1175-1180 (2009).
40. Fite, B.Z. et al. Magnetic resonance thermometry at 7T for real-time monitoring and correction of ultrasound induced mild hyperthermia. *PloS one* **7**, e35509 (2012).

41. McDannold, N.J., King, R.L., Jolesz, F.A. & Hynynen, K.H. Usefulness of MR Imaging-Derived Thermometry and Dosimetry in Determining the Threshold for Tissue Damage Induced by Thermal Surgery in Rabbits 1. *Radiology* **216**, 517-523 (2000).
42. McDannold, N., Vykhodtseva, N., Jolesz, F.A. & Hynynen, K. MRI investigation of the threshold for thermally induced blood–brain barrier disruption and brain tissue damage in the rabbit brain. *Magnetic resonance in medicine* **51**, 913-923 (2004).
43. Rudaya, A.Y., Steiner, A.A., Robbins, J.R., Dragic, A.S. & Romanovsky, A.A. Thermoregulatory responses to lipopolysaccharide in the mouse: dependence on the dose and ambient temperature. *American journal of physiology. Regulatory, integrative and comparative physiology* **289**, R1244-1252 (2005).
44. Pritchard, M.T. et al. Protocols for simulating the thermal component of fever: preclinical and clinical experience. *Methods (San Diego, Calif.)* **32**, 54-62 (2004).
45. Illing, A.C., Shawki, A., Cunningham, C.L. & Mackenzie, B. Substrate profile and metal-ion selectivity of human divalent metal-ion transporter-1. *Journal of Biological Chemistry* **287**, 30485-30496 (2012).
46. Nistala, G.J., Wu, K., Rao, C.V. & Bhalerao, K.D. A modular positive feedback-based gene amplifier. *Journal of biological engineering* **4**, 4 (2010).
47. Andersen, J.B. et al. New unstable variants of green fluorescent protein for studies of transient gene expression in bacteria. *Applied and environmental microbiology* **64**, 2240-2246 (1998).
48. Natori, Y., Kano, Y. & Imamoto, F. Characterization and promoter selectivity of Lactobacillus acidophilus RNA polymerase. *Biochimie* **70**, 1765-1774 (1988).
49. Mimee, M., Tucker, A.C., Voigt, C.A. & Lu, T.K. Programming a human commensal bacterium, Bacteroides thetaiotaomicron, to sense and respond to stimuli in the murine gut microbiota. *Cell systems* **1**, 62-71 (2015).
50. Tey, S.-K. Adoptive T-cell therapy: adverse events and safety switches. *Clinical & translational immunology* **3**, e17 (2014).
51. Chan, C.T., Lee, J.W., Cameron, D.E., Bashor, C.J. & Collins, J.J. 'Deadman' and 'Passcode' microbial kill switches for bacterial containment. *Nat Chem Biol* **12**, 82-86 (2016).
52. Gallagher, R.R., Patel, J.R., Interiano, A.L., Rovner, A.J. & Isaacs, F.J. Multilayered genetic safeguards limit growth of microorganisms to defined environments. *Nucleic Acids Res* **43**, 1945-1954 (2015).
53. Lang, K. & Chin, J.W. Cellular incorporation of unnatural amino acids and bioorthogonal labeling of proteins. *Chemical reviews* **114**, 4764-4806 (2014).
54. Handley, A., Schauer, T., Ladurner, A.G. & Margulies, C.E. Designing cell-type-specific genome-wide experiments. *Molecular cell* **58**, 621-631 (2015).
55. Grammel, M. & Hang, H.C. Chemical reporters for biological discovery. *Nature chemical biology* **9**, 475-484 (2013).
56. Ai, H.W., Olenych, S.G., Wong, P., Davidson, M.W. & Campbell, R.E. Hue-shifted monomeric variants of Clavularia cyan fluorescent protein: identification of the molecular determinants of color and applications in fluorescence imaging. *BMC biology* **6**, 13 (2008).
57. Shaner, N.C. et al. Improved monomeric red, orange and yellow fluorescent proteins derived from Discosoma sp. red fluorescent protein. *Nature biotechnology* **22**, 1567-1572 (2004).
58. Wielgus-Kutrowska, B., Narczyk, M., Buszko, A., Bzowska, A. & Clark, P.L. Folding and unfolding of a non-fluorescent mutant of green fluorescent protein. *Journal of Physics: Condensed Matter* **19**, 285223 (2007).

3.6: Supplementary Results

Supplementary Table 3-T1 – Mutant and wild type bioswitch performance

Variant	Fold Change	SEM (±)	T_{off}	T_{max}
TlpA	355	45	31.4	44.6
$TlpA_{36}$	370	63	31.4	44.6
$TlpA_{39}$	1523	434	31.4	44.6
TcI	1432	404	34.2	40
TcI_{38}	1032	160	32.4	40
TcI_{42}	1692	444	32.4	45.7

***** The reported T_{off} for each variant is the lowest temperature at which fluorescence could be detected above noise. T_{max} is the temperature at which fluorescence was maximal.

Supplementary Table 3-T2 – Genetic constructs used in the study

All plasmids were constructed using the pETDuet-1 backbone (EMD Biosciences) with the relevant thermal biosensor elements replacing multiple cloning sites 1 and 2.

Plasmid	Transcriptional Regulator(s)	Output Gene Product(s)
pTlpA-Wasabi	TlpA	mWasabi
pTlpA-Wasabi-NF	TlpA	Nonfluorescent mWasabi (S71T, G73A)
pTcI-Wasabi	TcI (cI852 Repressor, cI A67T)	mWasabi
pLacI241-Wasabi	LacI A241T (mutation made in pETDuet-1 LacI)	mWasabi
pLacI265-Wasabi	LacI G265D (mutation made in pETDuet-1 LacI)	mWasabi
pTetR89-Wasabi	TetR A89D	mWasabi
pTetR193-Wasabi	TetR I193N	mWasabi
pLon-Wasasbi	Lon Promoter (GenBank CP009072)	mWasabi
pRpoH-Wasabi	RpoH Promoter (GenBank CP009072)	mWasabi
pClp-Wasabi	ClpP-ClpX Promoter (Genbank CP009072)	mWasabi
pHtpG-Wasabi	HtpG Promoter (Genbank CP009072)	mWasabi
pDnaK-Wasabi	DnaK Promoter (Genbank CP009072)	mWasabi
pGrpE-Wasabi	GrpE Promoter (Genbank CP009072)	mWasabi
pLacIq-Wasabi	LacIq Promoter	mWasabi
$pTlpA_{SP}$-Wasabi	TlpA Promoter with putative Pribnow box scrambled	mWasabi
$pTlpA_{Reverse}$-Wasabi	TlpA Promoter as reverse complement	mWasabi
$pTlpA_{36}$-Wasabi	$TlpA_{36}$	mWasabi
$pTlpA_{39}$-Wasabi	$TlpA_{39}$	mWasabi
$pTcI_{38}$-Wasabi	TcI_{38}	mWasabi
$pTcI_{42}$-Wasabi	TcI_{42}	mWasabi
pCali2	$TlpA_{36}$, TcI	mWasabi, mCherry
pThermeleon	TcI, TlpA, cI_{wt} (under control of TlpA)	mWasabi, mCherry
pKillswitch	$TlpA_{36}$	CcdA with SsrA degradation tag

Sources of genetic elements: TlpA: B. Finlay, Univ. British Columbia; mWasabi: F. Arnold, Caltech; mCherry: S. Qi, Stanford; CcdB: pLenti X1 Zeo DEST plasmid (Addgene #17299); TetR: pENTR1A plasmid (Addgene #22265); all other elements: Gblock synthesis (IDT).

Supplementary Table 3-T3 – List of mutations in selected variants of TlpA and TcI

Construct	Nonsynonymous Mutations	Synonymous Mutations
$TlpA_{36}$	P60L, D135V, K187R, K202I, L208Q	
$TlpA_{39}$	D135V, A217V, L236F	
TcI_{38}	M1V, L65S, K68R, F115L, D126G, D188G	A50 (GCT -> GCC), E128 (GAG -> GAA), R129 (AGA -> AGG), T152 (ACA -> ACC), L185 (CTT -> CTC)
TcI_{42}	K6N, S33T, Y61H, L119P, F122C	L51 (TTA -> CTA)

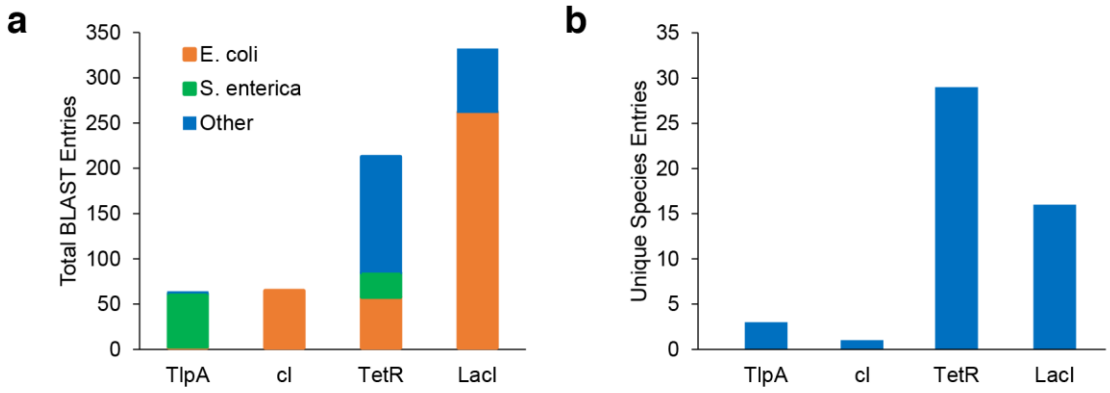

Supplementary Figure 3-S1 – Prevalence of repressor sequences in bacteria. (**a**) National Center for Biotechnology Information (NCBI) Basic Local Alignment Search Tool (BLAST) search results for the wild type tlpA, cI, tetR, and lacI genes showing the cumulative number of hits obtained. The NCBI nucleotide collection was searched with the source organism restricted to bacteria. Cloning vectors, synthetic constructs, and individual gene sequences were omitted; genomic and naturally occurring plasmid sequences were retained. Sequences with alignment lengths of less than 90% of the wild type protein sequence were not included. The lacI gene is distributed throughout many commonly utilized *E. coli* strains such as Nissle 1917 and BL21, whereas the cI gene is found in less widely used *E. coli* strains. (**b**) The number of bacterial species in which the selected repressors are found. Data were obtained as in (**a**) and substrains were binned together. TlpA is largely restricted to *S. enterica* and cI to *E. coli*; tetR and lacI can be found in a larger number of bacterial species.

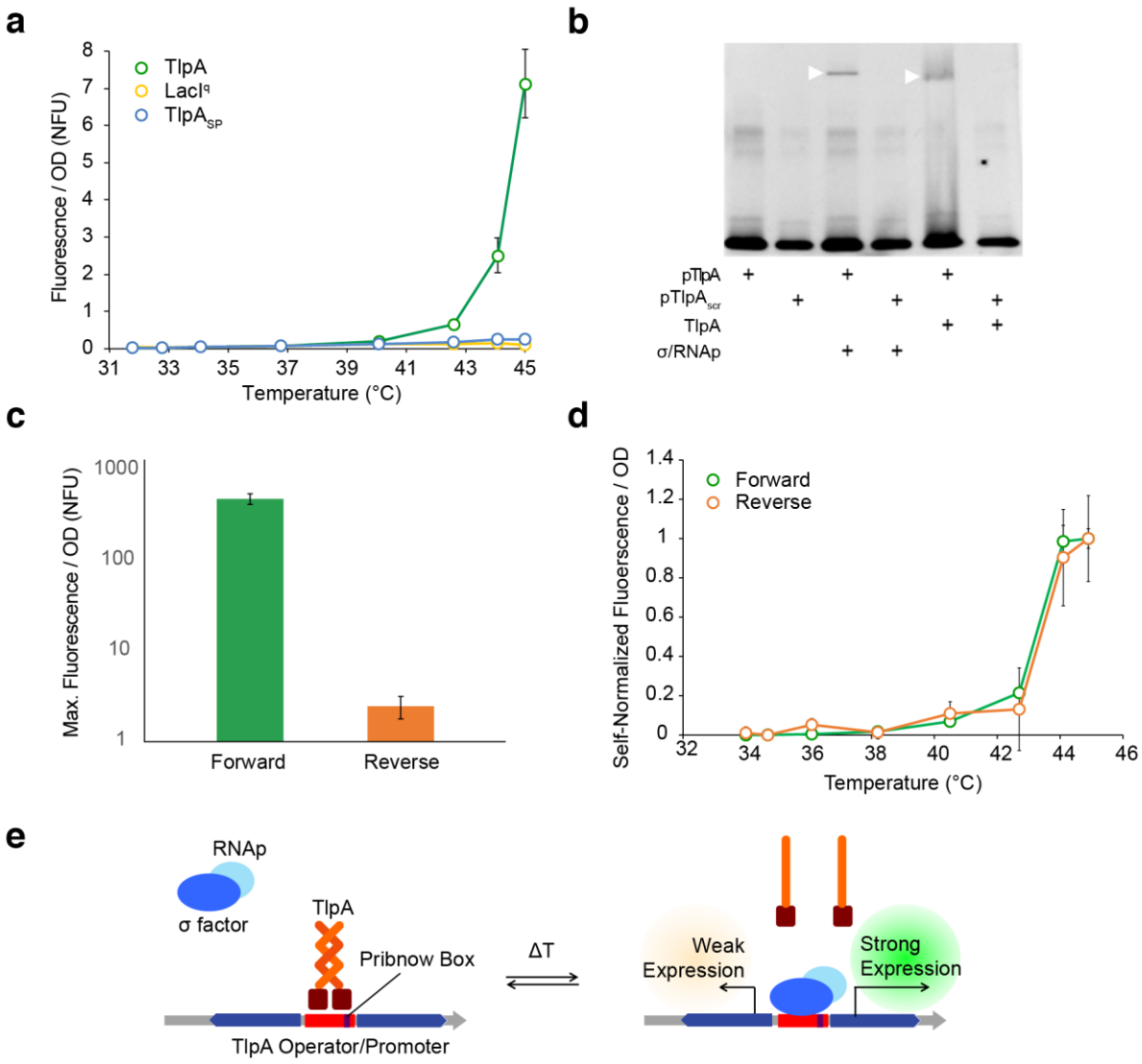

Supplementary Figure 3-S2 – Mechanisms and bidirectional activity of the TlpA operator. (**a**) OD-normalized expression of the GFP reporter gene under the control of TlpA, $LacI^q$, and $TlpA_{SP}$ (in which nucleotides within the Pribnow box of the operator are shuffled). (**b**) Electromobility shift assay using a FAM-labeled TlpA operator oligonucleotide, demonstrating association of the operator with both TlpA and the *E. coli* σ^{70}-RNAp holoenzyme. In contrast, scrambled TlpA operator fails to associate with these proteins. The TlpA and σ^{70}-RNAp concentrations used in this experiment (1 µM and 0.18 µM, respectively) were similar to previous literature.[7,8] (**c**) GFP expression driven by the TlpA operator in the canonical and flipped orientations at 44.1ºC. (**d**) Thermal induction profiles for GFP expression under the control of forward and reverse-oriented TlpA operator. Each curve is self-normalized to its maximal fluorescence intensity. (**e**) Proposed mechanism of TlpA-based thermal transcriptional regulation.

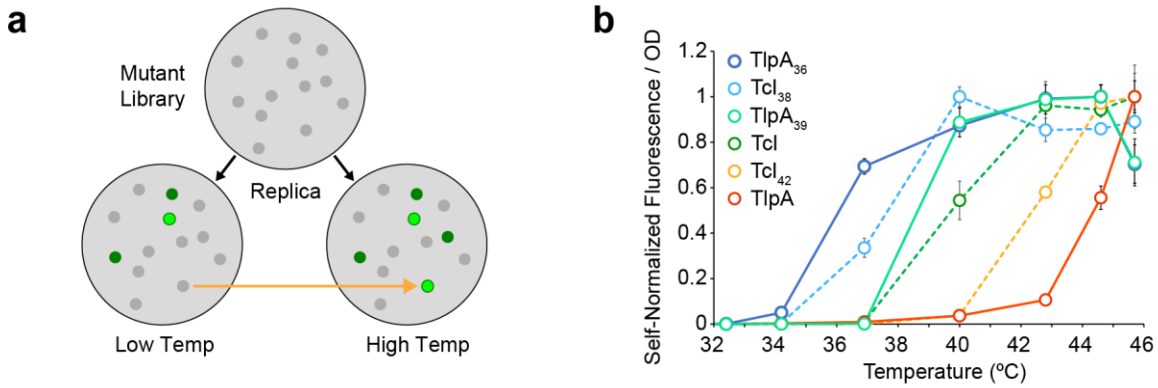

Supplementary Figure 3-S3 - Tuning the transition temperature of thermal bioswitches. (**a**) Illustration of the screening strategy used to identify temperature-shifted repressor variants. (**b**) Self-normalized fluorescence/OD profiles for the full set of TlpA (solid lines) and TcI (dashed lines) bioswitches, demonstrating the complete range of available transition temperatures.

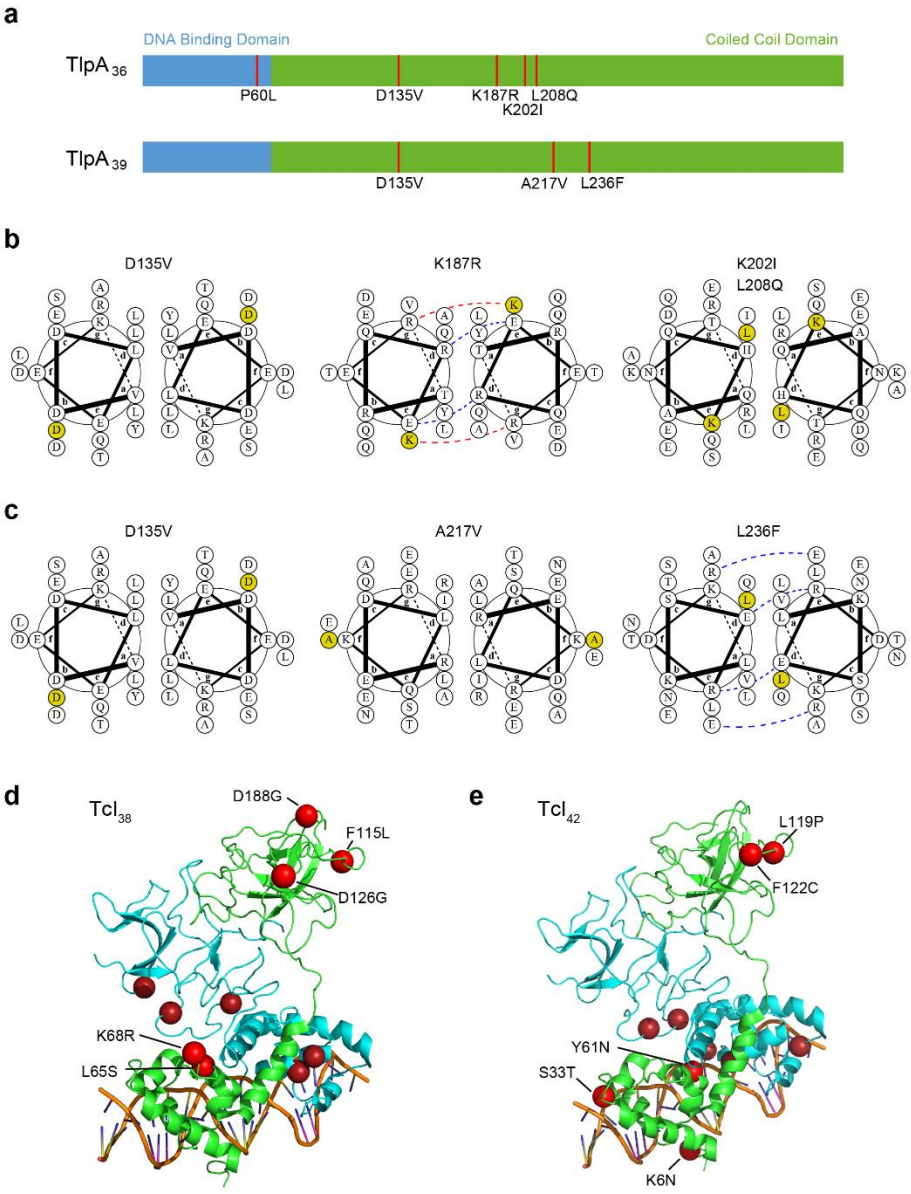

Supplementary Figure 3-S4 – Positions of mutations in selected variants of TlpA and TcI. (**a**) Schematic of mutation positions (red) within the predicted domain structure of $TlpA_{36}$ and $TlpA_{39}$. The DNA binding domain is depicted in blue and coiled-coil domain in green, as delineated by Koski et al[1]. The figure is drawn to the scale of the primary sequence. (**b**) Positions of mutations in $TlpA_{36}$ within the predicted structure of the coiled-coil interface as viewed down the long axis of the helix. Blue dashed lines represent predicted energetically favorable ionic interactions; red dashes indicate predicted repulsive ionic interactions. The coil register was assigned based on consensus between previous literature[1] and the structure prediction servers COILS[2], Paircoil2[3], and LOGICOIL[4]. The images were produced using DrawCoil 1.0[5]. The P60L mutation is not shown because it falls outside of the predicted coiled-coil region. (**c**) Positions of mutations in $TlpA_{39}$. Register prediction and illustration were performed as in (b). (**d**) Mutation positions (red) for the lambda repressor variant TcI_{38}. The crystal structure of the wild type lambda repressor (PDB code 3BDN) was used as the homology model[6]. The original temperature-sensitizing mutation A67T is not shown. The M1V

mutation is not depicted because residue 1 was not reported in the crystal structure. (**e**) Mutation positions (red) within the TcI_{42} variant.

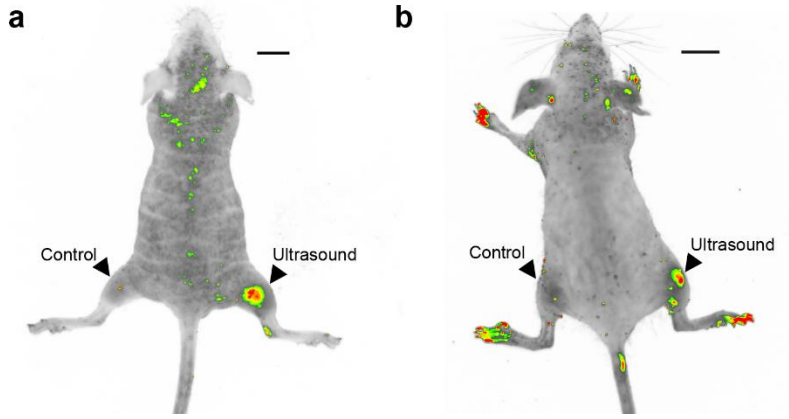

Supplementary Figure 3-S5 – Additional mice with ultrasound-activated gene expression. (**a**) and (**b**) Additional mice that underwent the experiment shown in Fig. 4e. The images are thresholded fluorescence maps of mice injected subcutaneously in both left and right hindlimbs with *E. coli* expressing GFP under the control of $TlpA_{36}$, following ultrasound activation at only the right hindlimb. Signal at mouse digits is the result of autofluorescence and varies from mouse to mouse; digits were neither injected with bacteria nor exposed to ultrasound.

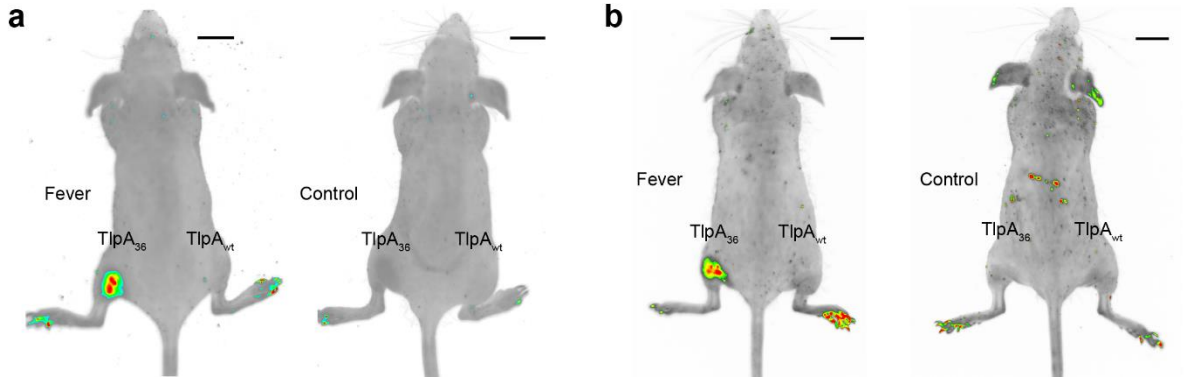

Supplementary Figure 3-S6 – Additional mice with fever-activated gene expression. (**a**) and (**b**) Additional pairs of mice that underwent the experiment shown in Fig. 5, b-c. Each panel shows thresholded fluorescence maps of one mouse that underwent fever induction after being injected subcutaneously with plasmids expressing $TlpA_{36}$- and TlpA-regulated GFP into the left and right hind limbs, respectively, with a paired mouse that was prepared identically but maintained at room temperature.

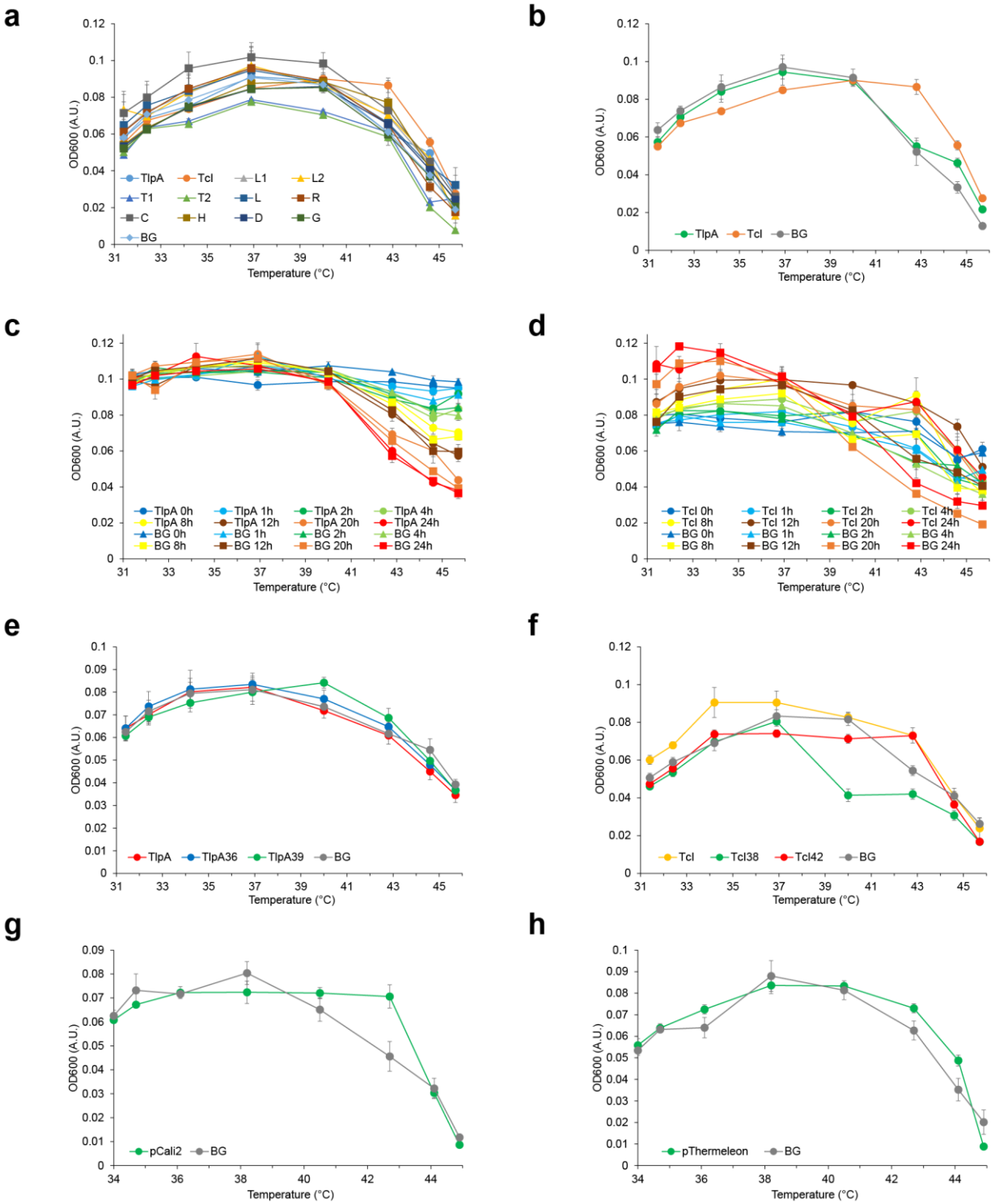

Supplementary Figure 3-S7. OD_{600} measurements for thermal induction profiles reported in main text. Blank-subtracted measurements of OD_{600} in 90 µL volumes in clear-bottom 96 well plates, corresponding to an optical path length of approximately 1.4 mm. Data corresponds to: (**a**) Fig. 1b; (**b**) Fig. 1c; (**c**) Fig. 1e; (**d**) Fig. 1f; (**e**) Fig. 2d; (**f**) Fig. 2e; (**g**) Fig. 3c; (**h**) Fig. 3g. BG = background.

3.7: Supplementary References

1. Koski, P., Saarilahti, H., Sukupolvi, S., Taira, S., Riikonen, P., Osterlund, K., … Rhen, M. A new alpha-helical coiled coil protein encoded by the Salmonella typhimurium virulence plasmid. *The Journal of Biological Chemistry* **267**, 12258–12265 (1992).
2. Lupas, A., Van Dyke, M., and Stock, J. Predicting Coiled Coils from Protein Sequences. *Science* **252**, 1162-1164 (1991).
3. McDonnel, A.V., Jiang, T., Keating, A.E., Berger B. Paircoil2: Improved prediction of coiled coils from sequence. *Bioinformatics* **22**, 356-358 (2006).
4. Vincent, T.L., Green, P.J., Woolfson, D.N. LOGICOIL—multi-state prediction of coiled-coil oligomeric state. *Bioinformatics* **29**, 69-76 (2013).
5. Grigoryan, G., Keating, A.E. Structural Specificity in Coiled-coil Interactions. *Current Opinion in Structural Biology* **18**, 477-483 (2008).
6. Stayrook. S.E., Jaru-Ampornpan, P., Ni, J., Hochschild, A., Lewis, M. Crystal structure of the lambda repressor and a model for pairwise cooperative operator binding. *Nature* **452**, 1022-1025 (2008).
7. Hurme, R., Berndt, K. D., Namork, E. & Rhen, M. DNA binding exerted by a bacterial gene regulator with an extensive coiled-coil domain. *The Journal of biological chemistry* **271**, 12626-12631 (1996).
8. Marr, M. T. & Roberts, J. W. Promoter Recognition As Measured by Binding of Polymerase to Nontemplate Strand Oligonucleotide. *Science* **276**, 1258-1260 (1997).

3.8: Detailed Author Contributions

Figure 3-1: DP designed and performed experiments.

Figure 3-2: DP and MA jointly designed experiments.

- MA performed experiment for **Fig. 3-2a**.
- MA collected data and DP performed analysis on **Fig. 3-2b**.
- MA performed experiment for **Fig. 3-2c**.
- DP performed experiment for **Fig. 3-2d**.

Figure 3-3: DP designed and performed experiments.

Figure 3-4:

- DP designed and performed experiments for **Fig 3-4 a-c**.
- MA designed and performed experiments for **Fig 3-4 d,e**.

Figure 3-5:

- MA designed and performed experiments for **Fig. 3-5 a-c**.
- MA designed experiment; MA and ALG collected data for **Fig. 3-5 d-f**.

Supplementary Figures

- **Fig 3-S1**: DP performed analysis.
- **Fig 3-S2**: DP designed and performed experiments for **S3-2 a, c, and d**. MA designed and performed experiments for **S3-2b**.
- **Fig. 3-S4**: DP performed analysis.
- **Fig. 3-S5**: MA and DP jointly performed experiment.
- **Fig. 3-S6**: MA performed experiment.

C h a p t e r 4

THERMAL BIOSWITCHES FOR MODULAR CONTROL OF PROTEIN DIMERIZATION

4.1: Introduction

The study and engineering of cellular function within the context of complex tissues and synthetic biomaterials necessitates the development of methods to enable external control of cellular signaling with high spatial and temporal specificity and deep tissue penetration[1]. Conditional protein-protein interactions (PPIs) are among the most widespread and versatile modalities employed by cells to regulate molecular signaling pathways[2]. Consequently, engineered PPIs have had an important role in studying the function of many proteins in the cell and the construction of synthetic cellular devices. In particular, widely used chemically-inducible dimerization domains such as FKBP/FRB[3] have enabled a vast array of applications ranging from the basic study of protein signaling[4] to the engineering of exogenously-gated chimeric antigen receptors for cellular immunotherapy[5]. Chemical dimerization is effective both in culture and in deep tissues based on the bioavailability of the chemical agent; however, this activity is poorly amenable to spatiotemporal regulation. In contrast, optically inducible dimerization domains such as Cry2/CIB1 offer exquisite spatial and temporal precision, enabling microscopic studies of processes such as the immune response[6] and cell motility[7], but are limited by the scattering of photons in deep tissue and other complex media.

Temperature offers an alternative mechanism for controlling biological signaling with several advantages over chemicals and light. Temperature can be applied to biological samples globally using simple heat sources or electromagnetic radiation, and can be applied locally deep within scattering media using technologies such as focused ultrasound, enabling spatiotemporal control with millimeter spatial resolution and temporal resolution on the order of seconds[1,8]. Previous work on thermal control of cellular signaling has focused on temperature-actuated transcription and translation, taking advantage of endogenous heat shock promoters[9,10], temperature-dependent RNA elements[11], or heterologously expressed protein-based transcriptional bioswitches[12]. In addition, temperature-sensitive variants of individual proteins have been used to study the function of these proteins in model systems[13,14]. While these pioneering approaches enable thermal control of specific aspects of cellular function, they lack the modularity of chemical and optical dimerizers.

Here we introduce a modular approach to controlling protein dimerization with temperature. Starting with a homodimeric temperature-dependent coiled-coil transcription factor from bacteria, we engineer a pair of heterodimeric protein association domains with sharp, tunable thermal unbinding. We demonstrate the ability of these "thermomers" to dynamically control protein localization in living mammalian cells. The resulting technology has the potential to provide versatile thermal control of protein-protein interactions in a variety of cell types, complementing the existing set of chemical and optical tools.

4.2: Results

As the starting point for our design of thermomers, we used the temperature-sensitive transcriptional repressor TlpA from *Salmonella typhimurium* due to its relatively simple architecture and well-characterized thermal behavior[15]. While no atomic-resolution structure of this protein exists, biochemical and bioinformatics studies have indicated that TlpA consists of an N-terminal DNA-binding domain and a C-terminal coiled-coil domain, the latter of which causes the protein to homodimerize in a temperature-dependent manner. As a dimer, TlpA binds to a cognate DNA operator sequence within its corresponding promoter and prevents transcription. The coiled-coil domain of TlpA undimerizes and uncoils above a temperature of ~42ºC, causing unbinding from the operator and allowing transcription to take place. This sharply cooperative transition happens over less than 3 ºC, as defined by 10% to 90% activation. We previously demonstrated that the thermal set-point of TlpA could be tuned through directed evolution without compromising cooperativity, and used its transcription factor activity to spatiotemporally control the function of engineered bacteria with ultrasound hyperthermia[12].

To turn TlpA into a modular protein-protein dimerization system, we first needed to convert it from a homodimer to a heterodimer. Most applications of inducible dimerization systems require the interacting modules to be heterodimeric to enforce selective binding between two desired molecular partners[16]. To redesign the wild type TlpA into a pair of heterodimeric coiled-coil species (**Fig. 4-1a**), we used rational mutagenesis guided by bioinformatic prediction of the TlpA dimerization domain. Coiled-coil domains typically consist of repetitive seven-amino acid residue sequences known as heptad repeats[17]. We used a

published annotation of the TlpA sequence[18], cross-referenced against a computational annotation from the COILS[19] prediction server, to establish the register of heptad repeats within the TlpA primary sequence. We then introduced charge-complementary pairs of residues[20] predicted either at conventional g-to-e' contacts or at alternative g-to-d' interfaces to disfavor homodimerization and favor heterodimerization (**Fig. 4-1, b-c**). The latter architecture occurs when large ionic sidechains at the core peripherally expose their charged termini as has been described for the Fos-Jun coiled coil interaction[21]. To maintain the highly switch-like thermal dissociation behavior of TlpA, we reasoned that the least perturbative positions for mutagenesis would be at existing interfacial ionic interaction sites in the wild type protein, which are present due to the C_2 symmetry of the parallel coiled-coil structure. We mutagenized all such positions one by one, replacing cationic residues with glutamate and anionic side chains with arginine or lysine. We expressed the resulting coiled-coil domains in *E. coli*, purified the proteins via affinity chromatography, and assayed their helical content over a relevant thermal range via circular dichroism spectroscopy (**Supplementary Fig. 4-S1**). From this initial screen we obtained a pair of charge-complemented mutants, dubbed TlpA-G_1A (E180R) and TlpA-G_1B (R179E), that demonstrated a sharp, sigmoidal switching profile with a notable upshift in threshold for an equimolar mixture of the mutant pair relative to pure solutions of either species (**Fig. 4-1d**).

To validate the *in vivo* functionality of the TlpA-G_1A and G_1B mutants, we utilized the ability of TlpA to modulate the expression of a fluorescent reporter gene in *E. coli*[12]. We constructed a temperature-inducible circuit containing two separate copies of the TlpA gene, with a TlpA operator upstream of a green fluorescent protein (GFP) and a red fluorescent protein (RFP).

To compare the repression efficiency of the G_1A/G_1A and G_1B/G_1B homodimers to that of the G_1A/G_1B heterodimer, we generated circuit variants containing two copies of TlpA-G_1A, two copies of TlpA-G_1B, or one copy of each TlpA strand (**Fig. 4-2a**). The thermal gene expression profiles of GFP showed all three circuits to produce a highly switch-like cooperative activation. However, the two homodimeric constructs had a clear downshift in their transition temperature compared to the heterodimeric construct containing both TlpA variants (**Fig. 4-2b**), confirming a stabilized heterotypic-association between the two coiled-coil strands. The RFP output displayed similar activation profiles (**Supplementary Fig. 4-S2**). Swapping the positions of the two TlpA copies within the vector did not significantly influence the expression profile, controlling for inadvertent stoichiometric effects (**Supplementary Fig. 4-S3**).

While the performance of the first-generation heterodimers was encouraging, we noted that the G_1A/G_1A and G_1B/G_1B circuit constructs still demonstrated an activation setpoint above 37 °C, indicating that the mutants retained the ability to homodimerize under typical mammalian homeostatic conditions. We therefore used our thermal GFP expression assay to evaluate a subset of additional rational mutant pairs selected from our original panel (**Supplementary Fig. 4-S4**), and chose the two best-performing pairs of substitutions from this subset to combine with TlpA G_1A and TlpA G_1B in all possible permutations. This resulted in the second-generation coiled-coil pairs dubbed TlpA $G_{2\text{-}1} – G_{2\text{-}4}$, each comprising a G_2A_n and a G_2B_n monomer (**Supplementary Table 4-T1**). In our bacterial bioswitch assay, all the heterodimeric circuits combining G_2A_n with its complementary G_2B_n displayed switch-like activation of reporter fluorescence (**Fig. 4-2c, Supplementary Fig. 4-S5**). In

contrast, the homodimeric constructs containing two copies of G_2A_n or G_2B_n were unable to propagate in a stable manner, consistently displaying deletions in the TlpA promoter or the fluorescent reporter gene, even when grown at 30 °C in recombination-deficient *E. coli*. We interpreted this as evidence that the second-generation variants are unable to form homodimeric interactions at the concentrations defined by our circuits, resulting in constitutive expression from the TlpA promoter and a strong metabolic burden to the host cell[22,23].

For additional confirmation of the dimerization preference of our engineered coiled-coils, we designed a biochemical assay based on covalent crosslinking and size-based gel separation. TlpA dimers can be crosslinked via $CuCl_2$-catalyzed oxidation of the protein's single cysteine residue[24]. To distinguish hetero- from homodimerization, we truncated one of the two TlpA sequences by removing its DNA binding domain, thereby altering its electrophoretic mobility on a polyacrylamide gel without perturbing its ability to dimerize (**Fig. 4-3a**). HA tags were added at the C-termini of both proteins to facilitate specific detection via Western blotting. We expressed the resulting pairs of truncated and full-length TlpA variants in *E. coli.* To validate this assay, we expressed a pair of wild-type TlpA coils and crosslinked them at 37 °C, after a thermal elevation to 45 °C, and after return to 37 °C. Three bands corresponding to the expected mixture of the two types of homodimers and one type of heterodimer were visible after crosslinking at 37 ºC, while crosslinking at the higher temperature resulted in the preponderance of monomers, which could be re-annealed by bringing the temperature back down to 37 ºC (**Fig. 4-3b**).

Substituting the wild type coiled-coils with our first-generation hetrodimerizing mutants resulted in preferential accumulation of the TlpA heterodimer at 37 °C (**Fig. 4-3c**). Constructs containing the second-generation variants demonstrated further reduction in the intensity of the homodimer bands in favor of the intermediate molecular weight heterodimer, with TlpA $G_{2\text{-}3}$ demonstrating the strongest heterodimeric enrichment. (**Fig. 4-3c, Supplementary Fig. 4-S6**). The first- and second-generation heterodimers both showed reversible dissociation at 45ºC (**Fig. 4-3d**). On the basis of these results, the TlpA $G_{2\text{-}3}$ pair was chosen as the thermomer construct for further experiments.

After validating our engineered heterodimeric TlpA thermomers, we set out to demonstrate their ability to be fused with other proteins and confer controlled protein-protein association in mammalian cells. We designed a construct wherein one TlpA-$G_{2\text{-}3}$ strand was N-terminally fused with the palmitoylation sequence of GAP43, thereby compartmentalizing it to the plasma membrane. The complementary strand was fused at the C-terminus to mScarlet-I (**Fig. 4-4a**), an RFP chosen for its robust fluorescence at elevated temperature (**Supplementary Fig. 4-S7**). To make this system compatible with mammalian homeostatic conditions, we combined the TlpA-$G_{2\text{-}3}$ heterodimerizing mutations with three previously described amino acid substitutions that lower the coiled-coil dissociation temperature to approximately 39 ºC[12].

Using live cell confocal microscopy of transiently transfected K562 cells, at physiological temperature we observed strong localization of red fluorescence to the plasma membrane (**Fig. 4-4b** and **Supplementary Fig. 4-S8**) and also to the Golgi apparatus (**Supplementary**

Fig. 4-S9). Increasing the cells' temperature using resistive heating above a threshold of 40 °C resulted in the redistribution of membrane fluorescence into the cytosol. As a control for non-specific thermal dissociation, cells in which the RFP was directly palmitoylated showed no redistribution of membrane fluorescence within this temperature range (**Fig. 4-4c**, **4-4d**, and **Supplementary Fig. 4-S10**). This confirms that RFP dissociation from the membrane is driven by a TlpA-mediated binding transition rather than disruption of membrane integrity.

To enable the use of the thermomer system with viral gene delivery and genomic integration, we generated a nonhomologous variant of the TlpA G_2A_3 strand (nhTlpA G_2A_3) in which all degenerate codons were mutagenized to synonymous triplets with minimal identity to the original sequence. This mutagenesis helps avoid template switching-mediated recombination during viral delivery of high-homology constructs[25]. The resulting open reading frame had 57.48% sequence identity to the parent sequence, with no more than 5 consecutive homologous nucleotides. Lentiviral delivery of a construct containing palmitoylated nhTlpA G_2A_3 and mScarlet-fused TlpA G_2B_3 resulted in robust temperature-induced dissociation of red fluorescence from the plasma membrane, similar to results from transient transfection (**Supplementary Fig. 4-S11**).

We used this virally-engineered K562 cell line to quantify the co-localization of RFP fluorescence intensity with signal from the plasma membrane as delineated by CellBrite Fix 488 staining (**Fig. 4-4e**). Cells with thermomer-mediated RFP targeting to the membrane demonstrated co-localization with the dye at physiological temperature, followed by loss of pixel correlation above 40 ºC (**Fig. 4-4f**). In contrast, control cells with directly palmitoylated

RFP demonstrate robust co-localization with the membrane stain throughout the temperature range tested, while free cytoplasmic RFP showed no correlation with the CellBrite dye (**Fig. 4-4f**). We also used the TlpA reporter cell line to evaluate the reversibility of TlpA-mediated membrane localization after heating. Membrane localization was released by a 5-minute incubation at 42 ºC. Upon cooling back to 37 °C, TlpA re-partitioned to the plasma membrane, indicating reversibility, albeit with slower kinetics than observed for dissociation (**Fig. 4-4g** and **Supplementary Fig. 4-S12 and 4-S13**).

4.3: Discussion

Our results establish heterodimeric TlpA coils as modular, tunable thermomers capable of conferring temperature-controlled protein-protein association and localization to genetically fused proteins. This technology complements the large existing repertoire of chemical and optical dimerizers used to control a wide range of protein and cellular functions[26]. The thermomer constructs also expand upon our previous work on temperature-stimulated transcriptional control[12] by enabling thermal actuation in arbitrary cell types and drastically increasing the kinetics of activation relative to that of gene expression. We anticipate that as external control of protein signaling becomes needed for more complex settings, such as cellular therapy[27] and engineered living materials[28], this will provide a role for temperature-based control modalities that offer spatiotemporal specificity and penetration depth beyond those afforded by systemic drug delivery or optical methods[1,8].

The simple architecture of the TlpA coiled-coil renders it an attractive domain for future work in controlling protein function. For example, conditionally dimeric coiled-coil fusions have previously been used to reconstitute and control a split mutant of RNAse T1[29] and to conditionally enact DNA binding by a bZIP domain upon photostimulation[30]. More broadly, coiled-coils have seen a diverse array of applications in biomaterials, affinity purification, assembly of bispecific or high avidity antibodies, and reconstitution of various split proteins or dimerization-dependent protein complexes[31,32].

To maximize its versatility as a tool for biology and medicine, future work on TlpA-based thermomers is needed to optimize construct size, modularity, and kinetics. At 371 residues, TlpA is nearly four times larger than its drug-responsive counterpart FKBP, which may hinder applications in gene delivery where sequence compactness is of premium importance. Truncation and mutagenesis approaches may offer a strategy by which the size of the thermomer system could be minimized without sacrificing the desired sharp thermal switching response. In addition, elucidating the mechanism responsible for the unique thermal cooperativity of TlpA would assist in future rational engineering efforts to modify performance and generate novel, orthogonal thermomers. Additionally, a thorough characterization of potential genetic fusion sites and optimal linker sequences would facilitate the widespread use of TlpA as a thermal fusion tag. In this study, we demonstrated that TlpA retains a cooperative thermal transition as an intact protein, as an isolated coiled-coil domain, and as a system with distinct fusion sites at the N and C-termini. However, additional engineering may be needed to accommodate fusion partners of different sizes and valency. Finally, we note that while detection of TlpA-RFP delocalization kinetics from the

plasma membrane appeared to be limited by the timescale of temperature elevation and image acquisition of our apparatus (approximately 2 minutes), re-association in some cells was significantly slower. It would be useful to investigate the factors that influence re-association, including diffusion and potential low-affinity contacts between unpartnered TlpA strands, their homodimeric partners and other constituents of the cell. With further optimization, thermomers promise to provide a high degree of control over a wide range of cellular processes with the versatile application of thermal energy.

4.4: Acknowledgements

The authors thank Mohamad Abedi and Andres Collazo for helpful discussions. Microscopy was performed at the Biological Imaging Facility of the Beckman Institute at Caltech. This research was supported by the Defense Advanced Research Projects Agency (D14AP0050), the Sontag Foundation and the Army Institute for Collaborative Biotechnologies (W911NF-19-D-0001). D.I.P. was supported by the NIH fellowship for Predoctoral Training in Biology and Chemistry (T32GM007616).

4.5: References

(1) Piraner, D. I.; Farhadi, A.; Davis, H. C.; Wu, D.; Maresca, D.; Szablowski, J. O.; Shapiro, M. G. Going Deeper: Biomolecular Tools for Acoustic and Magnetic Imaging and Control of Cellular Function. *Biochemistry* **2017**, *56* (39). https://doi.org/10.1021/acs.biochem.7b00443.

(2) Berggård, T.; Linse, S.; James, P. Methods for the Detection and Analysis of Protein – Protein Interactions. **2007**, 2833–2842. https://doi.org/10.1002/pmic.200700131.

(3) Spencer, D. M.; Wandless, T. J.; Schreiber, S. L.; Crabtree, G. R. Controlling Signal Transduction with Synthetic Ligands. *Science (80-.).* **1993**, *262* (5136), 1019–1024.

(4) Muthuswamy, S. K.; Gilman, M.; Brugge, J. S. Controlled Dimerization of ErbB Receptors Provides Evidence for Differential Signaling by Homo- and Heterodimers. *Mol. Cell. Biol.* **1999**, *19* (10), 6845–6857.

(5) Wu, C.-Y.; Roybal, K. T.; Puchner, E. M.; Onuffer, J.; Lim, W. A. Remote Control of Therapeutic T Cells through a Small Molecule-Gated Chimeric Receptor. *Science (80-.).* **2015**, *350* (6258). https://doi.org/10.1126/science.aab4077.

(6) Moser, B. A.; Esser-Kahn, A. P. A Photoactivatable Innate Immune Receptor for Optogenetic Inflammation. *ACS Chem. Biol.* **2017**, *12* (2), 347–350. https://doi.org/10.1021/acschembio.6b01012.

(7) Bugaj, L. J.; Choksi, A. T.; Mesuda, C. K.; Kane, R. S.; Schaffer, D. V. Optogenetic Protein Clustering and Signaling Activation in Mammalian Cells. **2013**, *10* (3). https://doi.org/10.1038/nmeth.2360.

(8) Maresca, D.; Lakshmanan, A.; Abedi, M.; Bar-Zion, A.; Farhadi, A.; Lu, G. J.; Szablowski, J. O.; Wu, D.; Yoo, S.; Shapiro, M. G. Biomolecular Ultrasound and Sonogenetics. *Annu. Rev. Chem. Biomol. Eng.* **2018**, *9*, 229–252. https://doi.org/10.1146/annurev-chembioeng-060817-084034.

(9) Guilhon, E.; Voisin, P.; de Zwart, J. a; Quesson, B.; Salomir, R.; Maurange, C.; Bouchaud, V.; Smirnov, P.; de Verneuil, H.; Vekris, a; et al. Spatial and Temporal Control of Transgene Expression in Vivo Using a Heat-Sensitive Promoter and MRI-Guided Focused Ultrasound. *J. Gene Med.* **2003**, *5* (4), 333–342. https://doi.org/10.1002/jgm.345.

(10) Liu, R. Y.; Corry, P. M.; Lee, Y. J. Regulation of Chemical Stress-Induced Hsp70 Gene Expression in Murine L929 Cells. *J. Cell Sci.* **1994**, *107*, 2209–2214.

(11) Krajewski, S. S.; Narberhaus, F. Temperature-Driven Differential Gene Expression by RNA Thermosensors. *Biochim. Biophys. Acta - Gene Regul. Mech.* **2014**, *1839* (10), 978–988. https://doi.org/10.1016/j.bbagrm.2014.03.006.

(12) Piraner, D. I.; Abedi, M. H.; Moser, B. A.; Lee-Gosselin, A.; Shapiro, M. G. Tunable Thermal Bioswitches for in Vivo Control of Microbial Therapeutics. *Nat. Chem. Biol.* **2017**, *13* (1), 75–80. https://doi.org/10.1038/nchembio.2233.

(13) Royal, D. C.; Bianchi, L.; Royal, M. A.; Lizzio, M.; Mukherjee, G.; Nunez, Y. O.; Driscoll, M. Temperature-Sensitive Mutant of the Caenorhabditis Elegans Neurotoxic MEC-4(d) DEG/ENaC Channel Identifies a Site Required for Trafficking or Surface Maintenance. *J. Biol. Chem.* **2005**, *280* (51), 41976–41986. https://doi.org/10.1074/jbc.M510732200.

(14) Cox, V. T.; Baylies, M. K. Specification of Individual Slouch Muscle Progenitors in Drosophila Requires Sequential Wingless Signaling. *Development* **2005**, *132*, 713–724. https://doi.org/10.1242/dev.01610.

(15) Hurme, R.; Berndt, K. D.; Normark, S. J.; Rhen, M. A Proteinaceous Gene Regulatory Thermometer in Salmonella. *Cell* **1997**, *90* (1), 55–64.

(16) Stanton, B. Z.; Chory, E. J.; Crabtree, G. R. Chemically Induced Proximity in Biology and Medicine. *Science (80-.).* **2018**, *359* (6380), 1–9. https://doi.org/10.1126/science.aao5902.

(17) Mason, J. M.; Arndt, K. M. Coiled Coil Domains: Stability, Specificity, and Biological Implications. *Chembiochem* **2004**, *5* (2), 170–176. https://doi.org/10.1002/cbic.200300781.

(18) Koski, P.; Saarilahti, H.; Sukupolvi, S.; Taira, S.; Riikonen, P.; Osterlund, K.; Hurme, R.; Rhen, M. A New Alpha-Helical Coiled Coil Protein Encoded by the Salmonella Typhimurium Virulence Plasmid. *J. Biol. Chem.* **1992**, *267* (17), 12258–12265.

(19) Lupas, a; Van Dyke, M.; Stock, J. Predicting Coiled Coils from Protein Sequences. *Science (80-.).* **1991**, *252* (5009), 1162–1164. https://doi.org/10.1126/science.252.5009.1162.

(20) Tripet, B.; Yu, L.; Bautista, D. L.; Wong, W. Y.; Irvin, R. T.; Hodges, R. S. Engineering a de Novo-Designed Coiled-Coil Heterodimerization Domain off the Rapid Detection, Purification and Characterization of Recombinantly Expressed Peptides and Proteins. *Protein Eng.* **1996**, *9* (11), 1029–1042. https://doi.org/10.1093/protein/9.11.1029.

(21) Azuma, Y.; Ku, T.; Yasunaga, J.; Imanishi, M.; Tanaka, G.; Nakase, I.; Maruno, T.; Kobayashi, Y.; Arndt, K. M.; Matsuoka, M.; et al. Controlling Leucine-Zipper Partner Recognition in Cells through Modification of a–g Interactions. *Chem Commun* **2014**, *50* (48), 6364–6367. https://doi.org/10.1039/c4cc00555d.

(22) Kawe, M.; Horn, U.; Plückthun, A. Facile Promoter Deletion in Escherichia Coli in Response to Leaky Expression of Very Robust and Benign Proteins from Common Expression Vectors. *Microb. Cell Fact.* **2009**, *8* (8), 1–8. https://doi.org/10.1186/1475-2859-8-8.

(23) Silva, F.; Queiroz, J. A.; Domingues, F. C. Evaluating Metabolic Stress and Plasmid Stability in Plasmid DNA Production by Escherichia Coli. *Biotechnol. Adv.* **2012**, *30* (3), 691–708. https://doi.org/10.1016/j.biotechadv.2011.12.005.

(24) Hurme, R.; Namork, E.; Nurmiaho-Lassila, E.-L.; Rhen, M. Intermediate Filament-like Network Formed in Vitro by a Bacterial Coiled Coil Protein. *J. Biol. Chem.* **1994**, *269* (14), 10675–10682.

(25) Delviks, K. A.; Pathak, V. K. Effect of Distance between Homologous Sequences and 3' Homology on the Frequency of Retroviral Reverse Transcriptase Template Switching. *J. Virol.* **1999**, *73* (10), 7923–7932.

(26) DeRose, R.; Miyamoto, T.; Inoue, T. Manipulating Signaling at Will: Chemically-Inducible Dimerization (CID) Techniques Resolve Problems in Cell Biology. *Pflügers Arch. - Eur. J. Physiol.* **2013**, *465* (3), 409–417. https://doi.org/10.1007/s00424-012-1208-6.

(27) Wu, C.-Y.; Rupp, L. J.; Roybal, K. T.; Lim, W. A. Synthetic Biology Approaches to Engineer T Cells. *Curr. Opin. Immunol.* **2015**, *35*, 123–130. https://doi.org/10.1016/j.coi.2015.06.015.

(28) Gilbert, C.; Ellis, T. Biological Engineered Living Materials – Growing Functional Materials with Genetically-Programmable Properties. *ACS Synth. Biol.* **2019**, *8* (1), 1–15. https://doi.org/10.1021/acssynbio.8b00423.

(29) Yuzawa, S.; Mizuno, T.; Tanaka, T. Activating an Enzyme by an Engineered Coiled Coil Switch. *Chem. Eur. J.* **2006**, *12*, 7345–7352. https://doi.org/10.1002/chem.200600007.

(30) Woolley, G. A.; Jaikaran, A. S. I.; Berezovski, M.; Calarco, J. P.; Krylov, S. N.; Smart, O. S.; Kumita, J. R. Reversible Photocontrol of DNA Binding by a Designed GCN4-BZIP Protein. *Biochemistry* **2006**, *45*, 6075–6084.

(31) Apostolovic, B.; Danial, M.; Klok, H.-A. Coiled Coils: Attractive Protein Folding Motifs for the Fabrication of Self-Assembled, Responsive and Bioactive Materials. *Chem. Soc. Rev.* **2010**, *39*, 3541–3575. https://doi.org/10.1039/b914339b.

(32) Muller, K. M.; Arndt, K. M.; Alber, T. Protein Fusions to Coiled-Coil Domains. In *Methods in Enzymology*; 2000; Vol. 328, pp 261–282. https://doi.org/10.1016/S0076-6879(00)28402-4.

4.6: Main Figures

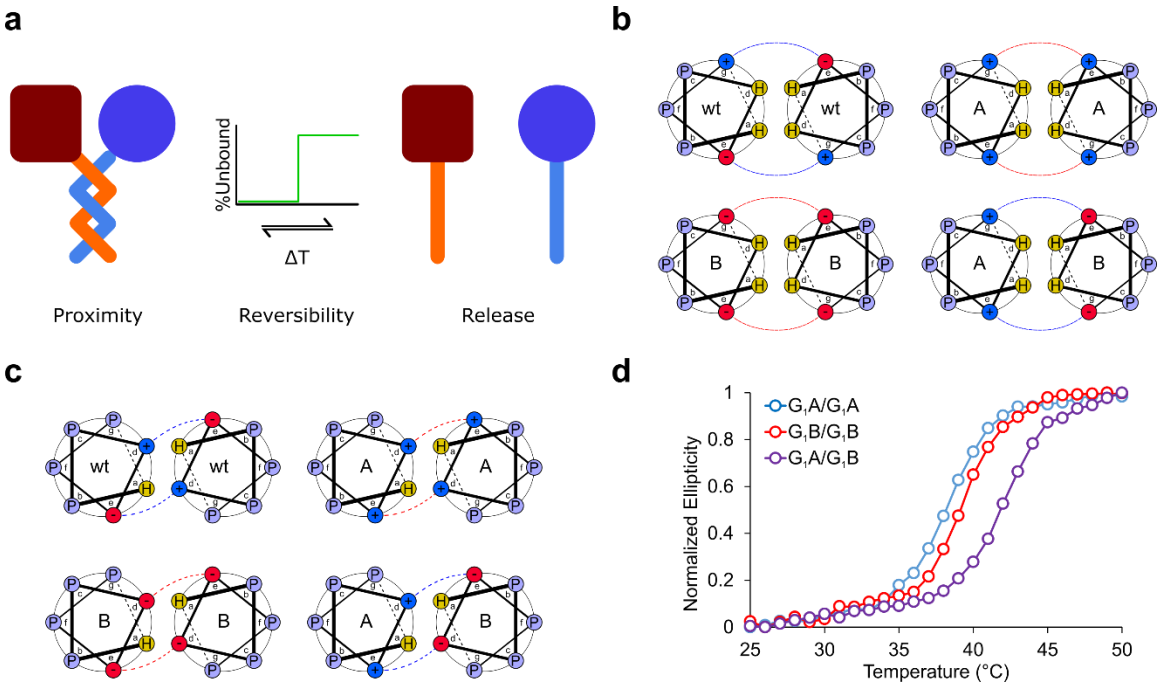

Figure 4-1: Engineering heterodimeric TlpA variants via charge-charge complementation. a) Illustration of TlpA-based thermomer system. Heterodimeric coiled-coil domains enable reversible association and dissociation of fusion partners as a sharp function of temperature. **b**) Diagram of heterodimeric coiled-coil design based on the introduction or modification of electrostatic contacts at the e-to-g' interface between adjacent α-helices. **c**) Diagram of predicted electrostatic contacts along the TlpA interface occurring in a nonconventional e-to-d' configuration. **d**) Normalized ellipticity of purified TlpA coiled-coil domain variants in isolation or as an equimolar mixture, measured at the 222 nm peak for α-helical spectra as a function of temperature. Data shown normalized from 0 to 1 on a per-sample basis.

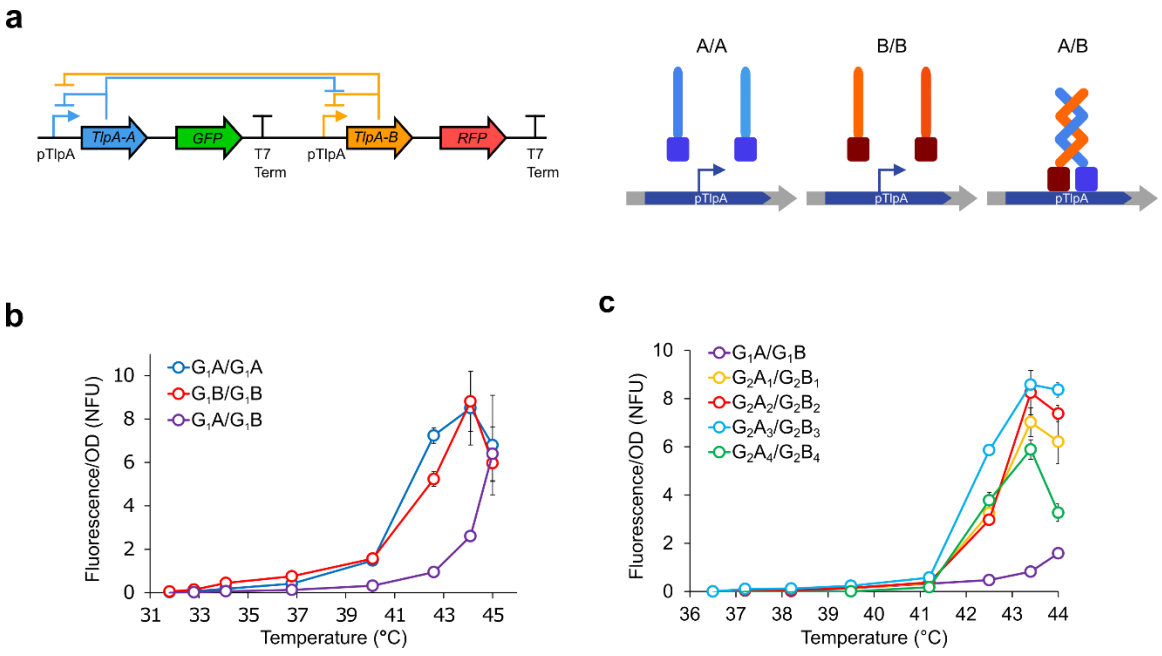

Figure 4-2: Evaluation of TlpA heterodimerization via reconstitution of promoter repression. **a**) Bacterial expression assay for heterodimerization preference. Left: diagram of bacterial genetic circuit containing two TlpA genes, each of which can encode one of the engineered variants. Bacteria harboring the G_1A/G_1A and G_1B/G_1B circuits can only produce the homodimeric coils, whereas the G_1A/G_1B circuits can produce either the homodimers or heterodimeric coils. Right: illustration of operator binding for engineered heterodimeric construct; only cells expressing both partners of the heterodimeric TlpA variant can repress the reporter gene at a certain temperature. **b**) OD-normalized fluorescence expression profile of *E. coli* harboring the plasmid constructs shown in **a**, with the single mutant G_1A and G_1B variants in the A and B positions, as a function of temperature (n = 3). Error bars represent ± s.e.m. NFU represents normalized fluorescent units. **c)** OD-normalized temperature-dependent fluorescence expression profiles of *E. coli* harboring plasmids bearing the four possible double mutant combinations of the G_1 variants and two additional candidate single mutations (n = 3). Only the heterodimeric pairings are shown. Error bars represent ± s.e.m.

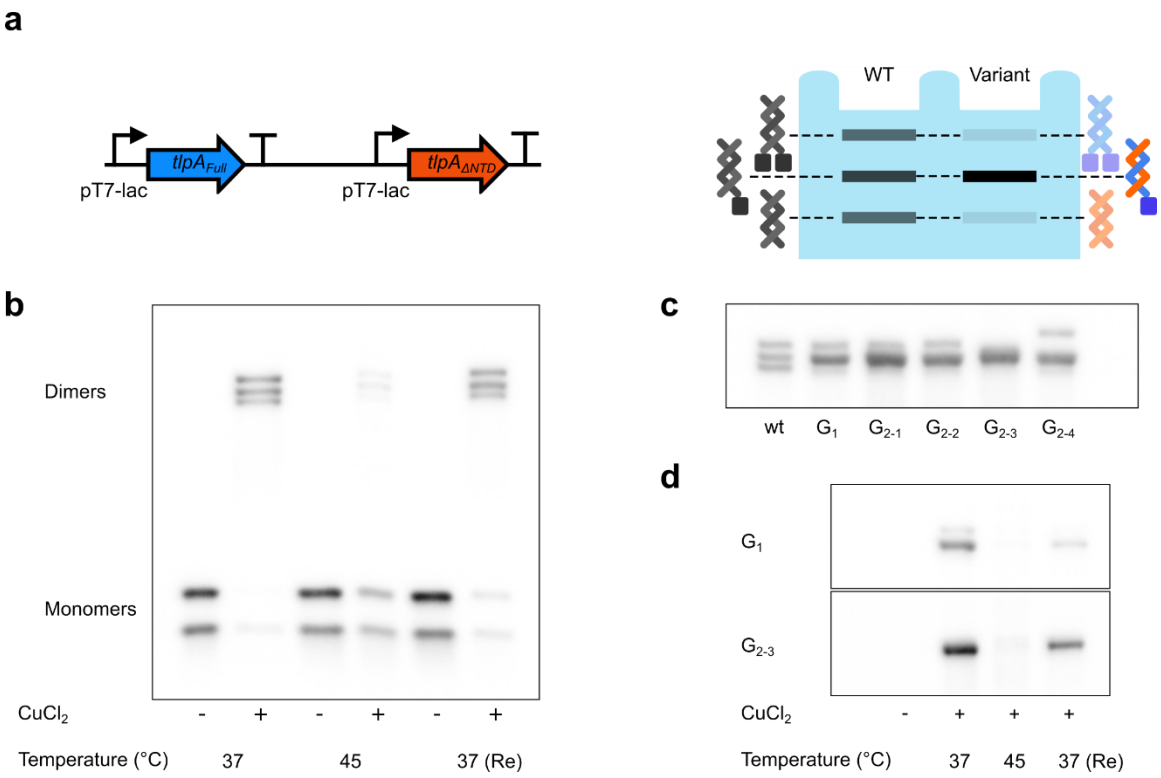

Figure 4-3: Validation of TlpA heterodimerization by electrophoresis. **a)** Left: diagram of genetic construct for simultaneous co-expression of engineered heterodimers of TlpA for biochemical assay. One open reading frame expresses the full length TlpA protein whereas the other ORF produces a truncated version missing its predicted N-terminal DNA-binding domain (ΔNTD). Each position can be occupied by any variant of TlpA, including the wild type protein and engineered mutants. Right: Diagram of the possible SDS-PAGE bands resulting from covalent crosslinking of the TlpA products expressed from this construct. The example in the left lane corresponds to the wild type homodimeric TlpA. The example in right lane corresponds to a pair of heterodimeric TlpA variants. **b)** Western blot of $CuCl_2$-catalyzed crosslinking reaction of wild-type TlpA in *E. coli* lysate followed by SDS-PAGE. Crosslinking was performed at 37 °C, at 45 °C, or at 37 °C to asses reannealing (Re) following a 10 minute incubation at 45 °C. Each condition is compared to a non-crosslinked control. The bottom bands on the gel show uncrosslinked monomers. **c)** $CuCl_2$ crosslinking, SDS-PAGE, and Western blot of the construct in **a** harboring wild type TlpA (wt), the first generation single mutant heterodimer (G_1), and the $G_{2\text{-}n}$ double mutant heterodimers. Crosslinking was performed at 37 °C. **d)** The thermal response of the G_1 and $G_{2\text{-}3}$ heterodimer constructs was analyzed in the absence and presence of $CuCl_2$ at 37 °C, 45 °C, or with 37 °C reannealing after 10 minute incubation at 45 °C.

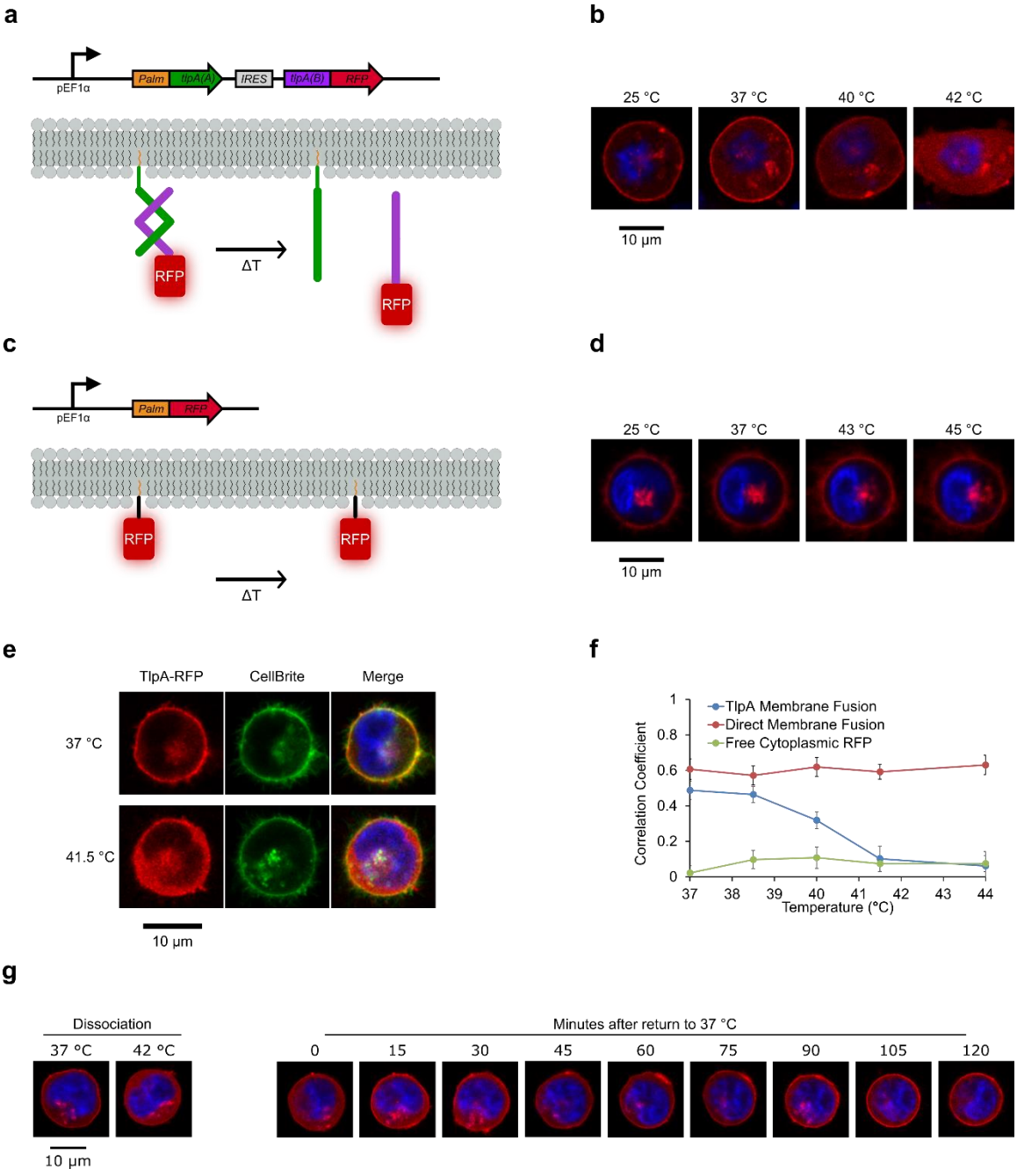

Figure 4-4: Membrane localization assay for TlpA activity in mammalian cells. a) Genetic construct (top) and schematic (bottom) for temperature-dependent localization of RFP at the plasma membrane. The $TlpA_{39}$-G_2A_3 strand is fused to a GAP43 palmitoylation motif, leading to its tethering to the lipid membrane. The partner $TlpA_{39}$-G_2B_3 strand is fused to RFP. At low temperature, the heterodimerization of these strands leads to RFP localization at the membrane. Upon heating, the RFP-fused strand dissociates from the membrane. **b**) Fluorescence images of a representative K562 cell transfected with the construct shown in **a**. Robust membrane localization of RFP fluorescence is observed at 25 °C and 37 °C. At 40 ºC, RFP begins to dissociate from the membrane, and by 42 °C red fluorescence is distributed throughout the cytoplasm. The nucleus is

stained in blue with Hoechst 33342 dye. **c**) Genetic construct (top) and experimental schematic (bottom) of directly palmitoylated RFP control. **d**) Fluorescence images of representative K562 cell transfected with the construct shown in **c,** displaying robust membrane localization throughout the temperature range tested. **e**) Representative fluorescence images of a K562 cell with a lentivirally delivered TlpA-mediated RFP localization construct (shown in **a**) and the membrane-staining dye CellBrite Fix 488. **f**) Pixel colocalization of RFP with the CellBrite 488 dye as a function of temperature in K562 cells stably expressing directly palmitoylated RFP (shown in **b**, n = 8), the TlpA-mediated membrane localization construct (shown in **a**, n = 15), and free cytosolic RFP (n = 8). Error bars represent ± s.e.m. **g**) Time series of fluorescent images of a representative K562 thermal reporter cell line before heating, after heating to 42 °C, and after re-equilibration to 37 °C. RFP re-accumulation at the plasma membrane was tracked in 15 minute intervals. Pixel intensity was normalized to the maximal per-image value.

4.7: Methods

Plasmid Construction and Molecular Biology

All plasmids were designed using the SnapGene software (GSL Biotech) and assembled via KLD mutagenesis or Gibson Assembly using enzymes from New England Biolabs. All plasmids and sequences will be deposited to Addgene. After assembly, constructs were transformed into NEB Turbo and NEB Stable *E. coli* (New England Biolabs) for growth and plasmid preparation. Constructs containing long homologous regions such, including all plasmids containing two TlpA ORFs, were propagated using NEB Stable. Thermal gene expression assays were performed in NEB Stable *E. coli*. Bacterial reporters of gene expression referred to in the text as GFP and RFP are mWasabi[1] and mCherry[2], respectively. The mammalian fusion protein fluorophore referred to in the text and figures as RFP is mScarlet-I[3]. TlpA, mCherry and mWasabi were obtained from our previous work[4]. mScarlet-I was obtained from AddGene (pmScarlet-i_C1, plasmid #85044). Coiled-coil structure prediction and helical wheel diagram annotation was performed using the software DrawCoil 1.0[5]. In the creation of dual-expression GFP/RFP thermal reporter plasmids such as that described in Fig. 1e, an additional terminator was placed upstream of each pTlpA promoter to suppress crosstalk from the weak upstream transcription previously observed from this element[4]. nhTlpA was designed using a homemade script to minimize codon homology while retaining protein sequence identity. Subsequently, 11 nucleotides were altered manually to minimize short repeats that prevented custom gene synthesis. The $nhTlpA_{39}$ gBlock was synthesized by Integrated DNA Technologies.

Bacterial Thermal Regulation Assay

Determination of temperature-dependent gene expression was performed as described previously[4]. Briefly, saturated precultures were diluted to OD_{600} = 0.1 and propagated at 30 °C until reaching OD_{600} = 0.3 as measured via Nanodrop 2000c (Thermo Scientific), at which point 25 uL aliquots were dispensed into PCR tubes with transparent caps (Bio-Rad) and incubated for 12 hours in a thermal gradient using a Bio-Rad C1000 Touch thermocycler. After thermal stimulus, fluorescence was measured using a Stratagene MX3005p qPCR (Agilent), after which cultures were diluted 4x, transferred into microplates (Costar black / clear bottom), and measured for OD_{600} using a Molecular Devices SpectraMax M5 plate reader. The background-corrected F/OD is reported as described previously[4].

Protein Expression and Purification for CD Spectroscopy

pET26b-based expression constructs were transformed into BL21-DE3 *E. coli* and grown on kanamycin-selective plates. Saturated overnight cultures were diluted 1 mL into 400 mL expression cultures and induced with a final IPTG (Sigma Aldrich) concentration of 1 mM at OD_{600} = 0.6. After 24 hours of expression at 25 °C, cultures were harvested by centrifugation using a JLA-16.250 rotor (Beckman Coulter) at 6,000 rpm and 4 °C for 8 minutes. Pellets were lysed using the detergent Solulyse in Tris Buffer (Genlantis) and debris was pelleted by centrifugation at 35,343 rcf in a JS-24.38 rotor (Beckman Coulter). Polyhistidine-tagged proteins were purified on an AKTA purifier (GE Healthcare) using 1 mL cOmplete columns (Roche) and buffer exchanged into 1x PBS (Corning) using Zeba spin desalting columns. Concentration was determined using the Pierce 660nm Protein Assay (Thermo Fisher Scientific) and proteins were stored at 4 °C until use. Proteins were subsequently analyzed within 24 hours of purification.

Circular Dichroism Spectroscopy

CD melting curves were taken using an Aviv Circular Dichroism Spectrophotometer (Model 60DS) at 222 nm with 0.1 minute equilibration time and 5 second averaging time. Purified proteins were diluted to 3 µM in 1x PBS and measured in a 1 mm quartz cuvette.

Temperature-dependent protein fluorescence measurement

Fluorescent proteins were purified as described above and diluted to 1 µM for analysis. 25 µL samples were placed in N=3 replicates in PCR strips with optically transparent caps (Bio Rad) into a Stratagene MX3005p qPCR (Agilent) for intensity mesaurements. Filter sets used for red, green, and blue proteins were ROX, FAM, and ATTO, respectively. Sample fluorescence was measured continuously as temperature was ramped from 25 °C to 50 °C in 1 °C increments and with 1 minute of equilibration time at each increment.

Mass-based validation of heterodimerization

Dual TlpA expression constructs were transformed into BL21-DE3 cells (NEB) and grown as 1 mL precultures in 2xYT/ampicillin for 20-24 hours at 30 °C in an Infors Multitron with shaking at 250 rpm. 10 µL saturated cultures were diluted into 4 mL 2xYT/ampicillin and returned to 30 °C. At OD_{600} – 0.6 to 0.7, cultures were induced with 4 µL of 1 M IPTG (Sigma Aldrich) and returned to 30 °C for 12 hours, at which point they were transferred into 2 mL centrifuge tubes (USA Scientific) and pelleted in a Beckman Microfuge 20 at maximum speed for 1 minute. Supernatant was carefully and completely aspirated with a pipette, and the pellet was weighed and frozen at -20 °C for at least 20 minutes. After

thawing, Solulyse in Tris Buffer (Genlantis) was added at 10 µL per 1 mg. Pellets were gently resuspended via pipetting and shaken in an Eppendorf ThermoMixer at room temperature (800 rpm for 20 minutes). Subsequently the tubes were spun at 13,000 rcf for 10 minutes and the lysate was diluted 5-fold in Solulyse in Tris Buffer. A pilot Western blot was performed and total TlpA band intensity was quantified for each variant, after which loading amounts for all variants were normalized to that of the wild type via dilution in Solulyse. For crosslinking, 1 µL of 50 mM $CuCl_2$ (Sigma Aldrich) was added to 10 µL lysate in an Eppendorf microcentrifuge tube. The lysate and $CuCl_2$ solution were pre-heated separately for 5 minutes prior to co-incubation. Subsequently, the lysate and crosslinker mixture was shaken at 800 rpm for 10 minutes in an Eppendorf ThermoMixer at the desired temperature. After 10 minutes of $CuCl_2$-catalyzed crosslinking, the reaction was quenched with 11 µL Laemmli buffer (Bio Rad). For uncrosslinked samples, 10 uL Laemmli buffer was added to the lysate at the appropriate temperature. SDS-PAGEwas performed using 7.5% pre-cast polyacrylamide gels (Bio Rad) run at 75 V for 140 minutes. Western blotting was performed using the Transblot Turbo apparatus and nitrocellulose membrane kit (Bio Rad). Transfer was performed at 25 V for 7 minutes. Membranes were blocked with 5% w/v Blotto milk (Santa Cruz Biotechnology) in 0.05% TBS-Tween for 1 hour at room temperature. Primary staining was performed using the mouse anti-HA sc-7392 antibody (Santa Cruz Biotech) overnight at 4 °C. Blots were then washed three times for 15 minutes at 4 °C with 0.05% TBS-Tween and stained for 4 hours with goat anti-mouse IgG-HRP sc-2005 (Santa Cruz Biotech) at room temperature. After three 15-minute washes, HRP visualization was performed using Supersignal West Pico PLUS reagent (Thermo Fisher Scientific). Imaging was performed in a Bio-Rad ChemiDoc MP gel imager.

Mammalian cell culture

K562 cells (gift of D. Baltimore) were cultured in RPMI 1640 media (Thermo Fisher Scientific) with 1x Penicillin/Streptomycin (Corning). Transient transfection was performed using Lonza 4D nucleofection with SF Cell Line buffer and the pre-programmed K562 protocol. Lentivirus was prepared using a third-generation viral vector and helper plasmids (gifts of D. Baltimore). Virus was packaged in HEK293T cells grown in 10 cm dishes after 2 days of transfection and concentrated via the Lenti-X reagent (Takara Bio). Infection was performed by resuspending viral pellets in 250 uL RPMI and spinfecting 1E6 K562 cells in 1 mL RPMI with 10 µL virus at 800 xg, 30 °C, for 90 minutes. Experiments were performed at least five passages after infection.

Live cell microscopy

Delta-T dishes (Bioptechs) were coated with 400 µL 0.1 mg/mL Poly-D Lysine (Sigma Aldrich) for 30 minutes. Meanwhile, 1E6 K562 cells were pelleted at 300 rcf for 5 minutes and resuspended in staining solution (1x PBS or HBSS with 2.5 µg/mL Hoechst 33342, Thermo Fisher Scientific). For Golgi staining, the solution (in HBSS) also contained BODIPY FL C_5-Ceramide complexed to BSA (Thermo Fisher Scientific, 50 nM final concentration). Cells were stained at room temperature for 10 minutes before being pelleted and resuspended in 1 mL RPMI 1640. For co-localization experiments, the staining solution (in HBSS) also contained CellBrite Fix 488 at 1x concentration as described in the product manual, and staining was performed at 37 °C for 10 minutes. After at least 20 minutes of coating, PDL was aspirated from the Delta-T dishes, which were then rinsed once with 1x

PBS and dried. Cells were then transferred to the Delta-T dishes, which where adhesively affixed to the swinging plates of an Allegra X-12 centrifuge with SX4750 rotor (Beckman Coulter) and centrifugated at 30 °C for 15 minutes at 300 rcf. Imaging was performed at the California Institute of Technology confocal microscopy facility using an LSM880 (Zeiss) with Airyscan. Cells with sufficient overall brightness to discern membrane contrast were imaged; the membrane localization of dimmer cells could not be discerned in our thermal imaging configuration but was observable under higher magnification on a conventional glass slide (**Supplementary Fig. 4-S14**). Delta-T dishes were mounted onto the thermal stage interfaced with a Bioptechs Delta T4 Culture Dish Controller and imaged using a 1080-378 C-Achroplan 40x/0.80 W objective. Airyscan processing was performed in 2D mode using default settings.

Image analysis

Image analysis was performed using the Zeiss Zen Black software for pre-processing and CellProfiler[6] for correlation quantification. Images were manually cropped to include only a single cell per ROI, with approximately 408x408 pixel FOVs. For cells with poor attachment to the plate, resulting in position offsets between the red, blue, and green channels, frame alignment between the red and green channels was performed in Zen Black. All available transformations were sampled and the best-aligned transformation on a per-cell basis was used. Blue channel alignment was performed in CellProfiler using the Mutual Information module, correlating the blue channel image with the inverted red channel image. Exported images were then loaded in CellProfiler and analyzed using a custom pipeline (**Supplementary File 4-F1)**. Briefly, cell boundaries were determined from red channel

using Hoescht 33342-stained nuclei as primary seed objects. Atypically bright green clusters frequently observed on the green channel were excluded from quantification, as were the Golgi-associated TlpA clusters on the red channel. Colocalization was calculated for the ROI defined between the outer cell membrane and the nucleus. The nucleus was excluded because it acts as a diffusion barrier to TlpA-RFP but not to free mScarlet-I. For the free mScarlet-I cell line in **Fig. 4-4f**, a modified pipeline using the CellBrite Fix 488 stain for cell boundary determination was used to improve the detection of cell edges (**Supplementary File 4-F2**). For the Direct Membrane Fusion data set in **Fig. 4-4f**, the 44 °C point was acquired in a separate experiment using the same cell line and is consistent with the 43 °C and 45 °C data points of the original data set (**Supplementary Fig. 4-S15**).

4.8: Supplementary Figures

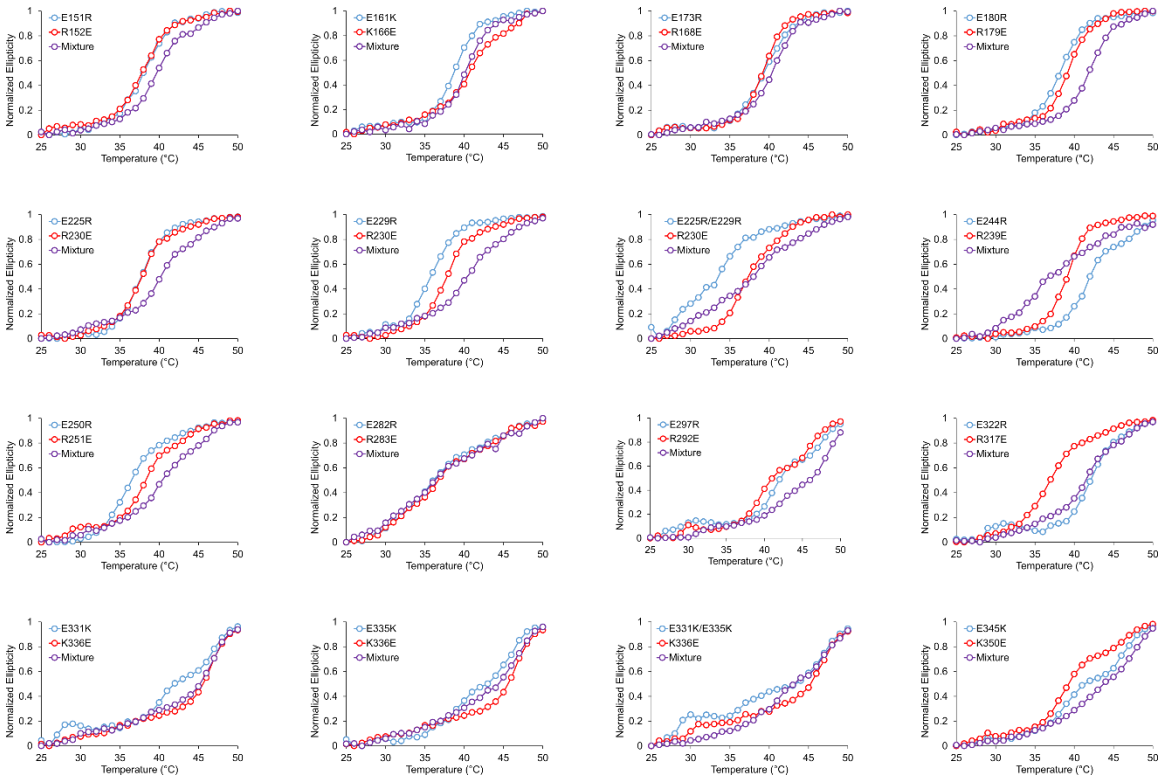

Supplementary Figure 4-S1: Circular dichroism melting curves of engineered TlpA variants. Coiled-coil fragments corresponding to residues 69-359 of TlpA were purified from *E. coli* and assayed via CD spectroscopy. Monitoring the ellipticity at 222 nm, corresponding the prototypical peak of the α-helical spectrum, enables tracking the conformation of TlpA as it transitions from the dimeric coiled-coil state to a monomeric random coil configuration.

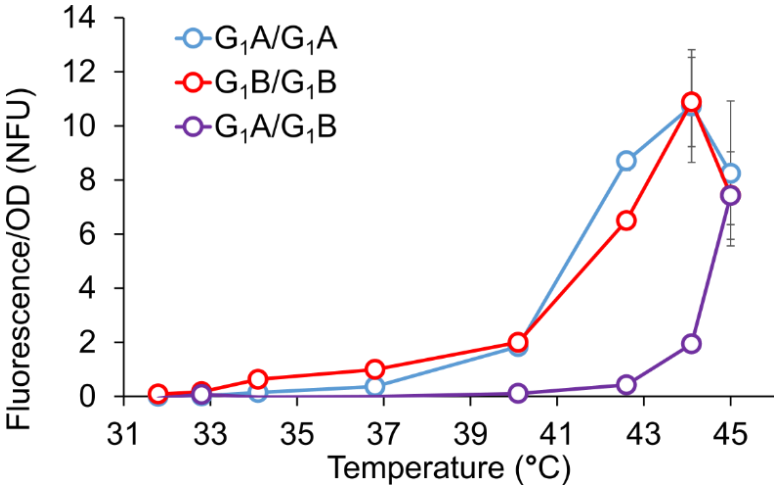

Supplementary Figure 4-S2: Thermal RFP expression profiles of the constructs shown in **Fig. 4-2b** (n = 3). Error bars represent ± s.e.m.

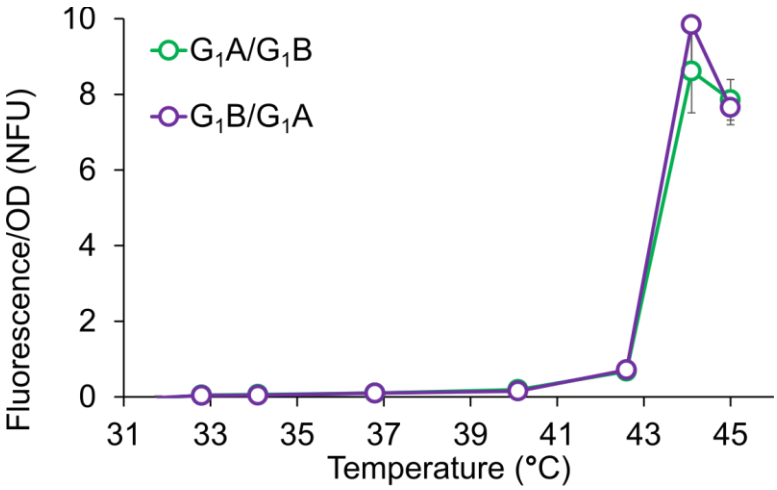

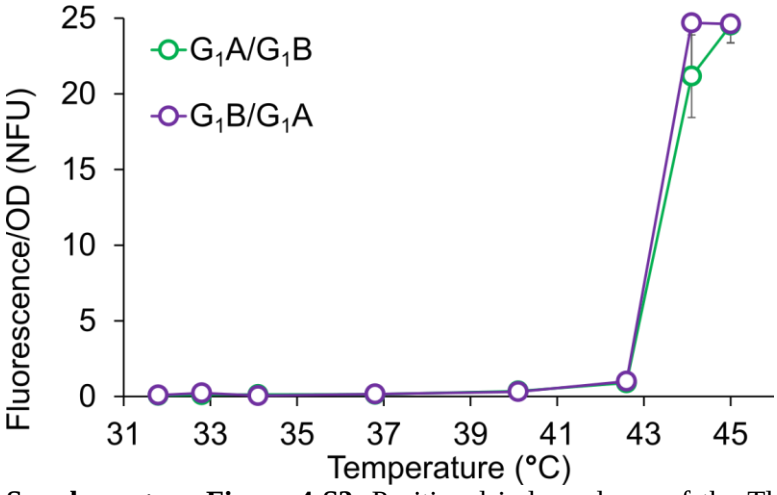

Supplementary Figure 4-S3: Positional independence of the TlpA co-expression construct. The positions of TlpA-G_1A and TlpA-G_1B within the heterodimer co-expression construct in **Fig. 4-2b** were exchanged and the thermal GFP (top) and RFP (bottom) expression profile was determined (n = 4). No significant differences were observed in the gene expression profile, thereby excluding position-dependent effects on TlpA behavior within the circuit. Error bars represent ± s.e.m.

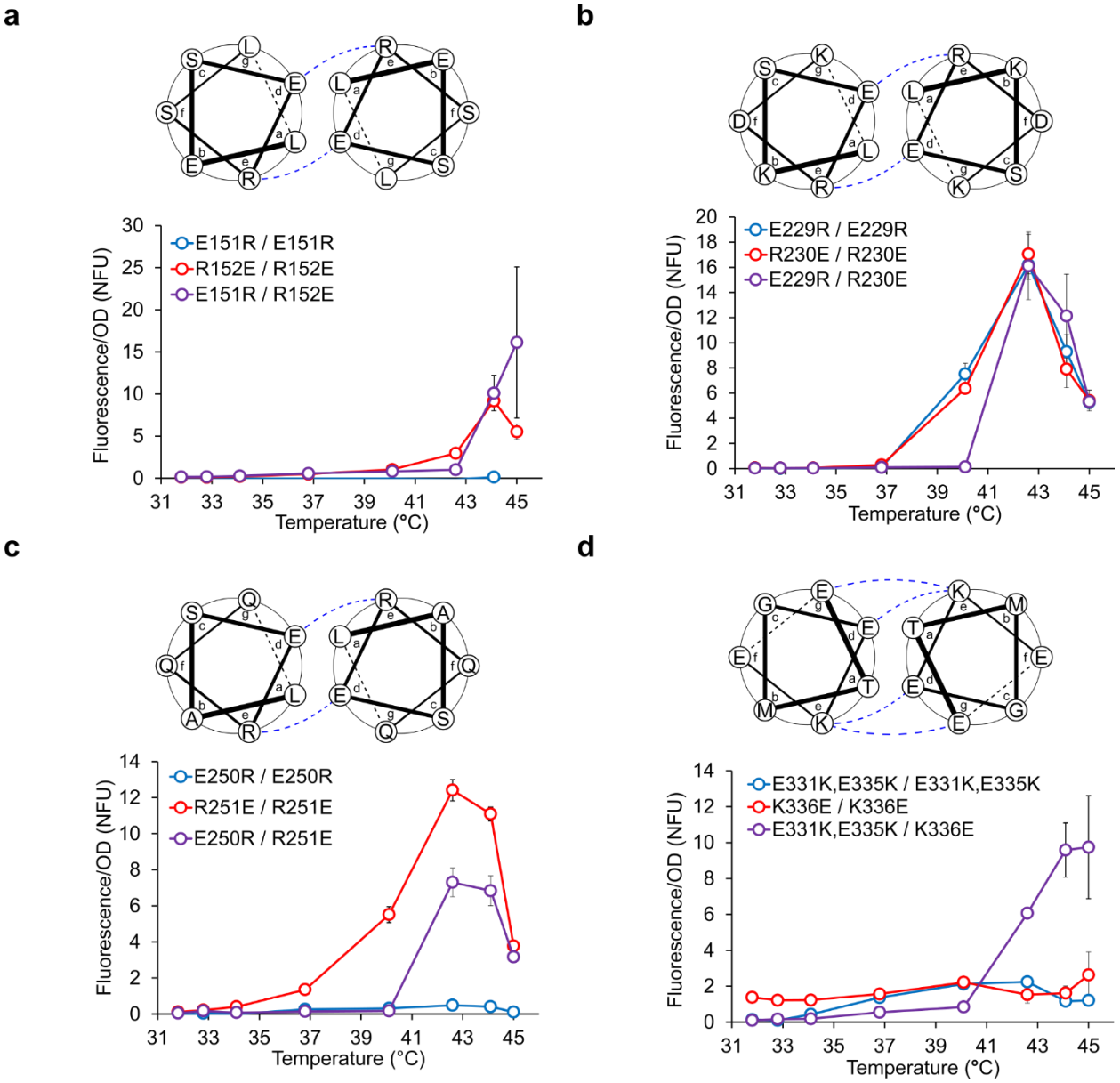

Supplementary Figure 4-S4: Screening of rationally designed mutant panel via bacterial thermal gene expression assay. Four positions in the TlpA coiled-coil were selected for mutagenesis based on the predicted similarity of their ionic interaction pattern to the G_1A/G_1B mutant pair according to the heptad repeat register prediction of Koski *et al*. The following mutations were examined: **a)** E151R and R152E **b)** E229R and R230E, **c)** E250R and R251E, and **d)** E331K/E335K and K336E. The predicted interaction pattern of the wild type protein is depicted (top), and the thermal GFP expression profile is reported (bottom). N = 3. The E229R/R230E and E250R/R251E pairs were selected for introduction into the TlpA-G_1A and G_1B variants. Error bars represent ± s.e.m.

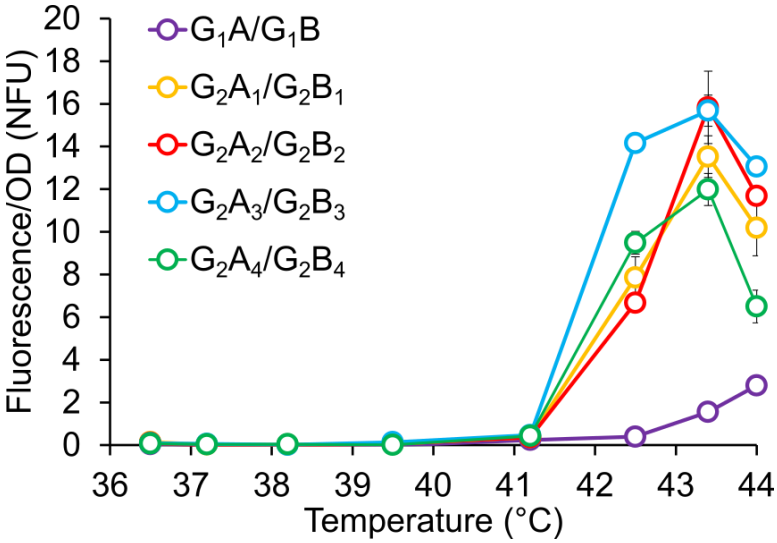

Supplementary Figure 4-S5: Thermal RFP expression profiles of the first and second-generation heterodimers shown in **Fig. 4-2c** (n = 3). Only the construct containing one copy of each heterodimeric strands are depicted because the X_nA/X_nB homodimeric construct were unable to propagate without accumulating deletion mutations in the TlpA promoters or fluorescent protein open reading frames. Error bars represent ± s.e.m.

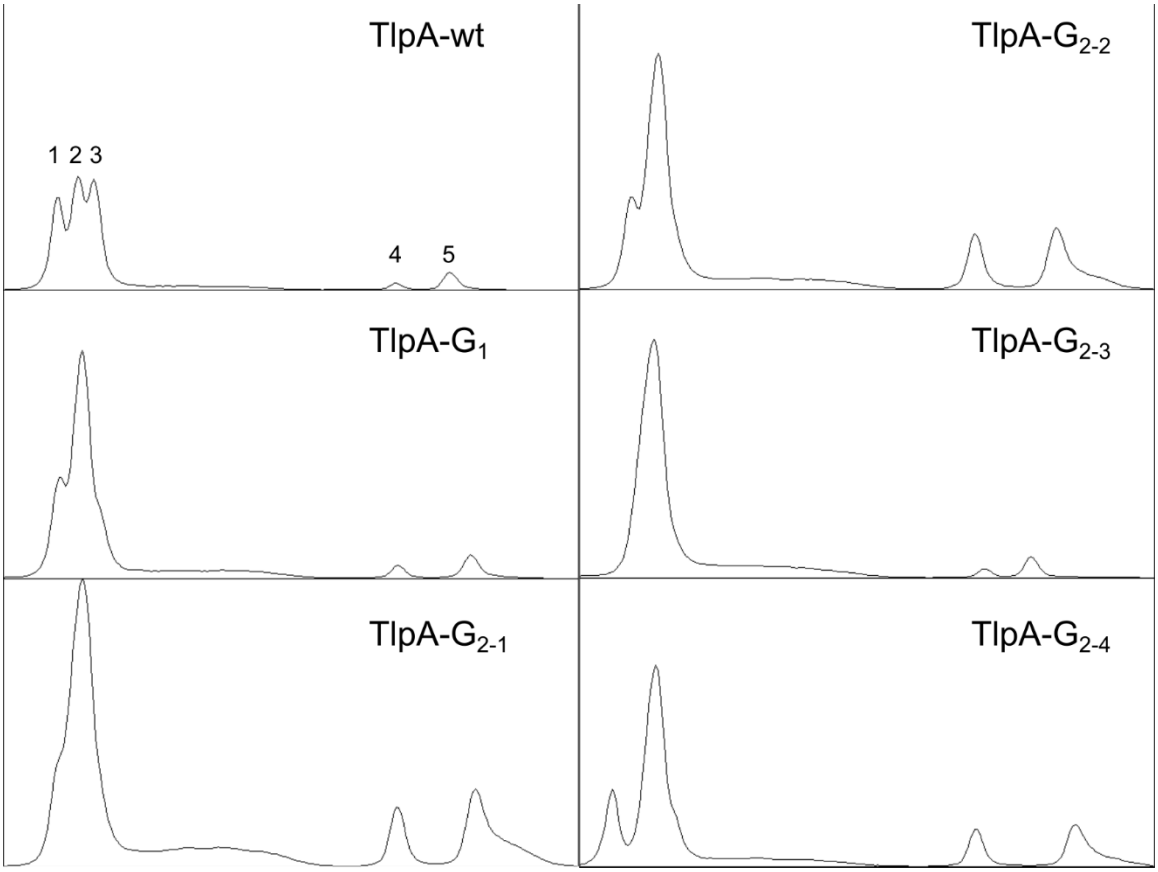

Supplementary Figure 4-S6: Western blot band intensity profiles of co-expressed full and truncated TlpA strands in **Fig. 4-3c**. Note that samples lacking a distinct band corresponding to the truncated homodimer (3), such as TlpA-G_1, nevertheless display higher band intensity for the truncated uncrosslinked strand (5) relative to the full-length uncrosslinked species (4), confirming that the lack of a low molecular weight homodimer at position 3 results from reduced homodimer affinity rather than full depletion of the light TlpA strand by heterodimer pairing. This is consistent with cationic and anionic TlpA variants having different homodimerization affinities at 37 °C.

a

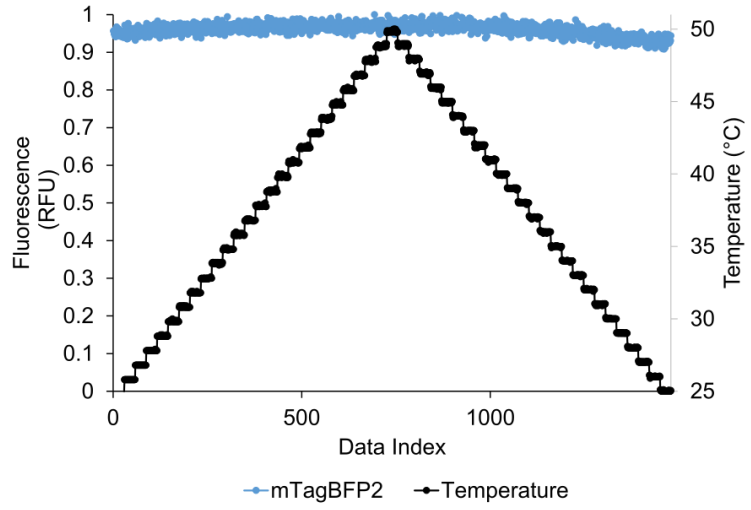
Fluorescence (RFU)
Temperature (°C)
Data Index
mTagBFP2
Temperature

b

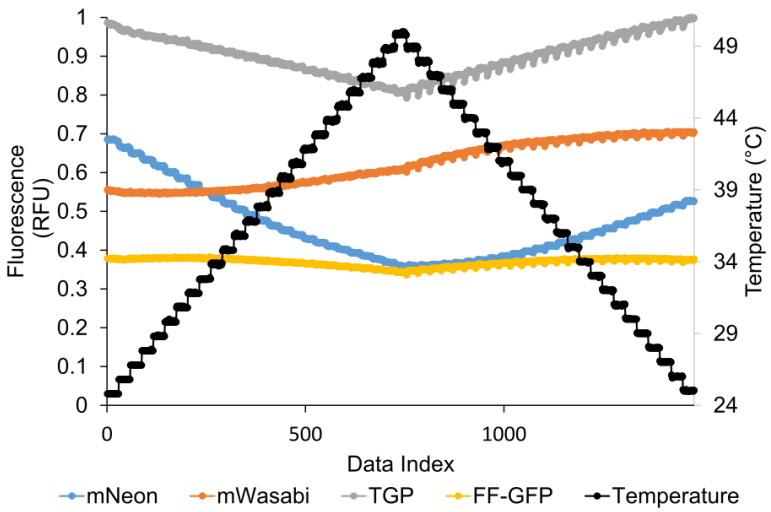
Fluorescence (RFU)
Temperature (°C)
Data Index
mNeon
mWasabi
TGP
FF-GFP
Temperature

c

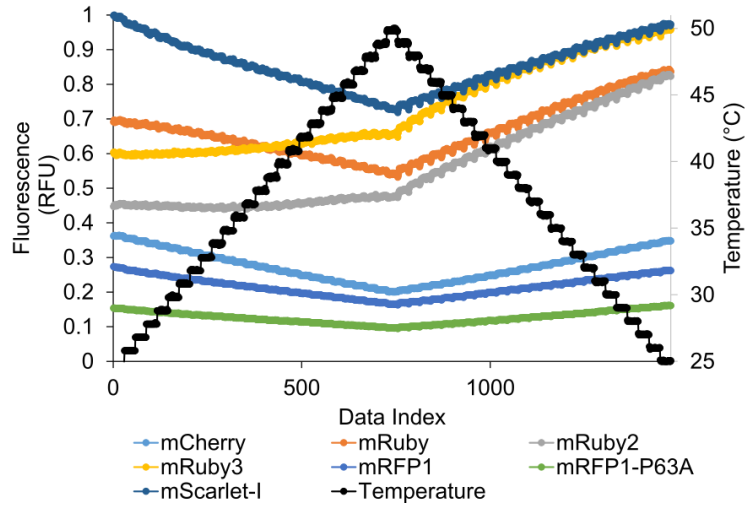
Fluorescence (RFU)
Temperature (°C)
Data Index
mCherry
mRuby
mRuby2
mRuby3
mRFP1
mRFP1-P63A
mScarlet-I
Temperature

Supplementary Figure 4-S7: Thermal stability of a panel of blue (**a**), green (**b**), and red (**c**) fluorescent proteins. Proteins were prepared in equimolar concentrations and their fluorescence was measured in an rtPCR thermocycler upon a thermal ramp from 25 °C to 50 °C and subsequent re-annealing to 25 °C, with readings taken continuously over 1 minute intervals. Signal intensity is normalized to the maximum for each given experiment. Because different filter sets were used for the three classes of proteins, relative brightness does not correlate between the red, green, and blue channels. While some proteins such as FF-GFP demonstrated more stable signal over the temperature range tested, the overall brightness was maximal in mScarlet-I and TGP. However, TGP demonstrated significant aggregation when expressed as an untagged cytosolic protein in mammalian cells so mScarlet-I was chosen as the reporter for subsequent experiments.

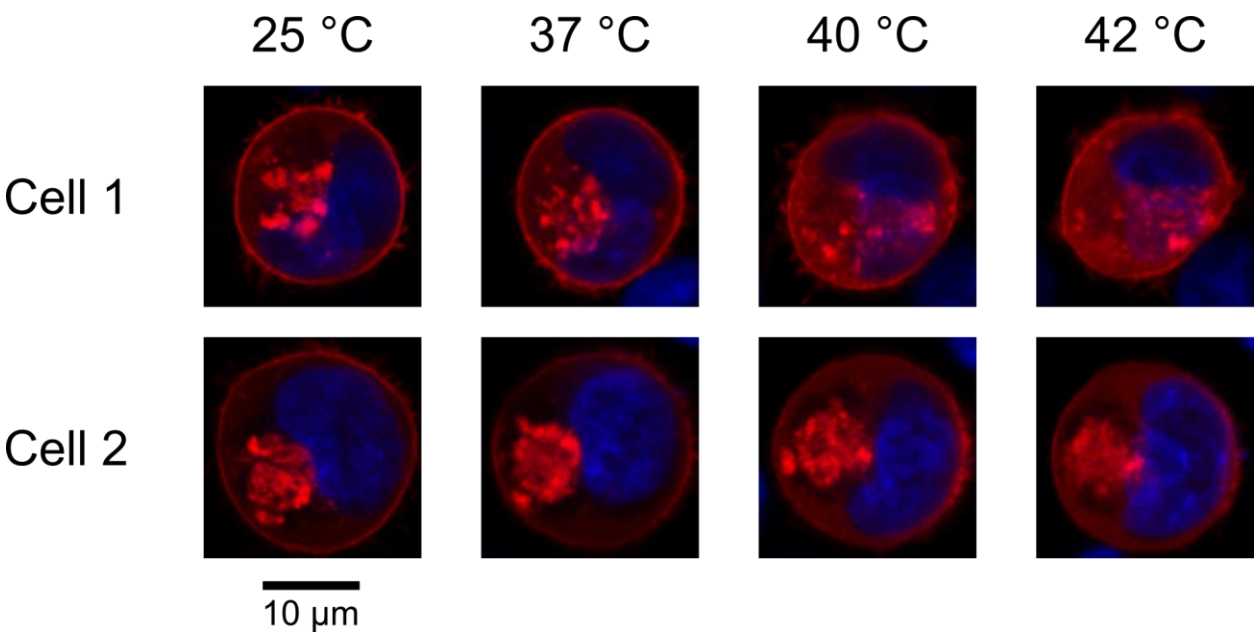

Supplementary Figure 4-S8: Additional replicates for TlpA membrane localization experiment in **Figure 4-4b**. Pixel intensity was normalized to the maximal per-image value.

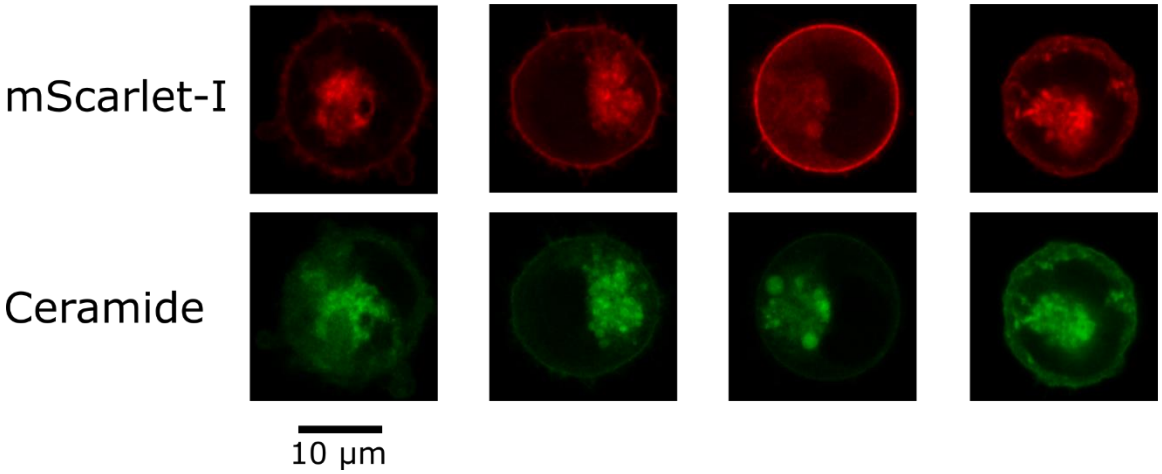

Supplementary Figure 4-S9: K562 cells transfected with the construct shown in **Fig. 4-4a** were stained with BODIPY-C5-Ceramide to label the Golgi transport pathway. Staining morphology was similar to the localization of the mScarlet-I TlpA cargo protein. Four representative cells are shown. Pixel intensity was normalized to the maximal per-image value.

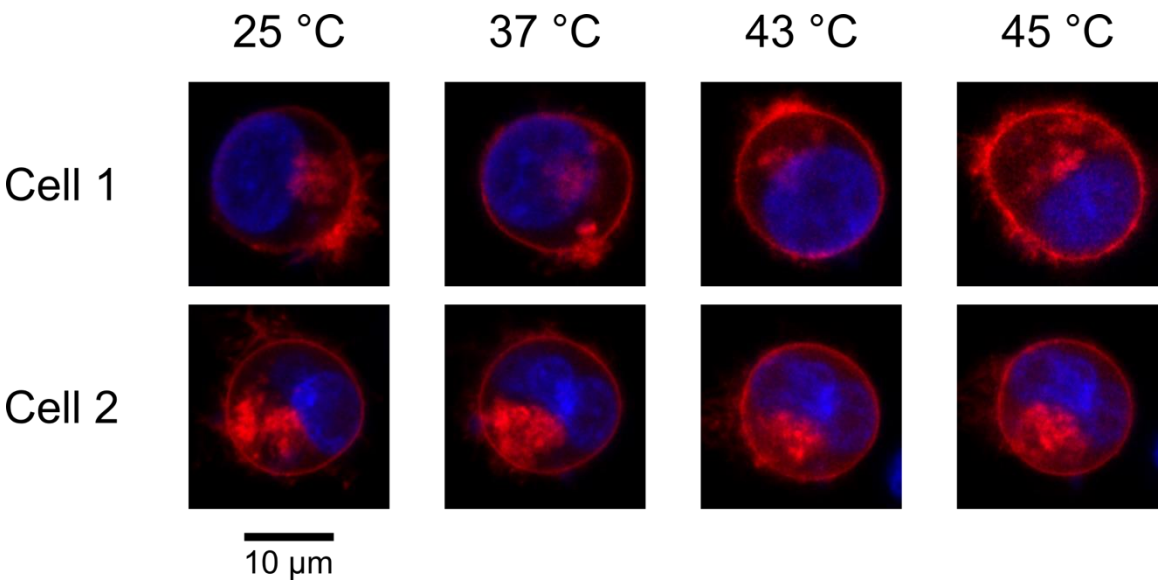

Supplementary Figure 4-S10: Additional replicates of K562 cells transfected with a construct bearing directly palmitoylated mScarlet-I, as in **Fig. 4-4d**. Robust membrane localization was observed up to 45 °C in most cells. Data presented are representative of two separate experiments. Pixel intensity was normalized to the maximal per-image value.

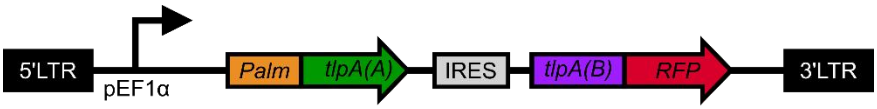
5'LTR
pEF1α
Palm
tlpA(A)
IRES
tlpA(B)
RFP
3'LTR

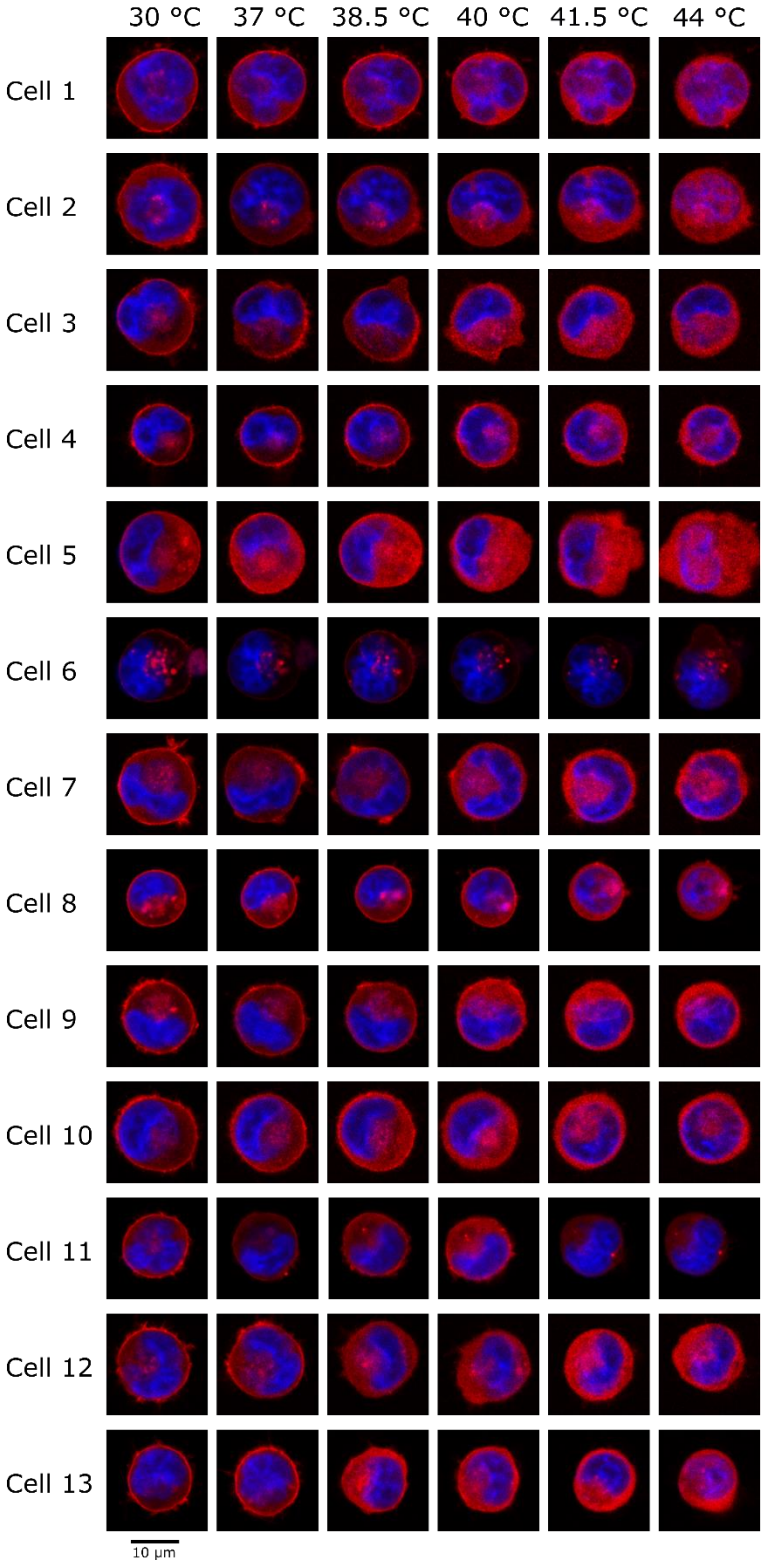
30 °C
37 °C
38.5 °C
40 °C
41.5 °C
44 °C
Cell 1
Cell 2
Cell 3
Cell 4
Cell 5
Cell 6
Cell 7
Cell 8
Cell 9
Cell 10
Cell 11
Cell 12
Cell 13
10 µm

Supplementary Figure 4-S11: Top: Lentiviral construct for membrane-localized RFP delivery containing nonhomologous $TlpA_{39}$-G_2A_3. Bottom: Fluorescence images at different temperatures of K562 cells lentivirally transduced with the nonhomologous TlpA-mediated membrane localization system. Pixel intensity was normalized to the maximal per-image value.

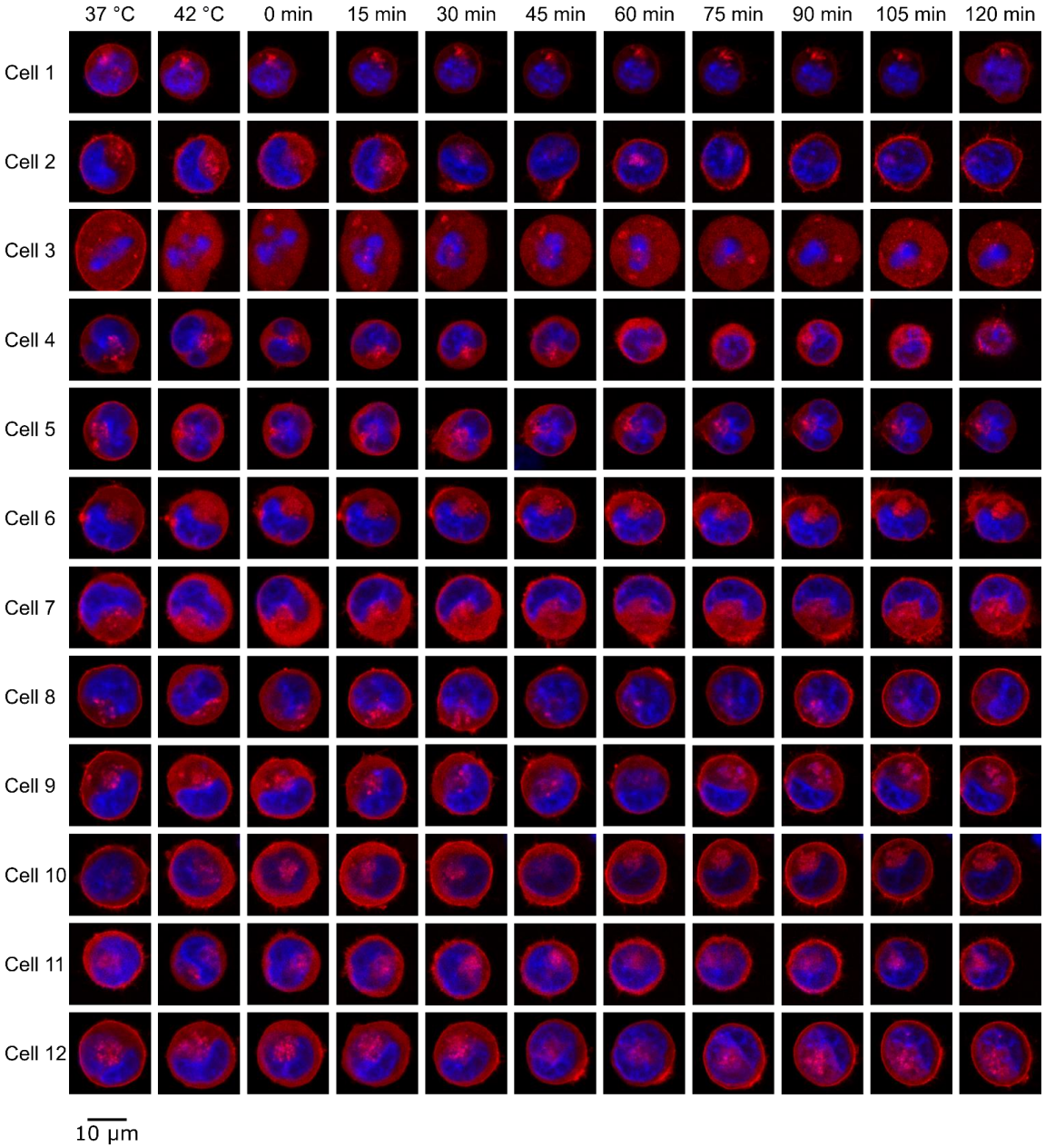

Supplementary Figure 4-S12: Replicates of the membrane delocalization reversibility assay shown in **Fig. 4-4g**. Pixel intensity was normalized to the maximal per-image value.

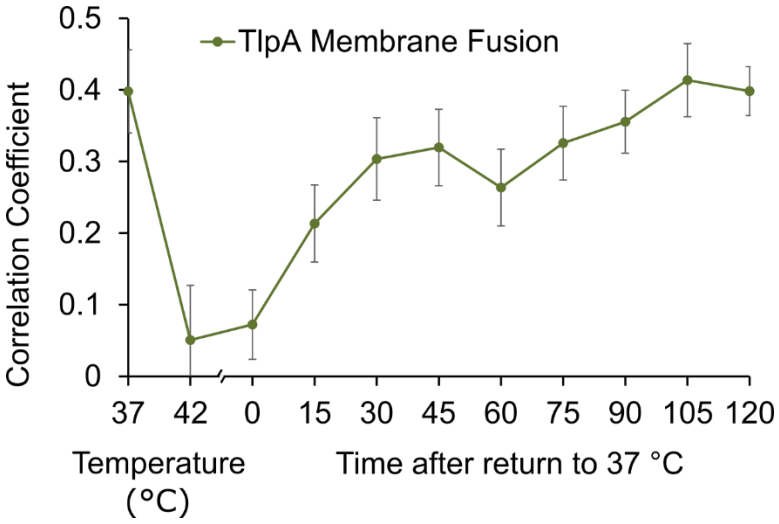

Supplementary Figure 4-S13: Reversibility of TlpA association in mammalian cells. K562 cells transduced with the lentiviral construct carrying the TlpA-mediated RFP membrane associated construct were assayed by confocal microscopy. Cells were imaged at 37 ℃, elevated to 42 ℃ for 5 minutes, and returned to 37 ℃, at which point they were imaged every 15 minutes. Error bars represent ± s.e.m.

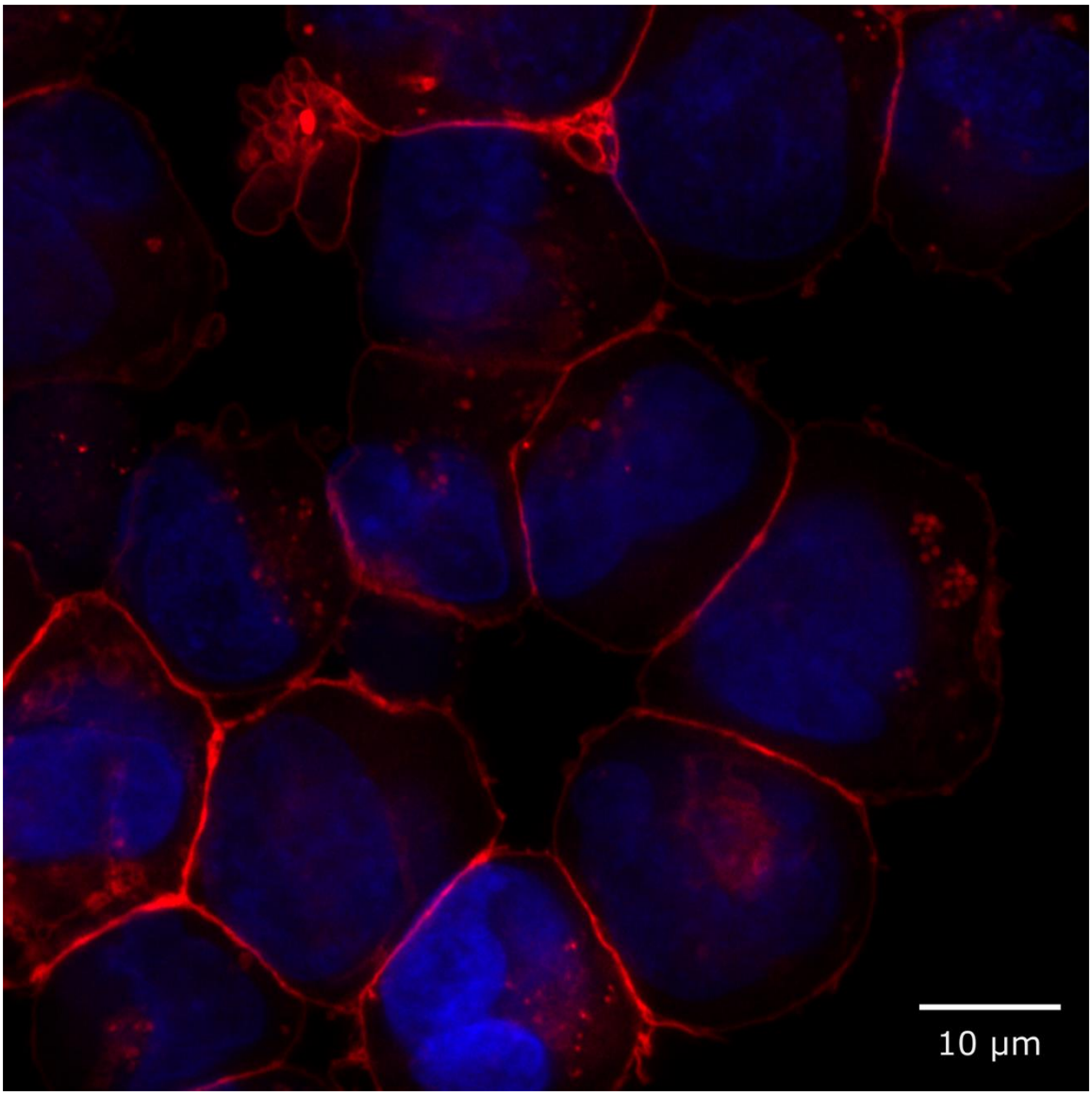

Supplementary Figure 4-S14: Confocal imaging of K562 cell line transduced with the lentiviral construct depicted in **Supplementary Figure 4-S11**. Cells were pelleted, deposited on a glass slide, sealed with a cover slip, and imaged on an LSM880 with a Plan-Apochromat 63x/1.4 Oil DIC M27 objective with oil immersion. Note that all cells, regardless of local cytoplasmic or membrane brightness, display visible RFP accumulation along the plasma membrane.

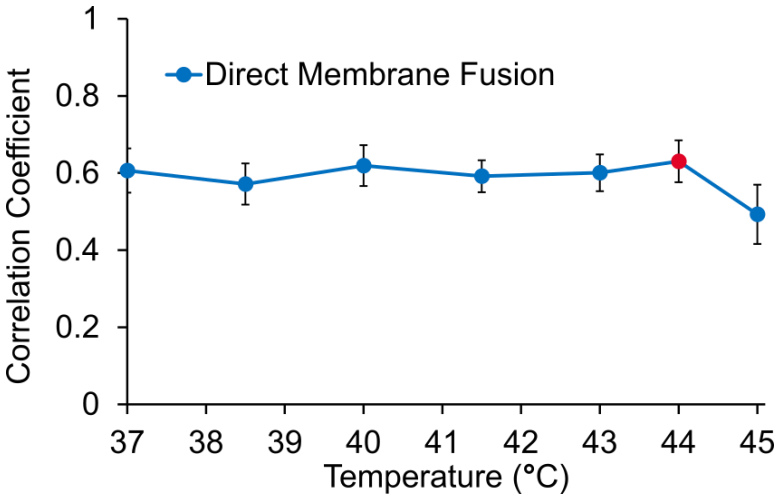

Supplementary Figure 4-S15: CellProfiler quantification of the two data sets contributing to the Direct Membrane Fusion curve in **Fig. 4-4f**. The data point acquired separately at 44 °C is highlighted in red.

Supplementary Table 4-T1: Second-generation TlpA mutants utilized in this study.

G_2A_1	E180R + E229R
G_2B_1	R179E + R230E
G_2A_2	E180R + R230E
G_2B_2	R179E + E229R
G_2A_3	E180R + E250R
G_2B_3	R179E + R251E
G_2A_4	E180R + R251E
G_2B_4	R179E + E250R

4.9: Supplementary References

(1) Ai, H.; Olenych, S. G.; Wong, P.; Davidson, M. W.; Campbell, R. E. Hue-Shifted Monomeric Variants of Clavularia Cyan Fluorescent Protein: Identification of the Molecular Determinants of Color and Applications in Fluorescence Imaging. *BMC Biol.* **2008**, *6*, 13. https://doi.org/10.1186/1741-7007-6-13.

(2) Shaner, N. C.; Campbell, R. E.; Steinbach, P. A.; Giepmans, B. N. G.; Palmer, A. E.; Tsien, R. Y. Improved Monomeric Red, Orange and Yellow Fluorescent Proteins Derived from Discosoma Sp. Red Fluorescent Protein. *Nat. Biotechnol.* **2004**, *22* (12), 1567–1572. https://doi.org/10.1038/nbt1037.

(3) Mastop, M.; Bindels, D. S.; Shaner, N. C.; Postma, M.; Gadella, T. W. J.; Goedhart, J. Characterization of a Spectrally Diverse Set of Fluorescent Proteins as FRET Acceptors for MTurquoise2. *Sci. Rep.* **2017**, *7* (1), 11999. https://doi.org/10.1038/s41598-017-12212-x.

(4) Piraner, D. I.; Abedi, M. H.; Moser, B. A.; Lee-Gosselin, A.; Shapiro, M. G. Tunable Thermal Bioswitches for in Vivo Control of Microbial Therapeutics. *Nat. Chem. Biol.* **2017**, *13* (1), 75–80. https://doi.org/10.1038/nchembio.2233.

(5) Grigoryan, G.; Keating, A. Structural Specificity in Coiled-Coil Interactions. *Curr. Opin. Struct. Biol.* **2008**, *18* (4), 477–483. https://doi.org/10.1016/j.sbi.2008.04.008.Structural.

(6) Carpenter, A. E.; Jones, T. R.; Lamprecht, M. R.; Clarke, C.; Kang, I. H.; Friman, O.; Guertin, D. A.; Chang, J. H.; Lindquist, R. A.; Moffat, J.; et al. CellProfiler: Image Analysis Software for Identifying and Quantifying Cell Phenotypes. *Genome Biol.* **2006**, *7* (10). https://doi.org/10.1186/gb-2006-7-10-r100.

Chapter 5

TOWARD HIGHLY SPECIFIC CONTROL OF BIOLOGICAL ACTIVITY USING TEMPERATURE-SENSITIVE PROTEIN TAGS

5.1: Toward Broader Implementations of TlpA-Based Bioswitches

Temperature-dependent bioswitches are poised to play a key role in a variety of applications of synthetic biology and biochemical engineering. In addition to their demonstrated ability to effect transcriptional control in response to both endogenous and exogenous thermal perturbations for cell therapy applications[1], they may also be utilized in industrial settings such as bacterial ghost production for vaccine development[2] and regulation of large-scale protein production[3]. The development of TlpA as a modular thermal bioswitch, as described in Chapter 4, enables a plethora of novel applications such as noninvasive control of protein function in living animals or potentially in cell-based human therapeutics. To realize this potential, TlpA-mediated thermal regulation must progress beyond proof-of-concept control of protein localization and demonstrate the ability to robustly modulate protein activity.

Biological systems for controlling protein-protein interactions via non-thermal mechanisms have been developed and may serve as templates for the expansion of the TlpA-controllable repertoire. Among the most famous of these strategies is the FKBP-based chemically inducible dimerization (CID) system developed by Crabtree and colleagues, which confers stable dimerization in the presence of the drug Rapamycin or derivatives thereof[4].

Subsequently, orthogonal CID systems based on ligands such as S-(+)-abscisic acid (ABA)[5] and a gibberellin derivative[6] have been developed. Recently, an antibody-based system for CID aimed at supporting cell therapy applications was introduced and may prove less immunogenic than previous technologies based on foreign proteins[7]. The broad implementation of CID for elucidating the behavior of biomolecules[8] has inspired optogenetic analogues such as the protein domain pairs Phy/PIF[9], FKF1/GI[10], and pMag/nMag[11], which combine the inducibility of their chemical predecessors with novel spatial and temporal axes of control. The wealth of previous work demonstrating the potential of inducible dimerization provides a roadmap along which the development of thermo-controllable dimerization agents can proceed. A variety of preliminary experiments have been conducted which may provide valuable insight for future TlpA engineering efforts.

5.2: Potential Approaches to High Resolution Structural Determination of TlpA

While previous work has suggested that TlpA consists of a globular N-terminal DNA binding domain and an elongated C-terminal coiled-coil[12,13], neither the atomic-resolution structure of the protein nor the mechanism for its uniquely sharp melting profile has been elucidated. Biological structure is intimately linked to function[14]; a detailed understanding of the atomic arrangement of TlpA may assist in both the determination of its enhanced switching profile relative to structurally similar proteins such as tropomysin[15,16], and also in the design of novel fusion proteins or orthogonally-dimerizing variants for multiplexed control.

The three main methods of biological structure determination are Nuclear Magnetic Resonance (NMR) spectroscopy, cryo-electron microscopy (Cryo-EM), and X-ray crystallography[17,18]. NMR structure determination is unique in its ability to sample proteins in their native aqueous environment[19]. However, the method is hampered by similarity in local chemical environments leading to chemical shift degeneracy in the spectra[20], which imposes a 30-50 kDa limit to the size of protein complexes amenable to this analysis. The TlpA dimer, consisting of two 41.5 kDa monomers, may be beyond the reach of this technique, particularly since the helical repeat structure of the coiled-coil results in high structural similarity along the length of the coil, further compressing the range of chemical environments and blending chemical shifts[21].

Cryo-EM, while reliant on flash freezing, also produces structures in a more native-like environment than crystallography. However, this method depends on imaging thousands of representative particles and averaging them to reconstruct an accurate high-resolution model. Previous low-resolution transmission electron microscopy images suggest that the length of TlpA may impart some conformational flexibility and that high expression of the protein may lead to packing into randomly arranged superstructures[22], both of which may impede reference averaging. A recent advance in Cryo-EM is the use of auxiliary scaffolding molecules to stabilize proteins structures while acting as fiducial markers for averaging, thereby enabling resolution of proteins which are too small to discern in isolation[23–25]. This methodology can be combined with the well-established capability of EM to visualize DNA origami superstructures[26]; in fact, intrinsically-disordered proteins of the nuclear pore have been characterized using this methodology, albeit at low resolution[27]. It is tempting to

imagine a DNA nanostructure containing the TlpA operator/promoter sequence implemented as a scaffold to stabilize protein conformation and enable EM-based structural characterization. Furthermore, if another DNA-binding domain can be attached to the C-terminus of TlpA, the protein could be stretched in an extended conformation inside of the DNA cage, thereby minimizing particle-to-particle structural variation.

The mainstay of structural biology to date has been X-ray crystallography. This method utilizes chemical perturbations administered in an empirically optimized fashion to generate proteinaceous crystals, the diffraction of which can be reconstructed into an electron density model. Crystallography can generate atomic resolution models of large proteins; notable solved structures include a 45 nm bundle consisting of 200-residue-helix fibrinogen monomers[28] (PDB 3GHG), an engineered 30 nm trimeric 300-residue coiled-coil containing a bacteriophage fiber gp26 protein[29] (PDB 4LIN), a similar 200-residue trimeric coiled-coil from phage HK620[30] (PDB 5BVZ), and the 40 nm dimeric coiled-coil tropomysin[31] (PDB 1C1G).

The crystallization process is poorly characterized and optimization varies on a protein-to-protein basis[32]. We have previously attempted to crystallize full length $TlpA^{1-371}$ and a truncated portion predicted to correspond to the coiled coil ($TlpA^{69-292}$) but all crystallization conditions from four 96-well screening plates (Hampton Research) produced non-crystalline aggregates. Challenges to crystallization included maintaining solubility at the requisite 10 mg/mL concentration, separation of the 80 kDa TlpA dimer from a 70 kDa contaminant protein which co-eluted with the desired product after histidine affinity purification, and

relatively low expression of the protein in soluble form (on the order of 1 mg per L of culture). A more focused structural study may employ tandem affinity, ion exchange, and size exclusion chromatography to obtain crystallographically pure samples of TlpA, and may also screen buffer conditions similar to those that enabled the previous determination of large alpha-helical proteins. Another potential strategy is fragment-based reconstruction in which the full length protein could be subdivided into smaller, potentially more soluble components. Finally, a DNA segment corresponding to the TlpA operator/promoter may bind to and stabilize the protein to enable crystallization[33].

5.3: Structural Inferences from Bioinformatics

In lieu of an atomic resolution structure, engineering efforts must be guided by bioinformatics and biochemical prediction. The current model of TlpA structure is guided by manual alignment of the primary amino acid sequence of the C-terminal domain with that of a prototypical coiled-coil heptad repeat motif[12], homology-based secondary structure prediction[13], circular dichroism spectroscopy suggesting high alpha-helical content[12,13,34], and the success of the rational introduction of heterodimerizing mutations informed by these predictions (Chapter 4). While these techniques hint at the general structural features of TlpA, they fail in two key respects. First, they do not provide insight into the mechanism of unique switching sharpness demonstrated by TlpA. Next, they fail to predict suitable locations for modification and functionalization of the protein.

The overall structure of TlpA is predicted to consist of an N-terminal globular domain followed by a C-terminal coiled coil, as predicted by manual annotation[12] and by three different software prediction packages. The linear structural prediction is summarized in **Fig. 5-1**, which aligns the secondary structure prediction assigned to TlpA by the software Jpred4[35] with the coiled-coil annotations ascribed by COILS[36], PairCoil2[37], and LOGICOIL[38], and also the manual annotation reported in the original publication by Koski et al[12]. It is evident that, while the C-terminal portion of the protein has a characteristic coiled-coil sequence as evidenced by its homology-based annotation, the per-residue register of the protein is not fully consistent with classical coiled-coil structure. The annotations from all three prediction servers demonstrate truncated heptad repeats and skips, which may indicate either failure of the homology-based algorithms to predict the possibility of the given residues at their respective positions in the coiled-coil structure, or deviations from the coiled-coil motif in the real protein structure. Such aberrations are interesting because they may influence the unique temperature-sensing abilities of TlpA. Previous studies have implicated breaks in predicted coiled-coil structure in influencing stability[39] or having other functional consequences such as binding of accessory proteins[40]. Understanding the fine details of the local structure at these positions is likely to aid in the elucidation of the thermo-sensing mechanism of this protein.

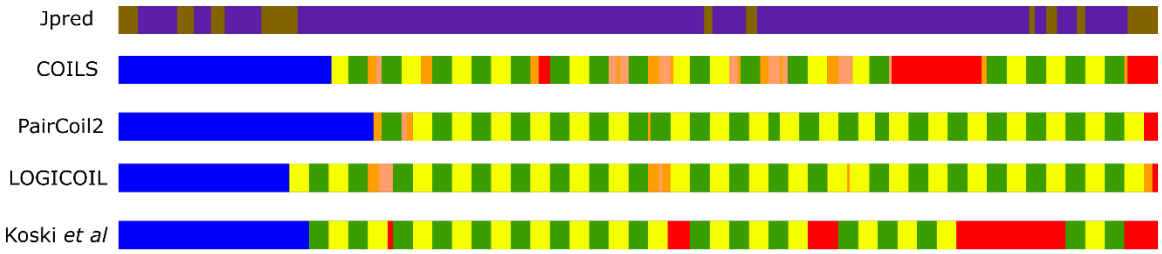

Figure 5-1: Sequence prediction annotation of TlpA. The primary sequence of TlpA is annotated by its predicted secondary structure (Jpred4, top) or for its predicted conformity to the characteristic heptad repeat pattern as described by the homology-based prediction software COILS, PairCoil2, and LOGICOIL, and as described in the initial report of the TlpA gene. In the Jpred4 prediction, brown segments indicate unstructured regions and purple blocks represent α-helices. In the coiled-coil predictions, the initial blue segments denote the N-terminal domain annotations and alternating yellow and green segments denote full heptad repeats. Orange and beige segments indicate regions which are predicted to be in a coiled-coil conformation but do not span for an entire heptad, indicating a shift in register. Red segments indicate predicted interruptions in the coiled-coil motif.

The initial discovery of TlpA was motivated in part by its sequence similarity to Tropomyosins (Tpm)s, which are elongated coiled-coil proteins (**Fig. 5-2a**) that regulate muscular contractions[41]. The sequence identity between TlpA and tropomyosins from various species ranges from 15.5 – 20.2%[12] and is clustered into three regions (**Fig. 5-2b**). While the sequence identity with TlpA is low even inside these clusters (**Supplementary Fig. 5-S1**), it is likely that the general structural heuristics of Tpm – that of an approximately 40 nm elongated parallel dimeric coiled-coil – are preserved in the TlpA protein. Both TlpA and Tropomyosin display relatively cooperative thermal unfolding compared to shorter leucine zippers, with 10%-90% dissociation ranges of 4-5 °C[34], 6-10 °C[16], and 20-25 °C[42] for TlpA, Tpm, and Fos/Jun, respectively. This length-dependent increase in coiled-coil folding cooperativity coincides with simulations predicting as such to a plateau of approximately 50 residues[43], a boundary between the lengths of Fos/Jun and the long TlpA and Tpm proteins. Nevertheless, the switching sharpness of TlpA is able to accommodate the transition between homeostatic temperature and mild hyperthermia (37 °C to 42 °C) whereas Tpm would be hard-pressed to unfold within this range, indicating that a structural feature unique to TlpA confers such cooperativity of unfolding. It is tempting to speculate that the break in predicted coiled-coil helical structure between two “coil islands” predicted by Koski et al, Jpred4, and COILS (**Fig. 5-1**) may enhance thermo-sensitivity, although these

predictions assign the interruptions to different positions within the primary sequence and as such are difficult to draw conclusions from. Interestingly, both TlpA and Tpm contain a singly cysteine residue which is known to be at the strand-strand interface, either from crystallographic data (Tpm) or its accessibility to $CuCl_2$-catalyzed oxidative crosslinking (TlpA). Interfacial cysteine residues have been implicated in redox sensing[44] and tropomyosin is known to be oxidized due to ROS formation upon myocardial infarction[45], which may inhibit its function in the sarcomere. While the function of the TlpA protein in its native context is unknown, and it is dispensable for the infectivity of the bacterium that carries it[46], the location of the *tlpA* gene in the virulence plasmid of Salmonella suggests a functional role in the host-pathogen interaction. It is known that Salmonella encounters an oxidative burst during macrophage uptake[47,48], suggesting a possible dual role for the protein in temperature and redox sensing. Previous work tracking TlpA auto-regulation demonstrated increased TlpA expression at 37 °C relative to 26 °C, and no increase in TlpA levels between 37 °C and 37 °C + 100 μM H_2O_2, but did not assay for expression at 26 °C +

H_2O_2 to determine if oxidative stress may sensitize the protein to de-repress its cognate promoter at a lower thermal threshold[46].

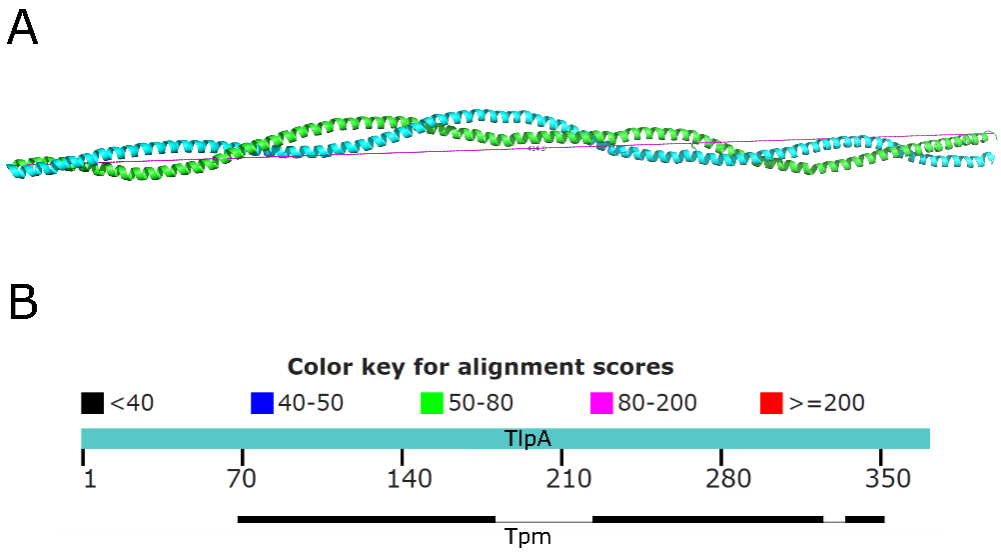

Figure 5-2: Structural similarity of TlpA to Tropomyosin. a) The crystal structure of an α-Tropomyosin dimer, a 284 residue 41 nm coiled-coil protein with relatively high homology to the TlpA coiled-coil domain (PDB 1C1G). **b**) Alignment of the TlpA protein sequence with that of α-Tropomyosin via the Basic Local Alignment Search Tool (BLAST).

5.4: Functional Inferences from Bioinformatics

The *tlpA* gene is found in the pSLT virulence plasmid of *Salmonella typhimurium*[46]. Previous characterization has demonstrated that the protein may be secreted by the bacterium via mechanisms other than direct cell-lysis, but it does not escape from endosomes into the host cytoplasm and as such this secretion may not be functionally relevant. Deletion of *tlpA* does not impact the infectivity or distribution of Salmonella during infection BALB/C murine hosts. It should be noted that this study did not measure the temperature of the mice after infection, and even direct LPS injection can produce only mild febrile response in BALB/C

mice[49], and that the thermal response is age-dependent[50]. As such, this result may not generalize to other scenarios of infection. However, the study did demonstrate TlpA activation upon transition from the external environment (26 °C) to host temperature (37 °C) *in vitro,* suggesting a functional role in this event. This thermal regime is lower than the biotechnological role for which we developed TlpA (sensation of hyperthermia above mammalian core temperature). This discrepancy may be explained by the low copy number of the pSLT virulence plasmid (1-2 plasmids per cell) compared to the >100 copy number of the ColE1-based plasmids utilized in our studies, in conjunction with the known concentration-dependence of the TlpA dissociation threshold[34].

Functional studies of TlpA have focused on its published role in auto-regulation via the 5'-3' promoter activity of the sequence directly upstream of the *tlpA* gene[34] (the TlpA operator/promoter). While TlpA auto-regulation certainly impacts the transcriptional set point of its own expression level, the fact that TlpA has not been deleted from the virulence plasmid suggests that it has an important functional role benefiting the bacteria, likely via additional TlpA-regulated components. One possibility is that TlpA binds to other cognate operator sequences within the virulence plasmid or in the bacterial chromosome; however, we were unable to find homologous sequences in either DNA molecule using BLAST alignment[51]. Another option is polycistronic regulation of one or more genes downstream of the TlpA repressor. We have demonstrated regulation in this fashion (see pThermeleon, Chapter 3). We have not performed experimental gene expression analysis of virulence plasmid-associated genes during infection, but the native context of TlpA positions the repressor upstream of another coding sequence in a manner which may enable polycistronic

regulation (**Fig. 5-3**). While the sequence between *tlpA* and the downstream ORF has not been annotated, we note that it contains an A/T-rich element (ATAAT) approximately 30 bp upstream of its start codon (roughly the same as the spacing between the TlpA promoter and the *tlpA* initiating methionine), implying that this UTR may itself function as a promoter. The downstream gene has high homology to YacC, a poorly-characterized periplasmic protein with unknown relevance to virulence[52]. Differential gene expression analysis of this YacC homologue upon heat shock can determine if the upstream TlpA regulates it in a polycistronic fashion. An alternative and intriguing possibility for the role of the TlpA system stems from our discovery that TlpA can function as a bidirectional promoter (Chapter 3, **Fig. 3-S2**). The reverse-complemented sequence upstream of the TlpA promoter contains an open reading frame in the correct orientation to be transcribed by reverse activity of the TlpA promoter (**Fig. 5-3**). Excitingly, the protein sequence of this gene bears high homology to YadA, an adhesin which serves as an essential virulence factor in several strains of *Yersinia*[53]. Future work may expand on the role of TlpA in regulating *Salmonella* infectivity, and particularly its putative function as a regulator of the native *yadA* homologue.

Figure 5-3: Endogenous sequence context of TlpA. Local sequence annotation of the *tlpA* locus on the pSLT virulence plasmid of *Salmonella typhimurium* (NCBI RefSeq NC_003277.1, bp 38,923 – 41,287).

5.5: Inferences from Structural and Functional Activity Assays

The TlpA-based platform for controlling gene expression, described in Chapter 3, can be utilized as a tool to investigate the functional outcomes of modifications to the TlpA repressor. While the requirement for an intact DNA binding domain limits the scope or perturbations accessible at the N-terminus of the protein, internal and C-terminal modifications may be freely examined. Comparison of reporter gene activation between circuits carrying the wild type *tlpA* gene and its derivatives can inform the role of some structural features, as well as the tolerance of the protein to modification at particular locations.

Analysis of deletions at the C-terminus demonstrates that, surprisingly, TlpA is highly sensitive to even small truncations in this region. **Fig. 5-4a** shows that even a 13 residue truncation, predicted by Koski et al to be outside of the coiled-coil region[12], greatly disrupts repression and cooperative dissociation of the repressor. The sensitivity of the TlpA C-terminus to modification is corroborated in **Fig. 5-4b** and **5-4c**, in which fusion of the anionic triplet Asp-Glu-Asp (DED) or a strongly cationic sequence (SV40 NLS) also results in disruption of activity. The addition of a short SLGSGS linker partially alleviates disruption, suggesting that proximity to the C-terminus is a factor in destabilization (**Fig. 5-4c**). This impediment of functionality is likely due to Coulombic repulsion between the like-charged residues symmetrically apposed between the two strands; partial charge neutralization via fusion of the cationic NLS sequence to the anionic DED motif alleviates the disruptive effect and even appears to stabilize the complex, possibly via charge cross-complementation (**Fig.**

5-4d). To examine the possibility of fusing protein domains to the TlpA C-terminus without inhibiting its function, we opted to screen hexahistidine tags as mild disruptive elements separated from the C-terminal residue of TlpA by a panel of flexible linkers (**Fig. 5-4e**). Three and five-residue linkers did not confer any stabilization over the no-linker condition. The fifteen-mer linker did alleviate destabilization at temperatures above 34.1 °C but appeared slightly de-repressed compared to unmodified TlpA at lower temperatures. In contrast, the 25-residue linker alleviated the disruptive effect of the His_6 tag at all temperatures tested. The L25 linker permits TlpA to tolerate the presence of a larger and more sterically hindered domain, the 40 kDa globular protein MBP (**Fig. 5-4f**). Similarly, while shorter linkers are unable to restore cooperative activation to C-terminal fusions of the SV40 NLS (**Fig. 5-4g**), the L25 linker restores tolerance for this modification, which even confers additional stability through an unexplored mechanism (**Fig. 5-4h**). The a79 NLS[54], which contains fewer charged residues, is also tolerated with the L25 linker but not with a shorter spacing region (**Fig. 5-4i**). Moving forward, a 25-residue flexible linker should be the default choice for fusing novel protein domains to the TlpA C-terminus when the application permits such an extended configuration.

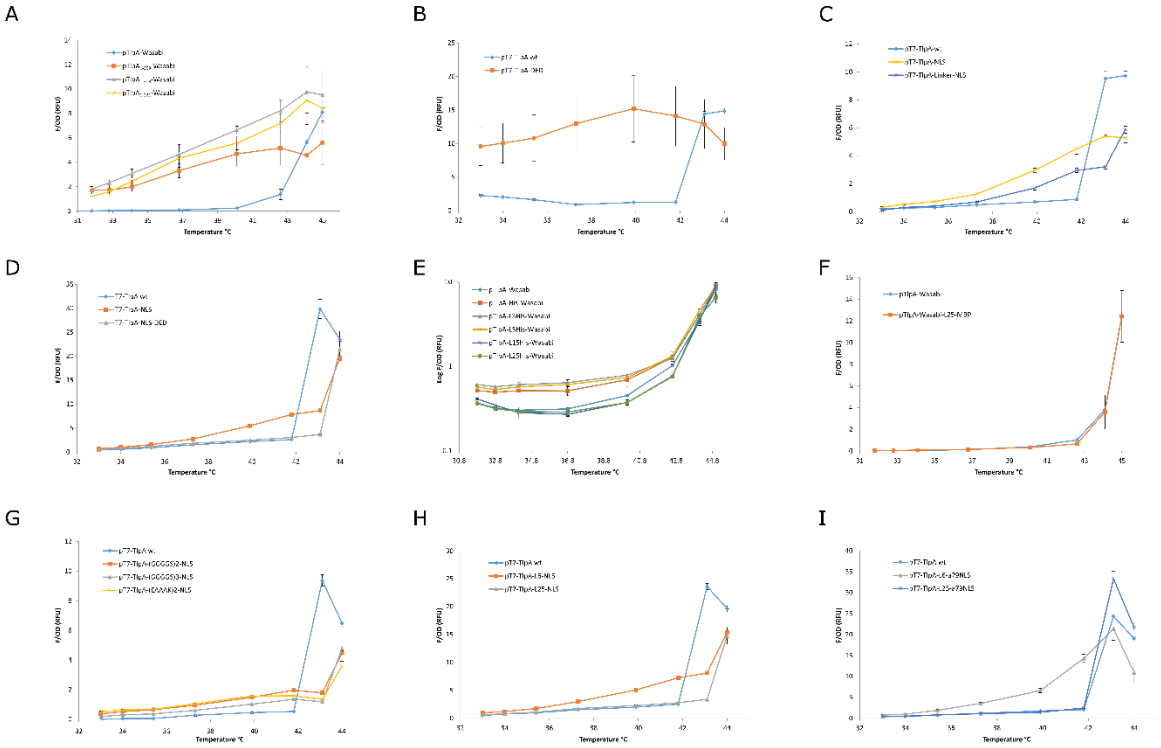

Figure 5-4: Tolerance of TlpA to Structural Perturbations. a) Thermal gene expression of bacteria carrying the standard TlpA-gated GFP expression reporter plasmid reporter in Chapter 3. The wild type TlpA demonstrates cooperative unbinding at a critical temperature centered around 44 °C as described previously, while truncations of the C-terminal 13, 63, or 150 residues (corresponding to the Koski *et al* annotations of the unstructured tail, third coiled-coil segment, and large inter-coil interruption, respectively). All truncations result in repressors displaying poor repression and non-cooperative thermal transitions. **b**) Fusion of TlpA to an Asp-Glu-Asp sequence at its C-terminus significantly inhibits the ability of the protein to repress its cognate promoter. **c**) Fusion of TlpA the SV40 NLS (PKKKRKV), either directly at the C-terminus or spaced by a short SLGSGS linker, promotes transcriptional leakage and abrogates the cooperativity of TlpA unfolding. **d**) Addition of an acidic Asp-Glu-Asp sequence to the TlpA-SLGSGS-NLS construct, separated from the NLS by a Gly-Ser liner, appears to stabilize TlpA repression, perhaps via associating with the basic charges on the partner TlpA strand. **e**) Thermal expression profile of TlpA variants with C-terminal His_6 tags spaced fused directly at the C-terminus or with linkers GGS (L3), GGGGS (L5), $(GGGGS)_3$ (L15), or $(GGGGS)_5$ (L25). While short linkers result in tag-induced inhibition of promoter repression, the L15 linker stabilizes the dimer at temperatures above 34.1 °C and the L25 linker stabilizes the tag at all temperatures. **f**) Thermal expression profile of TlpA compared to a variant with the large globular protein MBP fused at the C-terminus via the $(GGGGS)_5$ linker reveals no significant alteration in repression. **g**) TlpA variants fused to the SV40 NLS at the C-terminus, spaced by intermediate-length flexible linkers $(GGGGS)_2$ or $(GGGGS)_3$ or with the rigid α-helical linker $(EAAAK)_2$. The intermediate linkers are unable to rescue TlpA repression and cooperativity. **h**) Thermal expression profile of wild type TlpA compared to variants with the SV40 NLS fused at the C-terminus via a GGGGS or $(GGGGS)_5$ linker. The long flexible linker is able to tolerize the TlpA protein to the presence of the cationic NLS. **i**) Fusion of the alternative NLS a79 to the C-terminus of TlpA is disruptive when spaced by a SLGSGS but cooperativity and repression is recovered when separated by the L25 linker. *Note that panels **b**, **c**, **d**, **g**, **h**, and **i** utilize an alternative circuit construction in which a T7 promoter is positioned 5' to the TlpA operator/promoter.* All plots represent the mean of N = 3 +/- SEM.

In contrast to the C-terminus, N-terminal analysis of TlpA is difficult via a transcriptional readout due to the required presence of the DNA binding domain in this region. Previous analysis by Hurme et al[13] demonstrated via gel shift that internal deletions in the non-coiled-coil N-terminal domain (TlpA Δ31-43 and Δ61-43) result in loss of DNA binding whereas, surprisingly, the Δ165-320 mutant retained DNA binding (although temperature-dependence was not tested). We tested if the protein is able to accommodate the charged SV40 NLS as an insert between the putative DNA binding domain (residues 1-68) and the coiled-coil domain (residues 69-371) and found that this modification was not tolerated (**Fig. 5-5a**). Surprisingly, circular dichroism spectroscopy analysis of the TlpA coiled coil domain demonstrated that while fusion of a DED tag to the C-terminus destabilizes the protein, such modification of the N-terminus is much better tolerated (**Fig. 5-5b**). Notably, the thermal transition of the C-terminally-tagged variant remains switch-like, albeit with a loss of cooperativity. This suggests that the genetic repression assay may suffer from a minimal threshold of binding ability below which the protein fails to activate in a switch-like manner regardless of the behavior of its coiled-coil domain. Additionally, the near-wild type melting profile of the N-terminally DED-tagged coiled-coil domain suggests that the junction between the DNA binding domain and the coiled-coil domain strongly influences the ability of the protein to repress its promoter and that this geometry, rather than the thermostability of the cold-coil, may be disrupted in the N-terminal NLS fusion shown in **Fig. 5-5a**. To further investigate the effects of N-terminal modification, we swapped the DNA binding domain of TlpA for that of the Tet repressor, another dimerization-dependent DNA binding protein, and assayed its ability to repress the cognate TetR promoter. We fused the TetR DBD at various points within the N-terminal domain of TlpA (**Fig. 5-5c**). All variants

generated a similar reporter gene expression curve regardless of the fusion site chosen. Comparison of one variant to a repressor consisting of only the TetR DNA binding domain with no dedicated dimerization domain (**Fig. 5-5d**) also showed a similar curve, suggesting that fusion of TlpA provides no stabilization beyond the endogenous propensity of the TetR DBD to dimerize at high concentrations. The DNA specificity of coiled-coil DNA-binding proteins has previously been redirected via fusion of the λ cI DBD to the constitutive coiled-coil GCN4[55]. However, in our bacterial thermal transcriptional assay, constructs with cI DBD-TlpA fusion repressors (and also the cI DBD-GCN4 control) demonstrated no fluorescence above background at any temperature (**Fig. 5-5e**). It should be noted that, in contrast to its use in the literature to gate expression from the lambda P_R promoter[56], we utilized these constructs in the context of the pTcI-Wasabi backbone (Chapter 3) in which expression is driven by the strong P_R/P_L hybrid promoter. Unlike in the case of the isolated P_R, we are unable to clone a stable P_R/P_L-containing plasmid in the absence of a repressor, suggesting that the strong expression from this promoter represents a significant metabolic burden and selects for deletion variants. While the Sanger sequencing chromatograms of the TlpA and GCN4 cI-DBD fusion variants did not indicate any deletions or mutations in the promoter, reporter gene, or repressor, it cannot be ruled out that such an alteration occurred during the course of expression. Moving the chimeric cI/TlpA fusion genes into the literature-reported vector may represent a viable approach to assaying the effects of N-terminal TlpA modifications and mapping this boundary of the TlpA coiled-coil domain.

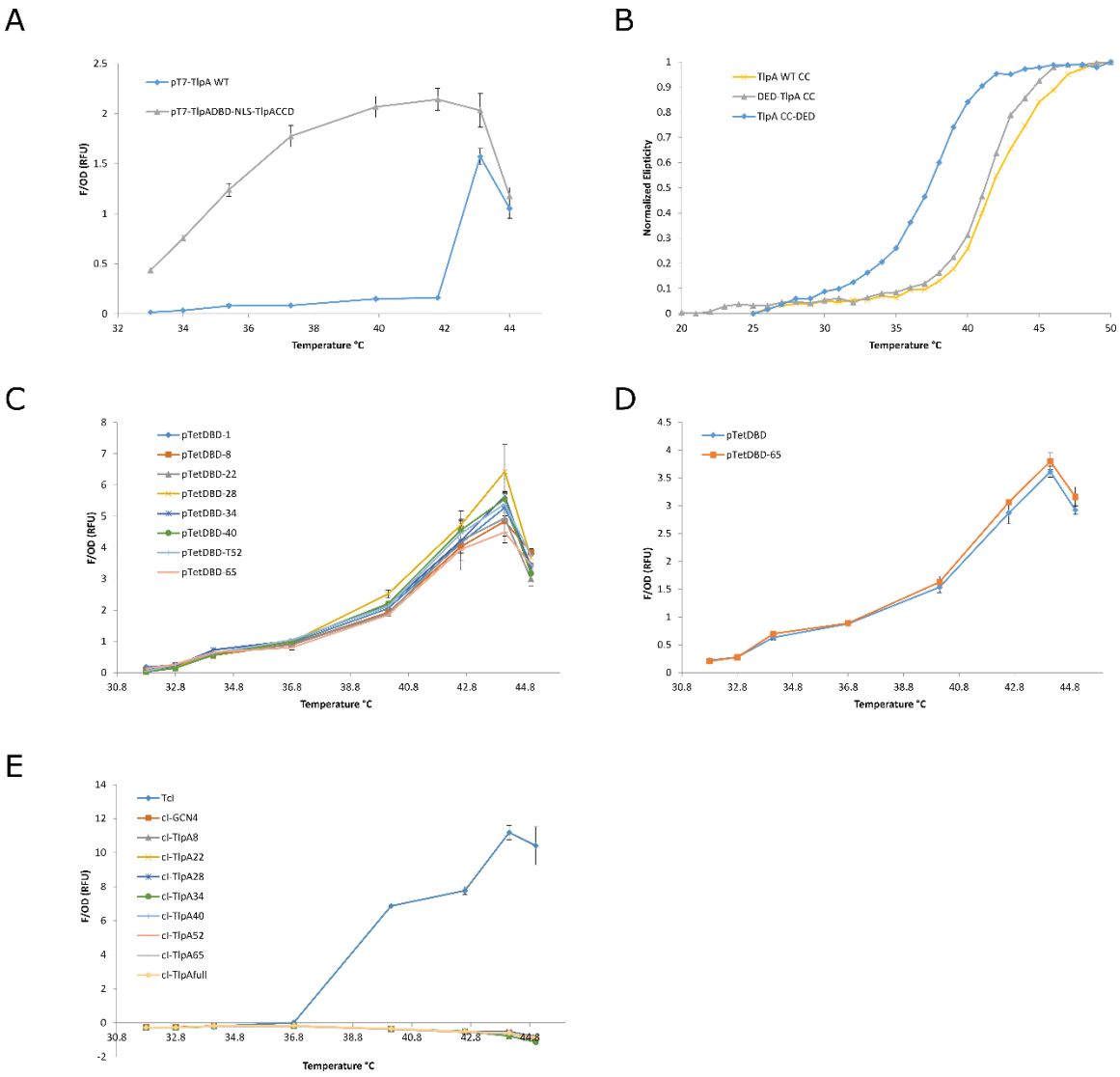

Figure 5-5: N-terminal modification of TlpA. a) Thermal gene expression profile of a TlpA promoter-gated GFP in the presence of wild type TlpA or a variant in which the SV40 NLS is inserted between the putative DNA binding domain and coiled-coil domains (C-terminal to residue 68). **b**) Circular dichroism melting plots tracking ellipticity at 222 nm of the putative TlpA coiled-coil domain (residues 69-359) and variants with the cationic Asp-Glu-Asp tag fused at the N or C-terminus. **c**) Thermal gene expression profiles of a tetA promoter-gated GFP in the presence of chimeric proteins consisting of the TetR DNA binding domain (residues 1-127) fused to TlpA at the indicated positions, spaced by a Gly-Thr linker. **d**) Thermal gene expression profile of ptetA-GFP gated by the TetR-TlpA chimera fused as position 8 within the TlpA DNA binding domain, or by the TetR DNA binding domain in isolation. **e**) Thermal gene expression profile of GFP driven by the tandem pR/pL promoter gated by TcI or a panel of cI DNA binding domain fusions to TlpA variants or to the GCN4 coiled-coil. All gene expression plots represent the mean of N = 3 +/- SEM.

Internal modifications within the TlpA coiled-coil also impact its function. One of the most interesting residues in the protein is its single cysteine, C318, which is predicted to reside at the strand-to-strand interface between TlpA monomers and, as shown in Chapter 4, can be oxidized to form a disulfide. CD Spectroscopic analysis shows that mutation of this residue to a serine destabilizes the coiled-coil, resulting in a lower T_m and a broader transition (**Fig. 5-6a**). Correspondingly, installment of this mutation into the reporter gene regulator circuit results in a significant downshift of the thermal transition (**Fig. 5-6b**). Interestingly, mutating this residue to an alanine, which lacks the terminal sulfhydryl or hydroxyl group, results in an intermediate phenotype, suggesting that while the serine hydroxyls may provide a steric clash leading to destabilization, the sulfhydryls of the cysteine pair may have a stabilizing effect. This stabilization could be due either to disulfide bond formation[57] or from enhanced van der Waals packing[58] of this residue. The lack of a significant crosslinked population in the absence of $CuCl_2$ (Chapter 4) suggests that, at least *in vitro*, the latter effect is dominant. Introduction of oxidants or reductants into the bacterial media during heat shock may elucidate the influence of redox sensing by C318 *in vivo*. Other interesting phenotypes can be observed using circular dichroism spectroscopy or *in situ* control of gene expression. Several residues including glutamate tend to be over-represented at the N-termini of alpha helices and act to stabilize the fold[59]; as such, we investigated if E67, falling just anterior to our annotation of the coiled-coil domain, could influence cooperative unbinding. **Fig. 5-6c** demonstrates little difference in the melting curves of our putative coiled-coil domain fragment ($TlpA_{69-359}$) and the same protein with an N-terminal $V_{66}E_{67}V_{68}$ triplet derived from the preceding N-terminal domain. However, this approach may be useful for future investigation; other residues such as proline are also enriched near the N-termini of helices

and the stretch of $TlpA_{60-65}$ contains two proline residues; comparative stability analysis of fragments containing one or both of these residues may aid in elucidation of the N-terminal helix cap (and thus a suitable fusion point at the N-terminus of the coiled-coil). Figure **5-6C** also shows that a sub-fragment of the coiled-coil domain truncated anterior to the interruption predicted by the COILS server (see **Fig. 5-1**) maintains its ability to unfold cooperatively, albeit at a lower thermal threshold and with weaker cooperativity than its intact counterpart. This fragment may be amenable to stabilization via random mutagenesis and selection (Chapter 3) for use as a fusion tag, wherein its shorter length relative to the wild type TlpA may confer advantages such as conforming to viral packaging limits and decreasing the probability of inducing a penalty to protein folding or expression. The weaker cooperativity of the fragment would also need to be repaired. As demonstrated in **Fig. 3-2B**, error-prone PCR variants of TlpA display a range of switching sharpness phenotypes, suggesting that this property is, like the T_m, amenable to optimization. Furthermore, a small sub-screen of alanine mutants targeting histidine residues predicted by COILS to pack into the strand-strand interface (**Fig. 5-6d**) revealed variant H254A, which demonstrated activation over an apparent span of only 1.5 °C. It would be interesting to determine if installment of this mutation into the truncated $TlpA_{69-276}$ fragment could counteract its apparent length-dependent penalty to switching sharpness. Much work remains to be done in elucidating the sequence determinants of TlpA behavior using rational truncations and mutagenesis. However, without structural data to guide engineering, such information will be invaluable in generating well-behaving TlpA fusions and even the limited scope of the work performed thus far has yielded useful variants for future applications.

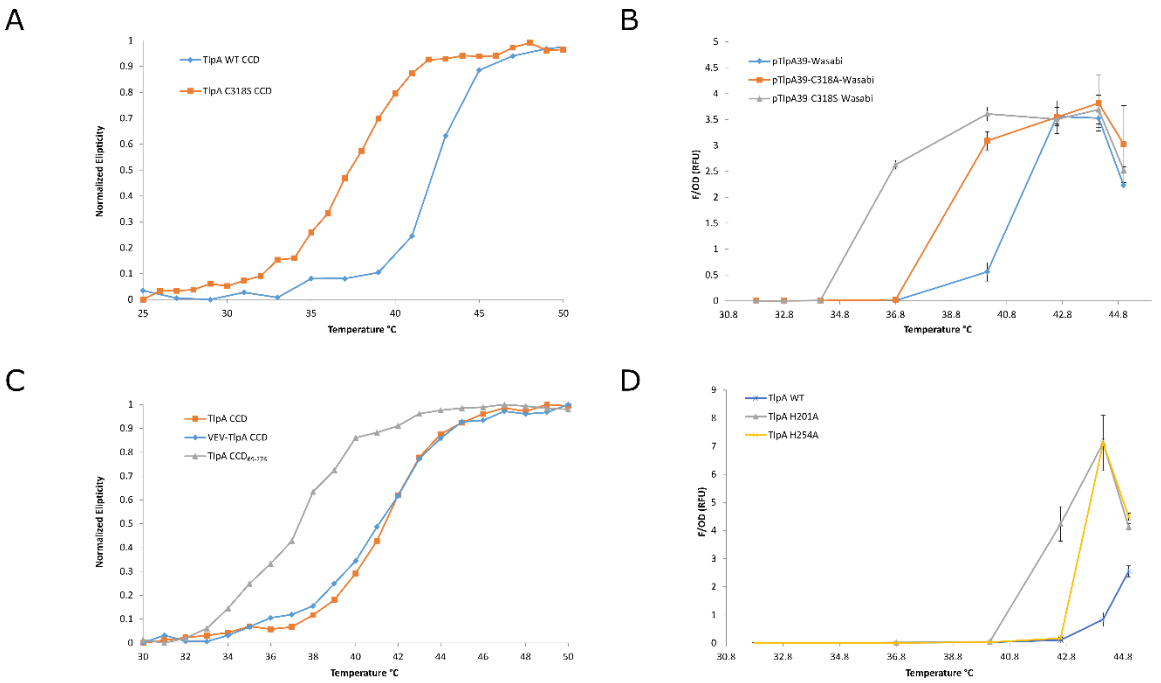

Figure 5-6: Internal modifications of TlpA a) Circular dichroism melting plots tracking ellipticity at 222 nm of the wild type TlpA coiled-coil fragment (residues 69-359) or a variant with the C318S mutation. **b**) Thermal gene expression profile of GFP driven by the pTlpA promoter in the presence of $TlpA_{39}$ or C318 mutants to alanine or cysteine. **c**) Circular dichroism melting plots tracking ellipticity at 222 nm of the TlpA coiled-coil fragment or structural derivatives VEV-TlpA CCD (TlpA residues 66-359) and the TlpA $_{69\text{-}276}$ variant corresponding to the sequence N-terminal to the large coiled-coil interruption predicted by Koski et al. **d**) Thermal gene expression profiles of pTlpA-driven GFP gated by wild type TlpA or core histidine mutants H201A and H254A. Note the unusually sharp transition displayed by the H254A variant. All gene expression plots represent the mean of N = 3 +/- SEM.

5.6: Local Structural Deformation and Activity Modulation

Many of the potential applications for TlpA as a modular bioswitch rely on the ability to fuse one or more proteins of interest to the coiled-coil dimer. To effectively realize this strategy it is important to understand the dynamics of the fusion points; i.e. the behavior of the N or C-termini of the TlpA strands. Coiled-coil denaturation often initiates via “fraying” from the ends of the molecule[60], indicating that local perturbations in these regions precedes global conformational shifts. This local variation in melting threshold has implications for designing

functional protein fusions to TlpA; for example, co-positioning of an enzyme with a corresponding inhibitor will be dependent on the thermal stability of its terminus of fusion rather than on the overall stability of the TlpA dimer or of the other terminus roughly 40 nm distant (**Fig. 5-7a**). Modifications to the termini of the coiled-coil, such as installation of residues that effectively cap the electric dipoles of the helices, may mitigate the fraying effect[61]. The methods described in the preceding section, while useful in assaying the overall behavior of the thermoswitch, are unable to provide information on about this specific aspect of denaturation. Circular dichroism spectroscopy reports on the overall α-helical content of the protein but cannot differentiate between local transitions at the termini vs. internal locations. The shallow linear increase in ellipticity with rising temperature that occurs prior to the main melting transition of coiled-coils is thought to result from fraying at the termini[62], but the technique cannot pinpoint the location at which this fraying occurs. In contrast to CD spectroscopy, the *in vivo* assay for TlpA-mediated transcriptional control is intrinsically dependent on the local stability of TlpA at the N-terminus; however, the dimer-stabilizing effects of DNA binding[63] are likely to mask local fraying (and may account for the lower pre-transition slope demonstrated by the pTlpA-Wasabi circuit and its derivatives relative to the CD spectrum of the purified TlpA protein). While a protein-ligand fusion will provide its own energetic stabilization to the complex if the k_D of the pair is measurable, the relative ΔG of this association may not match that of DNA-DBD binding and as such it would be useful to understand the dynamics of the coiled-coil terminus in isolation.

We have investigated several proximity-based optical approaches such as Forster Resonance Energy Transfer (FRET)[64], Proximity Imaging fluorescence (PRIM)[65], dimerization-

dependent fluorescence (ddXFP)[66], and split luciferase complementation (NanoBiT)[67], for determining the effects of local thermal perturbations to the TlpA structure. We first investigated the use of chemical fluorophores conjugated to the N-terminus of the TlpA coiled-coil. We utilized an N-terminal cysteine fusion to the putative coiled-coil fragment (Met-Cys-TlpA$_{69-359}$) and functionalized it with one of two maleimide-conjugated Alexa fluorescent dyes containing the spectral overlap necessary for FRET to occur. We reasoned that the internal C318 of TlpA is packed into the interface and would therefore be inaccessible for dye labeling, granting selective tracking of the labeled N-terminus. To correct for thermal effects on the dye itself we employed the method of Saccà et al[68], tracking emission intensity of the donor in the presence or absence of the acceptor. Using this approach, we computed the curve shown in **Fig. 5-7b**, which demonstrates a characteristic melting sigmoid with a slightly broader transition and lower T_m than the bulk melting profile observed by CD spectroscopy in **Fig. 5-5b**. While it is tempting to draw conclusions about the fraying behavior of the N-terminus from this data, further validation must be performed to assess potential technical challenges. One such challenge is in understanding the cause of sample-to-sample variation. In **Fig. 5-7c**, the FRET ratio is computed via the Saccà method from pairwise comparison of two wells containing donor-labeled TlpA and two wells containing a mix of donor and acceptor-labeled strands. The two different donor wells produce curves of varying switching sharpness, and it will be important to investigate possible causes of this variability, such as protein denaturation or aggregation, differential labeling efficiency, or potentially partial labeling of the internal cysteine. The latter issue may be circumvented by capitalizing on the single tryptophan residue present in the TlpA N-terminal domain at position 46, which can be directly utilized as a chemical handle via a

recently developed selective coupling reaction[69] or replaced with an azide-containing derivative for facile click labeling[70]. A further complexity, shown in **Fig. 5-7d**, is that despite producing similar curves after normalization, the raw FRET values are quite different between the four possible cross-pairings between two replicates. These differences could also be caused by the aforementioned factors but must be accounted for prior to drawing conclusions for this assay. A further complexity is the potential for thermal effects on dye fluorescence, and therefore on the FRET ratio itself. While the Saccà FRET formula accounts for dye-specific changes in intensity by background subtracting the signal from a reference donor fluorophore in the absence of the acceptor, temperature-induced changes to dye fluorescence may influence spectral overlap and the corresponding FRET efficiency. Therefore, dyes should be selected to minimize thermal effects. As shown in Figure **5-7E**, both the Alexa 546 donor and the Alexa 594 acceptor demonstrate changes in signal intensity upon thermal cycling. While Alexa 594 is relatively stable, displaying a 7% change in signal over four cycles between 25 °C and 50 °C and a 3.5% change within a single cycle, the Alexa 546 molecule shows a drastic 28% signal increase over the full experiment (9% within a single cycle). Both dyes show a characteristic drop in signal intensity as temperature increases followed by a return to a higher baseline upon cooling, resulting in overall signal growth over multiple temperature cycles. Importantly, the FRET ratio for free dye molecules shows no sign of a cooperative transition as a function of temperature (**Fig. 5-7f**) and has a smaller magnitude than the protein FRET signal at the same molecular concentration, suggesting that the transition observed with the dye-labeled protein is indeed induced by a conformational change.

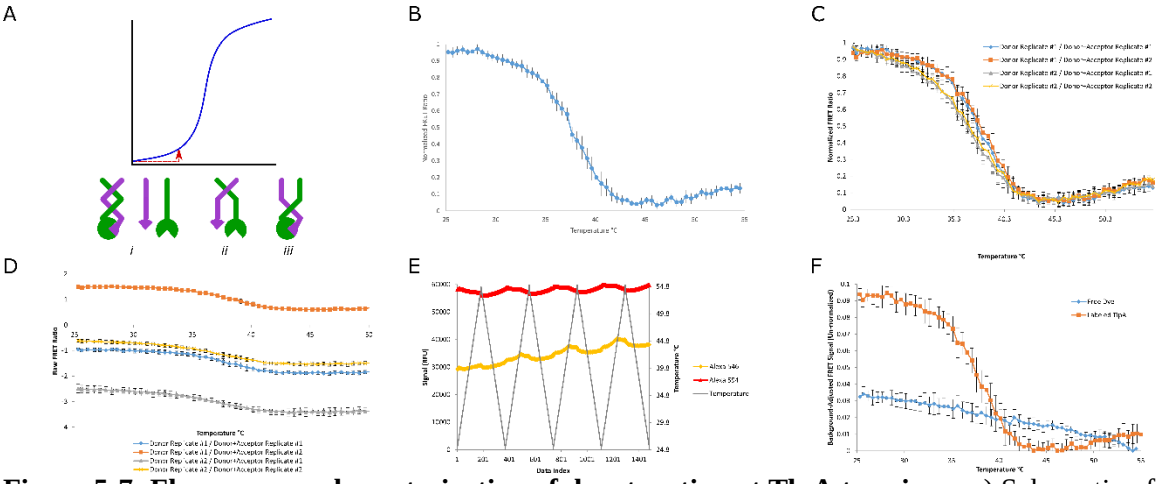

Figure 5-7: Fluorescence characterization of denaturation at TlpA terminus. a) Schematic of possible interpretations of the pre-transition increase in elipticity observed in circular dichroism analysis of TlpA denaturation. This increase can correspond to *i*: a mixed population of fully coiled dimers and fully uncoiled monomers, *ii*: partial uncoiling of TlpA at one terminus, which could potentially impact the dimerization of a locally fused protein, *iii*: partial uncoiling of TlpA at a terminus distal to a potential fusion protein which would not be impacted by the local denaturation. **b**) FRET melting curve computed according to the method of Saccà et al for the TlpA coiled coil fragment with a cysteine residue inserted at position 2 and fused to Alexa 546 or Alexa 594-maleimide conjugates. Data represents the mean of N = 2 donor wells and N = 2 donor/acceptor wells. **c**) FRET melting curve of the four possible combinations of donor and donor/acceptor wells averaged over three consecutive thermal ramps. **d**) The same data as in panel C, but with normalization omitted, demonstrating variable raw signal intensity. **e**) Fluorescence intensity of unreacted Alexa 546 or 594-maleimide conjugates over four thermal cycles between 25 and 55 °C. **f**) Comparison of non-normalized FRET intensity of TlpA-conjugated Alexa fluors or free dyes, averaged over there consecutive thermal cycles.

5.7: On the Concentration-Dependence of TlpA Dissociation

Some engineering applications may require precise control of the TlpA thermal setpoint. As previously reported in the literature, we observed that the melting temperature of TlpA is concentration dependent (**Fig. 5-8a**) and shifts by nearly 3 °C above 1 μM (**Fig. 5-8b**). While the strength of *tlpA* gene expression governs the protein concentration at a bulk level, cell-to-cell variability in protein level can be significant especially for systems without feedback inhibition[71]. To begin addressing this concern, we have investigated the possibility of generating covalent TlpA dimer fusions such that, regardless of the absolute protein

concentration in solution, local TlpA strand concentration could not fall below a minimum set by the linker length. Because the TlpA coiled-coil dimerizes in parallel orientation, a linker between the C-terminus of one strand and the N-terminus of its partner would need to span the predicted 30-40 nm length of the protein. Such a linker may be difficult to clone and would waste a significant amount of sequence space in a viral vector. Instead, we investigated the possibility of harnessing the SpyCatcher/SpyTag system for generating covalent isopeptide bonds spontaneously between two separately expressed proteins[72]. Structural modeling of a coiled-coil fused to the SpyCatcher domain predicted that the linker between the partner strand and its cognate SpyTag would need to span approximately 13 Ångstroms (**Fig. 5-8c**). We therefore constructed a variant of TlpA fused at the C-terminus to SpyCatcher and also built partner variants in which the TlpA is separated from the SpyTag moiety by Gly_3, Gly_5, and Gly_7 linkers. We found that the resulting constructs produced soluble proteins and that isopeptide bond formation occurred freely for all three variants (**Fig. 5-8d**). Unfortunately, the strong β-sheet component of the SpyCatcher domain interferes with circular dichroism analysis of the resulting constructs. Future investigation may be performed using TlpA-gated gene expression analysis, wherein the TlpA may be driven by a weak inducible promoter in a non-feedback configuration to determine its ability to repress its cognate promoter at increasingly low protein copy numbers.

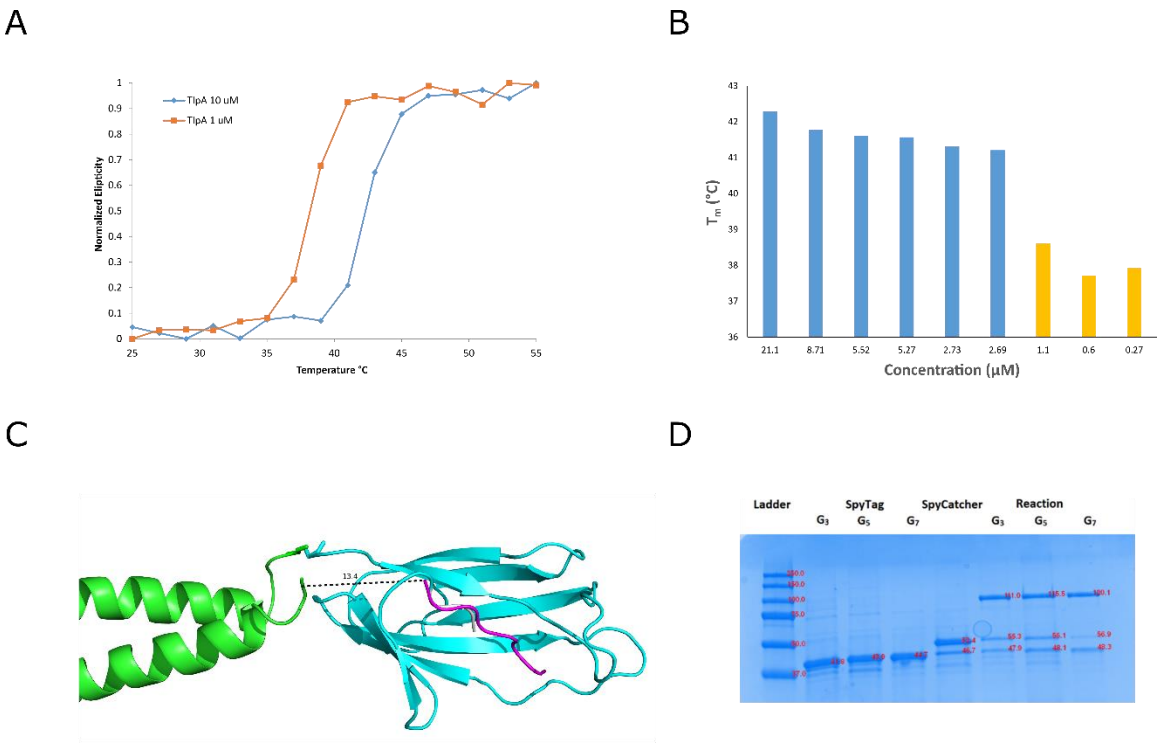

Figure 5-8: Concentration-dependence of TlpA Dissociation. a) Circular dichroism melting curves of the TlpA coiled-coil fragment at 10 μM and 1 μM concentration. Note the shift in T_m. **b**) T_m values computed from CD melting curves of the TlpA coiled-coil fragment at a range of concentrations between 21.1 and 0.27 μM. **c**) Structural modeling of a coiled-coil (Geminin, PDB 4BRY) fused to the SpyCatcher/SpyTag covalent complex (PDB 4MLI). **d**) Coomassie stained SDS-PAGE of *E. coli* lysate demonstrating the shift of unreacted TlpA-SpyTag (36 kDa) and TlpA-SpyCatcher (45 kDa) to a 91 kDa covalent fusion.

5.8: Discussion

The modular and simple structure of TlpA suggests that it could be functionalized and employed for a multitude of applications, following a developmental trajectory similar to that of chemically and optically inducible dimerization systems. Reaching this objective will require robust demonstration that TlpA is functional as a fusion to a variety of protein

domains including signaling proteins and enzymes. To date, the ability to fuse TlpA to proteins of interest has been hampered by a lack of concrete structural data. In the absence of an atomic resolution structure or firm evidence for the boundaries of the coiled-coil domain, TlpA domain fusions must begin from one or several educated inferences regarding the optimal junction site. High-resolution structures generated via X-ray crystallography or electron microscopy, in addition to fine-grained truncation and mutagenesis studies using circular dichroism spectroscopy or native transcriptional modulation in bacteria, may enable the production of functional and robust TlpA fusion proteins.

Thermal control remains the most accessible method to modulate biological function noninvasively and at depth within large animal models and in human patients (see Chapter 2). The lack of synthetic biology tools to confer temperature-responsive behavior to arbitrary proteins of interest greatly limits the range of applications available to this technology both in fundamental research and in the clinic. In prokaryotes, the TlpA and TcI thermal bioswitches have enabled ultrasound and fever-responsive transcription (Chapter 3). In the future, this technology may enable physicians to activate microbial therapeutics in a “point and click” fashion to increase the safety and efficacy of these treatments. In mammalian cells, such control is currently limited to heat shock promoters, which suffer from crosstalk with non-thermal stress pathways and a lack of temperature tunability. The advances described herein in using TlpA as a modular thermal bioswitch to control protein-protein interactions (Chapter 4) demonstrate the feasibility of imparting a novel, noninvasive control axis to any number of biological pathways of interest. Control of sub-cellular localization or inducible association with biological inhibitors of function can enable biomodulation in arbitrary cell

types, including in mammalian cells, on timescales of seconds or minutes. In the future, functional analysis of TlpA variants using platforms such as those discussed in this chapter can inform the design of bioactive protein-TlpA chimeras for scientific and clinical applications. We expect that our prototype TlpA-based bioswitch will serve as the foundation of a widespread method to utilize ultrasound-based or physiological hyperthermia as a new and important method to study biological processes, and potentially to enable the development of safer biological therapies.

5.9: Methods

Plasmid Construction and Molecular Biology

Plasmids were designed using SnapGene (GSL Biotech) and assembled via KLD mutagenes, Gibson Assembly, or restriction/ligation using enzymes from New England Biolabs. All plasmids and sequences will be uploaded as a supplemental file. After assembly, constructs were transformed into NEB Turbo, NEB10β, or NEB Stable *E. coli* (New England Biolabs) for growth and plasmid preparation. Thermal gene expression assays were performed in NEB10β. Fluorescent reporters and transcription repression genes and circuits were obtained from our previous work[1].

Thermal Regulation Assay

Determination of temperature-dependent gene expression was performed as described previously[1]. Saturated precultures were diluted to OD_{600} = 0.1 and propagated at 30 °C until reaching OD_{600} = 0.3 as measured via Nanodrop 2000c (Thermo Scientific). 25 uL aliquots were dispensed into PCR tubes with transparent caps (Bio-Rad) and incubated for 12 hours

in a thermal gradient using a Bio-Rad C1000 Touch thermocycler. After thermal stimulus, fluorescence was measured using a Stratagene MX3005p qPCR (Agilent), after which cultures were diluted 4x, transferred into microplates (Costar black / clear bottom), and measured for OD_{600} using a Molecular Devices SpectraMax M5 plate reader. The background-corrected F/OD is reported as described previously[1].

Protein Expression

pET26b-based expression constructs were transformed into BL21-DE3 *E. coli* and grown on kanamycin-selective plates. Saturated overnight cultures were diluted 1 mL into 400 mL expression cultures and induced with a final IPTG concentration of 1 mM at OD_{600} = 0.6. After 24 hours of expression at 25 °C, cultures were harvested by centrifugation using a JLA-16.250 rotor (Beckman Coulter) at 6,000 rpm and 4 °C for 8 minutes. Pellets were lysed using the detergent Solulyse in Tris Buffer (Genlantis) and debris was pelleted by centrifugation at 35,343 rcf in a JS-24.38 rotor (Beckman Coulter). Polyhistidine-tagged proteins were purified on an AKTA purifier (GE Healthcare) using 1 mL cOmplete columns (Roche) and buffer exchanged into 1x PBS (Corning) using Zeba 7K MWCO desalting columns (Thermo Fisher Scientific). Concentration was determined using the Pierce 660nm Protein Assay (Thermo Fisher Scientific) and proteins were stored at 4 °C until use.

Circular Dichroism Spectroscopy

CD melting curves were taken using an Aviv Circular Dichroism Spctrophotometer (Model 60DS) at 222 nm with 0.1 minute equilibration time and 5 second averaging time. Purified proteins were diluted to 10 µM (unless specified otherwise) in 1x PBS and measured in a 1 mm quartz cuvette.

Protein FRET measurement

10 mM stocks of Alexa 546 and Alexa 594-maleimide conjugates (Thermo Fisher Scientific) were prepared in anhydrous DMSO (Sigma Aldrich). Purified Met-Cys-TlpA was diluted to 2 µM in 1x PBS and split into two 50 uL aliquots. 10 mM Alexa-maleimide was added so as to achieve 10-fold molar excess of dye:protein. Reactions were performed overnight at room temperature. Dye was removed via filtration through 7,000 MWCO Zeba column. Labeled proteins were mixed in equal volumes (10 uL each species), heated to 45 °C for 10 minutes in an Eppendorf Thermomixer to promote strand exchange, and then cooled down to room temperature. For the donor-only sample required for calculating the temperature-corrected FRET ratio, the Alexa 546-labeled protein was mixed with 1x PBS instead of the Alexa 594-labeled variant. The 20 uL samples were transferred to optically clear PCR strips (Bio Rad) and donor fluorescence as a function of temperature was measured on the HXRX channel of the Stratagene MX3005p qPCR instrument.

5.10: References

1. Piraner, D. I., Abedi, M. H., Moser, B. A., Lee-Gosselin, A. & Shapiro, M. G. Tunable thermal bioswitches for in vivo control of microbial therapeutics. *Nat. Chem. Biol.* **13**, 75–80 (2017).
2. Szostak, M. P. *et al.* Bacterial ghosts : non-living candidate vaccines. **44**, (1996).
3. Valdez-Cruz, N. a, Caspeta, L., Pérez, N. O., Ramírez, O. T. & Trujillo-Roldán, M. a. Production of recombinant proteins in E. coli by the heat inducible expression system based on the phage lambda pL and/or pR promoters. *Microb. Cell Fact.* **9**, 18 (2010).
4. Spencer, D. M., Wandless, T. J., Schreiber, S. L. & Crabtree, G. R. Controlling signal transduction with synthetic ligands. *Science (80-.).* **262**, 1019–1024 (1993).
5. Liang, F.-S., Ho, W. Q. & Crabtree, G. R. Engineering the ABA Plant Stress Pathway for Regulation of Induced Proximity. *Sci. Signal.* **4**, 1–9 (2011).
6. Miyamoto, T. *et al.* Rapid and orthogonal logic gating with a gibberellin-induced dimerization system. *Nat. Chem. Biol.* **8**, 465–470 (2012).
7. Hill, Z. B., Martinko, A. J., Nguyen, D. P. & Wells, J. A. Human antibody-based chemically induced dimerizers for cell therapeutic applications. *Nat. Publ. Gr.* (2017). doi:10.1038/nchembio.2529
8. DeRose, R., Miyamoto, T. & Inoue, T. Manipulating signaling at will: chemically-inducible dimerization (CID) techniques resolve problems in cell biology. *Pflügers Arch. - Eur. J. Physiol.* **465**, 409–417 (2013).
9. Shimizu-Sato, S., Huq, E., Tepperman, J. M. & Quail, P. H. A light-switchable gene promoter system. *Nat. Biotechnol.* **20**, 1041–1044 (2002).
10. Yazawa, M., Sadaghiani, A. M., Hsueh, B. & Dolmetsch, R. E. Induction of protein-protein interactions in live cells using light. *Nat. Biotechnol.* **27**, 941–945 (2009).
11. Kawano, F., Suzuki, H., Furuya, A. & Sato, M. Engineered pairs of distinct photoswitches for optogenetic control of cellular proteins. *Nat. Commun.* **6**, 6256 (2015).
12. Koski, P. *et al.* A new alpha-helical coiled coil protein encoded by the Salmonella typhimurium virulence plasmid. *J. Biol. Chem.* **267**, 12258–12265 (1992).
13. Hurme, R., Berndt, K. D., Namork, E. & Rhen, M. DNA Binding Exerted by a Bacterial Gene Regulator with an Extensive Coiled-coil Domain. *J. Biol. Chem.* **271**, 12626–12631 (1996).
14. Sadowski, M. I. & Jones, D. T. The sequence–structure relationship and protein function prediction. *Curr. Opin. Struct. Biol.* **19**, 357–362 (2009).
15. Lehrer, S. S. & Qian, Y. Unfolding/refolding studies of smooth muscle tropomyosin. Evidence for a chain exchange mechanism in the preferential assembly of the native heterodimer. *J. Biol. Chem.* **265**, 1134–1138 (1990).
16. Lehrer, S. S. & Stafford, W. F. Preferential assembly of the tropomyosin heterodimer: equilibrium studies. *Biochemistry* **30**, 5682–5688 (1991).
17. Krishnan, V. & Rupp, B. Macromolecular Structure Determination: Comparison of X-ray Crystallography and NMR Spectroscopy. in *eLS* (John Wiley & Sons, Ltd, 2012). doi:10.1002/9780470015902.a0002716.pub2
18. Murata, K. & Wolf, M. Cryo-electron microscopy for structural analysis of dynamic biological macromolecules. *Biochim. Biophys. Acta - Gen. Subj.* **1862**, 324–334 (2018).
19. Frueh, D. P., Goodrich, A. C., Mishra, S. H. & Nichols, S. R. NMR methods for structural studies of large monomeric and multimeric proteins. *Curr. Opin. Struct. Biol.* **23**, 734–739 (2013).
20. Kumar, D. *et al.* Pseudo 5D HN(C)N experiment to facilitate the assignment of backbone resonances in proteins exhibiting high backbone shift degeneracy. *Chem. Phys.* **441**, 144–151 (2014).

21. Li, Y., Berthold, D. A., Gennis, R. B. & Rienstra, C. M. Chemical shift assignment of the transmembrane helices of DsbB, a 20-kDa integral membrane enzyme, by 3D magic-angle spinning NMR spectroscopy. *Protein Sci.* **17**, 199–204 (2008).
22. Hurme, R., Namork, E., Nurmiaho-Lassila, E.-L. & Rhen, M. Intermediate filament-like network formed in vitro by a bacterial coiled coil protein. *J. Biol. Chem.* **269**, 10675–10682 (1994).
23. Martin, T. G. *et al.* Design of a molecular support for cryo-EM structure determination. *Proc. Natl. Acad. Sci.* **113**, E7456–E7463 (2016).
24. Coscia, F. *et al.* Fusion to a homo-oligomeric scaffold allows cryo-EM analysis of a small protein. *Sci. Rep.* **6**, 30909 (2016).
25. Liu, Y., Gonen, S., Gonen, T. & Yeates, T. O. Near-atomic cryo-EM imaging of a small protein displayed on a designed scaffolding system. *Proc. Natl. Acad. Sci.* **115**, 3362–3367 (2018).
26. Kato, T., Goodman, R. P., Erben, C. M., Turberfield, A. J. & Namba, K. High-Resolution Structural Analysis of a DNA Nanostructure by cryoEM. *Nano Lett.* **9**, 2747–2750 (2009).
27. Ketterer, P. *et al.* DNA origami scaffold for studying intrinsically disordered proteins of the nuclear pore complex. *Nat. Commun.* **9**, 902 (2018).
28. Kollman, J. M., Pandi, L., Sawaya, M. R., Riley, M. & Doolittle, R. F. Crystal Structure of Human Fibrinogen. *Biochemistry* **48**, 3877–3886 (2009).
29. Bhardwaj, A., Casjens, S. R. & Cingolani, G. Exploring the atomic structure and conformational flexibility of a 320 Å long engineered viral fiber using X-ray crystallography. *Acta Crystallogr. Sect. D Biol. Crystallogr.* **70**, 342–353 (2014).
30. Bhardwaj, A. *et al.* Structural Plasticity of the Protein Plug That Traps Newly Packaged Genomes in Podoviridae Virions. *J. Biol. Chem.* **291**, 215–226 (2016).
31. Whitby, F. G. & Phillips, G. N. Crystal structure of tropomyosin at 7 Angstroms resolution. *Proteins Struct. Funct. Genet.* **38**, 49–59 (2000).
32. McPherson, A. & Cudney, B. Optimization of crystallization conditions for biological macromolecules. *Acta Crystallogr. Sect. F Struct. Biol. Commun.* **70**, 1445–1467 (2014).
33. Müller, I. Guidelines for the successful generation of protein–ligand complex crystals. *Acta Crystallogr. Sect. D Struct. Biol.* **73**, 79–92 (2017).
34. Hurme, R., Berndt, K. D., Normark, S. J. & Rhen, M. A proteinaceous gene regulatory thermometer in Salmonella. *Cell* **90**, 55–64 (1997).
35. Drozdetskiy, A., Cole, C., Procter, J. & Barton, G. J. JPred4: a protein secondary structure prediction server. *Nucleic Acids Res.* **43**, W389–W394 (2015).
36. Lupas, a, Van Dyke, M. & Stock, J. Predicting coiled coils from protein sequences. *Science (80-.).* **252**, 1162–1164 (1991).
37. McDonnell, A. V., Jiang, T., Keating, A. E. & Berger, B. Paircoil2: improved prediction of coiled coils from sequence. *Bioinformatics* **22**, 356–358 (2006).
38. Vincent, T. L., Green, P. J. & Woolfson, D. N. LOGICOIL--multi-state prediction of coiled-coil oligomeric state. *Bioinformatics* **29**, 69–76 (2013).
39. Kirwan, J. P. & Hodges, R. S. Transmission of Stability Information through the N-domain of Tropomyosin Is Interrupted by a Stabilizing Mutation (A109L) in the Hydrophobic Core of the Stability Control Region (Residues 97–118). *J. Biol. Chem.* **289**, 4356–4366 (2014).
40. Beasley, M. Conserved Disruptions in the Predicted Coiled-Coil Domains of Eukaryotic SMC Complexes: Implications for Structure and Function. *Genome Res.* **12**, 1201–1209 (2002).
41. Gunning, P. W., Hardeman, E. C., Lappalainen, P. & Mulvihill, D. P. Tropomyosin - master regulator of actin filament function in the cytoskeleton. *J. Cell Sci.* **128**, 2965–2974 (2015).
42. Mason, J. M., Schmitz, M. A., Muller, K. M. & Arndt, K. M. Semirational design of Jun-Fos coiled coils with increased affinity: Universal implications for leucine zipper prediction and

design. *Proc. Natl. Acad. Sci.* **103**, 8989–8994 (2006).
43. Vorov, O. K., Livesay, D. R. & Jacobs, D. J. Helix/coil nucleation: a local response to global demands. *Biophys. J.* **97**, 3000–9 (2009).
44. Fujiwara, Y., Takeshita, K., Nakagawa, A. & Okamura, Y. Structural Characteristics of the Redox-sensing Coiled Coil in the Voltage-gated H + Channel. *J. Biol. Chem.* **288**, 17968–17975 (2013).
45. Avner, B. S. *et al.* Myocardial infarction in mice alters sarcomeric function via post-translational protein modification. *Mol. Cell. Biochem.* **363**, 203–215 (2012).
46. Gal-Mor, O., Valdez, Y. & Finlay, B. B. The temperature-sensing protein TlpA is repressed by PhoP and dispensable for virulence of Salmonella enterica serovar Typhimurium in mice. *Microbes Infect.* **8**, 2154–62 (2006).
47. Husain, M. *et al.* Redox sensor SsrB Cys203 enhances Salmonella fitness against nitric oxide generated in the host immune response to oral infection. *Proc. Natl. Acad. Sci.* **107**, 14396–14401 (2010).
48. van der Heijden, J., Bosman, E. S., Reynolds, L. A. & Finlay, B. B. Direct measurement of oxidative and nitrosative stress dynamics in Salmonella inside macrophages. *Proc. Natl. Acad. Sci.* **112**, 560–565 (2015).
49. Lee, C., Zhong, L., Mace, T. A. & Repasky, E. A. Elevation in Body Temperature to Fever Range Enhances and Prolongs Subsequent Responsiveness of Macrophages to Endotoxin Challenge. *PLoS One* **7**, e30077 (2012).
50. Habicht, G. S. Body temperature in normal and endotoxin-treated mice of different ages. *Mech. Ageing Dev.* **16**, 97–104 (1981).
51. Altschul, S., Gish, W., Miller, W., Myers, E. & Lipman, D. Basic local alignment search tool. *J. Mol. Biol.* **215**, 403–410 (1990).
52. Deligios, M. Structural and functional genomic analysis of the salmonella enterica host-restricted serotype abortusovis. (Universita Degli Studi di Sassari, 2008).
53. Casutt-Meyer, S. *et al.* Oligomeric Coiled-Coil Adhesin YadA Is a Double-Edged Sword. *PLoS One* **5**, e15159 (2010).
54. Kosugi, S. *et al.* Six classes of nuclear localization signals specific to different binding grooves of importin alpha. *J. Biol. Chem.* **284**, 478–85 (2009).
55. Hu, J. C., O'Shea, E. K., Kim, P. S. & Sauer, R. T. Sequence requirements for coiled-coils: analysis with lambda repressor-GCN4 leucine zipper fusions. *Science* **250**, 1400–3 (1990).
56. Mariño-Ramírez, L., Campbell, L. & Hu, J. C. Screening Peptide/Protein Libraries Fused to the λ Repressor DNA-Binding Domain in E. coli Cells. in *E. coli Gene Expression Protocols* 235–250 (Humana Press, 2011). doi:10.1385/1-59259-301-1:235
57. Yin, X. *et al.* Contribution of Disulfide Bridges to the Thermostability of a Type A Feruloyl Esterase from Aspergillus usamii. *PLoS One* **10**, e0126864 (2015).
58. You, C., Huang, Q., Xue, H., Xu, Y. & Lu, H. Potential hydrophobic interaction between two cysteines in interior hydrophobic region improves thermostability of a family 11 xylanase from Neocallimastix Patriciarum. *Biotechnol. Bioeng.* **105**, n/a-n/a (2010).
59. Aurora, R. & Rosee, G. D. Helix capping. *Protein Sci.* **7**, 21–38 (1998).
60. Dragan, A. I. & Privalov, P. L. Unfolding of a Leucine zipper is not a Simple Two-state Transition. *J. Mol. Biol.* **321**, 891–908 (2002).
61. Fesinmeyer, R. M., Peterson, E. S., Dyer, R. B. & Andersen, N. H. Studies of helix fraying and solvation using 13 C′ isotopomers. *Protein Sci.* **14**, 2324–2332 (2005).
62. Kwok, S. C. & Hodges, R. S. Stabilizing and Destabilizing Clusters in the Hydrophobic Core of Long Two-stranded α-Helical Coiled-coils. *J. Biol. Chem.* **279**, 21576–21588 (2004).
63. Mohana-borges, R. *et al.* LexA Repressor Forms Stable Dimers in Solution. *J. Biol. Chem.* **275**, 4708–4712 (2000).

64. Piston, D. W. & Kremers, G.-J. Fluorescent protein FRET: the good, the bad and the ugly. *Trends Biochem. Sci.* **32**, 407–14 (2007).
65. De Angelis, D. a, Miesenböck, G., Zemelman, B. V & Rothman, J. E. PRIM: proximity imaging of green fluorescent protein-tagged polypeptides. *Proc. Natl. Acad. Sci. U. S. A.* **95**, 12312–6 (1998).
66. Alford, S. C., Ding, Y., Simmen, T. & Campbell, R. E. Dimerization-dependent green and yellow fluorescent proteins. *ACS Synth. Biol.* **1**, 569–575 (2012).
67. Dixon, A. S. *et al.* NanoLuc Complementation Reporter Optimized for Accurate Measurement of Protein Interactions in Cells. *ACS Chem. Biol.* (2015). doi:10.1021/acschembio.5b00753
68. Saccà, B., Meyer, R. & Niemeyer, C. M. Temperature-dependent FRET spectroscopy for the high-throughput analysis of self-assembled DNA nanostructures in real time. *Nat. Protoc.* **4**, 271–85 (2009).
69. Seki, Y. *et al.* Transition Metal-Free Tryptophan-Selective Bioconjugation of Proteins. *J. Am. Chem. Soc.* **138**, 10798–10801 (2016).
70. Italia, J. S., Addy, P. S., Wrobel, C. J. J., Crawford, L. A. & Lajoie, M. J. An orthogonalized platform for genetic code expansion in both bacteria and eukaryotes. *Nat. Chem. Biol.* **13**, 446–450 (2017).
71. Murphy, K. F., Adams, R. M., Wang, X. & Collins, J. J. Tuning and controlling gene expression noise in synthetic gene networks. *Nucleic Acids Res.* **38**, 2712–2726 (2010).
72. Zakeri, B. *et al.* Peptide tag forming a rapid covalent bond to a protein, through engineering a bacterial adhesin. *Proc. Natl. Acad. Sci. U. S. A.* **109**, E690-7 (2012).